

**Quantum-Mechanical Evaluation of the Thermodynamics and Kinetics of  
Environmentally-Relevant Actinide Reactions**

by

Will Martin Bender

A dissertation submitted in partial fulfillment  
of the requirements for the degree of  
Doctor of Philosophy  
(Earth and Environmental Sciences)  
in The University of Michigan  
2019

Doctoral Committee:

Professor Udo Becker, Chair  
Associate Professor Rose M. Cory  
Assistant Professor Brian R. Ellis  
Professor Mark E. Meyerhoff

Will Martin Bender

benderwm@umich.edu

ORCID: 0000-0003-1964-9240

© Will Martin Bender 2019

All Rights Reserved

# **DEDICATION**

*For my family, friends, and teachers.*

## ACKNOWLEDGEMENTS

Many people have played a role in my doctoral degree experience here at Michigan and I will try my best to thank them all here. To those who I may fail to acknowledge, know that I am sorry and that your impact was felt.

First off, I would like to thank my advisor, Udo Becker, for the opportunity to work with him at Michigan. Everything that I have accomplished here truly would not have been possible without your guidance, advice, and seemingly limitless source of new ideas. We only spoke briefly before I decided to come and it was a bit of a gut decision, but I really could not be happier with how it turned out. Thank you for giving me the freedom to pursue my interests and helping me find ways to stay positive and apply myself, especially when things didn't go as planned. In addition to Udo, I would like to thank the other members of my dissertation committee, Brian Ellis, Rose Cory, and Mark Meyerhoff, for their time and feedback throughout my candidacy. I would also like to thank Greg Dick who served as a committee member for several years before we had to make a change due to final scheduling conflicts.

I am also very grateful to the research group mates I overlapped with during my degree program: Sarah Walker, YoungJae Kim, Ke Yuan, Ben Gebarski, Sooyeon Kim, Peter Cook, Evan Killeen, Saumitra Saha, and Krishnamoorthy Arumugam. It would not have been the same without you all and you have all helped contribute to the work in this dissertation in some meaningful way. Thank you all for listening to practice presentations and providing constructive feedback, reading

drafts of proposals and manuscripts, helping with programming quandaries, sharing meals, and providing encouragement at odd hours. I would also like to thank Neal Hughes for his help in the lab during the initial stages of our group's foray into (photo)electrochemistry. Special thanks to Maria Marcano for all of her tireless efforts in our laboratory space; I don't know where our group would be without you.

I would also like to thank several people who enriched my experience here in the Department and provided me with opportunities outside of my research commitments. Thanks to Jackie Li, Adam Simon, Shelie Miller, and Michela Arnaboldi for letting me serve as a GSI and grader for your courses. My teaching experiences on campus and at Camp Davis were some of the highlights of my time as a graduate student. Thank you also to Gordon Moore and Zhongrui Li who provided the opportunity for me to work in Electron Microbeam Analysis Laboratory. I really learned a lot about the instruments while helping the diverse user-base achieve their analytical goals. Thank you to Marin Clark for allowing me to serve as a graduate student mentor for two years - it was my pleasure and honor.

Thank you to the many people who make our department and the graduate student experience function smoothly, particularly Anne Hudon, Nancy Kingsbury, Bill Wilcox, Craig Delap, Dhammika Dewasurendra, Stacey Wilkin, Paula Frank, and Mike Messina. You all helped me in so many ways, whether it was addressing maintenance issues in our lab space, fixing problems with our computing cluster, procuring reagents with student funds, or providing sage advice and reminders about all things degree-related. You are always there for us as graduate students and we would be in such big trouble without you.

I have had the pleasure of meeting many great people here during my time at Michigan. I will carry with me lots of fond memories, starting from the days sharing the big first year office

with Alyssa Abbey, Molly Blakowski, Sam Haugland, Sean Hurt, James Jolles, Evan Killeen, Erin Lynch, Mark Robbins, Collin Ward, and Spencer Washburn. Thanks also to Phoebe Aron, Tristan Childress, Alex Cusick, Joe El Adli, Sharon Grim, Pam Horsley, Tom Hudgins, Lucas Joel, Brian Konecke, Nikita La Cruz, David Levine, Amanda Loh, Ross Maguire, Juliana Mesa, Kyle Meyer, Mackenzie Moore, Jill Myers, Samantha Nemkin, Peng Ni, Xiaofei Pu, Alex Stefanov, Meghan Taylor, Kate Turner, Alex Tye, Meg Veitch, Kalli Washburn, and Ian Winkelstern for all the good times working and playing in our building, around town, and all over the world, from Canada to Chile. Particular thanks to my officemates of the last few years: Alex K., Sharon, Sarah, Sean, and Juliana. Your daily companionship was valued and enjoyed. Thank you also to my friends from childhood and college who I was lucky to have with me in Ann Arbor and the greater Midwest: Hayley Beckett, Sam Kollar, Stacey Rosenzweig, Taro Tomiya, and Julian Watanabe. It was a real treat to reconnect with you all in this new place. I am so glad to have met many friendly and fun people, including many more I failed to list here, and I look forward to more time spent together out in the “real” world.

I would like to thank many family members, my parents, Ruth and Dan, my sister, Anna, my Ann Arbor/Dexter/Chelsea-based grandparents, Marilyn and Dale, my Petoskey-based grandmother, Ruth, and my great aunt and uncle, Nancy and Wendel, for all of your love, support, and encouragement. I am especially grateful to my grandparents and extended family who live in Washtenaw County. We spent so many good times together over these years and I learned a lot from you all as you experienced a number of significant life moments – selling a beloved century farm, battling with degenerative disease, and eventually, the passing of Wendel and Dale. I am grateful to have been present to share in those experiences, however hard, and am so impressed by the perspective and grace with which you have handled it all. Overall, it has been such a pleasure

being so close to all of my extended family members in Michigan, the Midwest, and across all of the United States after so many years living in Japan. The visits, vacations, and holidays we have shared together have all played a key role recharging me emotionally over the course of the marathon that is a doctoral program.

Lastly, I would like to thank Zoe for her love, companionship, and patience. It has been a real and motivating joy living with you these past few years in Ann Arbor. I know we both look forward to what the future holds.

# TABLE OF CONTENTS

DEDICATION .....	ii
ACKNOWLEDGEMENTS .....	iii
LIST OF TABLES .....	x
LIST OF FIGURES .....	xi
ABSTRACT.....	xv
CHAPTER 1 Introduction.....	1
Actinide waste and the nuclear fuel cycle.....	2
Environmental geochemistry of actinides.....	4
Computational methods in geochemistry.....	6
Overview of research chapters.....	9
References.....	14
CHAPTER 2 Quantum-mechanical investigation of the structures and energetics of uranium and plutonium incorporation into the magnetite (Fe <sub>3</sub> O <sub>4</sub> ) lattice.....	22
Abstract.....	22
Introduction.....	23
Computational approach.....	29
The magnetite structure .....	29
Quantum-mechanical calculations.....	30
Periodic solids.....	31
Periodic molecules and clusters .....	33
Frequency calculations.....	34
Results.....	36

Physical and electronic structure of actinide-incorporated magnetites .....	36
Changes to the lattice and cation coordination .....	36
Electronic structure of incorporated phases .....	38
Energetics of incorporation reactions .....	43
Reactions with solid phases .....	43
Reactions with aqueous source and sink phases .....	48
Discussion .....	51
Comparison to available literature data .....	51
Calculated reaction energies and evaluating sources of error .....	53
Conclusions .....	58
Acknowledgements .....	60
Appendix 2A: Full suite of tested incorporation reactions and their energies .....	62
References .....	63
CHAPTER 3 Determining the kinetics of discrete aqueous redox reaction sub-steps using computational methods: Application to reactions of plutonyl ( $\text{PuO}_2^{+2+}$ ) with $\text{Fe}^{2+}$ , $\text{Fe}^{3+}$ , and hydroxyl radical ( $\bullet\text{OH}$ ) .....	70
Abstract .....	70
Introduction .....	72
Methodology .....	76
Defining sub-steps in a redox reaction and calculating their rates .....	76
Quantum-mechanical calculations .....	83
Results .....	86
Determination of the reactive radius .....	86
Collision rates and outer-sphere complex formation .....	87
Physical structure changes during the transition from outer-sphere to inner-sphere complex .....	89
Rates of outer- to inner-sphere complex transition .....	92
Electronic structure changes and the reduction of Pu .....	97
Discussion .....	99
Trends in reactive radii and impact on outer-sphere complex formation rate .....	99
Response of systems moving from outer- to inner-sphere .....	100
Expanding this framework to other systems .....	105

Conclusions.....	106
Acknowledgements.....	108
Appendix 3A: Testing of computational parameters .....	109
Basis set superposition error (BSSE).....	109
Zero-point vibrational energies .....	110
Choice of basis set .....	111
References.....	113
<b>CHAPTER 4 Resolving the kinetics of individual aqueous reaction steps of actinyl (<math>AnO_2^+</math> and <math>AnO_2^{2+}</math>; An = U, Np, and Pu) tricarbonate complexes with ferrous iron and hydrogen sulfide from first principles .....</b>	<b>119</b>
Abstract.....	119
Introduction.....	120
Computational methods .....	124
Results.....	129
Calculated reactive radii .....	130
Rates of outer-sphere complex formation .....	131
Formation of inner-sphere complexes and associated energy barriers.....	135
Testing of proton-coupled electron transfer as a mechanism for actinyl reduction .....	141
Discussion.....	145
Conclusions.....	151
Acknowledgements.....	155
References.....	156
<b>CHAPTER 5 Conclusions.....</b>	<b>164</b>
References.....	171

## LIST OF TABLES

<b>Table 2.1</b> Calculated hydration energies (in eV) for aqueous cation source and sink phases compared to experimental data .....	35
<b>Table 2.2</b> DFT+ <i>U</i> calculated bonding environment (coordination number, CN, and interatomic distances, R) of structurally-incorporated U in magnetite compared to selected computational and experimental values from the literature .....	40
<b>Table 2.3</b> DFT+ <i>U</i> calculated bonding environment (coordination number, CN, and interatomic distances, R) of structurally-incorporated Pu in magnetite.....	41
<b>Table 2.4</b> Selected DFT+ <i>U</i> calculated incorporation energies ( $\Delta E_{\text{inc}}$ , in eV) for U and Pu into magnetite with solid and aqueous source and sink phases .....	47
<b>Table 2.5</b> Example of the conversion process to aqueous source and sink phases for the incorporation of $\text{U}^{4+}$ into the octahedral $\text{Fe}^{2+}$ site of magnetite balanced by an $\text{Fe}^{2+}$ vacancy.....	49
<b>Table 2.6</b> All DFT+ <i>U</i> calculated incorporation energies ( $\Delta E_{\text{inc}}$ , in eV) for U and Pu into magnetite with solid and aqueous source and sink phases .....	62
<b>Table 3.1</b> Calculated reactive radii ( <i>R</i> ) for different reactant pairs, spin configurations, and computational parameters .....	87
<b>Table 3.2</b> Representative set of calculated half-lives ( $t_{1/2}$ ) of uncomplexed $\text{PuO}_2^{+(\text{aq})}$ as a function of reactant, concentration, and different computational settings .....	88
<b>Table 3.3</b> Calculated kinetic parameters for outer- to inner-sphere complex transitions .....	94
<b>Table 4.1</b> Calculated reactive radii ( <i>R</i> , in Å) for different $[\text{AnO}_2(\text{CO}_3)_3]^{x-6}$ -reductant <sup>a</sup> pairs....	131
<b>Table 4.2</b> Calculated half-lives ( $t_{1/2}$ ) of free actinyl tricarbonate complexes in solutions with the reductants $\text{Fe}^{2+}$ and $\text{H}_2\text{S}$ at different reactant concentrations .....	132
<b>Table 4.3</b> Calculated activation barrier parameters for reaction of actinyl tricarbonate complexes with $[\text{Fe}(\text{OH})_2(\text{H}_2\text{O})_4]^0$ and $[\text{H}_2\text{S}(\text{H}_2\text{O})_6]^0$ using the C-PCM solvation model .....	137

## LIST OF FIGURES

**Figure 2.1** The orthorhombic magnetite unit cell ( $\text{Fe}_{12}\text{O}_{16}$ , space group: *Imma*) viewed down its three crystallographic axes. Iron atoms are colored green ( $\text{Fe}^{2+}$ , octahedral), orange ( $\text{Fe}^{3+}$ , octahedral), and cream ( $\text{Fe}^{3+}$ , tetrahedral); oxygen atoms are shown in red. Unpaired spins on Fe are oriented upward in the octahedral cation positions and downward in tetrahedral sites resulting in a net spin moment of 16 for the ferromagnetic cell attributed to octahedral  $\text{Fe}^{2+}$ . A rhombohedral primitive cell, with the formula  $\text{Fe}_6\text{O}_8$ , was used for the quantum mechanical calculations in this study..... 30

**Figure 2.2** A view down the *b* axis of a  $2 \times 2$  supercell of  $\text{Pu}^{6+}$ -incorporated magnetite (formula unit:  $\text{Fe}_4\text{PuO}_8$ ). In this monoclinic structure, charge-balancing octahedral  $\text{Fe}^{3+}$  vacancies create distorted hexagonal channels running parallel to the *b* axis (out of the page). Fe atoms (all  $\text{Fe}^{2+}$ ) are shown in yellow and O in red. During optimization, Pu converges to an intermediate oxidation state between +4 and +5, based on spin density, and no Pu-O distances are found that are close those of plutonyl. .... 37

**Figure 2.3** Calculated partial density of states (PDOS) of the pure magnetite unit cell (upper) compared to that of a  $\text{U}^{5+}$ -incorporated magnetite with an octahedral Fe vacancy (lower;  $\text{Fe}_4\text{UO}_8$ ). Clear changes to the upper valence band below the band gap ( $E_{\text{gap}}$ ) due to the presence of U 5f orbitals are visible in the incorporated phase. The inset in the lower panel shows the PDOS of U and one coordinating O anion in the octahedral lattice position, revealing the hybridization of U 5f and O 2p orbitals responsible for bonding between these two atoms..... 45

**Figure 3.1** An idealized model showing the energy change in a system as a function of Pu–reactant distance. The distinct energy wells associated with the two complex types are shown, with this case representing a situation where the inner-sphere complex is the more energetically-favorable configuration. The activation energies of the outer- to inner-sphere transition reaction ( $E_{\text{a1}}$ ) and the back reaction ( $E_{\text{a1,back}}$ ) are shown, as are the position of the reactive radius (*R*), where the energy drops one  $k_B T$  unit below the bulk solution energy plateau, and the distance between the energy minima ( $x_1$ ) for this transition. .... 78

**Figure 3.2** The calculated energy surface for  $\text{PuO}_2^{2+}$  and  $\bullet\text{OH}$  shows energy steps associated with the formation of H bonds in the ferromagnetic vacuum state calculation. These bonds, shown for the step near 6 Å in Figure 3.3, are formed as  $\text{H}_2\text{O}$  and  $\text{OH}^-$  rearrange when the distance between Pu and the radical is decreased. The change in system energy reflects the number of new bonds that are formed. The dashed line shows the energy surface if the energy of these bonds forming is subtracted, resulting in a broad outer-sphere well, as opposed to three discrete outer-sphere

complex configurations (OSC 1-3), that yields slow kinetics for the transformation to the inner-sphere complex (ISC) at  $\sim 2.25$  Å. .... 81

**Figure 3.3** Optimized structures from sequential calculations in the ferromagnetic  $\text{PuO}_2^{2+}$  and  $\bullet\text{OH}$  distance series in vacuum. Pu – radical O (atom labeled “R”) distances are 6.5 and 6.25 Å for panels A and B respectively. Panel B represents the OSC 2 structure shown in Figure 3.2. Two new hydrogen bonds are formed at this distance between the starred atoms that corresponds to significant energy gain ( $\sim 75$  kJ/mol) for the system. Atom colors are red for O, white for H, and green for Pu. Hydrogen bonds are shown as dotted blue lines, all other bonds are in black..... 91

**Figure 3.4** Calculated concentrations of all component steps of the reaction between antiferromagnetic  $\text{PuO}_2^{2+}$  and  $\text{Fe}^{2+}$  in C-PCM. Concentrations of the uncomplexed reactants in the bulk solution (initially 1  $\mu\text{M}$  for  $\text{Fe}^{2+}$  and 1 nM for  $\text{PuO}_2^{2+}$ ), as well as the concentrations of the two outer-sphere (OSC 1 at 6.25 Å and OSC 2 at 5.5 Å) and one inner-sphere (ISC at 4.25 Å) complexes are evaluated over time using the transition rates derived from the energy versus reactant distance data for this system..... 96

**Figure 3.5** Bader charge and spin populations of the plutonyl molecule and Fe cation over the course of the ferromagnetic distance series in vacuum. Charge and spin remain constant over the bulk solution and outer-sphere distance range, but electron transfer from  $\text{Fe}^{2+}$  to  $\text{Pu}^{6+}$  takes place at 4.25 Å. This change in electronic structure is coincident with beginning of the inner-sphere energy well that has its minimum at a Pu-Fe distance of 3.75 Å..... 98

**Figure 3.6** Calculated energy surfaces for some select plutonyl and iron systems in vacuum. Energy surfaces show a variety of features including parabolic wells, sloped steps, and spikes. These changes in the energy surface are related to changes in the geometry (such as H bond formation and tilting of the plutonyl molecule) and also, in the  $\text{Fe}^{2+}$  reactions, transfer of electron density to reduce  $\text{Pu}^{6+}$  to  $\text{Pu}^{5+}$  at  $\sim 4$  Å. .... 103

**Figure 3.7** Comparison of the original calculated system energies (orange line) to those calculated with the counterpoise keyword and have the basis set superposition error (BSSE) correction applied (blue line) for the ferromagnetic  $\text{PuO}_2^+/\text{Fe}^{3+}$  reaction in vacuum..... 109

**Figure 3.8** Comparison of the relative energy vs. distance curves for the ferromagnetic  $\text{PuO}_2^+/\text{Fe}^{3+}$  system in vacuum with (blue line) and without (orange line) the inclusion of the zero-point vibrational energy as calculated using the frequency module of Gaussian 09. .... 110

**Figure 3.9** Energy vs. distance curves for the ferromagnetic  $\text{PuO}_2^+/\text{Fe}^{3+}$  system in vacuum using two different basis set combinations. The orange line represents our standard computational settings using the LANL2DZ basis with pseudopotentials on Fe and Pu. The blue line is the same series calculated with the AUG-cc-pVTZ all-electron correlation consistent basis set on H, O, and Fe. There is a significant shift in the trajectory of the curve with this basis set, however, the positions of energy minima corresponding to different complex configurations and the energy of forwards and backward reaction barriers do not result in different conclusions regarding the kinetics of this reaction. .... 111

**Figure 4.1** The calculated structure of  $[\text{UO}_2(\text{CO}_3)_3]^{4-}$ . The three carbonate groups are in bidentate coordination of the central  $\text{U}^{6+}$  in the linear uranyl molecule. The U- $\text{O}_{\text{ax}}$  bond length (labeled as

R), an indicator of oxidation state, is slightly longer than those found in uranyl water or hydroxide complexes. The U-O<sub>carbonate</sub> and U-C distances are also an important measure of the actinide valence in this configuration and all these distances increase if U<sup>6+</sup> is reduced to U<sup>5+</sup>. Analogous complexes and structural responses are observed for the complexes of neptunyl and plutonyl. 122

**Figure 4.2** A schematic energy vs. distance relationship showing the decrease in energy associated with bringing a reductant closer to an actinide (An) species in solution. The position of the reactive radius (*R*) is indicated, as are the activation energies (*E<sub>a</sub>*) for the forward and backward reactions and the distance between the two energy minima (*x*). These parameters are gathered from the calculated reaction distance series and used to evaluate the rates of transitions between different complex configurations..... 126

**Figure 4.3** Calculated energy versus distance curves for actinyl tricarbonate, [AnO<sub>2</sub>(CO<sub>3</sub>)<sub>3</sub>]<sup>x-6</sup>, complexes reacted with [Fe(OH)<sub>2</sub>(H<sub>2</sub>O)<sub>4</sub>]<sup>0</sup> and [H<sub>2</sub>S(H<sub>2</sub>O)<sub>6</sub>]<sup>0</sup>. Energies (in kJ/mol) are normalized so that zero represents the energy of the reactants in the bulk solution (An-reductant distances >9 Å). Outer- and inner-sphere energy minima are defined in the regions of 4.25-6 Å and 3-3.75 Å, respectively, and vary between different actinyls and valences. .... 133

**Figure 4.4** The structure of an outer-sphere complex of H<sub>2</sub>S with [UO<sub>2</sub>(CO<sub>3</sub>)<sub>3</sub>]<sup>4-</sup> at a U-S distance of 5.5 Å. At this distance, H<sub>2</sub>S has passed a proton via a neighboring water molecule to CO<sub>3</sub><sup>2-</sup> to form HCO<sub>3</sub><sup>-</sup> and HS<sup>-</sup>. The bicarbonate molecule remains in bidentate configuration at this distance, but as the HS<sup>-</sup> is brought closer to U, both the bicarbonate and adjacent carbonate will begin to bend out of the equatorial plane and rotate to become monodentate around the central actinyl. This motion will result in an energy barrier between outer- and inner-sphere energy minima. Similar structures are observed for the other actinyl complexes in reactions with H<sub>2</sub>S..... 135

**Figure 4.5** Panels A, B, and C show the approach of an [Fe(OH)<sub>2</sub>(H<sub>2</sub>O)<sub>4</sub>]<sup>0</sup> cluster towards [PuO<sub>2</sub>(CO<sub>3</sub>)<sub>3</sub>]<sup>5-</sup> at Pu-Fe distances of 6, 4, and 3.75 Å, respectively. These distances correspond to an outer-sphere complex (A), and inner-sphere complex (C), and a transition state between them (B). A water molecule forms a hydrogen bond to two carbonate groups in panel C, but in the transition to the inner-sphere complex this molecule is squeezed up out of the x-y plane which holds the carbonate groups, Pu, and Fe. In panel C, this molecule is now hydrogen bonded to one of the plutonyl O atoms. The energy cost associated with breaking the water hydrogen bonds the main source of the *E<sub>a</sub>* between the outer- and inner-sphere complex..... 138

**Figure 4.6** Panels A and B show the change in concentration of bulk aqueous uranyl tricarbonate along with inner- and outer-sphere complexes (OSC and ISC) with [Fe(OH)<sub>2</sub>(H<sub>2</sub>O)<sub>4</sub>]<sup>0</sup> over time starting from initial bulk uranyl and iron complex concentrations of 1 nM and 1 μM, respectively. The reaction with UO<sub>2</sub><sup>+</sup> in panel A has a small energy barrier for the formation of the ISC and, as such, the aqueous complex is rapidly converted to the ISC with no appreciable pool of OSC forming over time. The reaction of UO<sub>2</sub><sup>2+</sup> on the other hand has an activation energy large enough to allow for relatively rapid build up of the OSC followed by a slower increase in the concentration of the ISC. The concentrations in panel B are shown on a log scale to better capture the large concentration range..... 139

**Figure 4.7** Structures of a charge-neutral [FeUO<sub>2</sub>CO<sub>3</sub>(HCO<sub>3</sub>)<sub>2</sub>(H<sub>2</sub>O)<sub>6</sub>]<sup>0</sup> inner-sphere complex before (A) and after (B) a proton-coupled electron transfer (PCET) reaction. This particular

reaction has a  $\Delta E = 56$  kJ/mol. Alpha (blue) and beta (yellow) spin density are shown overlain on the structure and clearly describe the transition from a  $U^{6+}/Fe^{2+}$  to  $U^{5+}/Fe^{3+}$  electronic state. The overall spin multiplicity of the system is preserved as  $U^{5+}$  takes on beta (downward) spin orientation. The  $H^+$  is transferred from a water molecule to the uranyl O at the top of the structure and causes the  $U-O_{ax}$  bond to lengthen from 1.8 to 2.0 Å. The remaining U-O double bond also lengthens, to 1.87 Å, with reduction to  $U^{5+}$ . ..... 143

## ABSTRACT

The mobility of the early actinide (An) elements uranium, neptunium, and plutonium is dependent on a variety of different chemical processes. Many of these processes, including complex formation, adsorption to mineral surfaces, (co-)precipitation of mineral phases, and redox, are controlled by interactions at the atomic and molecular scale. Understanding the chemistry and behavior of the U, Np, and Pu at this fundamental level is critical to making informed decisions about the long-term geologic storage of spent nuclear fuel and remediation of contaminated sites. This dissertation applies quantum-mechanical modeling to study the thermodynamics, kinetics, and mechanisms of some of the aforementioned processes.

Structural incorporation of actinides into growing mineral phases is a potential pathway for immobilization. Chapter 2 of this dissertation explores the incorporation of U and Pu into magnetite ( $\text{Fe}_3\text{O}_4$ ), a corrosion product of steel. Actinide incorporation, from solid and aqueous sources with different oxidation states ( $\text{Pu}^{3+}$  and  $\text{An}^{4+/5+/6+}$ ), is explored using a multi-step computational approach. We find U and Pu assume the  $\text{An}^{5+}$  oxidation state when incorporated into the lattice via a coupled substitution mechanism. The atomic and electronic structures align with available data for synthetic U-incorporated magnetite and we present the first descriptions of Pu-incorporated phases. Comparable reaction energetics of Pu and U incorporation, preferentially from  $\text{An}^{4+}$  and  $\text{An}^{5+}$  sources, suggest magnetite may be an important sink for both elements in near-field environments of repositories.

Dissolved actinides, present in solution as actinyl molecules ( $\text{An}^{\text{V,VI}}\text{O}_2^{\text{x}+}_{(\text{aq})}$ ,  $\text{x} = 1$  or  $2$ ), may also react with  $\text{Fe}^{2+}$  and other redox-active species in a homogenous manner without the involvement of a mineral phase. Chapter 3 presents a new computational approach that combines collision theory and quantum-mechanical calculation to determine the thermodynamics and kinetics of discrete reaction sub-processes: (1) the collision of dissolved species to form an outer-sphere complex, (2) the transition from outer- to inner-sphere complex, and (3) electron transfer. For the reactions of plutonyl hydrolysis complexes with  $\text{Fe}^{2+}$ ,  $\text{Fe}^{3+}$ , and hydroxyl radical, energetically-favorable outer-sphere complexes are found to form rapidly. Subsequent conversion to the inner-sphere complex configuration is achieved after overcoming activation energy barriers which are mainly related to dehydration and reorganization of coordinating solvent molecules ( $\text{H}_2\text{O}$  and  $\text{OH}^-$ ) as An-reactant distances are decreased. Inner-sphere complex formation is coincident with reduction of  $\text{Pu}^{6+}$  by  $\text{Fe}^{2+}$ . The rate-limiting step for the tested reactions is predicted to be electron transfer given the favorable kinetics of the preceding sub-processes.

This computational approach is extended in Chapter 4 to study the reactions of uranyl, neptunyl, and plutonyl tricarbonate complexes with  $\text{Fe}^{2+}$  and  $\text{H}_2\text{S}$ . These common, stable complexes are known to inhibit actinide reduction in natural environments. The calculated kinetic parameters are in line with this understanding and in some cases, significant activation energy barriers are observed for the formation of inner-sphere complexes which necessitate disruption of the carbonate coordination environment. Spontaneous one-electron reduction of  $\text{An}^{6+}$  and  $\text{An}^{5+}$  is not observed and proton transfer, tested manually, from water and/or bicarbonate is necessary to induce reduction of  $\text{An}^{6+}$  to  $\text{An}^{5+}$ . These results suggest that the tricarbonate complex effectively shields actinyls from reduction and will maintain their solubility in environments with alkaline pH

and sufficient aqueous carbonate. The method used in Chapters 3 and 4 can now be applied to other reactant pairs and also, with some modification, reactions catalyzed by mineral surfaces.

# CHAPTER 1

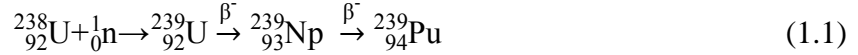
## Introduction

The speciation, toxicity, and mobility of metal contaminants in the environment is affected by a wide array of biogeochemical processes which include mineral growth and dissolution, adsorption and desorption of aqueous species to surfaces, and redox reactions.<sup>1-2</sup> These processes are linked and compete with each other under different chemical conditions. The behavior of metal contaminants in the environment has been a focus of field, laboratory, and computational research efforts for many decades.<sup>3-5</sup> Carcinogenic and radioactive compounds have drawn particular attention because of the hazards they pose to humans and other biota if released into surface or ground waters, soils, and/or the air. The components of nuclear waste represent one such group of compounds and the reactions of some of these elements (specifically uranium, as well as the anthropogenic elements neptunium and plutonium) in some environmentally-relevant scenarios are explored in this dissertation at the molecular and atomic scale using computational approaches. While this thesis focuses on the actinide elements, the general principles developed here (*i.e.*, the delineation of reaction mechanisms into individual reaction steps and the prediction of resulting reaction kinetics) can be applied to wide variety of geochemical processes.

## Actinide waste and the nuclear fuel cycle

Nuclear power generation and weapons production generates a range of different radioactive waste forms.<sup>6-7</sup> Starting from the ore extraction and processing stage, uranium-bearing mine tailings are exposed to the elements and are a source of radionuclide contamination to surface environments.<sup>8-10</sup> Subsequent enrichment of U increases the concentrations of specific fissile isotopes for power generation or use in nuclear warheads where controlled or runaway fission reactions generate new waste forms. Two major categories of these wastes are lighter fission products, which tend to have relatively short half-lives ( $t_{1/2}$ ), and the long-lived actinide waste products, which include the transuranic elements neptunium, plutonium, and americium. Spent nuclear fuel from a reactor typically contains approximately 3 to 4 atomic percent of these radioactive species that are the result of the  $^{235}\text{U}$  fission chain reaction process (the exact values are a function of the initial fuel chemistry and the extent of the fission reaction, referred to as “burn up”).<sup>11</sup>

Fission products, formed when the fissile actinide isotopes like  $^{235}\text{U}$  and  $^{239}\text{Pu}$  split apart, are highly-radioactive  $\beta^-$  and  $\gamma$  emitters. Isotopes like  $^{90}\text{Sr}$  and  $^{137}\text{Cs}$  have  $t_{1/2}$  values of 28.8 and 30.2 years, respectively, and are the major source of radiation and heat from spent nuclear fuel over the first few hundred years after removal from a reactor. After this period, the radioactivity of spent nuclear fuel becomes dominated by the long-lived actinide isotopes which include a significant component of the  $^{235}\text{U}$  and  $^{238}\text{U}$  fuel which remains as well as transuranic isotopes of Np, Pu, and Am.<sup>11</sup> These isotopes are generated via neutron capture and subsequent radioactive decay chains. For example, the fissile isotope  $^{239}\text{Pu}$  is generated from  $^{235}\text{U}$  via a multi-step process involving neutron capture followed by two subsequent and rapid  $\beta^-$  decay cycles (with half-lives of approximately 23 min and 2.3 days, respectively) via the following reaction:



Some of the transuranic isotopes have been generated via stellar processes in the universe<sup>12-14</sup> and in rare natural reactors on Earth (*e.g.*, at Oklo, Gabon), but the amounts are very small.<sup>15</sup>

These longer-lived actinide isotopes generally decay via the emission of an  $\alpha$  particle, which is equivalent to a  ${}^4\text{He}$  nucleus. These particles cannot penetrate basic protective measures like gloves, clothing, or even human skin. They are, however, a hazard if ingested via the consumption of contaminated water, food, or inhalation of particles into the respiratory track. Due to the higher mass of the particle,  $\alpha$  radiation is many times more damaging to the human body than  $\beta$  or  $\gamma$  radiation.<sup>16</sup> Actinides, like other heavy metals, are also toxic purely from the standpoint of metal poisoning and can have negative impacts on a range of bodily organs and processes.<sup>17</sup> The half-lives of isotopes like  ${}^{237}\text{Np}$  and  ${}^{239}\text{Pu}$  are long ( $t_{1/2} = 2.1$  million years and 24,110 years, respectively) and as such, the planning for the storage of these waste materials over thousands to millions of years must be considered. This issue presents a number of scientific, engineering, societal, and government policy challenges.<sup>6,18-19</sup>

The current consensus is to eventually store radioactive waste forms from nuclear power, defense, and medical applications underground in a geologic repository. The selection of repository sites and the design of the containment structures, as well as a number of other factors, remain areas of ongoing research and debate. At present, the United States has one geologic repository in operation that houses defense-related wastes. The facility, in the arid state of New Mexico, is called the Waste Isolation Pilot Plant<sup>20</sup> (WIPP) and houses waste in galleries deep inside of an evaporite deposit. The Yucca Mountain site in Nevada<sup>21</sup> was a long-time candidate to house the nation's nuclear waste, but the political and financial support for the project has stalled.

Elsewhere around the world, countries with nuclear power are at various stages of planning, construction, and implementation of centralized waste storage schemes. In Sweden, a centralized underground waste storage site for short-lived wastes has been in operation since 1988.<sup>22</sup> A site for a long-term geologic storage of spent nuclear fuel has been selected, but is still in the pre-construction phase. Finland is perhaps furthest along in constructing a waste repository for spent fuel from power-generating activities. The deep geologic repository, called Onkalo, carved into a gneissic bedrock is under construction presently and is expected to start receiving and storing waste by 2024.<sup>23</sup> Other countries like France, Germany, Japan, Belgium, Switzerland, the United States, and the United Kingdom are still in various stages of policy formation, site selection, design, and testing, with most still at least a decade away from even beginning construction.<sup>24</sup>

Throughout all phases of repository design, the potential for accidents and release of radionuclides into the environment must be considered. Indeed, at many locations across the world, actinide contaminants have already made their way into the environment as a result of human activities. These activities and events include nuclear weapons testing<sup>25</sup>, improper waste disposal at legacy sites<sup>26-27</sup> (e.g., shallow burial of waste drums at Hanford, WA), and accidents at nuclear power facilities<sup>28-29</sup> (e.g., Chernobyl, Ukraine, and Fukushima, Japan). Understanding how actinides behave under a variety of environmental and chemical conditions is critical to designing effective waste storage and remediation strategies.

## **Environmental geochemistry of actinides**

The environmental chemistry of the actinides is complex and depends on a number of different processes.<sup>30</sup> The speciation of actinides under different conditions, their various chemical reactions, and how these reactions may change the mobility of these contaminants are all important

factors to consider when characterizing the behavior of these elements in the environment. Broadly, the environmental chemistry of actinide elements is dominated by redox reactions.<sup>30-32</sup> Actinides are somewhat unique in their ability to assume a wide range of different oxidation states. In natural environments, the elements U, Np, and Pu can exist between +3 and +6. In natural environments, the most common oxidation states are +4, +5, and +6.<sup>31</sup> In laboratory settings, actinide metals can also be generated and for Np and Pu the +7 oxidation state is also accessible under certain chemical conditions.<sup>33</sup> In oxidizing environments, the actinides are soluble and mobile in the form of linear dioxocations. These molecules are called actinyls and have the formula  $An^{V,VI}O_2^{x+}_{(aq)}$ , where  $x = 1$  or  $2$  depending on the valence of the actinide center, +5 or +6, respectively. These species form complexes with a range of different organic and inorganic ligands including hydroxide, carbonate, and humic substances.<sup>34</sup> The formation of stable aqueous complexes can maintain the solubility of actinyls and make them less likely to participate in other chemical processes (*e.g.*, redox reactions, co-precipitation of mineral phases).<sup>34</sup> In lower oxidation states, +3 and +4, the actinide elements preferentially form insoluble oxide phases; one such phase is the U ore mineral uraninite,  $U^{IV}O_{2(s)}$ .<sup>35</sup>

In general, oxidizing environments cause actinide molecules to be more mobile, and reducing environments drive (co-)precipitation of insoluble compounds. As such, much of the research regarding actinide transport in the environment is focused on redox reactions. Redox reactions can proceed in either a homogeneous or heterogeneous fashion.<sup>36-37</sup> Homogeneous reactions take place in the dissolved phase, where the reductant and oxidant meet in solution, forming an outer- or inner-sphere complex, before taking part in an electron transfer reaction. Outer-sphere complexes exist when two fully solvated complexes are in contact with each other (*i.e.*, with one or more water molecules in between). Inner-sphere complexes occur at shorter

reactant-reactant distances occur when the reactants are partially decomplexed so that they are connected through a bridging ligand or ligand(s). If water is the coordinating species, this decomplexation is referred to specifically as dehydration. In general, inner-sphere complexes are known or expected to have faster rates of electron transfer relative to the outer-sphere configuration.<sup>38-41</sup>

Heterogeneous reactions, on the other hand, occur when the reaction involves a surface. An example would be if a dissolved actinyl molecule were to adsorb to an Fe<sup>2+</sup>-bearing mineral surface and be reduced via electron transfer from one (or more) Fe<sup>2+</sup> atoms present in the mineral.<sup>42</sup> Alternatively, a process is also considered to be heterogeneous if both an oxidant and reductant adsorb to a mineral surface which mediates the reaction, either priming adsorbed compounds for direct electron transfer or shuttling an electron from the reductant to the oxidant through the mineral surface.<sup>38,41</sup> The outer- and inner-sphere complex definitions can be applied again to heterogeneous reactions to describe the coordination environment of the adsorbed species. In the inner-sphere case, the bridging ligands would be part of the mineral surface (*e.g.*, hydroxylated O atoms in an oxide mineral).<sup>43</sup> In any given environment, homogeneous and heterogeneous processes are in competition with each other. The experimental<sup>44-49</sup> and computational<sup>38-39,50-55</sup> research communities have devoted significant effort to evaluating the thermodynamics and kinetics of these processes to establish an understanding of which reactions are the dominant controls on metal contaminant speciation.

## **Computational methods in geochemistry**

A variety of experimental and analytical approaches are available to scientists seeking to study the reactions that control metal contaminant mobility in the environment.<sup>56-58</sup> Field scale

observations of natural or engineered systems, as well as laboratory experiments and materials synthesis, all contribute to the understanding of these chemical processes. However, these approaches, and the analytical methods that support them, are subject to some limitations.<sup>59</sup> Computational approaches serve to support and confirm experimental findings and can also reveal certain fundamental aspects of reaction mechanisms that may be otherwise impossible to obtain.<sup>59-61</sup>

Computational methods in environmental geochemistry can generally be separated into two categories: molecular (or classical) mechanics and quantum mechanics.<sup>59</sup> Molecular mechanics modeling is based on the principles of classical physics and characterizes the structures and physical properties of solids, liquids, and gasses by using derived empirical datasets. These interatomic potentials can be calibrated to available experimental data, for example the lattice parameters of a mineral, heat capacity, or sound speeds.<sup>62</sup> If such data are unavailable, interatomic potentials can be derived from quantum-mechanical calculations. These models have the advantage of being relatively inexpensive from a computational standpoint. This makes them particularly well-suited for the modeling of dynamic systems with large numbers of molecules.<sup>63-65</sup> The approach is, however, subject to the quality of the underlying potential set and in some cases, potentials may not even be available for a given system. Additionally, this approach is not able to model in detail any aspects of the electronic structure of different materials. Atoms considered to have specific charges, but the detailed behavior of individual electrons and their contribution to the properties on the system is not considered. As such, any computational investigation of electronic spin configuration, band structure, or optical properties must instead use quantum mechanics.

Results of quantum-mechanical calculations are sometimes said to have come from *first principals*. This is because unlike with molecular mechanics, there are no empirical parameters that are given to the model to start with. Instead, the atomic system is set up and a specific number of electrons, or all, are considered explicitly. Then, the model solves for electronic wavefunction solutions to the Schrödinger equation, within a framework of provided inputs and assumptions, and determines the energies and distribution of the electrons in the system.<sup>59,66</sup> Depending on the number of atoms included in the model and the specific computational scheme selected, this procedure can become quite time consuming. To lessen computational expense, many studies use a pseudopotential that groups the contribution of some number of inner-shell electrons into a potential leaving a smaller number of valence electrons, those that are involved with bonding and electronic transitions, to be calculated explicitly. Additionally, different basis sets or plane wave cutoff energies, which approximate the electronic behavior of different atomic orbitals or the localization of electron density, respectively, can be selected to vary the computational rigor.

The calculation of actinide-bearing systems using quantum mechanics poses some unique challenges. Firstly, actinides have a large number of electrons and thus, pose practical limits on the number of atoms that can be included in any all-electron calculation (one where no pseudopotential is used). Additionally, actinides are heavy and the large nucleus causes relativistic contraction of the electronic energy levels.<sup>67-68</sup> Actinides also have unpaired electron spins in their valence shells for most of the prevalent oxidation states (with  $U^{6+}$  being a notable exception) and spin-orbit coupling and on-site Coulomb interaction of electrons can also affect the energy of these systems.<sup>69-70</sup> Computational treatment of these effects can be achieved by selecting specific parameters (*e.g.*, fully vs. scalar relativistic basis sets and pseudopotentials; Hubbard  $U$

parameters) and decisions must be made to weigh theoretical accuracy against computational expense.

Overall, computational methods have broad applications to environmental geochemistry and Earth sciences in general. The details of the theory behind quantum-mechanical calculations and their applicability to these systems will not be discussed here, but the reader is referred to several texts<sup>61,71-73</sup> and review articles<sup>59-60,66</sup> that describe these concepts in detail. The chemistry of actinide elements is heavily-influenced by their electronic structures and although they present computational challenges, they are an excellent candidate for investigation with quantum-mechanical approaches. Numerous studies have applied these methods to study the structures and properties of actinide-bearing solids and molecular species, adsorption of actinides on mineral surfaces, and homogeneous and heterogeneous redox reactions. The methodological development and lessons learned from these studies underpin the work of this dissertation.

## **Overview of research chapters**

This dissertation utilizes some of the computational approaches described above and applies them to investigate reactions of actinides with a mineral species (Chapter 2) and in solution with other redox-active species (Chapters 3 and 4). Chapter 2 presents a study of the thermodynamics of U and Pu incorporation into a solid Fe oxide mineral phase, magnetite ( $\text{Fe}_3\text{O}_4$ ). Co-precipitation of actinides with growing mineral phases is a way for them to be removed from solution and become effectively immobilized. Actinide incorporation into a range of different mineral structures, including various (oxyhydr)oxides<sup>46,62,74-77</sup>, silicate<sup>78-79</sup>, carbonates,<sup>80-82</sup> sulfate<sup>54,80</sup>, and phosphate<sup>83-84</sup> minerals is known to occur. These phases have been synthesized in laboratories and also occur in nature (*e.g.*, U incorporated into apatite and zircon which are used

for U/Pb age dating of rocks). From an environmental and waste storage perspective, the incorporation of actinides into Fe-bearing (oxyhydr)oxide phases is of considerable interest as these species are corrosion products of steel, which is a component of most waste storage casks.<sup>85-88</sup> If leaking from some form of containment structure, these minerals may be some of the first solid phases that a mobilized actinide would encounter. Early corrosion products, and those that form in anoxic environments, like magnetite, still contain  $\text{Fe}^{2+}$ , which has the potential to act as an electron donor and reduce higher-valent actinides to their insoluble  $\text{An}^{4+}$  states.<sup>50,89-90</sup>

While U-incorporated magnetite has been synthesized in laboratory settings and analyzed using a range of different instrumental methods, still some confusion surrounds the chemical state of U in these minerals. The work presented in Chapter 2 clarifies the preferred electronic state of U and explores Pu incorporation which has yet to be attempted in a laboratory setting. The energies of incorporation reactions with different solid and aqueous source and sink phases are presented to gauge which reactions are most likely to proceed in the environment. This study employs a density functional theory-based approach<sup>91-93</sup> that allows for the mixing of cluster (for aqueous species like uranyl and  $\text{Fe}^{3+}$  water complexes) and periodic solid (for oxide phases) models. The calculated structures of the U- and Pu-incorporated phases are compared to available literature data (for U-magnetite only as no data exist for Pu incorporation).<sup>46,62,76-77,94-95</sup> The calculated interatomic distance parameters can be used as a reference for the fitting of spectroscopic data from analysis of unknown experimental products. The sources of error inherent in the calculation methodology are detailed and the implications of the findings for U and Pu in repository near-field environments are discussed.

Chapter 3 moves on to use quantum-mechanical methods to study homogeneous redox reactions of actinides. In this chapter, a novel approach for determining the rates of different redox

reaction sub-steps is developed, described, and applied to the reactions of plutonyl hydrolysis complexes ( $\text{PuO}_2(\text{OH})_2(\text{H}_2\text{O})_3^0$  and  $\text{PuO}_2(\text{OH})(\text{H}_2\text{O})_4^0$ ) with three different reactants:  $\text{Fe}^{2+}$ ,  $\text{Fe}^{3+}$ , and hydroxyl radical ( $\bullet\text{OH}$ ). These three reactants were selected to compare the energetics and kinetics of reaction with a reductant ( $\text{Fe}^{2+}$ ) to two oxidants ( $\text{Fe}^{3+}$  and  $\bullet\text{OH}$ ). Hydroxyl radical is a relevant species to consider as it is one of the reactive compounds formed via  $\alpha$  radiolysis of water. The computational scheme employs a combination of classical chemistry calculations to model encounter complex formation in solution and quantum mechanics to calculate the energetics of outer- and inner-sphere complex formation and conversion. A series of sequential geometry optimization calculations is carried out over progressively smaller reactant distance increments. From these calculations, an energy versus distance plot can be generated and used to derive kinetic parameters (activation energy and attempt frequency and, from these, the reaction rate constant) that are used to calculate the kinetics of the transition between outer- and inner-sphere complexes (and the back reactions). The calculated kinetics sources of the energy barriers for the different tested reactions are compared and the extent of Pu reduction by  $\text{Fe}^{2+}$  is explored.

In the last research chapter (Chapter 4), the computational method of Chapter 3 is extended to investigate the reactions of stable uranyl, neptunyl, and plutonyl tricarbonate complexes ( $\text{AnO}_2(\text{CO}_3)_3^{5-/4-}$ ) with two reductants,  $\text{Fe}^{2+}$  and  $\text{H}_2\text{S}$ . These species are stable and form in environments with elevated carbonate concentrations, like the oceans and limestone-hosted groundwaters. These species have been the focus of considerable attention because they are some of the most commonly-occurring natural complexes of the actinyls and have the effect of maintaining their solubility, and therefore their mobility, particularly in solutions with alkaline pH. This study seeks to characterize the thermodynamics and kinetics of the reaction of these complexes with  $\text{Fe}^{2+}$  and  $\text{H}_2\text{S}$  to see if carbonate serves as an effective shield against reduction.

The importance of proton-coupled electron transfer is explored as a mechanism for reduction in these systems and the findings are evaluated in the context of the previous work on hydrolysis complexes (Chapter 3), other computational studies of these carbonate complexes, and a variety of experimental investigations.

The research presented in this dissertation is expected to result in a total of three publications. One of the chapters has been published, while the other two have been submitted for consideration by academic journals and are in varying stages of review:

Bender, W. M.; Becker, U., Determining the kinetics of discrete aqueous redox reaction sub-steps using computational methods: Application to reactions of plutonyl ( $\text{PuO}_2^{+2+}$ ) with  $\text{Fe}^{2+}$ ,  $\text{Fe}^{3+}$ , and hydroxyl radical ( $\bullet\text{OH}$ ). *American Journal of Science* **2018**, *318*, 893-920.

Bender, W. M.; Becker, U., Quantum-mechanical investigation of the structures and energetics of uranium and plutonium incorporated into the magnetite ( $\text{Fe}_3\text{O}_4$ ) lattice. *ACS Earth and Space Chemistry* (in review, as of Jan. 2019).

Bender, W. M.; Becker, U., Resolving the kinetics of individual aqueous reaction steps of actinyl ( $\text{AnO}_2^+$  and  $\text{AnO}_2^{2+}$ ; An = U, Np, and Pu) tricarbonato complexes with ferrous iron and hydrogen sulfide from first principles. *Radiochimica Acta* (in review, as of Jan. 2019).

In addition, work on side projects with other graduate students and collaborators during this degree program has resulted in two co-authored publications. The first is a methods paper that details the computational approach later applied to the incorporation of U and Pu into magnetite

(Chapter 2) and the second is an electrochemical atomic force microscopy study of Cr<sup>6+</sup> reduction on the surface of magnetite.

Shuller-Nickles, L. C.; Bender, W. M.; Walker, S. M.; Becker, U., Quantum-mechanical methods for quantifying incorporation of contaminants in proximal minerals. *Minerals* **2014**, *4* (3), 690-715.

Walker, S. M.; Marcano, M. C.; Bender, W. M.; Becker, U., Imaging the reduction of chromium(VI) on magnetite surfaces using in situ electrochemical AFM. *Chemical Geology* **2016**, *429*, 60-74.

## References

1. Warren, L. A.; Haack, E. A., Biogeochemical controls on metal behaviour in freshwater environments. *Earth-Science Reviews* **2001**, *54* (4), 261-320.
2. Borch, T.; Kretzschmar, R.; Kappler, A.; Van Cappellen, P.; Ginder-Vogel, M.; Voegelin, A.; Campbell, K., Biogeochemical redox processes and their impact on contaminant dynamics. *Environmental Science & Technology* **2010**, *44* (1), 15-23.
3. Korte, N. E.; Fernando, Q., A review of arsenic(III) in groundwater. *Critical Reviews in Environmental Control* **1991**, *21* (1), 1-39.
4. Gross, A., Reactions at surfaces studied by ab initio dynamics calculations. *Surface Science Reports* **1998**, *32* (8), 291-340.
5. Jenne, E. A., Adsorption of metals by geomedia: Data analysis, modeling, controlling factors, and related issues. In *Adsorption of metals by geomedia*, Jenne, E. A., Ed. Academic Press: San Diego, 1998; pp 2-76.
6. Burns, P. C.; Sigmon, G. E. In *Uranium - Cradle to grave*, Uranium - Cradle to Grave, Winnipeg, Burns, P. C.; Sigmon, G. E., Eds. Mineralogical Society of Canada: Winnipeg, 2013; pp 7-14.
7. Ewing, R. C., The nuclear fuel cycle: A role for mineralogy and geochemistry. *Elements* **2006**, *2* (6), 331-334.
8. Abdelouas, A., Uranium mill tailings: Geochemistry, mineralogy, and environmental impact. *Elements* **2006**, *2* (6), 335-341.
9. Abdelouas, A.; Lutze, W.; Nuttall, E., Chemical reactions of uranium in ground water at a mill tailings site. *Journal of Contaminant Hydrology* **1998**, *34* (4), 343-361.
10. Bernhard, G.; Geipel, G.; Brendler, V.; Nitsche, H., Uranium speciation in waters of different uranium mining areas. *Journal of Alloys and Compounds* **1998**, *271*, 201-205.
11. Bruno, J.; Ewing, R. C., Spent nuclear fuel. *Elements* **2006**, *2* (6), 343-349.
12. Huss, G. R.; Meyer, B. S.; Srinivasan, G.; Goswami, J. N.; Sahijpal, S., Stellar sources of the short-lived radionuclides in the early solar system. *Geochimica et Cosmochimica Acta* **2009**, *73* (17), 4922-4945.
13. Kuroda, P. K.; Myers, W. A., Plutonium-244 fission xenon and primordial xenon in the Allende meteorite. *Journal of Radioanalytical and Nuclear Chemistry* **1998**, *230* (1-2), 197-211.
14. Lachner, J.; Dillmann, I.; Faestermann, T.; Korschinek, G.; Poutivtsev, M.; Rugel, G.; von Gostomski, C. L.; Turler, A.; Gerstmann, U., Attempt to detect primordial Pu-244 on Earth. *Physical Review C* **2012**, *85* (1).

15. GauthierLafaye, F.; Holliger, P.; Blanc, P. L., Natural fission reactors in the Franceville basin, Gabon: A review of the conditions and results of a "critical event" in a geologic system. *Geochimica et Cosmochimica Acta* **1996**, *60* (23), 4831-4852.
16. Briner, W., The toxicity of depleted uranium. *International Journal of Environmental Research and Public Health* **2010**, *7* (1), 303-313.
17. ATSDR *Public health statement for uranium*; Centers for Disease Control and Prevention: Atlanta, 2013; p 11.
18. IAEA *Status and trends in spent fuel and radioactive waste management*; NW-T-1.14; IAEA: Vienna, 2018; p 57.
19. Johnson, J., Radioactive waste stranded as US shifts from nuclear energy. *Chemical & Engineering News* **2018**, *96* (37), 28-29.
20. Conca, J.; Kirchner, T., Environmental monitoring programs and public engagement for siting and operation of geological repository systems: experience at the Waste Isolation Pilot Plant (WIPP). *Geological Repository Systems for Safe Disposal of Spent Nuclear Fuels and Radioactive Waste* **2010**, (9), 678-718.
21. Bodvarsson, G. S.; Boyle, W.; Patterson, R.; Williams, D., Overview of scientific investigations at Yucca Mountain - the potential repository for high-level nuclear waste. *Journal of Contaminant Hydrology* **1999**, *38* (1-3), 3-24.
22. SKB - Our Operations. <http://www.skb.com/our-operations/sfr/> (accessed November 17, 2018).
23. Final disposal - Onkalo. [http://www.posiva.fi/en/final\\_disposal/onkalo](http://www.posiva.fi/en/final_disposal/onkalo) (accessed November 17, 2018).
24. Butler, D., France digs deep for nuclear waste. *Nature* **2010**, *466* (7308), 804-805.
25. Utsunomiya, S.; Kersting, A. B.; Ewing, R. C., Groundwater nanoparticles in the far-field at the Nevada test site: Mechanism for radionuclide transport. *Environmental Science & Technology* **2009**, *43* (5), 1293-1298.
26. Niles, K., The Hanford cleanup: What's taking so long? *Bulletin of the Atomic Scientists* **2014**, *70* (4), 37-48.
27. Qafoku, N. P.; Zachara, J. M.; Liu, C. X.; Gassman, P. L.; Qafoku, O. S.; Smith, S. C., Kinetic desorption and sorption of U(VI) during reactive transport in a contaminated Hanford sediment. *Environmental Science & Technology* **2005**, *39* (9), 3157-3165.
28. Grambow, B.; Poinssot, C., Interactions between nuclear fuel and water at the Fukushima Daiichi reactors. *Elements* **2012**, *8* (3), 213-219.

29. Steinhauser, G.; Brandl, A.; Johnson, T. E., Comparison of the Chernobyl and Fukushima nuclear accidents: A review of the environmental impacts. *Science of the Total Environment* **2014**, *470*, 800-817.
30. Maher, K.; Bargar, J. R.; Brown, G. E., Environmental speciation of actinides. *Inorganic Chemistry* **2013**, *52* (7), 3510-3532.
31. Choppin, G. R., Actinide speciation in the environment. *Journal of Radioanalytical and Nuclear Chemistry* **2007**, *273* (3), 695-703.
32. Silva, R. J.; Nitsche, H., Actinide environmental chemistry. *Radiochimica Acta* **1995**, *70* (1), 377-396.
33. Ikeda-Ohno, A.; Tsushima, S.; Takao, K.; Rossberg, A.; Funke, H.; Scheinost, A. C.; Bernhard, G.; Yaita, T.; Hennig, C., Neptunium carbonate complexes in aqueous solution: An electrochemical, spectroscopic, and quantum chemical study. *Inorganic Chemistry* **2009**, *48* (24), 11779-11787.
34. Szabo, Z.; Toraishi, T.; Vallet, V.; Grenthe, I., Solution coordination chemistry of actinides: Thermodynamics, structure and reaction mechanisms. *Coordination Chemistry Reviews* **2006**, *250* (7-8), 784-815.
35. Hazen, R. M.; Ewing, R. C.; Sverjensky, D. A., Evolution of uranium and thorium minerals. *Am Mineral* **2009**, *94* (10), 1293-1311.
36. Marcus, R. A.; Sutin, N., Electron transfers in chemistry and biology. *Biochimica et Biophysica Acta - Reviews in Bioenergetics* **1985**, *811* (3), 265-322.
37. Taube, H., *Electron transfer reactions of complex ions in solution*. Academic Press: New York, 1970; p 103.
38. Taylor, S. D.; Marcano, M. C.; Rosso, K. M.; Becker, U., An experimental and ab initio study on the abiotic reduction of uranyl by ferrous iron. *Geochimica et Cosmochimica Acta* **2015**, *156*, 154-172.
39. Collins, R. N.; Rosso, K. M., Mechanisms and rates of U(VI) reduction by Fe(II) in homogeneous aqueous solution and the role of U(V) disproportionation. *Journal of Physical Chemistry A* **2017**, *121* (35), 6603-6613.
40. Privalov, T.; Macak, P.; Schimmelpfennig, B.; Fromager, E.; Grenthe, I.; Wahlgren, U., Electron transfer in uranyl(VI)-uranyl(V) complexes in solution. *J Am Chem Soc* **2004**, *126* (31), 9801-9808.
41. Taylor, S. D.; Becker, U.; Rosso, K. M., Electron transfer pathways facilitating U(VI) reduction by Fe(II) on Al- vs. Fe-oxides. *Journal of Physical Chemistry C* **2017**, *121* (36), 19887-19903.

42. Skomurski, F. N.; Ilton, E. S.; Engelhard, M. H.; Arey, B. W.; Rosso, K. M., Heterogeneous reduction of  $U^{6+}$  by structural  $Fe^{2+}$  from theory and experiment. *Geochimica et Cosmochimica Acta* **2011**, *75* (22), 7277-7290.
43. Rustad, J. R., Molecular models of surface relaxation, hydroxylation, and surface charging at oxide-water interfaces. *Molecular Modeling Theory: Applications in the Geosciences* **2001**, *42*, 169-197.
44. Hixon, A. E.; Powell, B. A., Observed changes in the mechanism and rates of Pu(V) reduction on hematite as a function of total plutonium concentration. *Environmental Science & Technology* **2014**, *48* (16), 9255-9262.
45. Hua, B.; Xu, H. F.; Terry, J.; Deng, B. L., Kinetics of uranium(VI) reduction by hydrogen sulfide in anoxic aqueous systems. *Environmental Science & Technology* **2006**, *40* (15), 4666-4671.
46. Huber, F.; Schild, D.; Vitova, T.; Rothe, J.; Kirsch, R.; Schaefer, T., U(VI) removal kinetics in presence of synthetic magnetite nanoparticles. *Geochimica et Cosmochimica Acta* **2012**, *96*, 154-173.
47. Renock, D.; Mueller, M.; Yuan, K.; Ewing, R. C.; Becker, U., The energetics and kinetics of uranyl reduction on pyrite, hematite, and magnetite surfaces: A powder microelectrode study. *Geochimica et Cosmochimica Acta* **2013**, *118*, 56-71.
48. Begg, J. D.; Edelman, C.; Zavarin, M.; Kersting, A. B., Sorption kinetics of plutonium (V)/(VI) to three montmorillonite clays. *Appl Geochem* **2018**, *96*, 131-137.
49. Singer, D. M.; Chatman, S. M.; Ilton, E. S.; Rosso, K. M.; Banfield, J. F.; Waychunas, G. A., U(VI) sorption and reduction kinetics on the magnetite (111) surface. *Environmental Science & Technology* **2012**, *46* (7), 3821-3830.
50. Privalov, T.; Schimmelpfennig, B.; Wahlgren, U.; Grenthe, I., Reduction of uranyl(VI) by iron(II) in solutions: An ab initio study. *Journal of Physical Chemistry A* **2003**, *107* (4), 587-592.
51. Rosso, K. M.; Morgan, J. J., Outer-sphere electron transfer kinetics of metal ion oxidation by molecular oxygen. *Geochimica et Cosmochimica Acta* **2002**, *66* (24), 4223-4233.
52. Rosso, K. M.; Rustad, J. R., Ab initio calculation of homogeneous outer sphere electron transfer rates: Application to  $M(OH_2)_6^{3+/2+}$  redox couples. *Journal of Physical Chemistry A* **2000**, *104* (29), 6718-6725.
53. Taylor, S. D.; Marcano, M. C.; Becker, U., A first principles investigation of electron transfer between Fe(II) and U(VI) on insulating Al- vs. semiconducting Fe-oxide surfaces via the proximity effect. *Geochimica et Cosmochimica Acta* **2017**, *197*, 305-322.
54. Walker, S. M.; Becker, U., Uranyl (VI) and neptunyl (V) incorporation in carbonate and sulfate minerals: Insight from first-principles. *Geochimica et Cosmochimica Acta* **2015**, *161*, 19-35.

55. Wander, M. C. F.; Kerisit, S.; Rosso, K. M.; Schoonen, M. A. A., Kinetics of triscarbonato uranyl reduction by aqueous ferrous iron: A theoretical study. *Journal of Physical Chemistry A* **2006**, *110* (31), 9691-9701.
56. Vallet, V.; Macak, P.; Wahlgren, U.; Grenthe, I., Actinide chemistry in solution, quantum chemical methods and models. *Theoretical Chemistry Accounts* **2006**, *115* (2-3), 145-160.
57. Langmuir, D., *Aqueous environmental geochemistry*. Prentice-Hall: Upper Saddle River, New Jersey, 1997; p 600.
58. Altmaier, M.; Gaona, X.; Fanghanel, T., Recent advances in aqueous actinide chemistry and thermodynamics. *Chemical Reviews* **2013**, *113* (2), 901-943.
59. Cygan, R. T., Molecular modeling in mineralogy and geochemistry. *Molecular Modeling Theory: Applications in the Geosciences* **2001**, *42*, 1-35.
60. Felipe, M. A.; Xiao, Y. T.; Kubicki, J. D., Molecular orbital modeling and transition state theory in geochemistry. In *Molecular Modeling Theory: Applications in the Geosciences*, Cygan, R. T.; Kubicki, J. D., Eds. 2001; Vol. 42, pp 485-531.
61. Kubicki, J. D., *Molecular modeling of geochemical reactions*. Wiley: West Sussex, UK, 2016; p 422.
62. Kerisit, S.; Felmy, A. R.; Ilton, E. S., Atomistic simulations of uranium incorporation into iron (hydr)oxides. *Environmental Science & Technology* **2011**, *45* (7), 2770-2776.
63. Teppen, B. J.; Rasmussen, K.; Bertsch, P. M.; Miller, D. M.; Schafer, L., Molecular dynamics modeling of clay minerals. 1. Gibbsite, kaolinite, pyrophyllite, and beidellite. *Journal of Physical Chemistry B* **1997**, *101* (9), 1579-1587.
64. Tirlir, A. O.; Hofer, T. S., Structure and dynamics of the uranyl tricarbonate complex in aqueous solution: Insights from quantum mechanical charge field molecular dynamics. *Journal of Physical Chemistry B* **2014**, *118* (45), 12938-12951.
65. Zarzycki, P.; Kerisit, S.; Rosso, K. M., Molecular dynamics study of Fe(II) adsorption, electron exchange, and mobility at goethite ( $\alpha$ -FeOOH) surfaces. *Journal of Physical Chemistry C* **2015**, *119* (6), 3111-3123.
66. Sherman, D. M., Quantum chemistry and classical simulations of metal complexes in aqueous solutions. In *Molecular Modeling Theory: Applications in the Geosciences*, Cygan, R. T.; Kubicki, J. D., Eds. 2001; Vol. 42, pp 273-317.
67. Ermler, W. C.; Ross, R. B.; Christiansen, P. A., Ab initio relativistic effective potentials with spin-orbit operators. 6. Fr through Pu. *International Journal of Quantum Chemistry* **1991**, *40* (6), 829-846.
68. Ilton, E. S.; Bagus, P. S., Many-body effects in the 4f x-ray photoelectron spectroscopy of the U<sup>5+</sup> and U<sup>4+</sup> free ions. *Phys Rev B* **2005**, *71* (19).

69. Dudarev, S. L.; Botton, G. A.; Savrasov, S. Y.; Szotek, Z.; Temmerman, W. M.; Sutton, A. P., Electronic structure and elastic properties of strongly correlated metal oxides from first principles: LSDA+U, SIC-LSDA and EELS study of UO<sub>2</sub> and NiO. *Physica Status Solidi A* **1998**, *166* (1), 429-443.
70. Wang, J. W.; Ewing, R. C.; Becker, U., Electronic structure and stability of hyperstoichiometric UO<sub>2+x</sub> under pressure. *Phys Rev B* **2013**, *88* (2).
71. McQuarrie, D. A.; Simon, J. D., *Physical chemistry: A molecular approach*. University Science Books: United States, 1997; p 1360.
72. Tossell, J. A.; Vaughan, D. J., *Theoretical geochemistry: Applications of quantum mechanics in the Earth and mineral sciences*. Oxford University Press: New York, 1992; p 528.
73. Young, D. C., *Computational chemistry: a practical guide for applying techniques to real-world problems*. Wiley: New York, 2001; p 381.
74. Alessi, D. S.; Szymanowski, J. E. S.; Forbes, T. Z.; Quicksall, A. N.; Sigmon, G. E.; Burns, P. C.; Fein, J. B., Mineralogic controls on aqueous neptunium(V) concentrations in silicate systems. *Journal of Nuclear Materials* **2013**, *433* (1-3), 233-239.
75. Duff, M. C.; Coughlin, J. U.; Hunter, D. B., Uranium co-precipitation with iron oxide minerals. *Geochimica et Cosmochimica Acta* **2002**, *66* (20), 3533-3547.
76. Nico, P. S.; Stewart, B. D.; Fendorf, S., Incorporation of oxidized uranium into Fe (hydr)oxides during Fe(II) catalyzed remineralization. *Environmental Science & Technology* **2009**, *43* (19), 7391-7396.
77. Roberts, H. E.; Morris, K.; Law, G. T. W.; Mosselmans, J. F. W.; Bots, P.; Kvashnina, K.; Shaw, S., Uranium(V) incorporation mechanisms and stability in Fe(II)/Fe(III) (oxyhydr)oxides. *Environmental Science & Technology Letters* **2017**, *4* (10), 421-426.
78. Rak, Z.; Ewing, R. C.; Becker, U., Role of iron in the incorporation of uranium in ferric garnet matrices. *Phys Rev B* **2011**, *84* (15), 155128.
79. Rak, Z.; Ewing, R. C.; Becker, U., Ferric garnet matrices for immobilization of actinides. *Journal of Nuclear Materials* **2013**, *436* (1-3), 1-7.
80. Balboni, E.; Morrison, J. M.; Wang, Z. M.; Engelhard, M. H.; Burns, P. C., Incorporation of Np(V) and U(VI) in carbonate and sulfate minerals crystallized from aqueous solution. *Geochimica et Cosmochimica Acta* **2015**, *151*, 133-149.
81. Kelly, S. D.; Newville, M. G.; Cheng, L.; Kemner, K. M.; Sutton, S. R.; Fenter, P.; Sturchio, N. C.; Spotl, C., Uranyl incorporation in natural calcite. *Environmental Science & Technology* **2003**, *37* (7), 1284-1287.

82. Reeder, R. J.; Nugent, M.; Lamble, G. M.; Tait, C. D.; Morris, D. E., Uranyl incorporation into calcite and aragonite: XAFS and luminescence studies. *Environmental Science & Technology* **2000**, *34* (4), 638-644.
83. Oelkers, E. H.; Montel, J. M., Phosphates and nuclear waste storage. *Elements* **2008**, *4* (2), 113-116.
84. Thomson, B. M.; Smith, C. L.; Busch, R. D.; Siegel, M. D.; Baldwin, C., Removal of metals and radionuclides using apatite and other natural sorbents. *Journal of Environmental Engineering* **2003**, *129* (6), 492-499.
85. Dodge, C. J.; Francis, A. J.; Gillow, J. B.; Halada, G. P.; Eng, C.; Clayton, C. R., Association of uranium with iron oxides typically formed on corroding steel surfaces. *Environmental Science & Technology* **2002**, *36* (16), 3504-3511.
86. Duro, L.; Missana, T.; Ripoll, S.; Grive, M.; Bruno, J., Modelling of Pu sorption onto the surface of goethite and magnetite as steel corrosion products. In *Scientific Basis for Nuclear Waste Management XXVII*, Oversby, V. M.; Werme, L. O., Eds. 2004; Vol. 807, pp 659-664.
87. Oh, S. J.; Cook, D. C.; Townsend, H. E., Characterization of iron oxides commonly formed as corrosion products on steel. *Hyperfine Interactions* **1998**, *112* (1-4), 59-65.
88. Pearce, C. I.; Rosso, K. M.; Patrick, R. A. D.; Felmy, A. R., Impact of iron redox chemistry on nuclear waste disposal. In *Redox-Reactive Minerals: Properties, Reactions and Applications in Clean Technologies*, Ahmed, I. A. M.; Hudson-Edwards, K. A., Eds. 2017; Vol. 17, pp 229-272.
89. Ilton, E. S.; Boily, J. F.; Buck, E. C.; Skomurski, F. N.; Rosso, K. M.; Cahill, C. L.; Bargar, J. R.; Felmy, A. R., Influence of dynamical conditions on the reduction of U-VI at the magnetite-solution Interface. *Environmental Science & Technology* **2010**, *44* (1), 170-176.
90. Regenspurg, S.; Schild, D.; Schafer, T.; Huber, F.; Malmstrom, M. E., Removal of uranium(VI) from the aqueous phase by iron(II) minerals in presence of bicarbonate. *Appl Geochem* **2009**, *24* (9), 1617-1625.
91. Shuller, L. C.; Ewing, R. C.; Becker, U., Quantum-mechanical evaluation of Np-incorporation into studtite. *Am Mineral* **2010**, *95* (8-9), 1151-1160.
92. Shuller, L. C.; Ewing, R. C.; Becker, U., Np-incorporation into uranyl phases: a quantum-mechanical evaluation. *Journal of Nuclear Materials* **2013**, *434* (1-3), 440-450.
93. Shuller-Nickles, L. C.; Bender, W. M.; Walker, S. M.; Becker, U., Quantum-mechanical methods for quantifying incorporation of contaminants in proximal minerals. *Minerals* **2014**, *4* (3), 690-715.
94. Marshall, T. A.; Morris, K.; Law, G. T. W.; Mosselmans, J. F. W.; Bots, P.; Roberts, H.; Shaw, S., Uranium fate during crystallization of magnetite from ferrihydrite in conditions relevant to the disposal of radioactive waste. *Mineralogical Magazine* **2015**, *79* (6), 1265-1274.

95. Pidchenko, I.; Kvashnina, K. O.; Yokosawa, T.; Finck, N.; Bahl, S.; Schild, D.; Polly, R.; Bohnert, E.; Rossberg, A.; Gottlicher, J.; Dardenne, K.; Rothe, J.; Schafer, T.; Geckeis, H.; Vitova, T., Uranium redox transformations after U(VI) coprecipitation with magnetite nanoparticles. *Environmental Science & Technology* **2017**, *51* (4), 2217-2225.

## CHAPTER 2

# Quantum-mechanical investigation of the structures and energetics of uranium and plutonium incorporation into the magnetite ( $\text{Fe}_3\text{O}_4$ ) lattice

In review with *ACS Earth and Space Chemistry* as of January 2019

Co-authors: Will M. Bender and Udo Becker

### Abstract

Understanding the behavior of radionuclides is key to designing and implementing effective waste storage and remediation schemes. Incorporation into minerals is one process that may reduce the mobility of these contaminants. This study uses quantum-mechanical modeling to evaluate the incorporation of U and Pu into magnetite ( $\text{Fe}_3\text{O}_4$ ), a common mineral and steel corrosion product. The incorporation from solid and aqueous sources (*e.g.*,  $\text{PuO}_{2(s)}$  and  $\text{UO}_2^{2+}(\text{aq})$ ) with various oxidation states (Pu +3; U and Pu +4, +5, +6) is explored. Charge balancing is achieved via Fe lattice vacancies. Incorporation energies ( $\Delta E_{\text{inc}}$ ) depend strongly on the stability of different actinide oxide phases and hydration energies of aqueous species (*e.g.*,  $\Delta E_{\text{inc}}$  of 1.38 and 2.88 eV for  $\text{U}^{5+}$  from  $\delta\text{-U}_2\text{O}_5(s)$  and  $\text{UO}_2^+(\text{aq})$ , respectively). The calculated bonding environment of incorporated U ( $\text{U-O}_{\text{ax}} = 2.16\text{-}2.24 \text{ \AA}$ , CN = 2;  $\text{U-O}_{\text{eq}} = 2.30\text{-}2.34 \text{ \AA}$ , CN = 4) aligns with the range of experimental results. Analysis of incorporation energies, as well as charge and spin distribution within the Fe 3d and U 5f orbitals, indicate U prefers a valence state of

approximately  $U^{5+}$  in magnetite. The physical and electronic structures of Pu-magnetite, while lacking experimental comparison, suggest that Pu (in a slightly more reduced state between  $Pu^{5+}$  and  $Pu^{4+}$ ) could also be incorporated and perhaps with more flexibility given the comparable reaction energetics for simple substitution of  $Pu^{3+}$  for  $Fe^{3+}$  ( $\Delta E_{inc} = 2.00$  eV from  $Pu(OH)_3^0_{(aq)}$  vs.  $2.01$  eV from  $Pu(OH)_4^0_{(aq)}$ ). Overall, the results provide insight into potential immobilization pathways for actinides and serve as a reference for future characterization of actinide-incorporated magnetites.

## Introduction

Actinides, such as uranium and plutonium, are components of spent nuclear fuel and pose environmental health risks and engineering challenges due to their radioactivity and relatively long half-lives<sup>1</sup> (e.g.,  $t_{1/2}$  of  $^{239}Pu = 24,110$  a) compared to other nuclear waste species (such as the fission products  $^{90}Sr$  and  $^{137}Cs$  with  $t_{1/2}$  of 28.8 and 30.2 a, respectively). Understanding the (geo)chemistry of the actinides is critical to making informed decisions about the long-term storage of nuclear waste and responding to situations where these materials are released into the environment.

The behavior of U and Pu in the environment is complex. In general, the mobility of these radionuclides is highly dependent on their oxidation states. In natural environments, U and Pu can exist in a range of oxidation states; U exists in the +4, +5, and +6 valence states, while Pu can have an even wider range from +3 to +7.<sup>2-3</sup> For both elements, the tetravalent state is sparingly soluble under sufficiently reducing conditions. In other settings, this oxidation state preferentially forms an insoluble oxide phase. One example is the U ore mineral, uraninite ( $UO_2$ ,  $\log K_{sp} \approx -55$ ); Pu forms an isostructural phase.<sup>4</sup> The higher valences, +5 and +6, are soluble and mobile under a wide

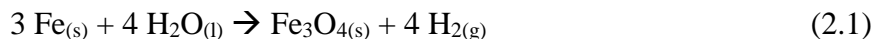
range of solution conditions (Eh, pH, ionic content and strength)<sup>3</sup>. These valences tend to form linear dioxocations called actinyl molecules with the formula:  $AnO_2^{x+}$  ( $An = U, Np, \text{ or } Pu; x = 1$  or 2 depending on the  $An$  valence). These actinyls, and their complexes with available ligands, are the dominant dissolved forms and their chemistry is key to understanding the mobility of these contaminants in the environment.

Actinide mobility in geologic environments is controlled by a suite of homogeneous and heterogeneous chemical processes including, but not limited to complexation, adsorption, redox, precipitation, colloidal transport, and incorporation.<sup>5-8</sup> Characterizing the variety of reactions that can occur is an important step towards qualifying the risks of actinide release into the environment from a waste repository, reactor site, mine, or natural geologic source. The aforementioned processes are interconnected and, in an idealized scenario with specific chemical conditions, may be considered to occur in sequence. First, aqueous complexes diffuse in solution and become adsorbed to a mineral surface. Here the metals form outer-sphere complexes in which water molecules are still present between the mineral surface and metal ion. These complexes may then become partially dehydrated such that the metal bonds directly to the mineral surface in an inner-sphere complex configuration. Depending on the mineral substrate and complex, the transition from outer- to inner-sphere complex may be slow or rapid. After forming an inner-sphere complex, the actinide may now be susceptible to redox reactions. The electron transfer process between a mineral and surface-complexed metal is aided if the mineral surface is semiconducting and/or contains redox-active metals in amenable oxidation states, such as  $Fe^{2+}$ .<sup>9-10</sup> Again, depending on the actinide and substrate pairing, their interaction may lead to either oxidation or reduction of the adsorbed species. The resulting change in oxidation state can have a significant impact on

solubility and can lead to precipitation of An-bearing phases or incorporation as trace element in an existing mineral host.

Incorporation is an intriguing process as it effectively immobilizes contaminants within a solid phase. Actinide species may be incorporated into mineral structures during mineral growth (a process often referred to as co-precipitation) or may slowly diffuse into a mineral from an overlying surface precipitate. However, under the temperature and pressure conditions present in most near-surface systems, solid-phase diffusion of relatively large cations is likely to be a slow process and incorporation during crystal growth is a more probable mechanism.

The incorporation of actinide cations into mineral phases has been explored in natural and engineered environments, as well as via computational techniques. A variety of minerals are known to accommodate actinides into their structures, including carbonates<sup>11-12</sup>, sulfates<sup>11-13</sup>, phosphates<sup>14</sup>, but a significant body of research has focused on the behavior of actinides in relation to iron (oxyhydr)oxides<sup>15-23</sup>, sulfides<sup>24-28</sup>, and silicates<sup>29-33</sup>, with one of the latter being considered as a nuclear waste form. One of the compounds that has attracted considerable interest is magnetite (Fe<sub>3</sub>O<sub>4</sub>).<sup>16,18-19,34-37</sup> The focus on magnetite and other Fe-bearing phases has in part been driven by the fact that these phases are all corrosion products of steel.<sup>38-39</sup> Steel is a component of the waste storage casks that may be used in geologic waste repositories and can corrode to form magnetite in wet, anoxic conditions via the reaction:



Equation 2.1 evolves hydrogen gas which creates locally reducing conditions, favoring the stability of magnetite, at least temporarily, over other Fe (oxyhydr)oxide corrosion products. If the environment becomes oxidizing, magnetite will be less stable and can potentially alter to form dominantly Fe<sup>3+</sup>-bearing minerals like hematite ( $\alpha$ -Fe<sub>2</sub>O<sub>3</sub>), maghemite ( $\gamma$ -Fe<sub>2</sub>O<sub>3</sub>), goethite

( $\alpha$ -FeOOH), and lepidocrocite ( $\gamma$ -FeOOH).<sup>38</sup> The interaction of actinides with some of these phases have been studied previously, but the work presented here will be limited to exploring magnetite.<sup>15,21,23,40-42</sup>

In addition to being a corrosion product of steel, magnetite is important to consider as it is present as an accessory phase in a variety of igneous, sedimentary, and metamorphic rocks. Some commonly magnetite-bearing rocks, such as granites and gneisses, are proposed as suitable hosts for deep geologic waste repositories.<sup>43</sup> Magnetite can also be produced as a product of microbial respiration pathways and is sometimes linked to the reduction of other metals, including U.<sup>44-45</sup>

Magnetite contains structural Fe<sup>2+</sup> that can serve as an electron donor to reduce actinides to more insoluble forms (*i.e.*, An<sup>3+</sup> and An<sup>4+</sup>). The interaction of magnetite with U<sup>46</sup>, and to a lesser extent Pu<sup>16,28</sup>, has been considered in terms of mineral surface processes as well as structural incorporation. Actinyl molecules readily form surface complexes on magnetite.<sup>47-48</sup> The formation of these complexes can lead to varying degrees of electron transfer from Fe<sup>2+</sup> to the actinide leading to a less oxidized actinyl form (*e.g.*, UO<sub>2</sub><sup>2+</sup> to UO<sub>2</sub><sup>+</sup>) or the precipitation of An-bearing phases on the mineral surface (*i.e.*, reduction of An<sup>5+/6+</sup> to An<sup>4+</sup>).<sup>46,49-50</sup> While the surfaces of magnetite tend to adsorb actinides, these surface species are not particularly stable over changing solution conditions. Specifically, more acidic and oxidizing solutions drive precipitates, particularly those comprised of actinyl molecules, like schoepite, (UO<sub>2</sub>)<sub>4</sub>O(OH)<sub>6</sub>·6 H<sub>2</sub>O, to (re)dissolve and/or form complexes with available ligands (*e.g.*, CO<sub>3</sub><sup>2-</sup>).<sup>2,5,51</sup>

In comparison, the structural incorporation of actinide contaminants as trace species in crystal structures has been shown to be stable over changing redox and solution conditions.<sup>18,35,41</sup> In these studies, U-bearing magnetites were subjected to oxidizing, acidic, and carbonate-bearing solutions to test their ability to retain U. Chemical and structural analyses of the solid sample

fractions following these treatments showed that surface precipitates and sorbates of U were preferentially returned to solution while structurally-incorporated U remained intact within the magnetite lattice, at least until solution conditions became so unfavorable such that magnetite began to dissolve.<sup>19</sup> In some cases, up to 94% of the U remained within the magnetite after 14 days of exposure to oxidizing conditions.<sup>18</sup> Longer exposure to oxidizing conditions, acidic solutions, and strong ligands can result in the full release of U to solution, but over the timeframes tested in these studies (between 4 and 14 days) structurally-incorporated U was relatively stable compared to surface sorbates and precipitates.<sup>18,41</sup>

X-ray absorption spectroscopy, including x-ray absorption near-edge spectroscopy (XANES) and extended x-ray fine structure (EXAFS), has allowed researchers to probe the chemical state and bonding environment of actinides incorporated into the structure of iron oxide phases. The oxidation state of incorporated U has been variously reported in the available literature, with several studies finding evidence for the +5 state.<sup>17-19,22-23,41</sup> There is also evidence that U<sup>5+</sup> can be stabilized in the form of a sorbate or precipitate on the surface of magnetite.<sup>52-53</sup> Pentavalent uranium has traditionally been considered to be unstable. In solution, U<sup>5+</sup> is prone to disproportionation in which two U<sup>5+</sup> react to create one oxidized (U<sup>6+</sup>) and one reduced species (U<sup>4+</sup>).<sup>54</sup> However, as evidenced by these recent experimental works, U<sup>5+</sup> may be an underappreciated species to consider when thinking about U redox processes in the environment.

Relative to U and due to its radiotoxicity and availability, Pu has a relatively small body of research related to its incorporation into mineral phases. Like U, aqueous Pu sorbs strongly to accessory Mn and Fe (oxyhydr)oxide minerals in rocks and can also undergo redox reactions.<sup>55-59</sup> However, to date, there have not been experimental co-precipitation studies documenting the incorporation of Pu into the lattices of these phases. Given the chemical similarities between the

actinides, it is likely Pu would share some of the same capacity for incorporation as U, but this has yet to be confirmed experimentally in minerals like magnetite. Furthermore, the coordination environment and charge state of structurally-incorporated Pu remains unknown. Studies of Pu sorption to magnetite<sup>28,36</sup> and zero-valent Fe<sup>55</sup> have found evidence of Pu reduction (Pu<sup>6+</sup> to Pu<sup>5+</sup> and/or Pu<sup>5+/6+</sup> to Pu<sup>4+</sup>) and stabilization of Pu<sup>3+</sup> under reducing conditions on these surfaces, but the reduction or stabilization of particular oxidation states in a lattice-bound environment has yet to be investigated.

To better understand the incorporation process for both of U and Pu, this study employs quantum-mechanical calculations to evaluate the energy of different incorporation reactions. Modeling the incorporation of aqueous phase contaminants into solid mineral phases poses some hurdles from a methodology standpoint. Generally, modeling a reaction requires that each reactant and product be calculated with exactly the same computational parameters. We build upon an approach first described and employed by Shuller, et al.<sup>60</sup> to describe similar co-precipitation reactions that contain both aqueous species (treated as molecular clusters) and mineral phases (periodic solids). By comparing the energies of reactions with different solid and aqueous actinide sources and replaced Fe sinks, we are able to make some inferences about the mechanism by which these actinides can be incorporated into the magnetite lattice. The employed computational approach also makes it possible to model the physical and electronic structures of the An-incorporated magnetite phases to determine whether or not actinides undergo changes to their oxidation states during incorporation. Finally, the calculated structures for the U- and Pu-incorporated phases can serve as references when future experiments seek to characterize unknown structures either from waste storage environments or laboratory syntheses.

## Computational approach

### *The magnetite structure*

Magnetite crystallizes in the inverse-spinel structure which contains octahedral and tetrahedral coordination sites for metal cations. In the normal spinel structure (as in the mineral spinel,  $\text{MgAl}_2\text{O}_4$ ), the divalent cations are hosted in tetrahedral sites, while the trivalent cations are located in the octahedral positions. In the magnetite lattice, this arrangement is altered such that  $\text{Fe}^{3+}$  is distributed evenly between the tetrahedral and octahedral sites, while the  $\text{Fe}^{2+}$  is housed entirely in octahedral sites. In terms of atomic positions, the symmetry of this structure is isometric; however, if the formal Fe charge and spin are considered as components of symmetry, the system lowers to orthorhombic.

The atomic positions and spin structure of magnetite has been determined as a function of temperature and pressure.<sup>61</sup> At the lower end of this spectrum, corresponding to the conditions expected near Earth's surface, magnetite is most stable in an *Imma* structure. This structure is a lower symmetry because Fe cations of different oxidation and spin states are considered to be different species. For the purposes of this study, symmetry will always be defined in this manner. This structure, shown in Figure 2.1, has been selected for this study as it is most representative of the environments we associate with radionuclide release, waste storage, and potential biological impacts. To lessen computational expense, a primitive cell (formula unit:  $\text{Fe}_6\text{O}_8$ ) of this structure was used for all calculations.

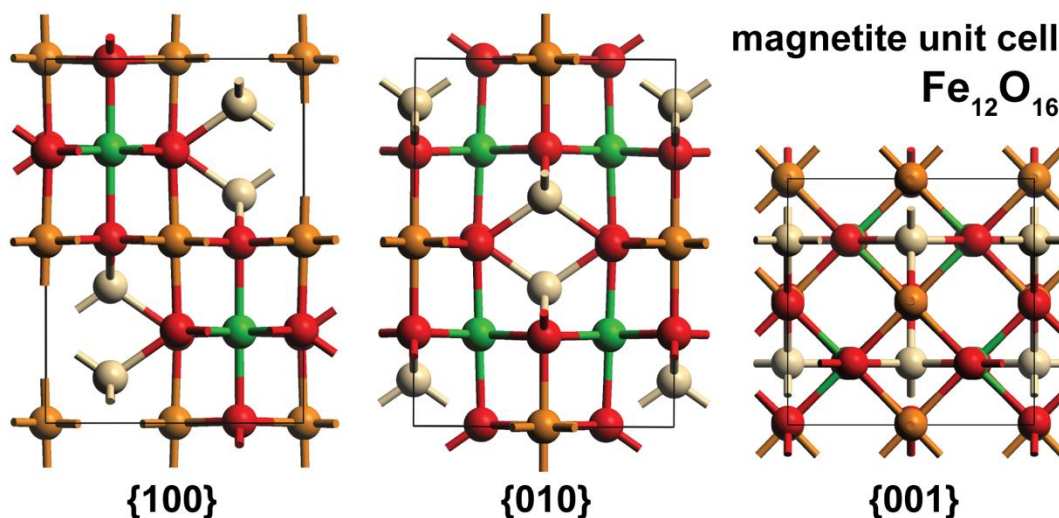


**Figure 2.1** The orthorhombic magnetite unit cell ( $\text{Fe}_{12}\text{O}_{16}$ , space group: *Imma*) viewed down its three crystallographic axes. Iron atoms are colored green ( $\text{Fe}^{2+}$ , octahedral), orange ( $\text{Fe}^{3+}$ , octahedral), and cream ( $\text{Fe}^{3+}$ , tetrahedral); oxygen atoms are shown in red. Unpaired spins on Fe are oriented upward in the octahedral cation positions and downward in tetrahedral sites resulting in a net spin moment of 16 for the ferromagnetic cell attributed to octahedral  $\text{Fe}^{2+}$ . A rhombohedral primitive cell, with the formula  $\text{Fe}_6\text{O}_8$ , was used for the quantum mechanical calculations in this study.

### *Quantum-mechanical calculations*

In the environment, the structural incorporation of trace metals into mineral structures involves complex multi-step interactions between solid and dissolved species. In a simplified approach, these reactions can be represented by the reactions of solid phases. In this case, magnetite reacts with a solid actinide (An) oxide to create an An-substituted magnetite and an iron oxide. Evaluating the energetics of these reactions is relatively straightforward and can be carried out using any computational approach suited for the modeling of periodic species. However, this simplified reaction is not particularly representative of the natural incorporation process. To get closer to that reality, we also determine the reaction energetics when the An source and Fe sink phases are aqueous.

To achieve this, a systematic conversion from the solid source and sink phases must be made. First, the solid species is converted to a charge-neutral periodic molecule. This molecule,

within periodic boundary conditions, is then converted to a charge-neutral cluster. The cluster is then dissociated into its charged components which are subsequently hydrated using a combination of explicitly-modeled water molecules and an implicit dielectric field. The specifics of this approach are outlined in detail by Shuller-Nickles, et al.<sup>62</sup> and has been applied to the incorporation of Np into studtite and boltwoodite,  $\text{NpO}_2^+$  and  $\text{UO}_2^{2+}$  into carbonate and sulfate minerals, and  $\text{U}^{6+}$  and  $\text{U}^{4+}$  incorporation into magnetite.<sup>11,60,63</sup> An example, showing the full complement of sub-reactions that are summed to generate the overall incorporation reaction is shown in the Results section.

### *Periodic solids*

A combination of computational approaches was used in this study to carry out the quantum mechanical calculations. All calculations were conducted using the Materials Studio 2017 R2 software package.<sup>64</sup> In this study, calculation of periodic solids was carried out using the Cambridge Serial Total Energy Package (CASTEP).<sup>65</sup> CASTEP is a density functional theory (DFT) code that utilizes planewave basis sets to approximate the Schrödinger equation within periodic boundary conditions. All CASTEP calculations were run using the generalized gradient approximation (GGA) with the Perdew Burke Ernzerhof (PBE) functional which accounts for electron exchange and correlation interaction between atoms.<sup>66</sup> Ultrasoft pseudopotentials were used minimize computational expense and approximate the interactions of core electrons with the valence shells. For O, Fe, U, and Pu there were respectively 6, 8, 14, and 16 valence electrons that were treated explicitly. A 600 eV cutoff energy was used for the planewave basis functions and k-points were spaced at a  $0.06 \text{ \AA}^{-1}$  interval for sampling of the Brillouin zone. The CASTEP total energies, which are related to the reaction energy of charge-neutral gas-phase species, were used to calculate the energy of the incorporation reactions ( $\Delta E_{\text{inc}}$ ).

In addition to the above parameters, CASTEP calculations allow for an atom-specific Hubbard  $U$  term to be specified. Calculations for the periodic species were carried out with this DFT+ $U$  approach. The Hubbard term is intended to account for on-site valence electron repulsion and exchange which is important for materials with unpaired electrons like U, Pu, and Fe to better capture the localization of the 3d and 5f electrons. Through the Materials Studio, Hubbard parameters are assigned as a single  $U$ - $J$  term for a given valence shell (p, d, f, etc.). Combined Hubbard terms for the U and Pu 5f shells (4.0 eV), and for the Fe 3d shell (4.06 eV) were used for these calculations. These values were selected to be in the range of those that have been shown to accurately reproduce the physical and electronic structures of actinide and Fe oxide phases within several percent of experimentally-determined values.<sup>61,67-71</sup> While the authors acknowledge that tweaking of the Hubbard parameters may result in improved accuracy, a full-fledged exploration of replicate optimization calculations using different  $U$  and  $J$  terms for the Fe, U, Pu, and mixed oxides is beyond the scope of this study.

The validity of this computational approach was tested by comparing the calculated lattice parameters to available experimentally-determined values for oxide phases. The DFT+ $U$  calculations produced better electronic structure results for a majority of the well-characterized oxide phases (*e.g.*, Fe<sub>2</sub>O<sub>3</sub>, Fe<sub>3</sub>O<sub>4</sub> and UO<sub>2</sub>) and accurate lattice parameters (within 3% of experimental data). The calculated bond distances in An-incorporated phases were nearly identical for both DFT and DFT+ $U$  methods, so in order to capture an electronic structure with more accurate electron localization on the metals, the DFT+ $U$  approach was taken and applied throughout.

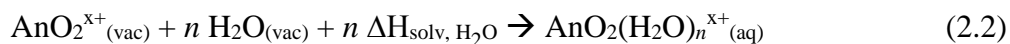
### *Periodic molecules and clusters*

To model reactions between dissolved actinides and solid magnetite, we employ a methodology that allows for reactions of solid species with aqueous clusters.<sup>62</sup> To have balanced reactions that go from periodic to cluster models, it is essential that we use a computational code that allows for the calculation of cluster and periodic species with the same theoretical treatment and parameters. One such program is DMol<sup>3</sup>.<sup>65,72</sup> Like CASTEP, DMol<sup>3</sup> is a DFT approach, but it uses atom-centered numerical basis sets instead of planewaves. In our case, we have selected a double numerical basis set with d-functions, DND version 3.5. As in CASTEP, we used a GGA/PBE functional setup for our calculations. DFT semi-core pseudopotentials were employed to approximate the effect of the core electrons for Fe, U, and Pu. These potentials include a certain degree of relativistic character and are designed specifically for use with DMol<sup>3</sup>.

For periodic molecule calculations, the dimensions of the periodic boundary conditions were set to be the smallest possible without any energy effects caused by the cell periodicity. To determine this, molecules were tested cubes with dimensions of 10, 12, 15, 20, and 25 Å to establish a suitably large size for the cell. The size of the molecule or complex resulted in some variation between the selected periodic boundary conditions, but a 15×15×15 Å box was determined to be suitably large with energy values changing less than 0.01 eV when the dimensions were increased. The symmetry for all periodic molecules boxes is *P1*.

To treat hydrated species in our calculations, we used a combination of implicit and explicit hydration approaches. Implicit hydration is achieved by placing the molecular clusters in a dielectric continuum model. Various models are available to computational chemists, but our study uses the module Conductor-like Screening Model (COSMO) available within the DMol<sup>3</sup> software package.<sup>73</sup> In COSMO, the dielectric constant ( $\epsilon$ ) of the solvent (water) was set to 78.54

corresponding to standard temperature and pressure conditions. Explicit hydration is achieved by placing explicit water molecules around the species of interest to simulate the first, second, or even higher-order hydration spheres. A general equation for an explicit hydration energy calculation is given in Equation 2.2:



Where An represents a soluble actinide species of charge (+5 or +6) and  $n$  is the number of water molecules in the first hydration shell. Our combined explicit and implicit hydration approach models the first coordination sphere with explicit water or hydroxide molecules ( $n = 3, 6, 7,$  and  $8$  for  $\text{Pu}^{3+}$ ,  $n = 4, 6, 7,$  and  $8$  for  $\text{An}^{4+}$ ,  $n = 5$  for  $\text{AnO}_2^{+2+}$ , and  $n = 6$  for  $\text{Fe}^{2+/3+}$ ) and then places these complexes into a dielectric field controlled by COSMO to simulate the contribution of higher-order hydration spheres. In addition, the solvation enthalpy of each explicitly-modeled water molecule ( $-0.42$  eV), when present in the reaction equation, is added as a correction factor. For our study, we have used a five-fold equatorial water coordination to represent the first hydration sphere for all actinyl species which is consistent with previous experimental and computational findings.<sup>54,74-75</sup> This combined hydration technique is much more accurate than using explicit water molecules or a dielectric model on their own. A selection of the calculated hydration energies, using DMol<sup>3</sup> values in the form of Equation 2.2, and their comparison to the experimental data<sup>76-77</sup> for  $\Delta H_{\text{hyd}}$  are presented in Table 2.1.

### *Frequency calculations*

Since the ultimate goal of these incorporation calculations is to determine equilibria of actinide ions between different solid and aqueous phases and their related partitioning coefficients, the Gibbs free energy ( $G$ ) of incorporation has to be evaluated, which requires phonon (or

frequency) calculations on optimized phases. These are computationally expensive and often have their own convergence problems; thus, these were only explored for a small set of reactions that were promising in terms of having relatively small incorporation energies. The standard approach used in this study evaluates a  $\Delta E$  of the incorporation reactions using the optimized electronic energy of the system from the CASTEP or DMol<sup>3</sup> equation. Frequency calculations on solids and molecules were performed in DMol<sup>3</sup> and necessitated a change to norm-conserving pseudopotentials. The translational, vibrational, and rotational components of the Gibbs free energy at 298.15 K were calculated and added to the previously calculated  $\Delta E$ . The calculations of the molecular species cover frequency-related processes within aqueous molecules; in addition, the hydration process changes the ordering of water around the aqueous complex which is covered by the entropy of hydration. For water and hydronium in the reaction equations, the difference between the experimental  $\Delta G$  and  $\Delta H$  of hydration<sup>78-79</sup> (0.15 and -0.85 eV, for H<sub>2</sub>O and H<sub>3</sub>O<sup>+</sup>, respectively) was added to the calculated value of G because these species did not include any modeled waters in the first coordination shell.

**Table 2.1** Calculated hydration energies (in eV) for aqueous cation source and sink phases compared to experimental data

Species	Calculated	Experiment ( $\Delta H$ ) <sup>a</sup>	% difference
Fe <sup>2+</sup>	-21.8	-20.2	+7.9
Fe <sup>3+</sup>	-46.8	-45.9	+1.9
UO <sub>2</sub> <sup>+</sup>	-7.5	-7.3	+0.7
UO <sub>2</sub> <sup>2+</sup>	-17.6	-17.3	+1.8
PuO <sub>2</sub> <sup>+</sup>	-7.8	-7.7	+0.6
PuO <sub>2</sub> <sup>2+</sup>	-18.7	-17.3	+8.1

<sup>a</sup>Experimental data for iron and actinyl hydration from Smith<sup>76</sup> and Gibson, et al.<sup>77</sup>, respectively.

## Results

### *Physical and electronic structure of actinide-incorporated magnetites*

#### *Changes to the lattice and cation coordination*

Incorporation of U and Pu into the magnetite lattice was attempted for four different initial actinide oxidation states: +3 for Pu and +4, +5, and +6 for both U and Pu. In all cases, the actinide replaces Fe in an octahedral lattice site as this site is larger than the tetrahedral one to host the larger actinide cations (typically between 0.85 and 1 Å). Substitution into the tetrahedral site was tested, but the structures did not converge, indicating these cations are too large for this lattice position. For Pu<sup>3+</sup>, a simple substitution mechanism was tested by replacing an Fe<sup>3+</sup> ion in the structure. However, for the other oxidation states, Fe cation vacancies were created by removing either another Fe<sup>2+</sup> or Fe<sup>3+</sup> from the octahedral position, depending on the valence of the actinide cation, to balance the charge of the unit cell. The removal of a tetrahedral Fe<sup>3+</sup> for charge-balancing was explored as well, but despite the fact that the vacancy would be smaller in size, these structures were unstable and thus, the octahedral vacancy approach was applied to all systems.

In all cases, the incorporation of the actinide cation results in a decrease in crystal symmetry. The An-incorporated lattices, referred to here according to their initial An oxidation states, have *C2/m* (An<sup>3+/4+/6+</sup>) or *P-1* (An<sup>5+</sup>) symmetry depending on the position of the lattice vacancy. A representative optimized structure of a vacancy-bearing An-incorporated magnetite (in this case Pu<sup>6+</sup>) is shown in Figure 2.2. In the presented orientation, it is easy to see the channels running along the crystallographic *b* axis that are created as a result of the charge-balancing Fe<sup>3+</sup> vacancies.

In accommodating the actinide cation, the volume of the primitive cell is modeled to increase by ~5-6%. The volume increases caused by U and Pu incorporation in the +4, +5, and +6 oxidation states are all comparable, but the simple substitution of  $\text{Pu}^{3+}$  results in significantly more (10%) swelling in the more rigid, vacancy-free lattice. The larger unit cell volumes of An-incorporated phases are the result of longer octahedral bond lengths between An and O relative to those of  $\text{Fe}^{2+}$  and  $\text{Fe}^{3+}$ . In magnetite, octahedral Fe-O bonds are all the same length (2.05 Å). There is no measurable difference between the  $\text{Fe}^{2+}$ -O and  $\text{Fe}^{3+}$ -O bonds in the octahedral coordination sites despite the difference in cation charge, likely due to rapid charge transfer between Fe in the lattice. In comparison, the  $\text{Fe}^{3+}$ -O bonds in the tetrahedral site are 1.89 Å. In U-incorporated magnetite, the U-O bonds in the octahedral site are lengthened asymmetrically, perhaps due to Jahn-Teller distortion, with  $\text{U-O}_{\text{eq}}$  ( $n = 4$ ) and  $\text{U-O}_{\text{ax}}$  ( $n = 2$ ) of 2.24 and 2.34 Å, respectively. The calculated U-O distances in these structures are distinctly longer than those found in the uranyl molecule (~1.78 Å for  $\text{UO}_2^{2+}(\text{aq})$ ) and are a clear indication that structural incorporation into

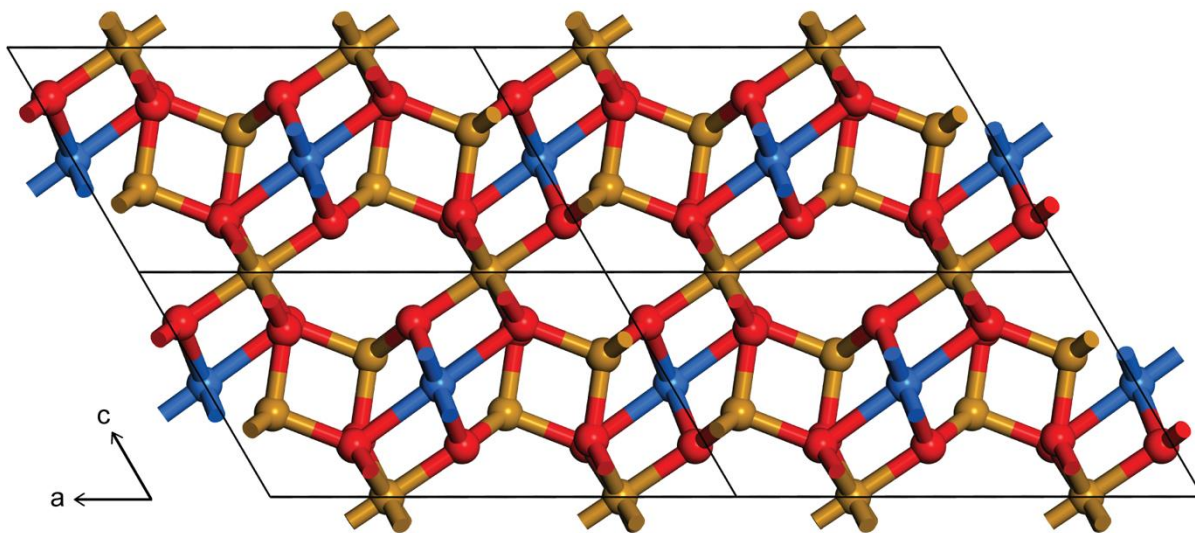


**Figure 2.2** A view down the  $b$  axis of a  $2 \times 2$  supercell of  $\text{Pu}^{6+}$ -incorporated magnetite (formula unit:  $\text{Fe}_4\text{PuO}_8$ ). In this monoclinic structure, charge-balancing octahedral  $\text{Fe}^{3+}$  vacancies create distorted hexagonal channels running parallel to the  $b$  axis (out of the page). Fe atoms (all  $\text{Fe}^{2+}$ ) are shown in yellow and O in red. During optimization, Pu converges to an intermediate oxidation state between +4 and +5, based on spin density, and no Pu-O distances are found that are close those of plutonyl.

magnetite does not preserve uranyl-like coordination and also favors oxidation states lower than +6. Cation-cation distances in the incorporated structure to the next-nearest Fe cation neighbors are 3.20 ( $n = 4$ ), 3.56 ( $n = 4$ ), and 3.78 Å ( $n = 2$ ). In the system where  $U^{6+}$  was initially incorporated and two  $Fe^{3+}$  were removed from the lattice, the structure converged to a less energetically-favorable bonding environment slightly different from what was found for the structures where  $U^{5+}$  and  $U^{4+}$  were the starting oxidation states. This less stable structure had shorter  $U-O_{eq}$  and  $U-O_{ax}$  bonds of 2.16 and 2.30 Å, respectively. The interatomic distances and coordination numbers for the most stable U-incorporated structure are presented and compared to some available values in the computational<sup>20,35,62</sup> and experimental<sup>18-19,35,37,41</sup> literature in Table 2.2.

For Pu incorporation, similar changes to the bond length were observed in the calculated structures with Pu-O bonds longer than original Fe-O bonds by several tenths of an ångström. In the  $Pu^{6+}$ -incorporated structure, the  $Pu-O_{eq}$  ( $n = 4$ ) and  $Pu-O_{ax}$  ( $n = 2$ ) bond lengths in the octahedral site are determined to be 2.22 and 2.32 Å, respectively. In the  $Pu^{3+}$ -bearing magnetite, which is unique in that it has no vacancy, the four equatorial Pu-O bonds are actually longer (2.35 Å) than those in the axial orientation (2.31 Å). These distance values, and several others, for the Pu-bearing structures are compiled Table 2.3.

### *Electronic structure of incorporated phases*

Quantum-mechanical calculations have the benefit of revealing the electronic structure in ways that atomistic methods cannot. With these calculations, it is possible to probe changes in the atomic charge and spin as well as the nature of bonding and orbitals within chemical systems. The potential change in oxidation state of the actinides during incorporation is of particular interest in the context of this study. To understand the changes in U, Pu, and Fe oxidation states, the

calculated Mulliken charge and spin values of incorporated phases are compared to those from reference oxide phases. Mulliken population analysis does not return exact formal charges or spins and generally underestimates by between one half and a third.<sup>80</sup> As mentioned in the Computational Approach section, electronic structure results differ slightly between the DFT and DFT+*U* methods. Using the DFT+*U* method, the separation of the cations, particularly Fe<sup>2+</sup> and Fe<sup>3+</sup>, was much clearer. In the standard DFT testing, the charge and spins were smeared across the different cation sites and this distinction was less clear. With the use of a Hubbard *U* term improving electron localization in the systems, Mulliken spin was a good indicator of oxidation state in the modeled systems when comparing to the reference oxide phases. In these calculations, we see clear reduction of the An<sup>6+</sup> valence state by Fe<sup>2+</sup>, resulting in lower An oxidation states in the lattice (intermediate spin values corresponding to an oxidation state between +5 and +4).

The incorporation of an actinide cation into the magnetite crystal lattice, and if necessary, the accompanying charge-balancing vacancy, results in changes to the electronic structure. One of these changes is the net number of unpaired spins in the lattice. Depending on the initial oxidation state of the U or Pu atom being introduced, the spin moment changes from its original value of 8 in the primitive unit cell to 4 (Pu<sup>4+</sup>), ±2 (U<sup>6+</sup>, U<sup>4+</sup>, and Pu<sup>5+</sup>), or 0 (U<sup>5+</sup> and Pu<sup>6+</sup>). The net spin of the system is unchanged only in the Pu<sup>3+</sup> case where both the actinide and the replaced Fe<sup>3+</sup> have 5 unpaired spins. In the calculations, the number of electrons is fixed and the spin configuration is given as a starting point. During the electronic optimization, electrons can reorganize to find the most energetically-favorable configuration.

In the case of U, the different starting configurations corresponding to the initial incorporation of U<sup>4+</sup>, U<sup>5+</sup>, and U<sup>6+</sup> converge to remarkably similar electronic states. In all three cases, population analysis reveals that U assumes an oxidation state between U<sup>4+</sup> and U<sup>5+</sup>, with a

Mulliken charge of 1.66-1.69 e. The number of unpaired spins on the U is consistent as well, with a value of ~2.11 across the three structures. Iron, on the other hand, converges to a charge of ~0.99 e with unpaired spin values of  $\pm 3.95$ -4.09, consistent with the values calculated for Fe<sub>2</sub>O<sub>3</sub>. The electronic configuration of U in magnetite is between that of UO<sub>2</sub> and U<sub>2</sub>O<sub>5</sub> which have calculated U Mulliken spin values of 2.57 and 1.59, respectively. This indicates that U<sup>6+</sup> that is

**Table 2.2** DFT+*U* calculated bonding environment (coordination number, CN, and interatomic distances, R) of structurally-incorporated U in magnetite compared to selected computational and experimental values from the literature

Phase	Bond	CN <sup>a</sup>	R (Å)	Method and source
Fe <sub>4</sub> UO <sub>8</sub>	U-O <sub>eq</sub>	4	2.24	DFT, this study
	U-O <sub>ax</sub>	2	2.34	
	U-Fe <sub>oct</sub>	4	3.20	
	U-Fe <sub>tet</sub>	2	3.56	
	U-Fe <sub>tet</sub>	4	3.78	
U-incorporated magnetite	U-O <sub>1</sub>	6-7	2.06-2.23	molecular mechanics <sup>20</sup>
	U-Fe <sub>1</sub>	5-6	3.12-3.25	"
	U-O <sub>2</sub>	6	2.15	DFT <sup>35</sup>
	U-Fe <sub>1</sub>	5	3.18	"
	U-O <sub>eq</sub>	4	2.13	DFT <sup>62</sup>
	U-O <sub>ax</sub>	2	2.26	"
	U-O <sub>1</sub>	3.3-5.0	2.19-2.21	EXAFS <sup>18</sup>
	U-O <sub>2</sub>	2-2.6	2.44-2.45	"
	U-Fe <sub>1</sub>	2.5-6	3.14-3.23	"
	U-Fe <sub>2</sub>	3.1	3.46	"
	U-O <sub>1</sub>	4-4.5	2.16-2.18	EXAFS <sup>19</sup>
	U-O <sub>2</sub>	1.5	2.42	"
	U-Fe <sub>1</sub>	2	3.15-3.20	"
	U-Fe <sub>2</sub>	2	3.69-3.72	"
	U-O <sub>1</sub>	2.2-3.0	2.18-2.26	EXAFS <sup>35</sup>
	U-O <sub>2</sub>	3.0-3.2	2.41-2.42	"
	U-Fe <sub>1</sub>	0.6-6.2	3.12-3.19	"
	U-Fe <sub>2</sub>	0.5-1.0	3.39-3.55	"
	U-O <sub>1</sub>	1.6 ± 0.2	2.23	EXAFS <sup>37</sup>
U-O <sub>2</sub>	3.3 ± 0.2	2.51	"	
U-Fe <sub>1</sub>	5.7 ± 1.5	3.39	"	

<sup>a</sup>Coordination numbers (CNs) are lower than expected for an octahedral site in some cases due to the chosen EXAFS fitting procedure and/or the presence of other phases in the sample (*e.g.*, UO<sub>2</sub> and/or adsorbed UO<sub>2</sub><sup>x+</sup>). In this study, U-Fe coordination is lower because of lattice vacancies.

**Table 2.3** DFT+*U* calculated bonding environment (coordination number, CN, and interatomic distances, R) of structurally-incorporated Pu in magnetite

Structure	Bond	CN <sup>a</sup>	R (Å)
Fe <sub>4</sub> PuO <sub>8</sub>	Pu-O <sub>eq</sub>	4	2.22
	Pu-O <sub>ax</sub>	2	2.32
	Pu-Fe <sub>oct</sub>	4	3.18
	Pu-Fe <sub>tet</sub>	4	3.54
	Pu-Fe <sub>tet</sub>	2	3.76
Fe <sub>5</sub> Pu <sup>III</sup> O <sub>8</sub>	Pu-O <sub>ax</sub>	2	2.31
	Pu-O <sub>eq</sub>	4	2.34
	Pu-Fe <sub>oct</sub>	4	3.15
	Pu-Fe <sub>oct</sub>	2	3.20
	Pu-Fe <sub>tet</sub>	2	3.60
	Pu-Fe <sub>tet</sub>	4	3.68

<sup>a</sup>In this study, Pu-Fe coordination in the Pu<sup>6+</sup>, Pu<sup>5+</sup>, and Pu<sup>4+</sup>-incorporated species is lower than would be expected in a pure magnetite lattice because of charge-balancing Fe vacancies.

incorporated into the magnetite lattice is reduced by structural Fe<sup>2+</sup>. When starting with a U<sup>5+</sup> or U<sup>4+</sup> in the structure, charge and spin on Fe are smeared such that different oxidation states in the U<sup>5+</sup> case, which had one remaining Fe<sup>2+</sup>, are no longer distinguishable. For both of these cases, the optimized U charge and spin are the same so the U oxidation state is nearly unchanged by electron transfer with Fe.

The electronic structure and configuration of Pu-incorporated phases are comparable to that of the U analogs. As with the U-bearing magnetite phase, Pu initially in the +6, +5, and +4 oxidation states all converge to essentially the same electronic configuration once incorporated into the magnetite lattice. Mulliken charge and spin on Pu are calculated to be ~1.55 e and 4.74-4.81, respectively. Iron has charge values of 1.05 e and a spin value of ±4.09, nearly identical to the modeled oxidation state of Fe in the U-incorporated phases. The Pu charge and spin in these phases, as was the case with U, corresponds to values in between those calculated for PuO<sub>2</sub> and Pu<sub>2</sub>O<sub>5</sub> (spin values of 4.86 and 4.58-4.77, respectively). This indicates that Pu prefers and

oxidation state of between  $\text{Pu}^{4+}$  and  $\text{Pu}^{5+}$  when incorporated via any of the vacancy-generating mechanisms we tested.

In the case of  $\text{Pu}^{3+}$ -incorporated structures, Pu has a slightly lower charge of 1.36 e and maintain a high spin value, consistent with  $\text{Pu}^{3+}$ , of 5.15. This value is significantly higher than in the other Pu structures and matches the Pu spin calculated for two different  $\text{Pu}_2\text{O}_3$  polymorphs (5.18 and 5.50). Unlike the other incorporated phases with vacancies, this structure retains distinct  $\text{Fe}^{2+}$  and  $\text{Fe}^{3+}$  cations in their original lattice positions. Three  $\text{Fe}^{3+}$  cations with a Mulliken spin value of 4.05-4.09 and two  $\text{Fe}^{2+}$  with spin of 3.75 are present in the lattice.

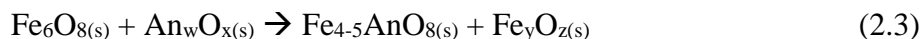
In addition to the charge and spin analyses, the calculations also return information about the orbital filling and the density of states. Density of states (DOS) analysis can show how different orbital energy distributions change when actinides are incorporated into the magnetite lattice. One comparison, between pure magnetite and  $\text{U}^{5+}$ -incorporated magnetite, is presented in Figure 2.3. Partial DOS, or PDOS, allows the density of states information to be tabulated for specific energy shells. This is powerful because it allows us to visualize the distribution of electronic orbitals in the lattice and provides another confirmation of U 5f density. In all modeled structures, actinide 5f orbitals hybridize with neighboring O 2p orbitals near the top of the valence band (see inset PDOS of U and one coordinating O in Figure 3). The presence of 5f electron density in the structure where U was initially set to the +6 oxidation state is another confirmation that U is reduced by structural  $\text{Fe}^{2+}$  in this structure over the course of the atomic and electronic optimization calculation. Iron 3d orbitals change somewhat in response to the incorporation of the actinide cation and the formation of vacancy site. The concentration of the Fe 3d orbitals in a more defined energy range is likely related to the smearing of Fe charge, mainly of  $\text{Fe}^{3+}$ , across the different Fe cations resulting in the uniform spin distributions seen in the population analyses of

incorporated phases. Looking at the calculated band structure of the magnetite phases, it also appears that the incorporation of an actinide and the creation of a charge-balancing vacancy causes an increase in the band gap ( $E_{\text{gap}}$ ) for these materials. In the case presented in Figure 2.3, U incorporation results in an increase in the band gap energy of about  $\sim 1$  eV.

### ***Energetics of incorporation reactions***

#### *Reactions with solid phases*

The incorporation of U and Pu into magnetite can, in the most basic terms, be evaluated by comparing the reaction of magnetite with a solid actinide oxide source to create An-incorporated magnetite and an Fe oxide sink via the following scheme:



Where the non-numerical subscripts represent the stoichiometric values necessary to balance the reaction for the involved An and Fe oxidation states. The evaluation of this basic reaction format is complicated by the numerous oxidation states available and the different polymorphs of actinide oxide phases that have been described. In addition to the different polymorphs, different spin configurations (ferromagnetic and antiferromagnetic) in the oxide phases allow for more combinations to be tested. While we did not test a fully comprehensive suite, a number of different polymorphs, as well as spin configurations for a subset of those species, were modeled and tested to assess their effect on the overall incorporation reaction energy. These solid phase incorporation energies are presented in the first row of each oxidation state sub-section in Table 2.4.

Overall, the net incorporation reaction energy for these solid-phase reactions is positive in all cases except for  $\text{Pu}^{6+}$  incorporation from  $\text{PuO}_3$ . The trend in reaction energies is different between U and Pu oxide sources. For U, incorporation is most favorable from the  $\text{U}^{4+}$  oxide phase,

followed by  $\text{U}_2\text{O}_5$ , and lastly  $\text{UO}_3$ . In the case of Pu, this favorability trend does not directly follow increasing oxidation state. The reaction energies (based on a given polymorph and/or spin configuration) order  $\text{Pu}^{6+} < \text{Pu}^{5+} < \text{Pu}^{3+} < \text{Pu}^{4+}$  in terms of favorability. Relatively unstable An-oxide species bias the product side of the reactions and favor the formation of the An-incorporated magnetite and an Fe-sink oxide: either wüstite ( $\text{FeO}$ ), hematite ( $\text{Fe}_2\text{O}_3$ ), and/or magnetite. This is likely to be a major reason behind the relative ordering of favorability for the solid phase Pu reactions. At this time,  $\text{Pu}_2\text{O}_5$  and  $\text{PuO}_3$  structures have not been described by analytical means. It is likely that these phases are stable at certain temperature and pressure conditions, but they may not be under standard temperature and pressure or in the 0 K environment modeled by our DFT calculations. In this study, the structures of  $\text{Pu}_2\text{O}_5$  and  $\text{PuO}_3$  are assumed to be analogs of  $\delta\text{-U}_2\text{O}_5$ ,  $\text{Np}_2\text{O}_5$ , and  $\gamma\text{-UO}_3$ .<sup>81-84</sup> The favorable, even negative, energies of incorporation for reactions of these Pu structures must be interpreted with some care.

The spin configuration of the different U and Pu oxide phases also has an effect on the energy, with some ferromagnetic and antiferromagnetic ordering causing dramatic changes in the incorporation energy: For example, the largest observed change is with the  $\text{Pu}_2\text{O}_5$  in the  $\text{Np}_2\text{O}_5$  structure, where antiferromagnetic ordering of the unpaired Pu spins is nearly 3 eV more energetically favorable than its ferromagnetic counterpart, making the calculated thermodynamics of incorporation significantly less favorable (note that this difference disappears when considering aqueous source and sink phases where there is no spin ordering). This suggests that like  $\text{Np}_2\text{O}_5$ ,  $\text{Pu}_2\text{O}_5$  may be more stable in an antiferromagnetic state.<sup>81</sup> Smaller changes are observed for other species, for example  $\text{PuO}_3$ , where a change in spin ordering only causes the energy to change on the order of  $\sim 0.1$  eV.

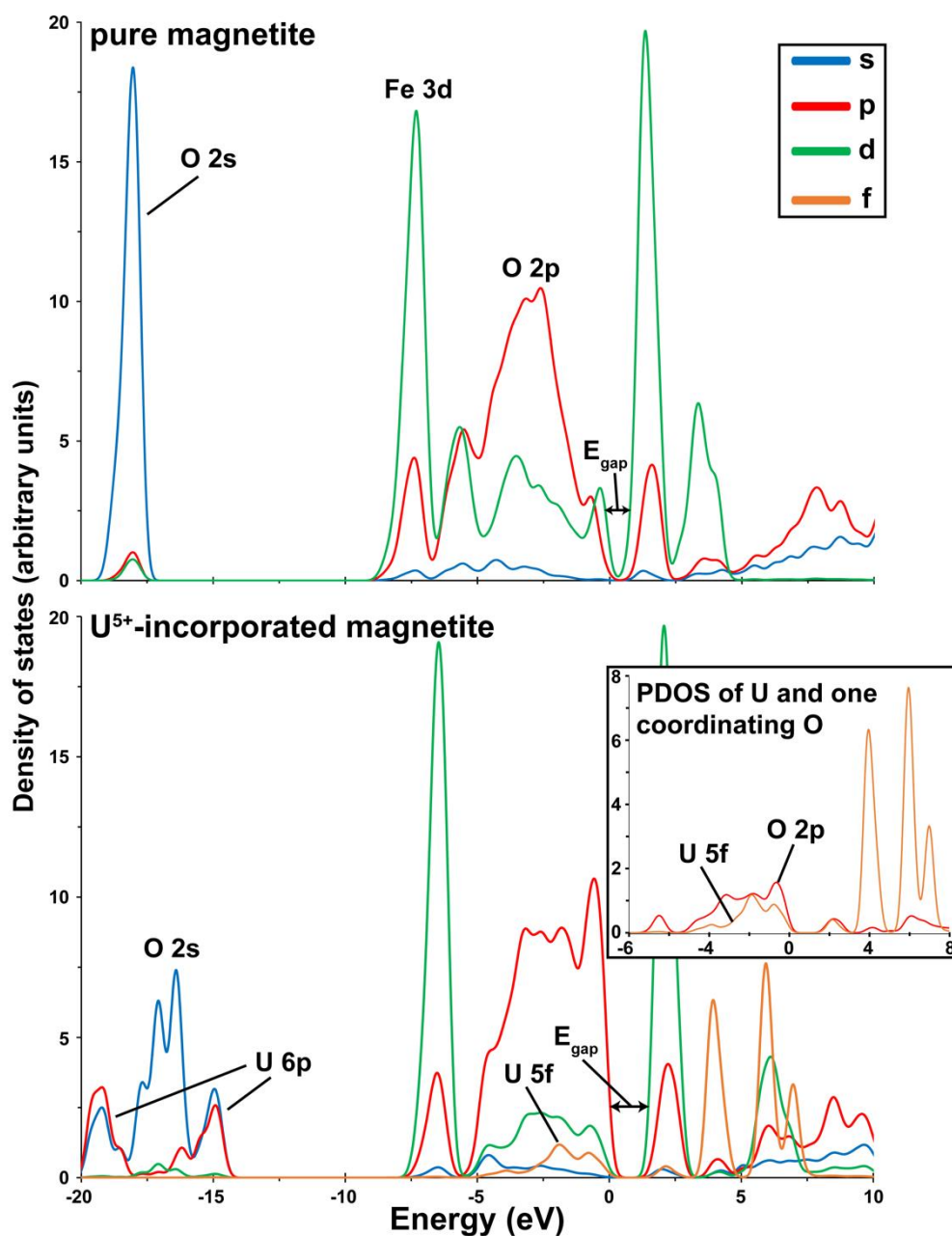
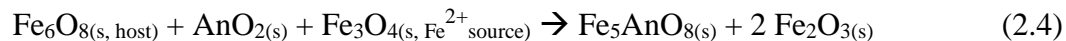


**Figure 2.3** Calculated partial density of states (PDOS) of the pure magnetite unit cell (upper) compared to that of a  $\text{U}^{5+}$ -incorporated magnetite with an octahedral Fe vacancy (lower;  $\text{Fe}_4\text{UO}_8$ ). Clear changes to the upper valence band below the band gap ( $E_{\text{gap}}$ ) due to the presence of U 5f orbitals are visible in the incorporated phase. The inset in the lower panel shows the PDOS of U and one coordinating O anion in the octahedral lattice position, revealing the hybridization of U 5f and O 2p orbitals responsible for bonding between these two atoms.

Broadly, the incorporation energies range from 0.20 to 2.11 eV for U and -1.21 to 3.69 eV for Pu. Aside from reactions with a PuO<sub>3</sub> source, all reactions show a positive incorporation energy indicating that these processes are not spontaneous at thermodynamic equilibrium. This is in line with the expectation that the incorporation of a foreign cation into such a small unit cell, along with the creation of a vacancy site in all cases except for Pu<sup>3+</sup>, would be an energetically uphill process. These energies are on the same order as others that have been reported for the incorporation of U, Np, and Pu from solid source phases into other mineral species.<sup>60,62-63</sup>

While all reactions described so far do not require the change of oxidation state of any atom, the incorporation of tetravalent U and Pu without the creation of a vacancy site was considered in this study as well via a reaction such as:



In the reaction mechanism in Equation 2.4 An<sup>4+</sup> replace an Fe<sup>3+</sup> in the magnetite host, and one Fe<sup>3+</sup> in the host has to turn into an Fe<sup>2+</sup>, as indicated by the transition of the second magnetite into one of the hematite formula units in Equation 2.4. The reaction energies by comparing actinide oxides with their actinide incorporated magnetite incorporation for circumneutral for U and even negative for Pu (about -1.6 eV); however, the more geochemically realistic process of incorporation from an aqueous solution was calculated to be prohibitively energetically downhill. One problem in these calculations was that the additional charge had to be distributed over a relatively small unit cell and would probably require the application of a larger, computationally-expensive supercell, which is beyond the scope of this study.

**Table 2.4** Selected DFT+*U* calculated incorporation energies ( $\Delta E_{\text{inc}}$ , in eV) for U and Pu into magnetite with solid and aqueous source and sink phases

Simplified reaction equations	V	An = U	An = Pu
<b>An<sup>III</sup> → Fe<sup>III</sup></b>			
$\text{An}^{\text{III}}_2\text{O}_3(\text{s}) + \text{Fe}^{\text{III}}(\text{s, mag}) \rightarrow \text{An}^{\text{III}}(\text{s, mag}) + \text{Fe}^{\text{III}}_2\text{O}_3(\text{s, hem})$	none	–	1.27 <sup>a</sup> 2.14 <sup>b</sup>
$\text{An}^{\text{III}}(\text{OH})_3^0(\text{aq}) + \text{Fe}^{\text{III}}(\text{s, mag}) \rightarrow \text{An}^{\text{III}}(\text{s, mag}) + \text{Fe}^{\text{III}}(\text{H}_2\text{O})_6^{3+}(\text{aq})$	none	–	2.00
$\text{An}^{\text{III}}(\text{OH})_3(\text{H}_2\text{O})_3^0(\text{aq}) + \text{Fe}^{\text{III}}(\text{s, mag}) \rightarrow \text{An}^{\text{III}}(\text{s, mag}) + \text{Fe}^{\text{III}}(\text{H}_2\text{O})_6^{3+}(\text{aq})$			3.00
$\text{An}^{\text{III}}(\text{OH})_3(\text{H}_2\text{O})_5^0(\text{aq}) + \text{Fe}^{\text{III}}(\text{s, mag}) \rightarrow \text{An}^{\text{III}}(\text{s, mag}) + \text{Fe}^{\text{III}}(\text{H}_2\text{O})_6^{3+}(\text{aq})$			3.77
<b>An<sup>IV</sup> → 2 Fe<sup>II</sup></b>			
$\text{An}^{\text{IV}}\text{O}_2(\text{s}) + 2 \text{Fe}^{\text{II}}(\text{s, mag}) \rightarrow \text{An}^{\text{IV}}(\text{s, mag}) + 2 \text{Fe}^{\text{II}}\text{O}(\text{s, wüs})$	Fe <sup>II</sup> <sub>oct</sub>	0.20	3.02
$\text{An}^{\text{IV}}(\text{OH})_4^0(\text{aq}) + 2 \text{Fe}^{\text{II}}(\text{s, mag}) \rightarrow \text{An}^{\text{IV}}(\text{s, mag}) + 2 \text{Fe}^{\text{II}}(\text{H}_2\text{O})_6^{2+}(\text{aq})$	Fe <sup>II</sup> <sub>oct</sub>	1.71	2.01
$\text{An}^{\text{IV}}(\text{OH})_4(\text{H}_2\text{O})_3^{2+}(\text{aq}) + 2 \text{Fe}^{\text{II}}(\text{s, mag}) \rightarrow \text{An}^{\text{IV}}(\text{s, mag}) + 2 \text{Fe}^{\text{II}}(\text{H}_2\text{O})_6^{2+}(\text{aq})$			1.05
<b>An<sup>V</sup> → Fe<sup>III</sup> + Fe<sup>II</sup></b>			
$\text{An}^{\text{V}}_2\text{O}_5(\text{s}) + \text{Fe}^{\text{II}}(\text{s, mag}) + \text{Fe}^{\text{III}}(\text{s, mag}) \rightarrow$ $\text{An}^{\text{V}}(\text{s, mag}) + \text{Fe}^{\text{III}}(\text{s, mag}) + \text{Fe}^{\text{II}}\text{O}(\text{s, wüs})$	Fe <sup>II</sup> <sub>oct</sub>	1.39 <sup>c</sup> 1.85 <sup>d</sup>	0.69 <sup>c</sup> 3.69 <sup>d</sup> 0.77 <sup>e</sup>
$\text{An}^{\text{V}}\text{O}_2(\text{H}_2\text{O})_5^+(\text{aq}) + \text{Fe}^{\text{II}}(\text{s, mag}) + \text{Fe}^{\text{III}}(\text{s, mag}) \rightarrow$ $\text{An}^{\text{V}}(\text{s, mag}) + \text{Fe}^{\text{III}}(\text{H}_2\text{O})_6^{3+}(\text{aq}) + \text{Fe}^{\text{II}}(\text{H}_2\text{O})_6^{2+}(\text{aq})$	Fe <sup>II</sup> <sub>oct</sub>	2.88	1.94
<b>An<sup>VI</sup> → 2 Fe<sup>III</sup></b>			
$\text{An}^{\text{VI}}\text{O}_3(\text{s}) + 2 \text{Fe}^{\text{III}}(\text{s, mag}) \rightarrow \text{An}^{\text{VI}}(\text{s, mag}) + \text{Fe}^{\text{III}}_2\text{O}_3(\text{s, hem})$	Fe <sup>III</sup> <sub>oct</sub>	2.11 <sup>g</sup>	-1.14 <sup>f</sup> -1.21 <sup>g</sup>
$\text{An}^{\text{VI}}\text{O}_2(\text{H}_2\text{O})_5^{2+}(\text{aq}) + 2 \text{Fe}^{\text{III}}(\text{s, mag}) \rightarrow \text{An}^{\text{VI}}(\text{s, mag}) + 2 \text{Fe}^{\text{III}}(\text{H}_2\text{O})_6^{3+}(\text{aq})$	Fe <sup>III</sup> <sub>oct</sub>	5.47	4.10

Column labeled “V” indicates the position of the charge-balancing lattice vacancy.

All energies represent the reaction of one Fe<sub>6</sub>O<sub>8</sub> magnetite unit to create one Fe<sub>4</sub>AnO<sub>8</sub> (An<sup>4+/5+/6+</sup>) or Fe<sub>5</sub>AnO<sub>8</sub> (Pu<sup>3+</sup>). Additional incorporation reactions and energies are presented in Table 2.6. The oxidation states of the incorporated actinides represent their initial conditions prior to electronic and atomic optimization of the solid phases – see text for description of the stable electronic configurations. Full notation of all mineral phases and stoichiometric H<sub>2</sub>O, H<sub>3</sub>O<sup>+</sup>, and OH<sup>-</sup> have been omitted in this table for clarity.

(s) = solid phase; (aq) = aqueous species; mag = magnetite structure; hem = hematite; wüs = wüstite; oct = octahedral lattice site

Different oxide polymorphs and spin configurations are labeled as follows: <sup>a</sup>fm *P-3ml* Pu<sub>2</sub>O<sub>3</sub>; <sup>b</sup>fm *Ia3* Pu<sub>2</sub>O<sub>3</sub>; <sup>c</sup>fm *Pbam* An<sub>2</sub>O<sub>5</sub>; <sup>d</sup>*P2* afm An<sub>2</sub>O<sub>5</sub>; <sup>e</sup>*P2/c* fm An<sub>2</sub>O<sub>5</sub>; <sup>f</sup>*I41/amd* fm AnO<sub>3</sub>; <sup>g</sup>*I41/amd* afm AnO<sub>3</sub>. The fm and afm notations represent ferromagnetic and antiferromagnetic spin ordering.

### *Reactions with aqueous source and sink phases*

While the incorporation from solid phases describes the thermodynamics of incorporation versus pure mineral or solid phases, in order better approximate incorporation mechanisms involving mineral contact with aqueous solutions, the reaction energies were evaluated using aqueous phases for the An source and the replaced Fe sink. The conversion from solid source and sink phases, like  $\text{UO}_2$  and  $\text{Fe}_2\text{O}_3$ , involves multiple steps and the use of different computational schemes (a mixture of periodic and cluster calculations). Within a given sub-equation, however, the computational approach and parameters are held constant. After taking the sum of all of these reactions, various intermediate species cancel on both sides of the equation and we are left with an overall reaction between solid magnetite host and an aqueous actinide source to form the incorporated phase and an aqueous iron sink. In these equations, explicit  $\text{H}_2\text{O}$ ,  $\text{H}_3\text{O}^+$ , and  $\text{OH}^-$  species are sometimes required on the reactant or product side to balance the charge and stoichiometry. It should be noted that these species have been omitted from the simplified equations shown in Table 2.4 for clarity. An example of all of the sub-reactions and their individual reaction energies is presented for the incorporation of  $\text{U}^{4+}$ , source from  $\text{U}(\text{OH})_4^0_{(\text{aq})}$ , in Table 2.5. Equivalent reaction steps, with appropriately adjusted balancing the charge, H, and O atoms, are summed to acquire incorporation reaction energies for all of the other different aqueous U and Pu sources that were tested.

The conversion to aqueous An source and Fe sink phases increases the incorporation energy for nearly all of the reactions. All of the reaction energies are positive and only a few are more favorable when compared to using solid An sources:  $\text{Pu}(\text{OH})_3^0_{(\text{aq})}$  vs. cubic  $\text{Pu}_2\text{O}_3_{(\text{s})}$ ,  $\text{Pu}(\text{OH})_4^0_{(\text{aq})}$ ,  $\text{Pu}(\text{OH})_4(\text{H}_2\text{O})_2^0_{(\text{aq})}$ , and  $\text{Pu}(\text{OH})_4(\text{H}_2\text{O})_3^0_{(\text{aq})}$  vs.  $\text{PuO}_2_{(\text{s})}$ , and  $\text{PuO}_2^+_{(\text{aq})}$  vs. the antiferromagnetic monoclinic  $\text{Pu}_2\text{O}_5$  structure (see Table 2.6 for reaction energies of all tested

**Table 2.5** Example of the conversion process to aqueous source and sink phases for the incorporation of U<sup>4+</sup> into the octahedral Fe<sup>2+</sup> site of magnetite balanced by an Fe<sup>2+</sup> vacancy

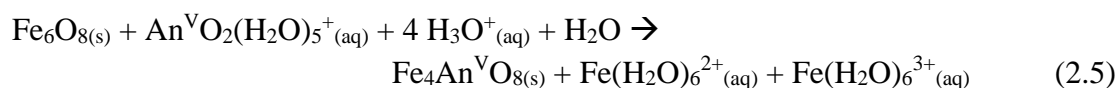
Reaction	$\Delta E_{\text{rxn}}$ (eV)
<b>Solid phase reaction (in CASTEP)</b>	
$\text{Fe}_6\text{O}_8(\text{s, mag}) + \text{UO}_2(\text{s, uran}) \rightarrow \text{Fe}_4\text{UO}_8(\text{s}) + 2 \text{FeO}(\text{s, wüs})$	0.20
<b>Source/sink conversion to periodic molecules (in CASTEP)</b>	
$\text{U}(\text{OH})_4(\text{pm}) \rightarrow \text{UO}_2(\text{s, uran}) + 2 \text{H}_2\text{O}(\text{pm})$	0.79
$2 \text{FeO}(\text{s, wüs}) + 10 \text{H}_2\text{O}(\text{pm}) \rightarrow 2 \text{Fe}(\text{OH})_2(\text{H}_2\text{O})_4(\text{pm})$	-1.56
<b>Periodic molecules to gas phase clusters (in DMol<sup>3</sup>)</b>	
$\text{U}(\text{OH})_4(\text{vac}) \rightarrow \text{U}(\text{OH})_4(\text{pm})$	0.02
$2 \text{Fe}(\text{OH})_2(\text{H}_2\text{O})_4(\text{pm}) \rightarrow 2 \text{Fe}(\text{OH})_2(\text{H}_2\text{O})_4(\text{vac})$	-0.02
$8 \text{H}_2\text{O}(\text{vac}) \rightarrow 8 \text{H}_2\text{O}(\text{pm})$	0.00
<b>Dissociation and ionization of clusters (in DMol<sup>3</sup>)</b>	
$2 \text{Fe}(\text{OH})_2(\text{H}_2\text{O})_4(\text{vac}) + 4 \text{H}_3\text{O}^+(\text{vac}) \rightarrow 2 \text{Fe}^{2+}(\text{vac}) + 16 \text{H}_2\text{O}(\text{vac})$	28.36
<b>Hydration of ions and balancing of protons (in DMol<sup>3</sup>)</b>	
$\text{U}(\text{OH})_4^0(\text{aq}) \rightarrow \text{U}(\text{OH})_4(\text{vac})$	0.66
$2 \text{Fe}^{2+}(\text{vac}) + 12 \text{H}_2\text{O}(\text{vac}) \rightarrow 2 \text{Fe}(\text{H}_2\text{O})_6^{2+}(\text{aq})$	-43.77
$4 \text{H}_3\text{O}^+(\text{aq}) \rightarrow 4 \text{H}_3\text{O}^+(\text{vac})$	15.72
$4 \text{H}_2\text{O}(\text{aq}) \rightarrow 4 \text{H}_2\text{O}(\text{vac})$	1.31
<b>Overall reaction with aqueous source and sink phases</b>	
$\text{Fe}_6\text{O}_8(\text{s}) + \text{U}(\text{OH})_4^0(\text{aq}) + 4 \text{H}_3\text{O}^+(\text{aq}) + 4 \text{H}_2\text{O}(\text{aq}) \rightarrow \text{Fe}_4\text{UO}_8(\text{s}) + 2 \text{Fe}(\text{H}_2\text{O})_6^{2+}(\text{aq})$	1.71

(s) = periodic solid phase, (pm) = periodic molecule, (vac) = gas-phase cluster, (aq) = cluster with COSMO applied, mag = magnetite, uran = uraninite, wüs = wüstite

aqueous source phases). The increase in incorporation energy for the other reactions is not uniform, but is in the range of 1.03-5.31 eV. Broadly, the incorporation of Pu from aqueous sources is slightly more favorable than equivalent U species in the +5 and +6 oxidation states. For An<sup>4+</sup>, the incorporation reactions involving the various tested hydroxide and water complexes, including U(OH)<sub>4</sub><sup>0</sup>, U(OH)<sub>4</sub>(H<sub>2</sub>O)<sub>3</sub><sup>0</sup>, are more favorable than their Pu counterparts (by 0.3 and 1.72 eV, respectively). Additionally, an increasing number in the number of explicit waters (from 2 to 4) included around the An(OH)<sub>4</sub>(aq) species results in a lowering of U incorporation energies while Pu shows the opposite trend. The highest incorporation energy ( $\Delta E_{\text{inc}} = 5.47$  eV) is calculated for

the reaction with  $\text{UO}_2(\text{H}_2\text{O})_5^{2+}_{(\text{aq})}$ . The reaction of the corresponding plutonyl species is also quite high ( $\Delta E_{\text{inc}} = 4.10 \text{ eV}$ ), although not the highest among the tested aqueous Pu species –  $\text{Pu}(\text{H}_2\text{O})_6^{3+}_{(\text{aq})}$  is the highest (see Table 2.6). The most favorable U and Pu reactions use  $\text{U}(\text{OH})_4(\text{H}_2\text{O})_3^0_{(\text{aq})}$  and  $\text{PuO}_2(\text{H}_2\text{O})_5^+_{(\text{aq})}$  with reaction energies of 1.05 and 1.94 eV, respectively.

To make statements about the equilibrium behavior of these incorporation reactions and the extent of incorporation into a mineral host, the Gibbs free energy of a reaction is required. To that end, frequency calculations for the species involved in the incorporation of U and Pu from an aqueous  $\text{AnO}_2^+_{(\text{aq})}$  source were performed to assess the impact of vibrational, translational, and rotational entropy, as well as the entropy changes related to the ordering of water around the aqueous ions or complexes, on the overall incorporation reaction energy. This entropy analysis is particularly relevant for these aqueous reactants where the ordering of water molecules around hydrated ions and molecules can significantly impact reaction thermodynamics. This type of calculation is time-consuming, particularly on the larger unit cells of the  $\text{An}_x\text{O}_x$  solid source phases, and as such, was only performed for  $\text{UO}_2^+_{(\text{aq})}$  and  $\text{PuO}_2^+_{(\text{aq})}$  incorporation, as these showed more favorable incorporation energies. For the following reaction:



The addition of the  $\Delta G$  terms lowers the incorporation reaction energies for U and Pu by 1.56 and 1.63 eV, respectively, to yield  $\Delta G_{\text{inc}}$  values of 1.32 and 0.31 eV (compare to the  $\Delta E_{\text{inc}}$  values in Table 2.4 of 2.88 and 1.94 eV). These results show that the net increase in entropy associated with the change in aqueous species on either side of the reaction and the incorporation of the An and creation of a vacancy site results makes for more favorable thermodynamics, albeit still with  $\Delta G_{\text{inc}} > 0$ .

## Discussion

### *Comparison to available literature data*

As mentioned in the Introduction section, a number of experimental studies have investigated the interaction of actinides and Fe-oxides, including magnetite. Some experiments have focused on the ability of magnetite surfaces to adsorb or mediate the precipitation of U- and Pu-bearing phases on their surfaces.<sup>15,28,36,46</sup> Other experiments have sought to simulate environments in which magnetite would precipitate from solution and take in actinides, mainly U, into its structure during growth.<sup>19,35,37,41,49</sup> The analytical approaches following these experiments generally seek to characterize two aspects of the reaction products: (1) the oxidation states of the metals present and (2) the coordination and structure of the cations. The results of these analyses are a useful comparison for our modeled structures and can validate, to a certain degree, the approach we have taken. Investigation of uranium's behavior has been far more widespread up until this time, largely due to safety and regulatory hurdles of working with Pu. Less quantitative information is available about the incorporation of Pu, but there is evidence that Pu can be reduced by Fe<sup>2+</sup> in and on minerals<sup>36,85</sup> and generally exhibits similar aqueous geochemical behavior to U.

One of the advantages of quantum-mechanical calculations is the ability to optimize specific structures with known atomic positions and/or oxidation states. The calculations in this study fix the position of the atoms in different coordination sites, but test different charge and spin configurations to identify the most stable one. Notably, the physical structures of our U-incorporated magnetites align with several of the bonding environments of structurally-incorporated U in the products of co-precipitation experiments.<sup>18,35,37</sup> On the whole, U, when structurally-incorporated into the magnetite lattice has a relatively specific bonding arrangement.

In the octahedral cation site, U develops two shorter axial bonds and four equatorial bonds. The axial bonds are longer than those that define the uranyl molecule in either its charge states (+1 or +2). This is an important distinguishing feature, because when preparing a sample for analysis it may be difficult, or even impossible, to fully separate different U-bearing phases from the fraction of the sample that contains true structural U in the Fe oxide. As a result, most authors report a range of different U-O distances that can be attributed to sorbed species, uranyl-bearing solid phases, and/or precipitated or encapsulated (non)stoichiometric  $\text{UO}_{2+x}$  (or possibly other U oxides).

The calculations presented here hone in on specific structures and return the bond distances and electronic state of structurally-incorporated U. The calculated U-O distances to nearest neighbor O atoms are in the range of those identified in experimental products. Cation-cation interaction distances between U-Fe are also in agreement with prior studies (see Table 2.2). On the experimental side, speciation and sorption of Pu to various mineral phases, including Fe-oxides, has been studied, but incorporation of Pu has yet to be explored to the same extent as U.<sup>14,16,36,86</sup> Therefore, without experimental results available for Pu structurally-bound within magnetite, the same verification of those results cannot be achieved. However, the modeled structures of Pu-magnetite are similar to U-magnetite. Since these phases have been generated in laboratory settings, it is reasonable then to assume from our findings that Pu-incorporation would occur as well.

The oxidation state of the incorporated U in the calculated structures aligns with what has been described in experiment as well. Coming from a uranyl source, U appears to be reduced when incorporated into the magnetite structure. Certainly, we do not see evidence for  $\text{U}^{6+}$  being stabilized and the population analysis results indicate that  $\text{U}^{5+}$  is likely the preferred state, in

agreement with recent work. Charge and spin are transferred rapidly in magnetite and it is possible that this behavior continues in the incorporated phases such that rapid electron transfer may take place between structural  $\text{Fe}^{2+}$  and  $\text{U}^{5+}$ , to provide bit of  $\text{U}^{4+}$  character. However, given that some experimental analyses have not detected a strong  $\text{U}^{4+}$  component in the structurally-incorporated phase, we are inclined to believe that  $\text{U}^{5+}$  is the most stable oxidation state for U in this Fe oxide structure.<sup>18-19,35,49</sup>

Although there is little experimental work available for comparison, the similarity between U and Pu in the calculated structures presented here is in line with the understanding of the behavior of these two actinides. Plutonium appears to undergo the same redox changes during incorporation into the magnetite lattice and prefers to adopt an oxidation state of  $\text{Pu}^{5+}$ , with some  $\text{Pu}^{4+}$  character due to the charge sharing from the remaining  $\text{Fe}^{2+}$  cations in the structure in the initially  $\text{Pu}^{5+}$ - and  $\text{Pu}^{6+}$ -incorporated structures. Bader population analysis<sup>87-88</sup> of U and Pu incorporated phases was performed to further verify these findings. The results show that Pu has approximately 0.5 e more electron density, indicating that it is closer to the tetravalent oxidation state than U in the same lattice configuration. Plutonium is more readily reduced than U and so this additional charge density relative to U is expected here.<sup>89</sup> Although the energies of incorporation for the solid and aqueous phase reactions are positive (save for the  $\text{PuO}_3$  solid source case), that U incorporation has been documented in experiment shows that Pu incorporation, which we calculate to have generally lower incorporation energies modeled here compared to U, is likely to be possible as well.

### ***Calculated reaction energies and evaluating sources of error***

Laboratory co-precipitation experiments are carried out over time scales and with solution chemistries that do not necessarily represent equilibrium conditions that would exist in natural

environments or long-term nuclear waste storage settings. The energies we determine for the tested incorporation reactions via our computational scheme do correspond to the equilibrium process. While the values for certain reactions may look rather high ( $\Delta E_{\text{inc}} > 2.50$  eV), incorporation could still occur over long enough time scales or if actinide concentrations and/or other solution conditions (Eh, pH, etc.) favor removal from solution.

While the computational approach taken here is a good approximation of the reaction that is expected to take place in the environment, it is important to note the ways in which these calculations do not fully capture some aspects of real-world process(es). Perhaps the most critical consideration is our treatment of hydration for the cluster species. Our calculated hydration energy values, while relatively close to those of determined via analytical methods or derived from thermodynamic data, are still not in complete agreement with experimental ones. If the hydration energy is large, even a small percent error can propagate a significant error in the overall reaction once the sub-steps are summed. The modeling of hydration is complex and is an area of ongoing research. We have found that increasing the number of explicit water molecules generally improves accuracy with respect to matching experimentally-determined values, but there is a limit to what which can be done in a reasonable amount of time given the current computational resources available. Our reactions explicitly model the first coordination sphere and approximate the contribution of further layers of coordination using the COSMO solvation model. In the future, more accurate hydration calculations, perhaps with the first two or three solvation spheres modeled explicitly may be possible on a wide scale; however, hydration spheres further out are also less oriented due to the weaker bond to the central ion and the dynamic character of water. Thus, if more and more hydration spheres are modeled using a static calculation, this would lead to an overestimation of hydration energies and only a quantum-mechanical molecular-dynamics

approach would appropriately capture this phenomenon. While this approach would have the benefit of being flexible enough to simulate elevated temperatures (*e.g.*, those of a repository environment), it would also add at least one order of magnitude to the computational effort of simulating hydration. For now, the values we have used in this study are suitable and allow for careful inferences, at least in a relative sense, to be made about the possible reaction pathways.

Another source of error in these hydration calculations, beyond the use of explicit water, is the dielectric continuum model that is used; in our case, COSMO. The COSMO model effectively calculates the Gibbs free energy ( $\Delta G_{\text{hyd}}$ ) contribution of the higher order spheres of hydration. The values are determined by calculating a solvation cavity around the molecular or ionic species that is explicitly modeled in the calculation. The size of the cavity is based on a catalog of atomic radii and the model determines the interaction of this cavity with the dielectric field to determine the non-electrostatic G contribution. This is added to the electronic internal energy (an approximation in our scheme for enthalpy, H) to generate the final COSMO energy that is used in our calculations. While COSMO adds a flavor of G to the energy, the static calculations do not determine any of the translational, rotational, or vibrational components of the entropy that would also affect  $\Delta G_{\text{hyd}}$ . As a result, the COSMO energy is left in a place where it is not as directly comparable with  $\Delta H_{\text{hyd}}$  or  $\Delta G_{\text{hyd}}$ , although we find that the calculated values agree best with the available experimentally-determined enthalpies of hydration (see Table 2.1).

Including entropy changes during incorporation may be another way to nudge up the sophistication and thermodynamic changes of the Gibbs free energies of formation in our calculations. Determining the entropy of solid (and aqueous) phases requires frequency calculations to be carried out. These calculations are computationally-intensive and so for the purposes of this study have only been performed for a select number of examples in order to

estimate the influence on the overall reaction energies. The size of some of the An oxides, for example  $\delta$ -U<sub>2</sub>O<sub>5</sub> which has a unit cell formula of U<sub>16</sub>O<sub>40</sub>, make frequency calculations essentially prohibitive for the purposes of the thermodynamic and structural understanding that we want to achieve here. The calculated thermodynamic values for the An<sup>5+</sup> incorporation reactions indicate that the  $\Delta G_{\text{inc}}$  of these reactions may in some cases be even more favorable than the  $\Delta E_{\text{inc}}$  values that we have determined and listed in Table 2.4. From this work, we believe that taking into account the changes in entropy associated with hydrating different may be the most important aspect to consider. The entropy change resulting from a more disordered incorporated solid structure was found to be quite small and had negligible effects on the overall reaction energy (on the order of 0.02 eV) relative to the large >1.5 eV changes associated with the transition to  $\Delta G_{\text{inc}}$  for reactions with aqueous species. Similarly small changes to the incorporation reaction energy were observed when the solid vibrational entropy changes were tabulated for uranyl and neptunyl incorporation into carbonate and sulfate minerals from solid sources.<sup>11</sup>

One final area in which future calculations may be able to improve the accuracy of these results is to test the incorporation of U, Pu, and other contaminants into larger supercells of magnetite and other mineral phases. Our calculations substitute a single actinide cation into the Fe<sub>6</sub>O<sub>8</sub> primitive cell, resulting in a relatively large change to the crystal chemistry. The creation of the vacancy for the majority of the reactions is also significant as one in six cation sites is left empty to balance the excess charge of the substituted species – a very high proportion of the lattice. It is expected then that the energies for incorporation to this degree would be relatively unfavorable. That some of the reaction energies are less than 1 eV is remarkable given the disruption of the original magnetite lattice. Given unlimited computational power and time, the testing the incorporation of a single actinide cation into a significantly larger cell could lower the

energy of the incorporation reactions further and allow other charge-balancing mechanisms to be explored successfully (*e.g.*, the reduction of structural  $\text{Fe}^{3+}$ ).

We tested a single reaction case with a unit cell twice as large ( $\text{Fe}_{12}\text{O}_{16}$ ) for the same  $\text{U}^{4+}$  incorporation reaction (generating  $\text{Fe}_{10}\text{UO}_{16}$ ) used in the frequency calculations. While the increased cell size allows for more relaxation within the cell, the cell as such is less able to compensate for the perturbation introduced by the incorporation. In the smaller primitive cell, fewer atoms need to be adjusted in order to make significant changes to the lattice parameters and so optimization of the cell is achieved with relative ease. As a result, the use of a doubly-large cell increases the energy of incorporation (by 0.58 eV) and only very large cells would be able to buffer this effect and decrease incorporation energies again. Cells of this size could be tested with atomistic models, but quantum-mechanical treatment of large unit cells is beyond the scope of this study as the doubling of number of atoms increases computational effort about eightfold.

Lastly, the calculated incorporation energies are subject to some biases based on the different source and sink phases used. While different polymorphs and spin configurations were tested for a number of the different An oxides, the effort was not all-encompassing. There is a wide range of polymorphs for a number of these phases and likely multiple spin configuration to be tested for each. For the purposes of this study, the number of polymorphs and spin configurations was limited. We focused the testing to the polymorphs that would be most stable at near-ambient conditions, while recognizing that co-precipitation happen at elevated temperatures if it were to take place in the immediate near-field of decaying radioactive waste. Even within this relatively small suite of the possible solid source phases, the effect on the incorporation energies was quite large, with changes up to 3 eV. Further testing of the multitude of different An oxides, as well as different aqueous species (*e.g.*, different hydrolysis species and complexes with other ligands) will

be required to capture the full chemical picture and develop a greater understanding of which reactions, at least by comparing their energies in a relative sense, are most likely to proceed in An-contaminated environments.

## Conclusions

Magnetite, and other Fe-bearing (oxyhydr)oxide minerals, are potentially some of the first solid materials that a mobilized actinide species could encounter if leaked from a waste storage cask or other engineered setting. The presence of  $\text{Fe}^{2+}$  in the magnetite structure is critical because it has the ability to donate an electron to an oxidized and mobile actinide species, like an actinyl. This process may occur on the mineral surface, but can also take place if these ions are incorporated into the mineral structure. Laboratory co-precipitation and batch sorption experiments have shown that magnetite has an affinity for U and Pu in solution and that, at least in the case of U, structural incorporation is an effective means of removing U from the aqueous phase. The incorporated actinides are less sensitive to changes in the redox or solution conditions and do not return to solution as easily as adsorbed or surface-precipitated species.

Characterization of these experimental products has led to some questions about the state of U incorporated into the magnetite lattice. The calculations presented in this study tested a number of different charge and spin configurations and reveal that U prefers an oxidation state of approximately +5 in magnetite. This finding is in line with recent experimental findings and builds on a body of research that shows the pentavalent state may be more stable than the previously appreciated in certain geochemical settings, even those with abundant  $\text{Fe}^{2+}$  where full reduction to  $\text{U}^{4+}$  would perhaps be expected.<sup>49,53</sup> The calculated bonding environment of U in our structures

shows larger U-O distances than have been reported by some previous DFT calculations and EXAFS data, but is within the range of values that have been measured (see Table 2.2).

The incorporation of Pu into the magnetite structure proceeds similar to that of U, with an oxidation state, as revealed by 5f electron spin density, of between +4 and +5 being preferred. Incorporation via simple substitution of  $\text{Pu}^{3+}$  for  $\text{Fe}^{3+}$  was also explored. In this case, no redox change is observed and the incorporation reaction energies are on the same order as those for the higher valences, indicating that this process may also be possible, if only at highly reducing conditions where  $\text{Pu}^{3+}$  is present as an aqueous source.<sup>28</sup> Overall, the incorporation reaction energies calculated here support the reduction of higher-valent actinides to  $\text{An}^{5+}$  and  $\text{An}^{4+}$  states, with charge and spin states providing evidence that  $\text{U}^{5+}$  and a slightly more reduced  $\text{Pu}^{5+/4+}$  are the dominant incorporated forms. Energies of incorporation slightly favor  $\text{An}^{4+}$  incorporation, but the difference between those energies and those for  $\text{An}^{5+}$  species (both solid and aqueous) may be due to biases in the reactants of the equation. For example, the relative hydration energies of  $\text{An}(\text{OH})_4^0$  and  $\text{AnO}_2^+$ . Frequency calculations on a subset of the  $\text{An}^{5+}$  incorporation reactions indicate that this type of analysis may yield even more favorable reaction thermodynamics for certain reactions. In the case of the tested incorporation of  $\text{AnO}_2^+(\text{aq})$ ,  $\Delta G_{\text{inc}}$  values are significantly more favorable than  $\Delta E_{\text{inc}}$ . As increasingly powerful computational resources become available to the research community, full-fledged analyses of thermodynamic parameters may improve the accuracy of future investigations of incorporation reactions, particularly those that involve the (de)hydration of various source and sink phases.

The bond distances presented here for the different An-incorporated structures agree with previous work on U incorporation into the magnetite lattice. It is envisioned that these results will serve as a reference for future characterization of experimental products, especially for Pu for

which no other structural data exist at this time. Here, the structures of Pu-incorporated magnetite are presented for the first time and notable difference between Pu<sup>3+</sup> and higher-valent Pu incorporation exist. The Pu<sup>3+</sup>-magnetite structure is unique in that the octahedral site distorts to have four shorter equatorial Pu-O lengths and two longer axial lengths. This is the opposite of what is observed for any of the other tested U and Pu configurations and along with XANES results, may serve as an indicator for the presence of this highly-reduced species in magnetite.

While we concede that different sources of error exist in the calculations, the computational formalism used results in significant cancellation of errors on both sides of the incorporation reaction equation and with careful interpretation, relative statements about reaction energetics can be made. There is significant room for further exploration of these reactions and systems and we recommend further investigation of the most accurate methods of hydration treatment and testing of incorporation into larger mineral cells (*i.e.* lower bulk actinide concentrations), and attempting different charge balancing schemes beyond the vacancy-creation approach pursued in this paper (*e.g.*, coupled substitution with a lower-valent metal or coincident reduction of Fe<sup>3+</sup> to Fe<sup>2+</sup>). We hope that computational approach presented here can continue to be built upon and applied other mineral-contaminant interactions and that the results of computational efforts can continue to serve as a valuable complement to the work of experimentalists.

## **Acknowledgements**

The authors are grateful for the support from the U.S. Department of Energy's (DOE) Office of Science, Office of Basic Energy Sciences (BES), Chemical Sciences, Geosciences, & Biosciences (CSGB) Division for the topics of Heavy Element Chemistry and Geoscience (grant number DE-FG02-06ER15783). The authors would like to thank Ben Gebarski, Lindsay

Shuller-Nickles, and Sarah Walker for their valuable advice regarding the computational approach used in this research. The authors would also like to thank Chongxuan Liu for his editorial handling and four anonymous reviewers for their comments and suggestions that greatly improved the quality of this manuscript during its submission to *ACS Earth and Space Chemistry*.

## Appendix 2A: Full suite of tested incorporation reactions and their energies

**Table 2.6** All DFT+*U* calculated incorporation energies ( $\Delta E_{inc}$ , in eV) for U and Pu into magnetite with solid and aqueous source and sink phases

Simplified reaction equations	V	An = U	An = Pu
<b>An<sup>III</sup> → Fe<sup>III</sup></b>			
$An^{III}_2O_{3(s)} + Fe^{III}_{(s, mag)} \rightarrow An^{III}_{(s, mag)} + Fe^{III}_2O_{3(s, hem)}$	none	–	1.27 <sup>a</sup> 2.14 <sup>b</sup>
$An^{III}(OH)_3^0_{(aq)} + Fe^{III}_{(s, mag)} \rightarrow An^{III}_{(s, mag)} + Fe^{III}(H_2O)_6^{3+}_{(aq)}$	none	–	2.00
$An^{III}(OH)_3(H_2O)_3^0_{(aq)} + Fe^{III}_{(s, mag)} \rightarrow An^{III}_{(s, mag)} + Fe^{III}(H_2O)_6^{3+}_{(aq)}$			3.00
$An^{III}(OH)_3(H_2O)_4^0_{(aq)} + Fe^{III}_{(s, mag)} \rightarrow An^{III}_{(s, mag)} + Fe^{III}(H_2O)_6^{3+}_{(aq)}$			3.40
$An^{III}(OH)_3(H_2O)_5^0_{(aq)} + Fe^{III}_{(s, mag)} \rightarrow An^{III}_{(s, mag)} + Fe^{III}(H_2O)_6^{3+}_{(aq)}$			3.77
$An^{III}(H_2O)_6^{3+}_{(aq)} + Fe^{III}_{(s, mag)} \rightarrow An^{III}_{(s, mag)} + Fe^{III}(H_2O)_6^{3+}_{(aq)}$			4.76
<b>An<sup>IV</sup> → 2 Fe<sup>II</sup></b>			
$An^{IV}O_{2(s)} + 2 Fe^{II}_{(s, mag)} \rightarrow An^{IV}_{(s, mag)} + 2 Fe^{II}O_{(s, wüs)}$	Fe <sup>II</sup> <sub>oct</sub>	0.20	3.02
$An^{IV}(OH)_4^0_{(aq)} + 2 Fe^{II}_{(s, mag)} \rightarrow An^{IV}_{(s, mag)} + 2 Fe^{II}(H_2O)_6^{2+}_{(aq)}$	Fe <sup>II</sup> <sub>oct</sub>		1.71
$An^{IV}(OH)_4(H_2O)_2^0_{(aq)} + 2 Fe^{II}_{(s, mag)} \rightarrow An^{IV}_{(s, mag)} + 2 Fe^{II}(H_2O)_6^{2+}_{(aq)}$			1.28
$An^{IV}(OH)_4(H_2O)_3^0_{(aq)} + 2 Fe^{II}_{(s, mag)} \rightarrow An^{IV}_{(s, mag)} + 2 Fe^{II}(H_2O)_6^{2+}_{(aq)}$			1.05
$An^{IV}(OH)_2(H_2O)_4^{2+}_{(aq)} + 2 Fe^{II}_{(s, mag)} \rightarrow An^{IV}_{(s, mag)} + 2$			4.32
$Fe^{II}(H_2O)_6^{2+}_{(aq)}$			4.44
<b>An<sup>V</sup> → Fe<sup>III</sup> + Fe<sup>II</sup></b>			
$An^V_2O_{5(s)} + Fe^{II}_{(s, mag)} + Fe^{III}_{(s, mag)} \rightarrow$ $An^V_{(s, mag)} + Fe^{III}_{(s, mag)} + Fe^{II}O_{(s, wüs)}$	Fe <sup>II</sup> <sub>oct</sub>		1.39 <sup>c</sup> 1.85 <sup>d</sup>
			0.69 <sup>c</sup> 3.69 <sup>d</sup> 0.77 <sup>e</sup>
$An^VO_2(H_2O)_5^+_{(aq)} + Fe^{II}_{(s, mag)} + Fe^{III}_{(s, mag)} \rightarrow$ $An^V_{(s, mag)} + Fe^{III}(H_2O)_6^{3+}_{(aq)} + Fe^{II}(H_2O)_6^{2+}_{(aq)}$	Fe <sup>II</sup> <sub>oct</sub>		2.88 1.94
<b>An<sup>VI</sup> → 2 Fe<sup>III</sup></b>			
$An^{VI}O_{3(s)} + 2 Fe^{III}_{(s, mag)} \rightarrow An^{VI}_{(s, mag)} + Fe^{III}_2O_{3(s, hem)}$	Fe <sup>III</sup> <sub>oct</sub>		-1.14 <sup>f</sup> -1.21 <sup>g</sup>
$An^{VI}O_2(H_2O)_5^{2+}_{(aq)} + 2 Fe^{III}_{(s, mag)} \rightarrow An^{VI}_{(s, mag)} + 2 Fe^{III}(H_2O)_6^{3+}_{(aq)}$	Fe <sup>III</sup> <sub>oct</sub>		5.47 4.10

The column labeled “V” indicates the position of the lattice vacancy, if present. All energies represent the reaction of one Fe<sub>6</sub>O<sub>8</sub> magnetite unit to create one Fe<sub>4</sub>AnO<sub>8</sub> (An<sup>4+/5+/6+</sup>) or Fe<sub>5</sub>AnO<sub>8</sub> (Pu<sup>3+</sup>). The oxidation states of the incorporated actinides represent their initial conditions prior to electronic and atomic optimization of the solid phases – see text for description of the stable electronic configurations. Full notation of all mineral phases and stoichiometric H<sub>2</sub>O, H<sub>3</sub>O<sup>+</sup>, and OH<sup>-</sup> have been omitted for clarity.

(s) = solid phase; (aq) = aqueous species; mag = magnetite structure; hem = hematite; wüs = wüstite; oct = octahedral lattice site. <sup>a</sup>fm *P-3ml* Pu<sub>2</sub>O<sub>3</sub>; <sup>b</sup>fm *Ia3* Pu<sub>2</sub>O<sub>3</sub>; <sup>c</sup>fm *Pbam* An<sub>2</sub>O<sub>5</sub>; <sup>d</sup>P2 afm An<sub>2</sub>O<sub>5</sub>; <sup>e</sup>P2/c fm An<sub>2</sub>O<sub>5</sub>; <sup>f</sup>*I41/amd* fm AnO<sub>3</sub>; <sup>g</sup>*I41/amd* afm AnO<sub>3</sub> (fm and afm represent ferromagnetic and antiferromagnetic spin ordering in the oxide phases)

## References

1. Baum, E. M.; Ernesti, M. C.; Knox, H. D.; Miller, T. R.; Watson, A. M., *Nuclides and isotopes chart of the nuclides*. Seventeenth ed.; Bechtel Marine Propulsion Corporation: Schenectady, NY, 2010; p 94.
2. Maher, K.; Bargar, J. R.; Brown, G. E., Environmental speciation of actinides. *Inorganic Chemistry* **2013**, *52* (7), 3510-3532.
3. Kersting, A. B., Plutonium transport in the environment. *Inorganic Chemistry* **2013**, *52* (7), 3533-3546.
4. Langmuir, D., Uranium solution-mineral equilibria at low temperatures with applications to sedimentary ore deposits. *Geochimica et Cosmochimica Acta* **1978**, *42* (6), 547-569.
5. Choppin, G. R., Actinide speciation in the environment. *Journal of Radioanalytical and Nuclear Chemistry* **2007**, *273* (3), 695-703.
6. Geckeis, H.; Lutzenkirchen, J.; Polly, R.; Rabung, T.; Schmidt, M., Mineral-water interface reactions of actinides. *Chemical Reviews* **2013**, *113* (2), 1016-1062.
7. Santschi, P. H.; Honeyman, B. D., Radionuclides in aquatic environments. *Radiation Physics and Chemistry* **1989**, *34* (2), 213-240.
8. Silva, R. J.; Nitsche, H., Actinide environmental chemistry. *Radiochimica Acta* **1995**, *70* (1), 377-396.
9. Taylor, S. D.; Becker, U.; Rosso, K. M., Electron transfer pathways facilitating U(VI) reduction by Fe(II) on Al- vs. Fe-oxides. *Journal of Physical Chemistry C* **2017**, *121* (36), 19887-19903.
10. Taylor, S. D.; Marcano, M. C.; Becker, U., A first principles investigation of electron transfer between Fe(II) and U(VI) on insulating Al- vs. semiconducting Fe-oxide surfaces via the proximity effect. *Geochimica et Cosmochimica Acta* **2017**, *197*, 305-322.
11. Walker, S. M.; Becker, U., Uranyl (VI) and neptunyl (V) incorporation in carbonate and sulfate minerals: Insight from first-principles. *Geochimica et Cosmochimica Acta* **2015**, *161*, 19-35.
12. Balboni, E.; Morrison, J. M.; Wang, Z. M.; Engelhard, M. H.; Burns, P. C., Incorporation of Np(V) and U(VI) in carbonate and sulfate minerals crystallized from aqueous solution. *Geochimica et Cosmochimica Acta* **2015**, *151*, 133-149.
13. Lin, J. R.; Sun, W.; Desmarais, J.; Chen, N.; Feng, R. F.; Zhang, P.; Li, D.; Lieu, A.; Tse, J. S.; Pan, Y. M., Uptake and speciation of uranium in synthetic gypsum (CaSO<sub>4</sub>•2 H<sub>2</sub>O): Applications to radioactive mine tailings. *Journal of Environmental Radioactivity* **2018**, *181*, 8-17.

14. Thomson, B. M.; Smith, C. L.; Busch, R. D.; Siegel, M. D.; Baldwin, C., Removal of metals and radionuclides using apatite and other natural sorbents. *Journal of Environmental Engineering* **2003**, *129* (6), 492-499.
15. Dodge, C. J.; Francis, A. J.; Gillow, J. B.; Halada, G. P.; Eng, C.; Clayton, C. R., Association of uranium with iron oxides typically formed on corroding steel surfaces. *Environmental Science & Technology* **2002**, *36* (16), 3504-3511.
16. Duro, L.; Missana, T.; Ripoll, S.; Grive, M.; Bruno, J., Modelling of Pu sorption onto the surface of goethite and magnetite as steel corrosion products. In *Scientific Basis for Nuclear Waste Management XXVII*, Oversby, V. M.; Werme, L. O., Eds. 2004; Vol. 807, pp 659-664.
17. Ilton, E. S.; Pacheco, J. S. L.; Bargar, J. R.; Shi, Z.; Liu, J.; Kovarik, L.; Engelhard, M. H.; Felmy, A. R., Reduction of U(VI) incorporated in the structure of hematite. *Environmental Science & Technology* **2012**, *46* (17), 9428-9436.
18. Marshall, T. A.; Morris, K.; Law, G. T. W.; Mosselmans, J. F. W.; Bots, P.; Roberts, H.; Shaw, S., Uranium fate during crystallization of magnetite from ferrihydrite in conditions relevant to the disposal of radioactive waste. *Mineralogical Magazine* **2015**, *79* (6), 1265-1274.
19. Roberts, H. E.; Morris, K.; Law, G. T. W.; Mosselmans, J. F. W.; Bots, P.; Kvashnina, K.; Shaw, S., Uranium(V) incorporation mechanisms and stability in Fe(II)/Fe(III) (oxyhydr)oxides. *Environmental Science & Technology Letters* **2017**, *4* (10), 421-426.
20. Kerisit, S.; Felmy, A. R.; Ilton, E. S., Atomistic simulations of uranium incorporation into iron (hydr)oxides. *Environmental Science & Technology* **2011**, *45* (7), 2770-2776.
21. Kerisit, S.; Bylaska, E. J.; Massey, M. S.; McBriarty, M. E.; Ilton, E. S., Ab initio molecular dynamics of uranium incorporated in goethite (alpha-FeOOH): Interpretation of x-ray absorption spectroscopy of trace polyvalent metals. *Inorganic Chemistry* **2016**, *55* (22), 11736-11746.
22. Massey, M. S.; Lezama-Pacheco, J. S.; Jones, M. E.; Ilton, E. S.; Cerrato, J. M.; Bargar, J. R.; Fendorf, S., Competing retention pathways of uranium upon reaction with Fe(II). *Geochimica et Cosmochimica Acta* **2014**, *142*, 166-185.
23. McBriarty, M. E.; Soltis, J. A.; Kerisit, S.; Qafoku, O.; Bowden, M. E.; Bylaska, E. J.; De Yoreo, J. J.; Ilton, E. S., Trace uranium partitioning in a multiphase nano-FeOOH system. *Environmental Science & Technology* **2017**, *51* (9), 4970-4977.
24. Scott, T. B.; Tort, O. R.; Allen, G. C., Aqueous uptake of uranium onto pyrite surfaces; reactivity of fresh versus weathered material. *Geochimica et Cosmochimica Acta* **2007**, *71* (21), 5044-5053.
25. Renock, D.; Mueller, M.; Yuan, K.; Ewing, R. C.; Becker, U., The energetics and kinetics of uranyl reduction on pyrite, hematite, and magnetite surfaces: A powder microelectrode study. *Geochimica et Cosmochimica Acta* **2013**, *118*, 56-71.

26. Wersin, P.; Hochella, M. F.; Persson, P.; Redden, G.; Leckie, J. O.; Harris, D. W., Interaction between aqueous uranium(VI) and sulfide minerals - spectroscopic evidence for sorption and reduction. *Geochimica et Cosmochimica Acta* **1994**, *58* (13), 2829-2843.
27. Moyes, L. N.; Jones, M. J.; Reed, W. A.; Livens, F. R.; Charnock, J. M.; Mosselmans, J. F. W.; Hennig, C.; Vaughan, D. J.; Patrick, R. A. D., An X-ray absorption spectroscopy study of neptunium(V) reactions with mackinawite (FeS). *Environmental Science & Technology* **2002**, *36* (2), 179-183.
28. Kirsch, R.; Fellhauer, D.; Altmaier, M.; Neck, V.; Rossberg, A.; Fanghanel, T.; Charlet, L.; Scheinost, A. C., Oxidation state and local structure of plutonium reacted with magnetite, mackinawite, and chukanovite. *Environmental Science & Technology* **2011**, *45* (17), 7267-7274.
29. Rak, Z.; Ewing, R. C.; Becker, U., Role of iron in the incorporation of uranium in ferric garnet matrices. *Phys Rev B* **2011**, *84* (15), 155128.
30. Rak, Z.; Ewing, R. C.; Becker, U., Ferric garnet matrices for immobilization of actinides. *Journal of Nuclear Materials* **2013**, *436* (1-3), 1-7.
31. Idemitsu, K.; Okubo, N.; Inagaki, Y.; Arima, T.; Akiyama, D.; Konashi, K.; Watanabe, M., Plutonium migration in compacted bentonite with iron corrosion for 15 Years. *MRS Advances* **2017**, *2* (12), 693-698.
32. Begg, J. D.; Edelman, C.; Zavarin, M.; Kersting, A. B., Sorption kinetics of plutonium (V)/(VI) to three montmorillonite clays. *Appl Geochem* **2018**, *96*, 131-137.
33. Alessi, D. S.; Szymanowski, J. E. S.; Forbes, T. Z.; Quicksall, A. N.; Sigmon, G. E.; Burns, P. C.; Fein, J. B., Mineralogic controls on aqueous neptunium(V) concentrations in silicate systems. *Journal of Nuclear Materials* **2013**, *433* (1-3), 233-239.
34. Lu, B. Q.; Li, M.; Zhang, X. W.; Huang, C. M.; Wu, X. Y.; Fang, Q., Immobilization of uranium into magnetite from aqueous solution by electrodepositing approach. *Journal of Hazardous Materials* **2018**, *343*, 255-265.
35. Pidchenko, I.; Kvashnina, K. O.; Yokosawa, T.; Finck, N.; Bahl, S.; Schild, D.; Polly, R.; Bohnert, E.; Rossberg, A.; Gottlicher, J.; Dardenne, K.; Rothe, J.; Schafer, T.; Geckeis, H.; Vitova, T., Uranium redox transformations after U(VI) coprecipitation with magnetite nanoparticles. *Environmental Science & Technology* **2017**, *51* (4), 2217-2225.
36. Powell, B. A.; Fjeld, R. A.; Kaplan, D. I.; Coates, J. T.; Serkiz, S. M., Pu(V)O<sub>2</sub><sup>+</sup> adsorption and reduction by synthetic magnetite (Fe<sub>3</sub>O<sub>4</sub>). *Environmental Science & Technology* **2004**, *38* (22), 6016-6024.
37. Huber, F.; Schild, D.; Vitova, T.; Rothe, J.; Kirsch, R.; Schaefer, T., U(VI) removal kinetics in presence of synthetic magnetite nanoparticles. *Geochimica et Cosmochimica Acta* **2012**, *96*, 154-173.

38. Oh, S. J.; Cook, D. C.; Townsend, H. E., Characterization of iron oxides commonly formed as corrosion products on steel. *Hyperfine Interactions* **1998**, *112* (1-4), 59-65.
39. Dunn, D. S.; Bogart, M. B.; Brossia, C. S.; Cragolino, G. A., Corrosion of iron under alternating wet and dry conditions. *Corrosion* **2000**, *56* (5), 470-481.
40. Begg, J. D.; Zavarin, M.; Kersting, A. B., Plutonium desorption from mineral surfaces at environmental concentrations of hydrogen peroxide. *Environmental Science & Technology* **2014**, *48* (11), 6201-6210.
41. Nico, P. S.; Stewart, B. D.; Fendorf, S., Incorporation of oxidized uranium into Fe (hydr)oxides during Fe(II) catalyzed remineralization. *Environmental Science & Technology* **2009**, *43* (19), 7391-7396.
42. Zhao, P. H.; Begg, J. D.; Zavarin, M.; Tumey, S. J.; Williams, R.; Dai, Z. R. R.; Kips, R.; Kersting, A. B., Plutonium(IV) and (V) sorption to goethite at sub-femtomolar to micromolar concentrations: Redox transformations and surface precipitation. *Environmental Science & Technology* **2016**, *50* (13), 6948-6956.
43. Neretnieks, I., Some aspects of release and transport of gases in deep granitic rocks: possible implications for nuclear waste repositories. *Hydrogeology Journal* **2013**, *21* (8), 1701-1716.
44. Konhauser, K. O., Diversity of bacterial iron mineralization. *Earth-Science Reviews* **1998**, *43* (3-4), 91-121.
45. Williamson, A. J.; Morris, K.; Law, G. T. W.; Rizoulis, A.; Charnock, J. M.; Lloyd, J. R., Microbial reduction of U(VI) under alkaline conditions: implications for radioactive waste geodisposal. *Environmental Science & Technology* **2014**, *48* (22), 13549-13556.
46. El Aamrani, S.; Gimenez, J.; Rovira, M.; Seco, F.; Grive, M.; Bruno, J.; Duro, L.; de Pablo, J., A spectroscopic study of uranium(VI) interaction with magnetite. *Applied Surface Science* **2007**, *253* (21), 8794-8797.
47. Scott, T. B.; Allen, G. C.; Heard, P. J.; Randell, M. G., Reduction of U(VI) to U(IV) on the surface of magnetite. *Geochimica et Cosmochimica Acta* **2005**, *69* (24), 5639-5646.
48. Duff, M. C.; Coughlin, J. U.; Hunter, D. B., Uranium co-precipitation with iron oxide minerals. *Geochimica et Cosmochimica Acta* **2002**, *66* (20), 3533-3547.
49. Ilton, E. S.; Boily, J. F.; Buck, E. C.; Skomurski, F. N.; Rosso, K. M.; Cahill, C. L.; Bargar, J. R.; Felmy, A. R., Influence of dynamical conditions on the reduction of U-VI at the magnetite-solution Interface. *Environmental Science & Technology* **2010**, *44* (1), 170-176.
50. Singer, D. M.; Chatman, S. M.; Ilton, E. S.; Rosso, K. M.; Banfield, J. F.; Waychunas, G. A., U(VI) sorption and reduction kinetics on the magnetite (111) surface. *Environmental Science & Technology* **2012**, *46* (7), 3821-3830.

51. Djogic, R.; Sipos, L.; Branica, M., Characterization of uranium(VI) in seawater. *Limnology and Oceanography* **1986**, *31* (5), 1122-1131.
52. Yuan, K.; Ilton, E. S.; Antonio, M. R.; Li, Z. R.; Cook, P. J.; Becker, U., Electrochemical and spectroscopic evidence on the one-electron reduction of U(VI) to U(V) on magnetite. *Environmental Science & Technology* **2015**, *49* (10), 6206-6213.
53. Yuan, K.; Renock, D.; Ewing, R. C.; Becker, U., Uranium reduction on magnetite: Probing for pentavalent uranium using electrochemical methods. *Geochimica et Cosmochimica Acta* **2015**, *156*, 194-206.
54. Arnold, P. L.; Love, J. B.; Patel, D., Pentavalent uranyl complexes. *Coordination Chemistry Reviews* **2009**, *253* (15-16), 1973-1978.
55. Crane, R. A.; Dickinson, M.; Scott, T. B., Nanoscale zero-valent iron particles for the remediation of plutonium and uranium contaminated solutions. *Chemical Engineering Journal* **2015**, *262*, 319-325.
56. Duff, M. C.; Hunter, D. B.; Triay, I. R.; Bertsch, P. M.; Reed, D. T.; Sutton, S. R.; Shea-Mccarthy, G.; Kitten, J.; Eng, P.; Chipera, S. J.; Vaniman, D. T., Mineral associations and average oxidation states of sorbed Pu on tuff. *Environmental Science & Technology* **1999**, *33* (13), 2163-2169.
57. Novikov, A. P.; Kalmykov, S. N.; Utsunomiya, S.; Ewing, R. C.; Horreard, F.; Merkulov, A.; Clark, S. B.; Tkachev, V. V.; Myasoedov, B. F., Colloid transport of plutonium in the far-field of the Mayak Production Association, Russia. *Science* **2006**, *314* (5799), 638-641.
58. Lu, N.; Cotter, C. R.; Kitten, H. D.; Bentley, J.; Triay, I. R., Reversibility of sorption of plutonium-239 onto hematite and goethite colloids. *Radiochimica Acta* **1998**, *83* (4), 167-173.
59. Conroy, N. A.; Zavarin, M.; Kersting, A. B.; Powell, B. A., Effect of natural organic matter on plutonium sorption to goethite. *Environmental Science & Technology* **2017**, *51* (1), 699-708.
60. Shuller, L. C.; Ewing, R. C.; Becker, U., Np-incorporation into uranyl phases: a quantum-mechanical evaluation. *Journal of Nuclear Materials* **2013**, *434* (1-3), 440-450.
61. Bengtson, A.; Morgan, D.; Becker, U., Spin state of iron in Fe<sub>3</sub>O<sub>4</sub> magnetite and *h*-Fe<sub>3</sub>O<sub>4</sub>. *Phys Rev B* **2013**, *87* (15), 155141.
62. Shuller-Nickles, L. C.; Bender, W. M.; Walker, S. M.; Becker, U., Quantum-mechanical methods for quantifying incorporation of contaminants in proximal minerals. *Minerals* **2014**, *4* (3), 690-715.
63. Shuller, L. C.; Ewing, R. C.; Becker, U., Quantum-mechanical evaluation of Np-incorporation into studtite. *Am Mineral* **2010**, *95* (8-9), 1151-1160.
64. BIOVIA *Materials Studio*, 2017 R2; Dassault Systèmes: San Diego, CA, 2016.

65. Segall, M. D.; Lindman, P. J. K.; Probert, M. J.; Pickard, C. J.; Hasnip, P. J.; Clark, S. J.; Payne, M. C., First-principles simulation: ideas, illustrations and the CASTEP code. *Journal of Physics - Condensed Matter* **2002**, *14* (11), 2717-2744.
66. Perdew, J. P.; Burke, K.; Ernzerhof, M., Generalized gradient approximation made simple. *Phys Rev Lett* **1996**, *77* (18), 3865-3868.
67. Amadon, B., A self-consistent DFT+DMFT scheme in the projector augmented wave method: applications to cerium, Ce<sub>2</sub>O<sub>3</sub> and Pu<sub>2</sub>O<sub>3</sub> with the Hubbard I solver and comparison to DFT+U. *Journal of Physics - Condensed Matter* **2012**, *24* (7), 075604.
68. Dudarev, S. L.; Botton, G. A.; Savrasov, S. Y.; Szotek, Z.; Temmerman, W. M.; Sutton, A. P., Electronic structure and elastic properties of strongly correlated metal oxides from first principles: LSDA+U, SIC-LSDA and EELS study of UO<sub>2</sub> and NiO. *Physica Status Solidi A* **1998**, *166* (1), 429-443.
69. Dudarev, S. L.; Castell, M. R.; Botton, G. A.; Savrasov, S. Y.; Muggelberg, C.; Briggs, G. A. D.; Sutton, A. P.; Goddard, D. T., Understanding STM images and EELS spectra of oxides with strongly correlated electrons: a comparison of nickel and uranium oxides. *Micron* **2000**, *31* (4), 363-372.
70. Dudarev, S. L.; Manh, D. N.; Sutton, A. P., Effect of Mott-Hubbard correlations on the electronic structure and structural stability of uranium dioxide. *Philosophical Magazine B* **1997**, *75* (5), 613-628.
71. Jomard, G.; Amadon, B.; Bottin, F.; Torrent, M., Structural, thermodynamic, and electronic properties of plutonium oxides from first principles. *Phys Rev B* **2008**, *78* (7), 075125.
72. Delley, B., From molecules to solids with the DMol<sup>3</sup> approach. *Journal of Chemical Physics* **2000**, *113* (18), 7756-7764.
73. Klamt, A.; Schuurmann, G., COSMO: A new approach to dielectric screening in solvents with explicit expressions for the screening energy and its gradient. *Journal of the Chemical Society Perkin Transactions 2* **1993**, *0* (5), 799-805.
74. Spencer, S.; Gagliardi, L.; Handy, N. C.; Ioannou, A. G.; Skylaris, C. K.; Willetts, A.; Simper, A. M., Hydration of UO<sub>2</sub><sup>2+</sup> and PuO<sub>2</sub><sup>2+</sup>. *Journal of Physical Chemistry A* **1999**, *103* (12), 1831-1837.
75. Hay, P. J.; Martin, R. L.; Schreckenbach, G., Theoretical studies of the properties and solution chemistry of AnO<sub>2</sub><sup>2+</sup> and AnO<sub>2</sub><sup>+</sup> aquo complexes for An = U, Np, and Pu. *Journal of Physical Chemistry A* **2000**, *104* (26), 6259-6270.
76. Smith, D. W., Ionic hydration enthalpies. *Journal of Chemical Education* **1977**, *54* (9), 540-542.
77. Gibson, J. K.; Haire, R. G.; Santos, M.; Marcalo, J.; de Matos, A. P., Oxidation studies of dipositive actinide ions, An<sup>2+</sup> (An = Th, U, Np, Pu, Am) in the gas phase: synthesis and

characterization of the isolated uranyl, neptunyl, and plutonyl ions  $\text{UO}_2^{2+(\text{g})}$ ,  $\text{NpO}_2^{2+(\text{g})}$ , and  $\text{PuO}_2^{2+(\text{g})}$ . *Journal of Physical Chemistry A* **2005**, *109* (12), 2768-2781.

78. Camaioni, D. M.; Schwerdtfeger, C. A., Comment on "Accurate experimental values for the free energies of hydration of  $\text{H}^+$ ,  $\text{OH}^-$ , and  $\text{H}_3\text{O}^+$ ". *Journal of Physical Chemistry A* **2005**, *109* (47), 10795-10797.

79. Marcus, Y., *Ion solvation*. John Wiley: Chichester, 1985; p 306.

80. Young, D. C., *Computational chemistry: a practical guide for applying techniques to real-world problems*. Wiley: New York, 2001; p 381.

81. Forbes, T. Z.; Burns, P. C.; Skanthakumar, S.; Soderholm, L., Synthesis, structure, and magnetism of  $\text{Np}_2\text{O}_5$ . *J Am Chem Soc* **2007**, *129* (10), 2760-+.

82. Brincat, N. A.; Parker, S. C.; Molinari, M.; Allen, G. C.; Storr, M. T., Ab initio investigation of the  $\text{UO}_3$  polymorphs: Structural properties and thermodynamic stability. *Inorganic Chemistry* **2014**, *53* (23), 12253-12264.

83. Molinari, M.; Brincat, N. A.; Allen, G. C.; Parker, S. C., Structure and properties of some layered  $\text{U}_2\text{O}_5$  phases: A density functional theory study. *Inorganic Chemistry* **2017**, *56* (8), 4468-4473.

84. Siegel, S.; Hoekstra, H. R., Bond lengths in gamma-uranium trioxide. *Inorganic & Nuclear Chemistry Letters* **1971**, *7* (5), 455-459.

85. Hixon, A. E.; Powell, B. A., Observed changes in the mechanism and rates of Pu(V) reduction on hematite as a function of total plutonium concentration. *Environmental Science & Technology* **2014**, *48* (16), 9255-9262.

86. Begg, J. D.; Zavarin, M.; Zhao, P. H.; Tumey, S. J.; Powell, B.; Kersting, A. B., Pu(V) and Pu(IV) sorption to montmorillonite. *Environmental Science & Technology* **2013**, *47* (10), 5146-5153.

87. Bader, R. F. W.; Anderson, S. G.; Duke, A. J., Quantum topology of molecular charge distributions. 1. *J Am Chem Soc* **1979**, *101* (6), 1389-1395.

88. Bader, R. F. W.; Nguyendang, T. T.; Tal, Y., Quantum topology of molecular charge distributions. II. Molecular structure and its change. *Journal of Chemical Physics* **1979**, *70* (9), 4316-4329.

89. Tsushima, S.; Wahlgren, U.; Grenthe, I., Quantum chemical calculations of reduction potentials of  $\text{AnO}_2^{2+}/\text{AnO}_2^+$  (An = U, Np, Pu, Am) and  $\text{Fe}^{3+}/\text{Fe}^{2+}$  couples. *Journal of Physical Chemistry A* **2006**, *110* (29), 9175-9182.

## CHAPTER 3

### **Determining the kinetics of discrete aqueous redox reaction sub-steps using computational methods: Application to reactions of plutonyl ( $\text{PuO}_2^{+2+}$ ) with $\text{Fe}^{2+}$ , $\text{Fe}^{3+}$ , and hydroxyl radical ( $\bullet\text{OH}$ )**

Citation:

Bender, W. M.; Becker, U., Determining the kinetics of discrete aqueous redox reaction sub-steps using computational methods: Application to reactions of plutonyl ( $\text{PuO}_2^{+2+}$ ) with  $\text{Fe}^{2+}$ ,  $\text{Fe}^{3+}$ , and hydroxyl radical ( $\bullet\text{OH}$ ). *Am J Sci* **2018**, *318*, 893-920.

[doi: 10.2475/09.2018.02](https://doi.org/10.2475/09.2018.02)

#### **Abstract**

The solubility and mobility of actinides, such as plutonium, are highly-dependent on their oxidation state, with the penta- and hexavalent species forming soluble actinyl ions (for example,  $\text{PuO}_2^{+2+}$ ). While significant data exist on the equilibrium thermodynamics of these species, the kinetic datasets for actinide reactions are less robust. To understand these reactions in greater detail, this study assesses the degree to which different sub-steps affect the overall rate of an aqueous reaction. In this approach, reactions are broken into three steps: (1) the diffusion of reactants toward each other in solution to form an outer-sphere complex, (2) the transition from outer- to inner-sphere complex, and (3) the transfer of an electron. We address encounter frequency using collision theory and the last two steps using quantum-mechanical modeling to analyze the energy, as well as atomic charges and spins, as a function of distance between the two reactants.

This approach is applied to the reactions of  $\text{PuO}_2^{2+}$  and  $\text{PuO}_2^+$  hydrolysis species with  $\text{Fe}^{2+}$ ,  $\text{Fe}^{3+}$ , and hydroxyl radical ( $\bullet\text{OH}$ ) at high pH. Regardless of the hydration treatment scheme or spin configuration (explicit vs. explicit with an implicit continuum model; ferromagnetic vs. antiferromagnetic), once species are within distances of 7.3-11.0 Å, the formation of an outer-sphere complex is found to be energetically favorable. This process proceeds rapidly even at low, environmentally-relevant plutonyl concentrations. The half-life of plutonyl in the bulk solution (that is, that which has not yet formed an outer-sphere complex) is found to be <2 min even with initial concentrations as low as the pM range, increasing rapidly if concentrations are more elevated. A program was developed in this study to determine the concentrations of different species over time based on the activation energies and rate constants derived from quantum-mechanical energy curves. Results from this program indicate that the outer-sphere configuration(s) are consumed over similar time scales as those of outer-sphere complex formation due to collision and then convert quickly to thermodynamically-favorable inner-sphere complexes.

From the quantum-mechanical calculations, changes in system energy versus reactant distance reveal the transition from outer- to inner-sphere complex, along with specific changes to the physical and electronic structure. The energy gain associated with hydrogen bonding between the first hydration spheres drives the reaction to form progressively interconnected complexes. In the models with  $\text{Fe}^{2+}$ , charge and spin analysis confirms the formation of the inner-sphere complex is coincident with the reduction of  $\text{Pu}^{5+}$  and  $\text{Pu}^{6+}$ . Since there is no change in angular (spin) momentum of the overall system when the spins of Fe and plutonyl assume opposite directions (antiferromagnetic case) during this redox process, such a spin configuration is more likely to further electron transfer. Overall, the derived kinetics of the conversion between different complex

configurations indicate that collision and outer-to-inner sphere conversion of these reactions proceed quickly and are likely not rate-limiting for these systems.

This methodology can provide insight into rate-limiting sub-processes and allow us to explore the redox behavior of Pu and other metals in greater detail. The computational scheme can now be reasonably extended to determine the kinetics of complex formation at mineral-solution interfaces and also combined with Marcus theory calculations to determine explicit electron transfer rates for complex-dependent redox processes.

## **Introduction**

Redox reactions in the environment serve as important controls on metal contaminant speciation and mobility. These reactions can result in the dissolution of metal source phases (that is, minerals) or can convert metal species to more soluble, toxic, or bioavailable forms.<sup>1-3</sup> Under different conditions, these same reactions can also proceed in the opposite direction to sequester metals in solid phases or create less labile aqueous species.<sup>4-6</sup> For any system, a suite of possible reactions exists. Which reactions will dominate and determine the equilibrium distribution of species in a system can, to a first order, be predicted by evaluating the relevant standard reduction potentials.

Standard reduction potentials for specific, individual redox reactions can be determined either experimentally or derived from thermodynamic data. With these values in hand, the possible reactions in a multi-component system can be evaluated at specific chemical conditions (for example, pH, Eh, and solute concentrations). While this can be done by hand, it is generally made more painless with the aid of computer software such as The Geochemist's Workbench<sup>7</sup> or Visual MINTEQ.<sup>8</sup> This is a powerful and widely used approach, however, it is often the case that the

modeled equilibrium distribution of species does not accurately describe an observed natural or laboratory system. A number of factors may play a role in this disparity, including the quality and applicability of the underlying thermodynamic data to the modeled systems, but a key consideration is that the observed system may not actually be at equilibrium.

In order to understand these systems that are away from equilibrium, reaction kinetics must be considered. From a predicative modeling perspective, this poses a significant challenge. Kinetic models are inherently more complicated mathematically and also require more data inputs. Currently, kinetic datasets are relatively limited in their scope of geochemically-relevant reactions when compared to the data available for equilibrium conditions.<sup>9</sup> This gap is shrinking, but may never be fully closed due to the sheer number of possible reactions and range of conditions ( $T$ , pH, Eh, et cetera) that need to be explored.

To complement the continuing experimental efforts and to meet increasing demand for kinetic data, computational approaches are likely to play an important role. With growing computational power and resources available to the scientific community, rigorous theoretical modeling approaches can be applied to questions regarding geochemically-relevant reactions, in solution and at mineral surfaces, and their kinetics.<sup>10-12</sup> This study presents an approach to kinetic calculations that can look specifically at different reaction sub-processes and applies this methodology to the reactions of soluble plutonium species with a suite of redox-active reactants:  $\text{Fe}^{2+}$ ,  $\text{Fe}^{3+}$ , and hydroxyl radical ( $\bullet\text{OH}$ ).

Plutonium is a radioactive transuranic element produced during the nuclear fuel cycle. While trace amounts of Pu have been generated in the solar system<sup>13</sup> and by natural reactors in Earth's history, as happened at Oklo in Gabon<sup>14</sup>, generally Pu is considered an anthropogenic element. As such, the main Pu hazards are related to the production and handling of nuclear fuels,

nuclear waste (re)processing and storage, the manufacture and use of nuclear weapons, and accidents at nuclear power generation stations. For some of these exposure pathways, risk will be tied to the transport of Pu in a given environment after its release.

If released into the environment, Pu is mobile in its oxidized states.<sup>15</sup> Penta- and hexavalent Pu form stable, linear dioxo-cations called plutonyl ( $\text{PuO}_2^{\text{x}+}_{(\text{aq})}$ ). These species have either a 1+ or 2+ net charge depending on the valence of the Pu center. Uranium and neptunium form analogous compounds called uranyl and neptunyl, respectively. In natural systems, these species are typically coordinated by ligands, such as carbonate ( $\text{CO}_3^{2-}$ ), that maintain their solubility and may lower their ability to participate in reactions that may reduce their mobility, namely reduction.<sup>16-17</sup> Redox reactions are the main control on how soluble these actinide species are and in order to understand their behavior in aqueous environments at or near Earth's surface we must determine which specific reactions are likely to occur and how they compete with each other. Only with this knowledge will we be able to accurately predict how Pu, and other contaminants of concern, travel in aqueous systems.

For the purposes of this study, the focus has been narrowed to the interactions of plutonyl, both as  $\text{PuO}_2^+$  and  $\text{PuO}_2^{2+}$ , with the aforementioned reactants:  $\text{Fe}^{2+}$ ,  $\text{Fe}^{3+}$ , and  $\bullet\text{OH}$ . The interaction of  $\text{Fe}^{2+}$  is of considerable interest as it is a common naturally-occurring reductant present in many environments, both as a dissolved species and in mineral structures. Additionally, Fe-bearing compounds are expected to be some of the first that leaked actinides would encounter in a geologic waste repository setting as most waste storage cask designs include some steel component that would be potentially subjected to corrosive conditions.<sup>18</sup> This interest in actinide interactions with Fe has led to a range of studies evaluating the ability of these species to participate in both heterogeneous and homogenous redox reactions (that is, those with and without a mediating

surface).<sup>19-22</sup> These studies reveal that the interplay of Pu and U with Fe species is complex and numerous questions about the kinetics of different reactions, specifically those that could reduce actinyl ions, remain.

Hydroxyl radical ( $\bullet\text{OH}$ ) is the neutral radical form of the hydroxide ion ( $\text{OH}^-$ ). It is one of several reactive species formed via the radiolysis of water, and thus can be found in solutions containing species undergoing radioactive decay, like Pu. The impact of water radiolysis products on actinides has been examined in previous studies<sup>23-24</sup> and the potential for these species to influence oxidation states and, therefore, solubility, of actinides is an area of outstanding interest. In addition, engineered water treatment systems sometimes employ Fenton's reagent, a strongly oxidizing solution containing  $\bullet\text{OH}$  generated through the reaction of  $\text{Fe}^{2+}$  and  $\text{H}_2\text{O}_2$ . While destructive oxidation of organic compounds is generally the goal in the cases where this reagent is used, its impact on metals is also of interest, particularly for waters that may have a mixed organic and inorganic contaminants or systems where the reaction of  $\text{Fe}^{2+}$  with  $\text{H}_2\text{O}_2$  produced naturally via photochemical or radiolytic means is expected.<sup>25-26</sup>

To evaluate the redox behavior of Pu in chemically-complex systems, we need to determine what reactions are possible and determine their respective rates. However, there are significant challenges when it comes to working experimentally with Pu and other transuranic species. Chief among these is that experiments can only be carried out in laboratories licensed and equipped to deal with these highly-radioactive and regulated materials. With these safety and logistical hurdles in mind, computational investigation is especially attractive. In addition to bypassing the dangers of working with Pu in a laboratory setting, computational approaches allow for detailed breakdown of potential sub-steps that comprise a redox reaction. Such specific probing is not possible for all systems with current experimental and analytical methods. Looking at these sub-steps individually

we can determine which is rate-limiting and see if that changes depending on the system in question. In addition, computational approaches provide insight into potential reaction mechanisms. Overall, this study focuses on aqueous, homogeneous reactions and lays the conceptual framework for breaking down the overall redox process into three discrete steps, with the first two treated explicitly here.

Specifically in this study, we evaluate the energy as a reaction proceeds from a stage at which plutonyl and reactant ( $\text{Fe}^{2+}$ ,  $\text{Fe}^{3+}$ , or  $\bullet\text{OH}$ ) coordination complexes are far away from each other to the point where they form an inner-sphere complex. First, the species must meet in solution to form an outer-sphere complex and the rate of this step is determined using collision theory. After that, the outer-sphere complex must overcome an energy barrier to partially decompose the two distinct coordination spheres in order to form an inner-sphere complex. This phase of the reaction is examined quantum-mechanically. A full kinetic treatment of electron transfer, for example using Marcus theory, is beyond the scope of this study; however, spin density and electron transfer along the reaction path will be described. Special attention will be given to the role of hydrogen bond formation and breaking, which has a significant influence on the overall reaction kinetics.

## **Methodology**

### *Defining sub-steps in a redox reaction and calculating their rates*

A redox reaction is generally written in a single line or broken into its component half reactions. As written, this reaction corresponds specifically to the electron transfer from one species to another. However, in order for this reaction to occur there are steps that must take place first. To calculate the rates of different sub-steps in a redox reaction, we must first determine which

processes occur in sequence and which computational approach to apply to each. In the framework presented here, a redox reaction is broken down into three steps.

First in this order of operations, the reactants must meet each other in solution and form an encounter complex. For the purposes of this framework, we will consider the encounter complex to be analogous to the first outer-sphere complex configuration assumed by the plutonyl and other reactant, each with fully intact first coordination shells of water around them. The rate of this process can be calculated using aqueous collision theory. Initially developed for the gas phase<sup>27</sup>, this concept is now extended to describe aqueous systems and describes the number of particle collisions<sup>28</sup>, which is equal to the number of outer-sphere complexes formed, per second as a function of the concentration of the species, their diffusion velocities, and a distance, called the reactive radius, within which a collision is deemed to have occurred. The expression we use to describe this is given in Equation 3.1:

$$r = \pi R^2 v N_A [X][Y] \quad (3.1)$$

Where  $R$  is the reactive radius (in dm),  $v$  is the geometric mean of the diffusion velocities (in dm/s) of the two reactants (X and Y), and  $N_A$  is Avogadro's number. When considering systems where  $[Y] \gg [X]$ , much of Equation 3.1 can be grouped to comprise a pseudo first-order rate constant of between  $\sim 3,150$ - $10,800 \text{ s}^{-1}$  when  $[Y] = 1 \text{ }\mu\text{M}$ . The variability here is tied to the different  $R$  and  $v$  values for the systems in this study. Using Equation 3.1, the calculation of different rates of outer-sphere complex formation is relatively straightforward. The only value that is not immediately obvious is the reactive radius of the system.

One way to determine  $R$ , is to perform a series of quantum-mechanical calculations at different reactant-reactant distances. Plotting the overall system energy versus that distance, we can derive  $R$  by looking for the position at which the energy of the system drops off from the

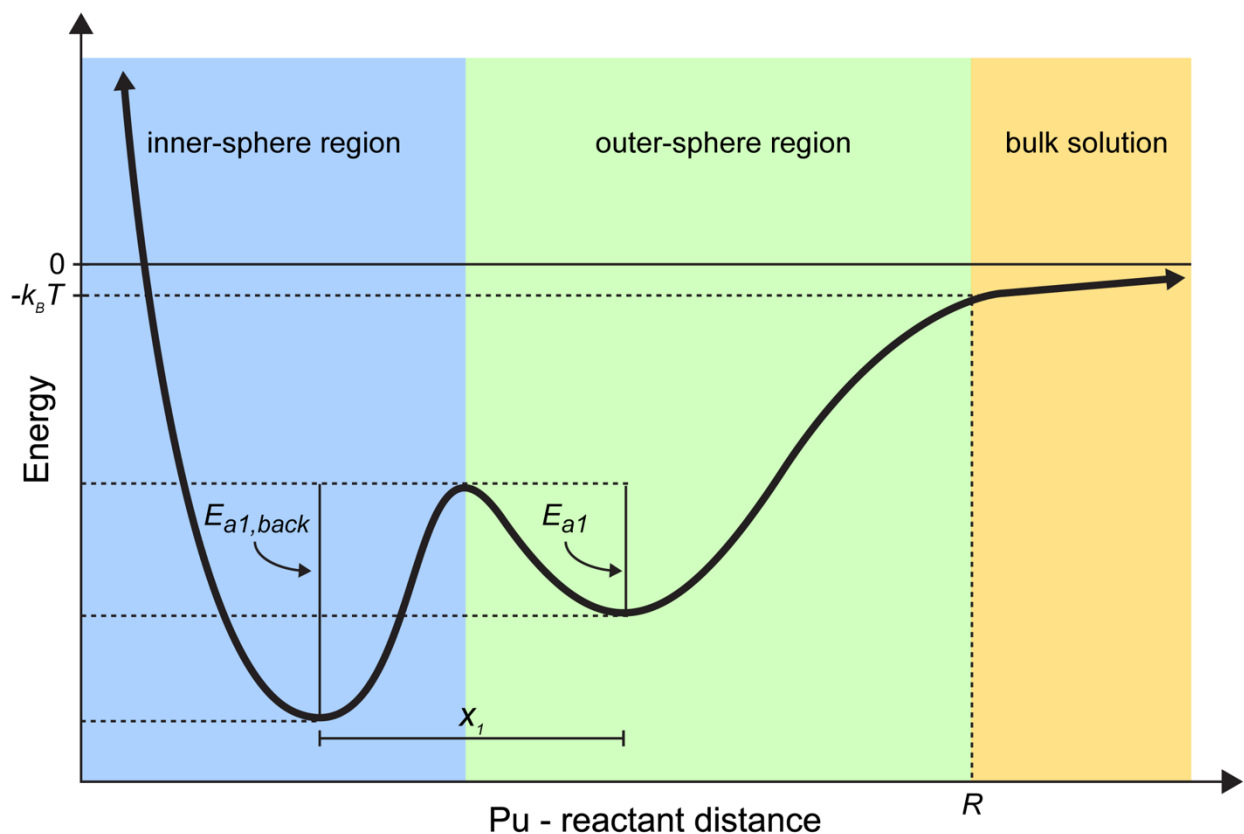


**Figure 3.1** An idealized model showing the energy change in a system as a function of Pu–reactant distance. The distinct energy wells associated with the two complex types are shown, with this case representing a situation where the inner-sphere complex is the more energetically-favorable configuration. The activation energies of the outer- to inner-sphere transition reaction ( $E_{a1}$ ) and the back reaction ( $E_{a1,back}$ ) are shown, as are the position of the reactive radius ( $R$ ), where the energy drops one  $k_B T$  unit below the bulk solution energy plateau, and the distance between the energy minima ( $x_1$ ) for this transition.

energy plateau found at large reactant distances. This position is labeled on the idealized energy versus distance surface shown in Figure 3.1. Specifically, we define the position of  $R$  to be that at which the energy of the system has dropped by one  $k_B T$  unit ( $\sim 2.5$  kJ/mol) below that energy plateau. Within the reactive radius, the slope of energy versus distance is favorable such that further attraction of the two species is essentially irreversible and they will proceed to get closer until a local energy minimum is reached that represents an outer-sphere coordination environment.

Upon forming an outer-sphere complex, the second step is the transition from an outer-sphere to an inner-sphere complex. This involves the reactants moving closer together and sharing

some of their ligand bonding partners. Then, if brought even closer, they may lose several of their coordinating ligands (for example, water molecules for aqueous complexes as described in this study, or carbonate molecules in carbonated actinyl complexes) and exist together within a single, continuous coordination cavity. In our systems, the coordinating ligands are simple and the first hydration spheres are modeled explicitly with a combination of H<sub>2</sub>O and OH<sup>-</sup>. This process of bringing the reactants closer together and breaking, and possibly reforming, bonds to coordinating ligands requires some energy. This energy is a barrier between the outer-sphere and inner-sphere complexes and shows up as a hump or spike in the calculated energy surface. In Figure 3.1, this simple example shows an activation energy ( $E_{a1}$ ) for the transition from the outer- to inner-sphere configuration. Similar features are observed for our tested systems, but some species show multiple energy barriers along the path to the inner-sphere complex, representing different outer-sphere complex geometries.

There are a different approaches for how to determine the rate at which the transition from outer- to inner-sphere complex occurs. The first is to consider the outer-sphere complex as a harmonic oscillator. This assumption allows the energy surface at the outer-sphere complex position to be treated as that of a spring. A parabolic function, rearranged in the form of Equation 3.2, can be fit to the data.

$$E = \frac{1}{2}k_s(x - x_o)^2 \quad (3.2)$$

From this equation, we can extract the spring constant,  $k_s$ , which can then be used, along with the mass of the oscillating species,  $m$ , to determine an attempt frequency ( $A$ ) for the oscillating system as described in Equation 3.3:

$$A = \frac{1}{2\pi} \sqrt{\frac{k_s}{m}} \quad (3.3)$$

This attempt frequency, along with the activation energy ( $E_a$ ), gas constant ( $R$ ), and temperature ( $T$ ), can then be related using the familiar Arrhenius equation (Equation 3.4) to return a rate constant ( $k_r$ ) for this process.

$$k_r = Ae^{\frac{-E_a}{RT}} \quad (3.4)$$

This procedure can be carried out for back reactions as well, using the parabola fit for the inner-sphere energy well (our intermediate outer-sphere configurations) and the associated activation energy for the outward-moving reaction (for example,  $E_{a1,back}$  in Figure 3.1).

A second approach for determining the transition rate between an outer-sphere and inner-sphere complex is to use a method originally applied for diffusion of atoms in a periodic system<sup>29</sup>. This approach is useful because some of the features observed in the energy versus distance plots in this study are not fit well by parabolic functions. These features have more of a step-like shape, with a steep decrease in energy leading to a local minimum, followed by a more parabolic increase in energy as the Pu-reactant distance is decreased further (examples of these features can be seen on the energy surface in Figure 3.2). These sharp energy decreases correspond to specific changes in the complex geometries, specifically, the formation of new hydrogen bonds between members of the two coordination spheres. To treat this bond formation as a harmonic oscillator would not be appropriate and so instead, the approach of Reich, et al.<sup>29</sup> is employed. This approach, shown in Equation 3.5, utilizes only the mass of the species, the activation energy, and the distance ( $x$ ) to energy minimum on the other side of a given energy barrier.

$$A = \frac{1}{\sqrt{2}} \sqrt{\frac{E_a}{mx^2}} \quad (3.5)$$

The attempt frequencies derived in this way can then be used in the Arrhenius equation as with the other approach. To check the validity of this approach to model the energy surface features that had a steep drop in energy on one side, a parabola was constructed to fit the smoother side of

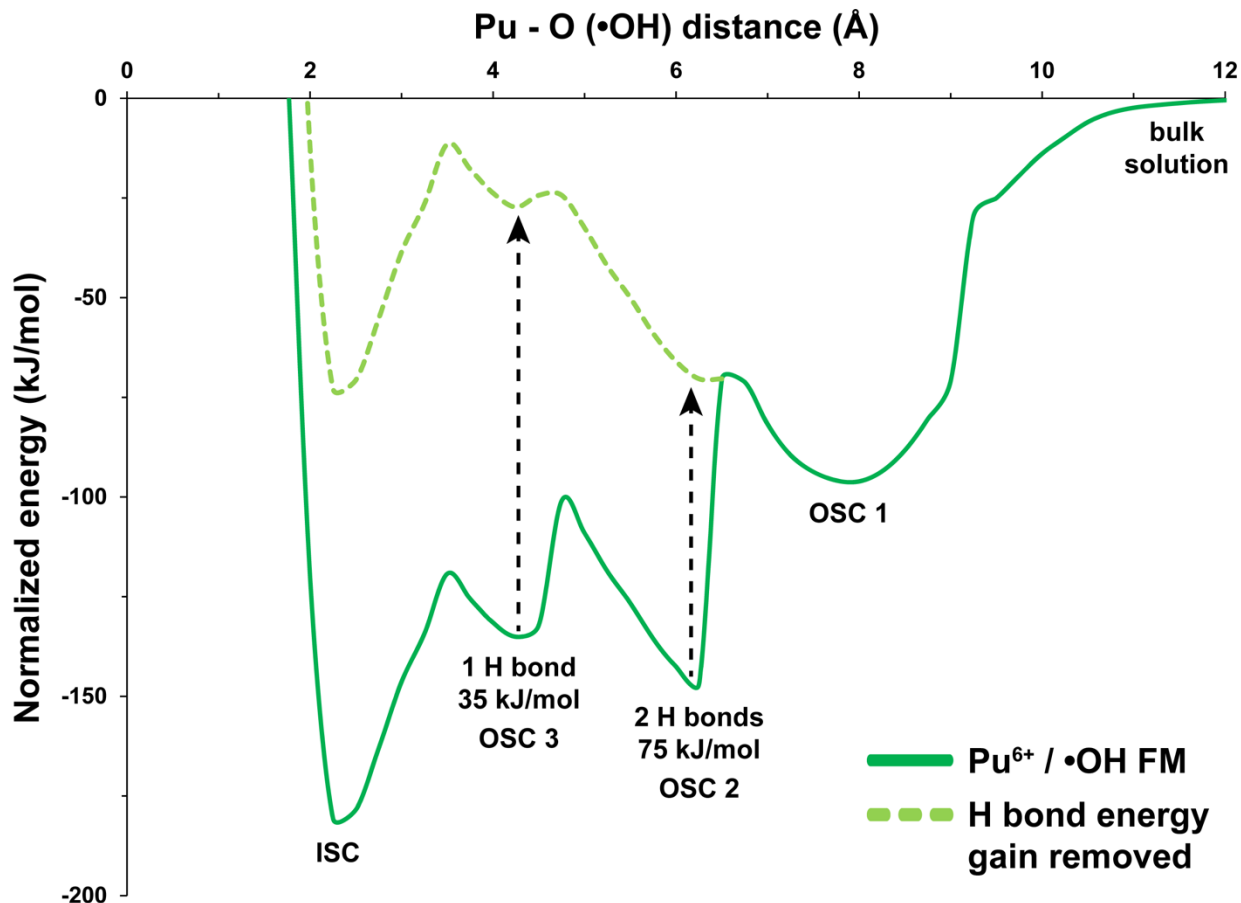


**Figure 3.2** The calculated energy surface for  $\text{PuO}_2^{2+}$  and  $\bullet\text{OH}$  shows energy steps associated with the formation of H bonds in the ferromagnetic vacuum state calculation. These bonds, shown for the step near 6 Å in Figure 3.3, are formed as  $\text{H}_2\text{O}$  and  $\text{OH}^-$  rearrange when the distance between Pu and the radical is decreased. The change in system energy reflects the number of new bonds that are formed. The dashed line shows the energy surface if the energy of these bonds forming is subtracted, resulting in a broad outer-sphere well, as opposed to three discrete outer-sphere complex configurations (OSC 1-3), that yields slow kinetics for the transformation to the inner-sphere complex (ISC) at  $\sim 2.25$  Å.

the energy “well” (typically the side towards shorter distances). By doing this, we are assuming that once the system drops in energy down the steep step, it will proceed to harmonically oscillate in its new bonding configuration. Comparing the approaches, we find that the calculated attempt frequencies are only different by less than a factor of 2, with the higher of the two values coming from Equation 3.5. Given the relatively small difference between the approaches, the second method is applied for energy features that have this asymmetric shape for convenience as no data

fitting is required. This error can be considered relatively small because the variability of H bond formation and breaking typically causes a higher variation in reaction rates than the approach chosen.

After the rates of transition between different complexes are determined, both for forward and back reactions, the last step in the redox process is the electron transfer. Electron transfer rates can be determined experimentally, but these approaches can only be applied to systems or reactions in which inner- and outer-sphere complexes and/or pre- and post-electron transfer states show marked differences in some spectroscopically measurable characteristic (for example, color). These rates have generally been calculated for strongly-colored transition metal-organic compound complexes that are highly-conjugated and exhibit distinct differences between either the inner- and outer-sphere configuration or with regards to the charge of the metal center.<sup>30</sup> Actinides do form distinctly colored complexes for specific oxidation states, but the color change is not necessarily uniform over a variety of ligands and is not specific to inner- or outer-sphere complexation with other species.

With these limitations in mind, the calculation of electron transfer rates is an attractive option for many systems. Marcus Theory allows for the rates of electron transfer between species to be calculated.<sup>31-32</sup> However, this approach is time-consuming and it is not yet easy to screen a wide range of reactions. For the purposes of this study, we investigate electron transfer in a semi-kinetic way by looking at how energy changes correspond to variations in atomic charge and spin over the course of the calculated reactant-distance series.

The three sub-steps described above control the progression of redox reactions in solution. These steps are also applicable to reactions at mineral-solution interfaces where the inner- and outer-sphere complexes are formed between an aqueous species and the outer-most surface atoms

of a mineral phase. Depending on the reactants in question, as well as a variety of other factors (for example, solution chemistry, temperature) the rate-limiting step may vary. With the computational approaches employed here, we are able to break these down and investigate which step is rate-limiting for a given reaction. While the absolute values of the rates for the different sub-processes may not be entirely verifiable with experimental approaches, the overall reaction rate may be and, at the very least, calculated rates can be compared to make statements about the relative likelihood and rate of reaction for different species. A major goal of this study is to use plutonyl reactions as a proof-of-concept for this computational framework, particularly for the first two sub-steps, and generate some kinetic rates for sub-reactions that are relevant for the control of Pu mobility in surface water and groundwater environments.

### *Quantum-mechanical calculations*

In this study, the density functional theory (DFT) code, Gaussian 09 (Revision.A02)<sup>33</sup> was used to calculate the physical geometries, electronic properties, and overall energies of the modeled chemical systems. Calculations were carried out using the B3LYP hybrid functional<sup>34-36</sup> along with the LANL2DZ basis and pseudopotential set.<sup>37-39</sup> This pseudopotential set includes relativistic effects for Pu. The pseudopotential and basis set information was collected from the EMSL Basis Set Library.<sup>40-41</sup> A subset of test calculations were performed using the more rigorous all-electron correlation consistent basis (AUG-cc-pVTZ) for H, O, and Fe, but the changes to the shape of calculated energy versus distance surfaces and population analysis results were found to be minimal.<sup>42-44</sup> Testing of several other computational parameters, the inclusion of zero-point vibrational energy and the basis set superposition error, was also performed. These details of these calculations are discussed in Appendix 3A: Testing of computational parameters

Cluster models of plutonyl (as  $\text{PuO}_2^{2+}$  or  $\text{PuO}_2^+$ ) and one of three reactants ( $\text{Fe}^{2+}$ ,  $\text{Fe}^{3+}$ , or  $\bullet\text{OH}$ ) were constructed and serve as the basis for the investigation of potential redox reactions. In these models, hydration is treated in two ways. First, all models include explicit water molecules that comprise the first hydration sphere. The models were made charge neutral by replacing some of the coordinating water molecules with  $\text{OH}^-$ . For example, in our plutonyl clusters, one or two of the five equatorial water molecules are replaced with  $\text{OH}^-$  to create the charge-neutral hydrolysis species  $\text{PuO}_2(\text{OH})^0$  and  $\text{PuO}_2(\text{OH})_2^0$ . Initially, these  $\text{OH}^-$  are positioned such that at least one water molecule lies between them in the coordination ring around the Pu center. A similar approach is applied to  $\text{Fe}^{2+}$  and  $\text{Fe}^{3+}$ , with  $\text{OH}^-$  replacing two or three waters in the octahedral coordination environment respectively. The  $\text{OH}^-$  groups were positioned in the input orientation such that they would be on the outside of the colliding complexes and repulsion between  $\text{OH}^-$  groups would be minimized. These hydrolysis complexes of plutonyl and iron cations form in high pH environments and the results that are derived from their interaction are only directly relevant to those conditions. Additionally, collisions in real solutions take place in random orientations, but in this study we will consider just one input orientation that seeks to minimize electrostatic repulsion between ligands that could hinder inner-sphere complex formation. The complexes were also made charge neutral to minimize the energy gain associated with purely electrostatic attraction of two coordination complexes to each other. In addition to explicit hydration, replicate distance series were carried out using an implicit hydration model, C-PCM, developed by Cossi, et al.<sup>45</sup>. This model simulates the contribution of higher-order spheres of hydration with a homogeneous dielectric field around the first coordination sphere(s), but does not add more atoms to the system.

To test the impact of unpaired spin arrangement on the thermodynamics and kinetics on the systems, high-spin ferromagnetic and antiferromagnetic configurations were calculated for all

of the systems. In the ferromagnetic calculations, all unpaired spins were set in the upward orientation (filling the alpha orbitals). In antiferromagnetic calculations, the species with the larger number of unpaired spins was set in the spin up orientation and the other species was set to be spin down (in beta orbitals). This results in systems with net upward spin of varying magnitudes. The number of unpaired electrons in the high-spin configurations of  $\text{PuO}_2^{2+}$ ,  $\text{PuO}_2^+$ ,  $\text{Fe}^{2+}$ ,  $\text{Fe}^{3+}$ , and  $\bullet\text{OH}$  is 2, 3, 4, 5, and 1, respectively. As an example, the net number of unpaired spins for the  $\text{PuO}_2^+/\text{Fe}^{2+}$  system is 7 in the ferromagnetic and 1 in the antiferromagnetic arrangement. The antiferromagnetic coupling systems have the advantage of preserving angular momentum during the transfer of an electron. In other words, in these reactions, the net number and orientation of spins in the system does not change.

To determine the change in system energy versus distance, geometry optimization calculations were carried out at fixed reactant distances. In these calculations, the Pu center of the plutonyl molecule and one molecule of the reactant coordination complex (the Fe cation or O atom of  $\bullet\text{OH}$ ) were held fixed. The coordinates of all other atoms were allowed to optimize freely to achieve the lowest energy configuration. Starting from a relatively large Pu-reactant distance, on the order of  $\sim 12\text{-}15 \text{ \AA}$ , sequential geometry optimizations were carried out at progressively smaller distances, in increments of  $0.25 \text{ \AA}$ , down to a distance of  $\sim 2 \text{ \AA}$ . In some of the calculations at the greater distance end of the series, a larger step size of  $0.5 \text{ \AA}$  was used where the energy slope was very small and fine distance resolution was not necessary to capture the energy trend. The finer increment was used at distances near and within the reactive radius in order to capture the shape of the energy surface and potential energy barriers with more detail. Calculations were performed sequentially using the previously optimized geometry, with the reactant species and all of its coordinating molecules shifted closer by the given distance increment, as a starting point. A

wavefunction guess from the previous calculation was also taken as a starting point to facilitate more rapid electronic convergence. Following geometry optimization, Bader population analysis was performed at each step to analyze the change in atomic charge and spin in the system as the distance between the reactants was decreased.

## Results

### *Determination of the reactive radius*

Sequential geometry optimization calculations reveal distinct reactive radii for the different systems that were tested. Reactive radius varies with the reactants and also with the computational parameters used, specifically whether or not an implicit hydration scheme is applied and which spin configuration is used. In vacuum, the reactive radii are found to be larger than those determined from the C-PCM calculations. In the Fe-bearing systems, antiferromagnetic spin coupling leads to smaller reactive radii except for the explicitly hydrated ferromagnetic  $\text{PuO}_2^{2+}/\text{Fe}^{2+}$  case. Overall, regardless of using, or not using, an implicit hydration scheme, all reactive radii for reactions of plutonyl with Fe cations reactions are between 7.3-10.9 Å. The reactive radii for the  $\text{PuO}_2^{2+}/\text{Fe}^{2+}$  are smaller than those of the  $\text{PuO}_2^{+}/\text{Fe}^{3+}$  system, but the difference is more noticeable in the ferromagnetic case.

For the plutonyl/ $\bullet\text{OH}$  systems, reactive radii are found to be in a similar distance range (8.2-11.0 Å), but are slightly larger than those calculated for the Fe pairs. Here again, the C-PCM hydration model leads to smaller reactive radii and, as seen with  $\text{Fe}^{2+}$  and  $\text{Fe}^{3+}$ , this approach can cause the radius to shrink by nearly 2 Å in some cases. This effect is expected due to the electric screening of the dielectric fluid (or, in a real system, of the actual water). However, in others, the change is less pronounced and the reactive radius decreases by <0.3 Å using this model. With  $\bullet\text{OH}$ ,

the effect of the spin configuration on the reactive radius is not consistent. Going from a ferromagnetic to antiferromagnetic arrangement increases the reactive radius for reaction with  $\text{PuO}_2^+$  and decreases it for reaction with  $\text{PuO}_2^{2+}$ . The full suite of calculated reactive radii for the different reactive pairs and computational parameters (hydration treatment and spin configuration) is presented in **Table 3.1**.

**Table 3.1** Calculated reactive radii ( $R$ ) for different reactant pairs, spin configurations, and computational parameters

		Reactive radius of system (in Å) <sup>a</sup>				
Spin configuration <sup>b</sup>	Hydration model <sup>c</sup>	$\text{PuO}_2^{2+}$		$\text{PuO}_2^+$		
		$\text{Fe}^{2+}$	$\bullet\text{OH}$	$\text{Fe}^{2+}$	$\text{Fe}^{3+}$	$\bullet\text{OH}$
FM	Explicit w/ C-PCM	8.9	11.0	10.0	10.8	9.7
		7.7	10.0	7.7	9.5	8.3
AFM	Explicit w/ C-PCM	9.7	8.7	10.9	9.9	10.1
		7.3	8.5	7.7	7.7	8.2

<sup>a</sup> Systems are charge neutral through the substitution of  $\text{OH}^-$  into the coordination spheres of the plutonyl and Fe species. The unit angstrom (Å) is equal to  $10^{-10}$  m.

<sup>b</sup> Ferromagnetic (FM) and antiferromagnetic (AFM) configurations all have net alpha spin.

<sup>c</sup> The C-PCM calculations apply the implicit hydration model on top of the included first hydration sphere that is still modeled explicitly.

### *Collision rates and outer-sphere complex formation*

Using the reactant pair-specific reactive radius, the rate of outer-sphere complex formation can be evaluated for any reactant concentrations. As outer-sphere complexes are formed, the bulk solution concentration of free species decreases. Thus, this collision rate is only applicable as an instantaneous rate for a given set of concentrations. As outer-sphere complexes form, the rate must be recalculated to reflect the decreasing concentration of free, uncomplexed reactants in solution. Through iterative rate calculation, the concentration trends for each species can be revealed.

Broadly, initial outer-sphere complex formation rates are found to be high, over a range of concentrations, for the tested reactions. Rates decrease with decreasing reactant concentration, but even at low concentrations, the nearly all reactants meet to form outer-sphere complexes within fractions of a second. For clarity, and to better understand the time scales over which this process takes place, the data are presented as reactant half-lives ( $t_{1/2}$ ). This value represents the amount of time it takes for half of the initial concentration of the less concentrated species (in our models plutonyl is always considered to be less concentrated than the other reactant) has formed an outer-sphere complex. Table 3.2 presents the  $t_{1/2}$  values for a representative subset of the calculated reactions over several concentration regimes.

The marginally slower rate for the reaction with  $\bullet\text{OH}$  can be explained by its slower diffusion velocity relative to the charged iron species. For reactions with a fast transition from outer- to inner-sphere complex, outer-sphere complex also has an extremely brief half-life. As outer-sphere encounter complexes are formed from collision of the uncomplexed coordination compounds in solution, they are quickly converted to progressively closer outer-sphere complexes (when those configurations are present), and finally to an inner-sphere complex. For all of the tested reactive pairs, the inner-sphere configuration is significantly more energetically favorable and the relative concentration of this species grows rapidly over short time scales.

**Table 3.2** Representative set of calculated half-lives ( $t_{1/2}$ ) of uncomplexed  $\text{PuO}_2^+(\text{aq})$  as a function of reactant, concentration, and different computational settings

<b>[PuO<sub>2</sub><sup>+</sup>]</b>	<b>[Fe<sup>x+</sup> or •OH]</b>	<b>PuO<sub>2</sub><sup>+</sup>/Fe<sup>2+</sup> C-PCM, FM</b>	<b>PuO<sub>2</sub><sup>+</sup>/Fe<sup>2+</sup> C-PCM, AFM</b>	<b>PuO<sub>2</sub><sup>+</sup>/•OH vacuum, FM</b>	<b>PuO<sub>2</sub><sup>+</sup>/•OH C-PCM, FM</b>
<b>1 μM</b>	<b>1 mM</b>	19.4 μs	22.2 μs	8.1 μs	11.4 μs
<b>1 nM</b>	<b>1 μM</b>	19.4 ms	21.9 ms	8.1 ms	11.3 ms
<b>1 pM</b>	<b>1 nM</b>	19.4 s	21.9 s	81.3 s	113.3 s

Diffusion velocities derived from experimentally-determined diffusion coefficients of monovalent plutonyl<sup>46-47</sup>, ferrous and ferric iron<sup>48</sup>,  $\bullet\text{OH}$ <sup>49</sup>, and the ionic radii of Shannon.<sup>50</sup>

### *Physical structure changes during the transition from outer-sphere to inner-sphere complex*

Starting from the input geometries and global charge and spin parameters, the tested systems display a range of changes in their physical and electronic structures as they are brought closer together. At the initial reactant distance of 12-15 Å, depending on the system in question, the two reactant complexes are effectively separated with minimal interaction. The energy surface at these distances larger than the reactive radius is essentially flat, with a very small positive slope.

At these distances, no significant geometry or electronic structure changes are observed. However, at distances just larger than the reactive radius, some systems do begin to exhibit changes in their atomic arrangements. At this distance, plutonyl has a tendency to tilt from its initial position and angle one of its  $O_{\text{axial}}$  atoms towards the incoming reactant. The input geometry sets the initial plutonyl position along the  $z$  axis with a  $90^\circ$  angle between the plutonyl  $O_{\text{axial}}$  atoms, the Pu center, and the incoming reactant (either an Fe cation or the O of the  $\bullet\text{OH}$ , some distance away along the  $x$  axis). The tilting of the plutonyl is particularly pronounced in some of the Fe-bearing systems models as the  $O_{\text{axial}}$  positions itself to be closer to the incoming Fe cation. This tilting of the plutonyl requires reorganization of the coordinating  $\text{H}_2\text{O}$  and  $\text{OH}^-$  and results in the energy penalty. No significant change in the charge or spin density distribution is observed during this process.

Following any energy hump at the lip of the reactive radius, all models show an increase in slope. As the system moves down the energy surface over decreasing reactant distances, new features are observed. In some cases, parabolic wells are formed with energy barriers rising up on the inward side of a local minimum (see FM  $\text{PuO}_2^{2+}/\bullet\text{OH}$  energy surface at 7.75 Å in Figure 3.2). These features are in good agreement with the idealized model presented in Figure 3.1. In others, downward-sloping step-like features are formed, with energy decreasing significantly at the edge of the step without any detectable energy barrier.

A final feature is one where energy progressively increases as the distance decreases, only to decrease sharply at a given point and start a new, sometimes parabolic, increase at a lower energy level. Figure 3.2 shows two examples of these features at  $\sim 4$  and  $7 \text{ \AA}$  for the ferromagnetic  $\text{PuO}_2^{2+}/\bullet\text{OH}$  system calculated in vacuum. The atomic structures from the  $6.5$  and  $6.25 \text{ \AA}$  positions, corresponding to the top and bottom of the first steep energy drop, are presented in Figure 3.3. The structures reveal that the cause of these steep decreases in energy is related to the formation of H bonds. During the transition from the first outer-sphere complex (OSC 1) to the second (OSC 2) in Figure 3.2, two hydrogen bonds are formed resulting in an energy gain of approximately  $75 \text{ kJ/mol}$ . The second feature, the transition to the final outer-sphere complex configuration (OSC 3) in this system, is related to the formation of just one additional H bond. The energy gain at this position is about half of that for the earlier step. These sharp changes in system energy are related to H bond formation and observed in nearly all of the  $\bullet\text{OH}$  systems that were tested.

The three different types of features in the energy surface all record changes in either the physical or electronic structure. In the outer-sphere region, the transitions between different complex conformations are related to changes in the H bonding arrangement of the coordinating  $\text{H}_2\text{O}$  and  $\text{OH}^-$  molecules. As the clusters are brought together, the merging of the hydration spheres of the two compounds leads to some temporary unfavorable atomic arrangements. Were the atoms not permitted to relax as they are in the geometry optimization calculations, the energies of the system would be very high, mainly due to short interatomic distances. Instead, the atoms are allowed to relax and find the most energetically-favorable arrangement. In doing so,  $\text{H}_2\text{O}$  and  $\text{OH}^-$  move out of the way and allow for the transition from outer- to inner-sphere complex. It is through this process that the coordinating ligands have the opportunity to form new hydrogen bonds with their nearest neighbors. Depending on the system, these changes to the H bonding network can

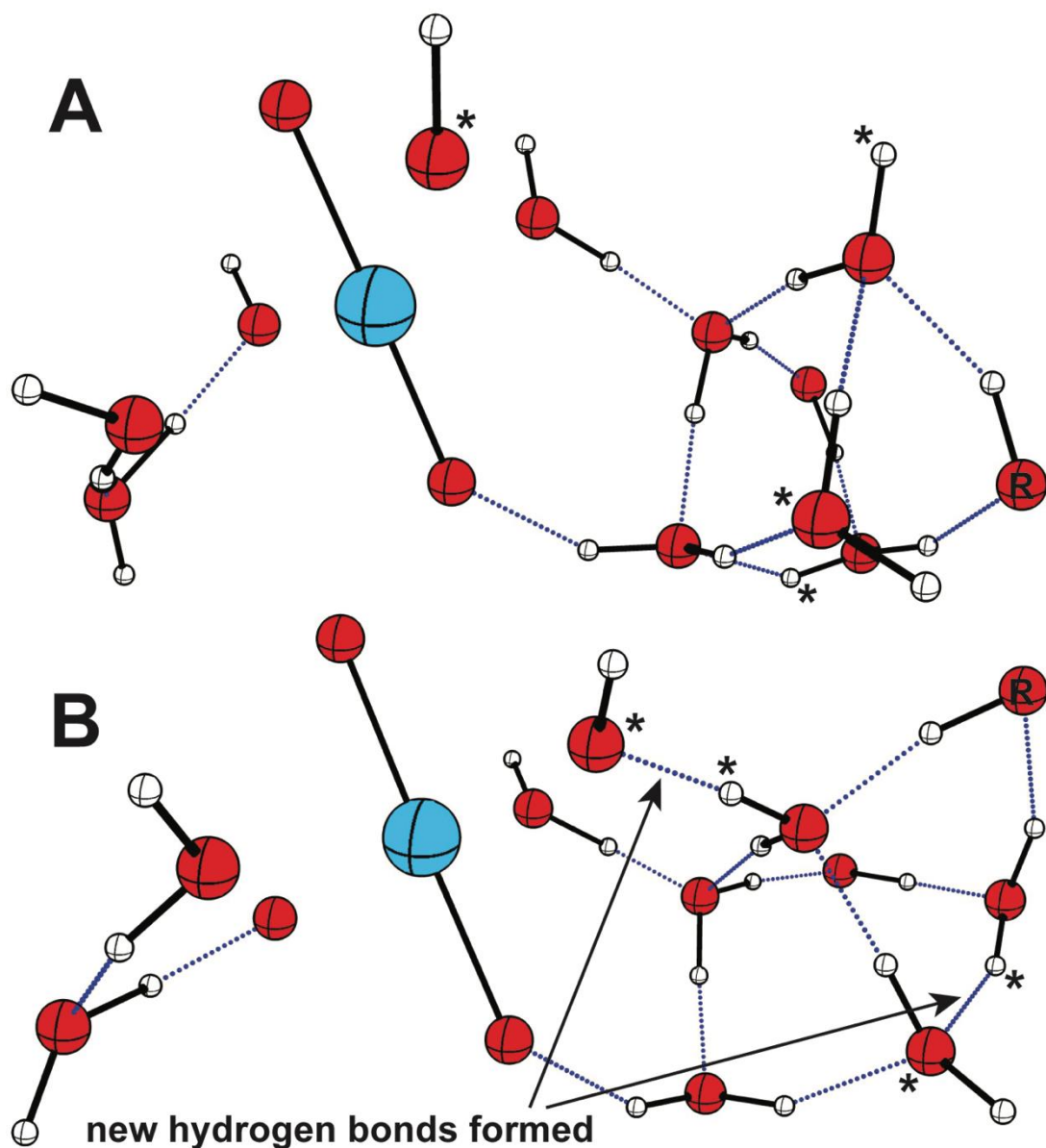


**Figure 3.3** Optimized structures from sequential calculations in the ferromagnetic  $\text{PuO}_2^{2+}$  and  $\bullet\text{OH}$  distance series in vacuum. Pu – radical O (atom labeled “R”) distances are 6.5 and 6.25 Å for panels A and B respectively. Panel B represents the OSC 2 structure shown in Figure 3.2. Two new hydrogen bonds are formed at this distance between the starred atoms that corresponds to significant energy gain ( $\sim 75$  kJ/mol) for the system. Atom colors are red for O, white for H, and green for Pu. Hydrogen bonds are shown as dotted blue lines, all other bonds are in black.

either happen smoothly, leading to downward sloping energy surfaces or parabolic features, as is generally observed for the Fe-bearing systems, or as sort of “snap” relaxation at the end of an increasingly unfavorable energy progression, as we see for the  $\bullet\text{OH}$  radical calculations.

To see how H bonding affects the overall energy change over the distance series, and the associated kinetics of the transitions, the energy gained from these bonds was removed to see how the energy surface changed. As shown in the dashed line in Figure 3.2, the energy of the inner-sphere complex is significantly less favorable without the energy gains of three H bonds that were formed over the course of the reaction. The change in the shape of the energy surface associated with this correction for the H bonds creates a broad outer-sphere well that has an energy minimum lower than that of the inner-sphere complex. The transition between these two complexes derived using this new energy surface is found to be prohibitively slow and the inner-sphere complex is not reached. This emphasizes that although the H bonds formed in these reactions distort the energy surface from something like the idealized, smooth surface in Figure 3.1, their energy contribution drives the reaction towards the inner-sphere configuration.

### ***Rates of outer- to inner-sphere complex transition***

Local energy minima found on the calculated energy surfaces correspond to different outer- and inner-sphere complex configurations. In the idealized schematic presented in Figure 3.1 it is implied that there are just two minima representing distinct outer- and inner-sphere structures. Our findings indicate that the process is often more complicated with multiple outer-sphere configurations with different H-bond networks along the path to an inner-sphere complex. For a few of the systems, there are even marginally different inner-sphere configuration options as well, with shallow shoulder minima present in some of the inner-sphere energy wells.

In order to determine the rates of transition between these different configurations, the kinetic parameters (activation energy,  $E_a$  and attempt frequency,  $A$ ), must be determined for each well. For the symmetrical wells, fitting the corresponding section of data, generally using 5 or more data points, with a polynomial function is straightforward and  $R^2$  values for these fits are

between 0.85-0.99. However, since all of the minima do not show up as clearly parabolic structures on the energy surface, as is described above and shown in Figure 3.2, we are required to use a different approach to extract the attempt frequency for these transitions.

The simplest approach is that of Reich, et al.<sup>29</sup>, as shown in Equation 3.5. Comparing the calculated attempt frequencies, we find that this approach is in good agreement with fully parabolic fits. We are confident then, that the approach can be applied to the partial parabolic wells that have steep energy steps on one side. The difference between attempt frequencies calculated via the methods is approximately a factor of two. Attempt frequencies calculated from the energy minima across all of the reactions are on the order of  $10^{11}$ - $10^{12}$  s<sup>-1</sup>. These values are in alignment with the vast majority of experimentally-determined attempt frequencies from the literature, which have a histogram peak just above  $10^{11}$  s<sup>-1</sup>.<sup>51</sup> The data used to calculate attempt frequencies and rate constants for the forward and backward reactions across all tested systems is provided in Table 3.3. With these data, the rates of transition over various energy barriers can be derived. As an example, first reaction listed, ferromagnetic PuO<sub>2</sub><sup>2+</sup> with Fe<sup>2+</sup> in vacuum, the rate constant of the inward reaction, with a nearly negligible activation energy of 1.7 kJ/mol is  $5.5 \times 10^{11}$  s<sup>-1</sup> and the back reaction, with its high activation energy of 106.6 kJ/mol, is  $1.8 \times 10^{-6}$  s<sup>-1</sup>.

In this study, attempt frequencies were calculated using the mass of a mole of •OH or Fe as the harmonic species. With this in mind, the high attempt frequencies, and correspondingly high rates of transition between energy wells, may be partly explained by this assumption. In reality, the effective mass of the harmonic oscillator is likely larger than just that of the reactant. That particle brings along with it some of its coordinating species: H<sub>2</sub>O and/or other ligands. These would increase the effective harmonic mass and lower the attempt frequency and any associated transition rate for either the forward or backward reaction from a given energy well. It is difficult

**Table 3.3** Calculated kinetic parameters for outer- to inner-sphere complex transitions

	Spin	Hydration	Reactant	Activation energies ( $E_a$ , in kJ/mol) and distances between minima ( $x$ , in Å)	
<b>PuO<sub>2</sub><sup>2+</sup></b>	FM	Explicit hyd. in vacuum	Fe <sup>2+</sup>	$E_{a1}$ : 1.7, $E_{a1,back}$ : 106.6, $x = 0.75$	
			•OH	$E_{a1}$ : 23.2, $E_{a1,back}$ : 76.6, $x = 1.75$ $E_{a2}$ : 46.0, $E_{a2,back}$ : 34.2, $x = 2$ $E_{a3}$ : 15.8, $E_{a3,back}$ : 61.4, $x = 2$	
			Fe <sup>2+</sup>	$E_{a1}$ : 30.36, $E_{a1,back}$ : 113.9, $x = 1$	
		C-PCM	•OH	$E_{a1}$ : 4.7, $E_{a1,back}$ : 32.2, $x = 1.75$ $E_{a2}$ : 12.3, $E_{a2,back}$ : 15.1, $x = 2$ $E_{a3}$ : 19.5, $E_{a3,back}$ : 65.8, $x = 2.25$	
			Explicit hyd. in vacuum	Fe <sup>2+</sup>	$E_{a1}$ : 5.8, $E_{a1,back}$ : 41.2, $x = 2$ $E_{a2}$ : 4.6, $E_{a2,back}$ : 177.3, $x = 1.75$
				•OH	$E_{a1}$ : 7.4, $E_{a1,back}$ : 37.9, $x = 1.5$ $E_{a2}$ : 12.2, $E_{a2,back}$ : 92.5, $x = 4.25$
	AFM	C-PCM	Fe <sup>2+</sup>	$E_{a1}$ : 45.7, $E_{a1,back}$ : 166.3, $x = 0.75$ $E_{a2}$ : 11.7, $E_{a2,back}$ : 162.6, $x = 1.25$	
			•OH	$E_{a1}$ : 0.8, $E_{a1,back}$ : 28.3, $x = 1$ $E_{a2}$ : 36.4, $E_{a2,back}$ : 9.6, $x = 1.5$	
		Explicit hyd. in vacuum	Fe <sup>2+</sup>	$E_{a1}$ : 9.9, $E_{a1,back}$ : 58.2, $x = 1.25$	
			Fe <sup>3+</sup>	$E_{a1}$ : 7.3, $E_{a1,back}$ : 50.6, $x = 1.75$ $E_{a2}$ : 4.8, $E_{a2,back}$ : 3.3, $x = 0.75$ $E_{a3}$ : 13.14, $E_{a3,back}$ : 49.3, $x = 1.75$	
	<b>PuO<sub>2</sub><sup>+</sup></b>	FM	C-PCM	•OH	$E_{a1}$ : 18.8, $E_{a1,back}$ : 21.9, $x = 2.5$ $E_{a2}$ : 11.5, $E_{a2,back}$ : 8.2, $x = 0.75$ $E_{a3}$ : 29.9, $E_{a3,back}$ : 30.1, $x = 1$
				Fe <sup>2+</sup>	$E_{a1}$ : 2.4, $E_{a1,back}$ : 19.4, $x = 0.5$ $E_{a2}$ : 16.08, $E_{a2,back}$ : 2.08, $x = 0.75$
Fe <sup>3+</sup>				$E_{a1}$ : 7.55, $E_{a1,back}$ : 95.84, $x = 2.75$	
Explicit hyd. in vacuum			•OH	$E_{a1}$ : 2.6, $E_{a1,back}$ : 32.3, $x = 2.25$ $E_{a2}$ : 22.8, $E_{a2,back}$ : 3.0, $x = 1.25$ $E_{a3}$ : 14.4, $E_{a3,back}$ : 11.8, $x = 0.75$	
			Fe <sup>2+</sup>	$E_{a1}$ : 1.4, $E_{a1,back}$ : 90.0, $x = 1.75$	
			Fe <sup>3+</sup>	$E_{a1}$ : 8.8, $E_{a1,back}$ : 86.7, $x = 2.25$ $E_{a2}$ : 2.7, $E_{a2,back}$ : 31.5, $x = 1$ $E_{a3}$ : 0.8, $E_{a3,back}$ : 2.9, $x = 0.5$	
AFM		C-PCM	•OH	$E_{a1}$ : 25.7, $E_{a1,back}$ : 5.0, $x = 1.5$ $E_{a2}$ : 24.4, $E_{a2,back}$ : 28.5, $x = 1.75$ $E_{a3}$ : 57.6, $E_{a3,back}$ : 100.8, $x = 1.5$	
			Fe <sup>2+</sup>	$E_{a1}$ : 1.5, $E_{a1,back}$ : 32.5, $x = 0.75$ $E_{a2}$ : 4.9, $E_{a2,back}$ : 105.5, $x = 1.25$	
			Fe <sup>3+</sup>	$E_{a1}$ : 2.9, $E_{a1,back}$ : 25.6, $x = 1.75$	
		Explicit hyd. in vacuum	•OH	$E_{a1}$ : 21.9, $E_{a1,back}$ : 71.0, $x = 2.75$ $E_{a2}$ : 25.4, $E_{a2,back}$ : 41.0, $x = 1.25$	

to say whether this effective mass would remain constant through the transition between different outer-sphere complexes, so for simplicity we have opted to consider just the reactant itself. As an example of much this mass value might affect the calculations, rate constants for ferromagnetic  $\text{PuO}_2^{2+}$  and  $\text{Fe}^{2+}$  in vacuum (presented in the prior paragraph using the minimum mass) decrease by 40% to  $3.3 \times 10^{11} \text{ s}^{-1}$  and  $1.1 \times 10^{-6} \text{ s}^{-1}$  for the forward and backward reactions, respectively, when the mass of the full coordination species,  $\text{Fe}(\text{OH})_2(\text{H}_2\text{O})_4^0$ , is used. For simplicity, the rates for the rest of the systems are calculated and evaluated using the smallest possible harmonic mass.

A computer program was developed to evaluate these rates and see how the concentrations of different species might evolve over time during a reaction. Providing the initial reactant concentrations, the positions of energy minima, and the activation energies separating them, the program calculates the collision and complex transition rates for the forward and backward reactions. The concentrations of different intermediate species were quantified over small time increments, on the order of several thousandths of the aqueous  $\text{PuO}_2^{1+/2+}$  half-life, to quantify and visualize the residence times of the reactants in different configurations. The program is able to show that for many of the systems, the inner-sphere complex is quickly reached, with the initial outer-sphere complex converted rapidly through any intermediate outer-sphere configurations to reach the inner-sphere complex. A plot showing how the concentrations of these species develop over time for the reaction of  $\text{PuO}_2^{2+}$  with  $\text{Fe}^{2+}$  in an antiferromagnetic spin arrangement with the C-PCM implicit hydration scheme is presented in Figure 3.4. This system has two different outer-sphere complexes (OSC 1 and OSC 2, depending on the H-bond network) at progressively closer distances. The energy barrier between OSC 2 and the inner-sphere complex (ISC) is small, such that very little of this species is ever present in the system. Overall, the  $\text{PuO}_2^{2+}$  in the bulk solution

is drained rapidly and the [ISC] is the dominant Pu-bearing species after ~25 ms. The concentration of  $\text{Fe}^{2+}$ , which is in excess, remains essentially unchanged on this log plot.

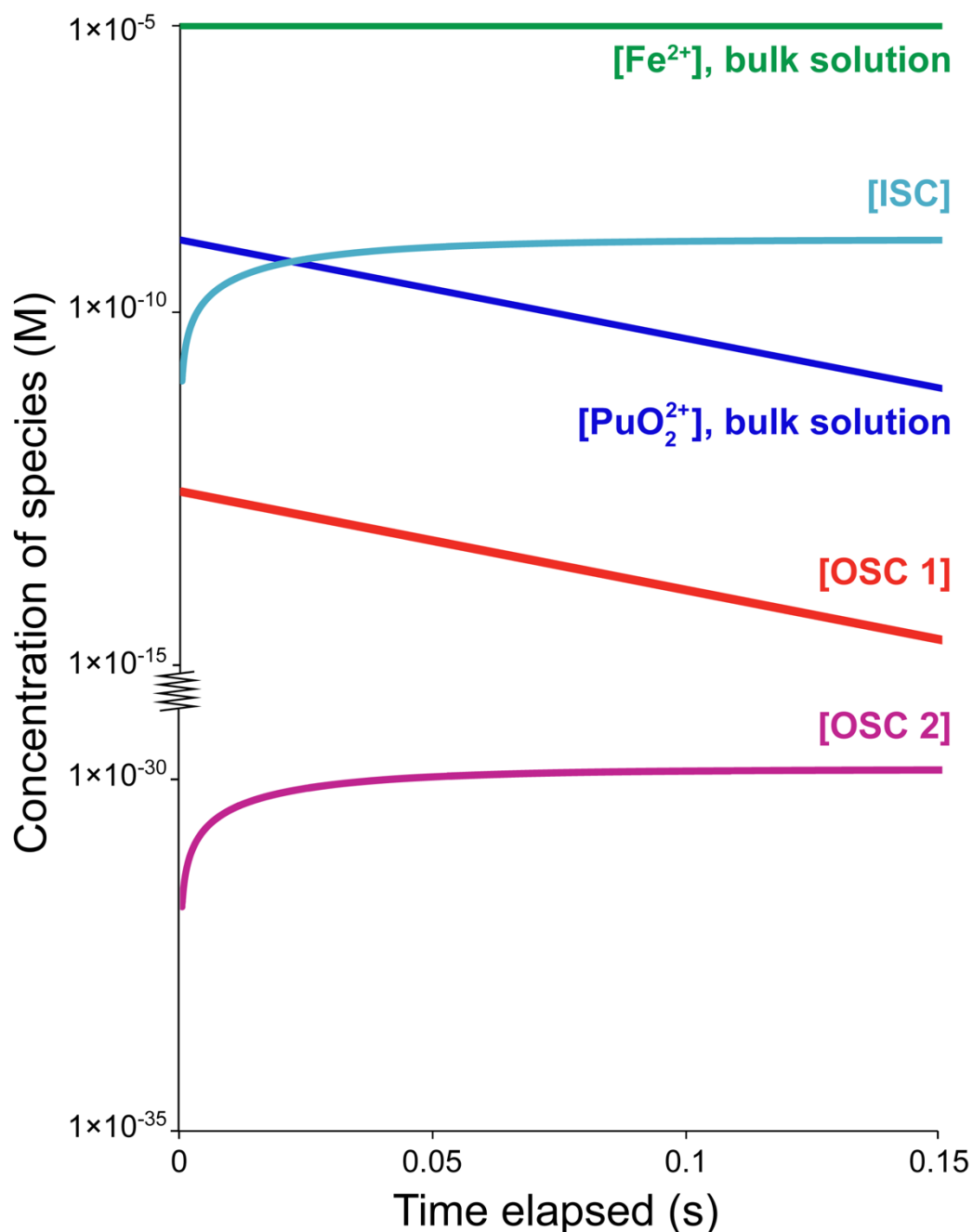


**Figure 3.4** Calculated concentrations of all component steps of the reaction between antiferromagnetic  $\text{PuO}_2^{2+}$  and  $\text{Fe}^{2+}$  in C-PCM. Concentrations of the uncomplexed reactants in the bulk solution (initially  $1 \mu\text{M}$  for  $\text{Fe}^{2+}$  and  $1 \text{ nM}$  for  $\text{PuO}_2^{2+}$ ), as well as the concentrations of the two outer-sphere (OSC 1 at  $6.25 \text{ \AA}$  and OSC 2 at  $5.5 \text{ \AA}$ ) and one inner-sphere (ISC at  $4.25 \text{ \AA}$ ) complexes are evaluated over time using the transition rates derived from the energy versus reactant distance data for this system.

### *Electronic structure changes and the reduction of Pu*

To determine the change in electronic structure over the course of the distance series, Bader population analysis was performed on the optimized wavefunctions. The Bader methodology is somewhat more sophisticated than Mulliken population analysis as it takes the actual electron distribution around the atoms and integrates the electron or spin density between charge density bottlenecks.<sup>52-53</sup> These bottleneck positions that separate atoms are defined where the second derivative of the electron distribution function, the so-called Laplacian, is equal to zero. Initial charge and spin conditions are found to be applied as expected to the individual coordination complexes at large reactant distances. As the distance between the species is decreased, changes in the charge and the number of unpaired spins reveal that electron transfer does not proceed until an inner-sphere complex is formed, if at all.

The clearest evidence of electron transfer is found in the modeled reactions with  $\text{Fe}^{2+}$ . Both ferromagnetic and antiferromagnetic spin arrangements show the transfer of a single electron from  $\text{Fe}^{2+}$  to  $\text{Pu}^{5+}$  or  $\text{Pu}^{6+}$ . This process is revealed in the spin population where the number of unpaired spins on Pu increases by  $\sim 1$  (in  $\text{PuO}_2^{2+}$  from 2 to 3; in  $\text{PuO}_2^+$  from 3 to 4). This transition is clearest in the vacuum calculations (see example of these data in Figure 3.5), whereas in the C-PCM models, initial charge and spin assignment, even using the fragment implementation in Gaussian, tends to favor the post-electron transfer configuration from the initial calculation. The only C-PCM series which shows a distinct charge and spin change is the one for the antiferromagnetic reaction of  $\text{PuO}_2^{2+}$  with  $\text{Fe}^{2+}$ . In this system, spin change on the plutonyl molecule, and corresponding change on  $\text{Fe}^{2+}$ , does happen albeit taking place as soon as the reactive radius is reached.

Reactions of plutonyl with  $\bullet\text{OH}$  and  $\text{Fe}^{3+}$ , as expected, do not show evidence of reduction of Pu. Oxidation of  $\text{PuO}_2^+$  by  $\bullet\text{OH}$  could have been possible, but charge and spin data for both spin

configurations and hydration schemes do not suggest significant change in the electronic configuration for either reactant. The plots of atomic charge and spin for these models are smooth with no changes visible unless the reactant is forced very close to the Pu center. At this point, the changes correspond to very unfavorable system energies and are not thought represent conditions that a real-world system would reach.

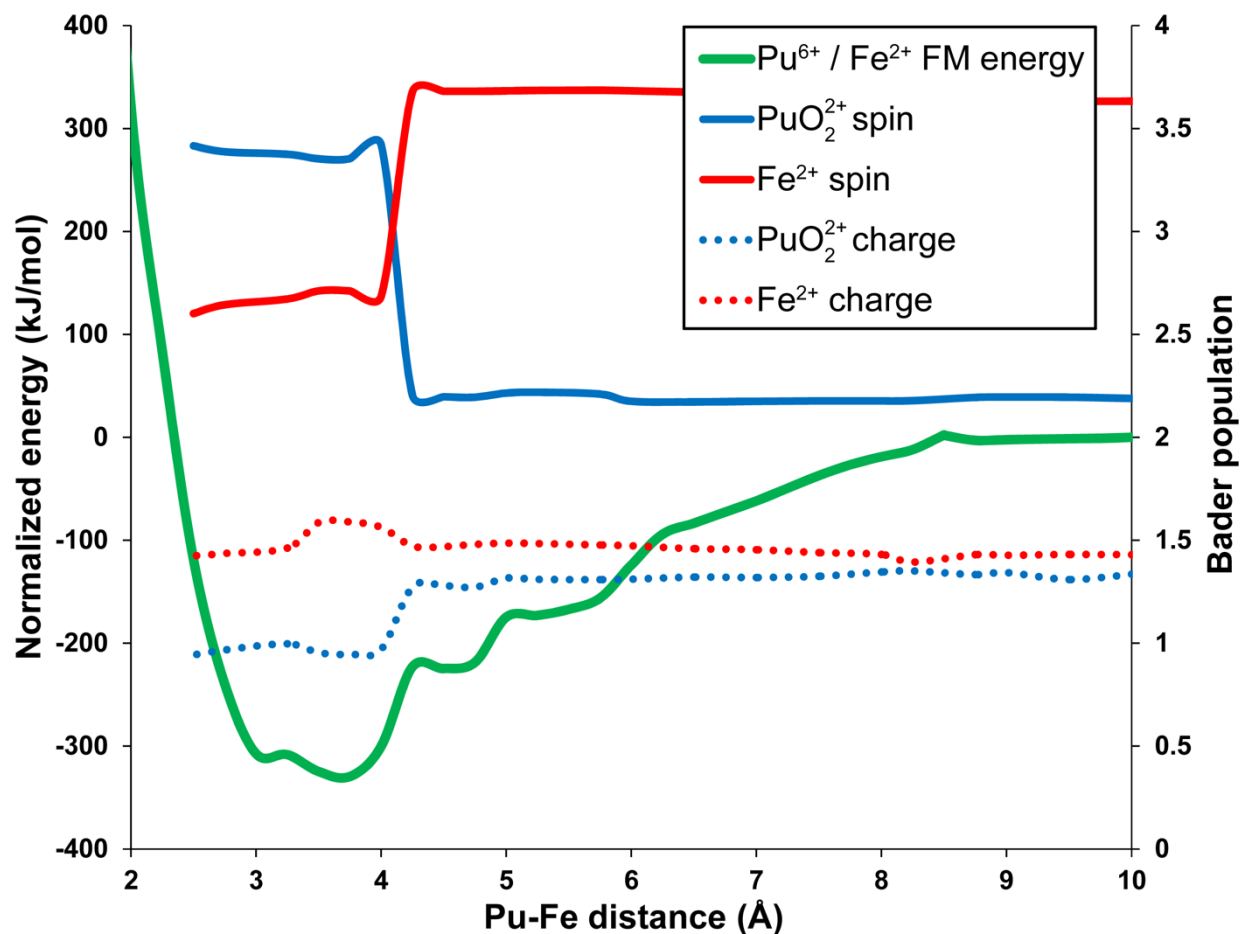


**Figure 3.5** Bader charge and spin populations of the plutonyl molecule and Fe cation over the course of the ferromagnetic distance series in vacuum. Charge and spin remain constant over the bulk solution and outer-sphere distance range, but electron transfer from Fe<sup>2+</sup> to Pu<sup>6+</sup> takes place at 4.25 Å. This change in electronic structure is coincident with beginning of the inner-sphere energy well that has its minimum at a Pu-Fe distance of 3.75 Å

## Discussion

### *Trends in reactive radii and impact on outer-sphere complex formation rate*

Reactive radii calculated for the plutonyl Fe and •OH systems fall within a relatively small range ( $\sim 3 \text{ \AA}$ ) regardless of the computational parameters applied or the charge and spin scheme tested. What this suggests is that for small ions or molecules coming close to plutonyl, the energy gain associated with the formation of an outer-sphere complex is felt at a distance approximately one-and-a-half to two times the diameter of the coordination complex. Initially, this energy gain is associated with the formation of an H bond between the coordinating species around the plutonyl and other reactant. This energy gain is seen in the energy versus distance plots as a marked increase in slope from gently sloping region at distances greater than the reactive radius.

This shallow slope of the energy surface at larger reactant distances is caused by the long-range electrostatic interactions between the two coordination complexes. This slope has been verified to be related to Coulomb attraction by calculating the sum of all interactions between the atoms of the two complexes over a range of distances greater than the reactive radius. This slope derived from the Coulomb interaction energy matches that from the quantum-mechanical calculations and explains the relatively small energy gain associated with bringing the complexes closer together in the bulk solution distance regime. This also confirms that it is only within the reactive radius that forces other than the electrostatic interaction begin to contribute to the overall energy of the system.

For calculations conducted using the C-PCM implicit hydration scheme, the reactive radius is found to be smaller. This result is related to the charge screening effect of the modeled solvent, water<sup>54</sup>. This screening of the two species (and their coordinating ligands) from each other extends

the shallow electrostatic energy slope further, closer to the first (or only, depending on the system) outer-sphere energy minima position. The decrease in reactive radius that accompanies the use of the C-PCM model versus the simple explicit hydration scheme is variable, but generally it appears that the effect is stronger for the Fe-bearing systems, particularly those in the antiferromagnetic spin configuration. The electrostatic interaction of Fe<sup>2+</sup> and Fe<sup>3+</sup> with plutonyl and coordinating OH<sup>-</sup> is more pronounced than that of the neutral •OH species.

These different reactive radii lead to slightly different calculated collision rates and within a given system the effect of changing the hydration model is can increase or decrease the  $t_{1/2}$  of uncomplexed free plutonyl by approximately 40% (see Table 3.2 for an example). However, these reaction rates to form outer-sphere complexes are still very fast and in practical terms, the effect of changing the reactive radius by  $<2 \text{ \AA}$  is relatively minor. The concentration of the species initially, particularly that which is in higher concentration, will have the biggest impact on the kinetics of this step in the reaction. In the case where one reactant is in significantly higher concentration than the other, as would be expected for most environmental releases of Pu<sup>55-56</sup>, where even contaminated sites may only have sub-nM concentrations, the  $t_{1/2}$  of the outer-sphere complex can be calculated simply by evaluating Equation 3.6:

$$t_{1/2} = \frac{\ln 2}{\pi R^2 v N_A [Y]} \quad (3.6)$$

Where  $t_{1/2}$  is seconds provided that the reactive radius ( $R$ ) is in dm, the diffusion velocity ( $v$ ) is in dm/s, and the concentration of the species in excess,  $[Y]$ , is in mol/dm<sup>3</sup>.

### ***Response of systems moving from outer- to inner-sphere***

In the idealized conceptual framework of Figure 3.1, the reaction pathway and associated energy surface is straightforward. The free reactants in their individual coordination environments

begin as separated species in the bulk solution. They eventually encounter each other at a distance such that the formation of an outer-sphere complex is favorable. To get to the more even more thermodynamically-favorable inner-sphere complex (again, an assumption made in this idealized case), an activation barrier must be overcome. After this, the back reaction out of the inner-sphere well will be unlikely and the concentration of said complex will grow until chemical conditions change or the system undergoes some sort of reaction.

We find that in our tested systems there are numerous cases where the single outer- and inner-sphere well model does not apply. Instead, many of the systems have a number of different outer-sphere complex configurations, each separated by an energy barrier. These energy barriers are found to be related to changes in the coordination environment of the two species, namely the H bonding network of H<sub>2</sub>O and OH<sup>-</sup>, as well as transfer of H<sup>+</sup> from H<sub>2</sub>O to OH<sup>-</sup> to effectively change where OH<sup>-</sup> is located in the coordination sphere. Another style of H<sup>+</sup> transfer is observed in the models showing reduction of Pu. In these cases, a proton is transferred from one of the H<sub>2</sub>O molecules coordinating Fe and becomes bonded to one of the O<sub>axial</sub> of the actinyl. Both styles of H<sup>+</sup> transfer have been observed in previous studies of actinyl reactions with Fe<sup>2+</sup>. The transfer of H<sup>+</sup> has been observed in other computational studies of actinides, where it is also found to be tied to electron transfer.<sup>57</sup>

The calculated geometries of our outer- and inner-sphere complexes show similarities to those calculated for the uranyl hydrolysis species, UO<sub>2</sub>(OH)<sub>2</sub><sup>0</sup>, and its outer- and inner-sphere complexes with Fe<sup>2+</sup> and Fe<sup>3+</sup>. Plutonium-iron distances in our models correlate better for the inner-sphere cases when compared to U-Fe distances.<sup>57-58</sup> In the inner-sphere complexes, our calculated distances are 3.75-4.0 Å. With the multiple outer-sphere configurations that we find along the energy surfaces, only a subset of reactions have energy minima at the positions of

4.75-4.9 Å that have been previously described as corresponding to outer-sphere complexes for uranyl and Fe<sup>2+</sup>, but all have a local minimum within 0.75 Å of that distance range.

The calculated changes in system energy and geometry as a function Pu-reactant distance have been described in the earlier sections. The only clear trends are that the •OH models tend towards more of the “snap” geometry changes versus the generally smoother features in the Fe-bearing systems and that Fe shows more dramatic plutonyl titling-related energy spikes near the reactive radius (see Figure 3.6 for examples of Fe energy versus distance relationships). For H bonding, the same types of changes in the coordination structure can result in different energy surface features for different systems, so the exact nature of the different shapes in the plots is not quite clear. One might infer that the smoother surfaces as seen in the Fe calculations indicate that the system has some greater degree of flexibility in its coordination environment that allows the change in the H bonding network to happen more fluidly. The use of the C-PCM hydration model appears to enhance this in most of the systems as generally smoother energy surfaces are observed for calculations using this hydration scheme. From a geometry optimization standpoint, the use of C-PCM can, in some cases, make the systems harder to converge as there are more energetically-acceptable configurations for the coordinating water molecules to assume. In vacuum, the electrostatic relationships dominate the system and the different conformations that are acceptable within the energy convergence criteria are relatively few.

Moving forward, it may be valuable to consider how the systems respond to the addition of more explicit waters to the models. While this will add computational expense, it may help by making the overall energy of the system less dependent on the making or breaking of one or two H bonds. The presence of more water molecules, perhaps comprising the second hydration shell around the reactants, may also make it easier for rearrangement of these molecules. The result

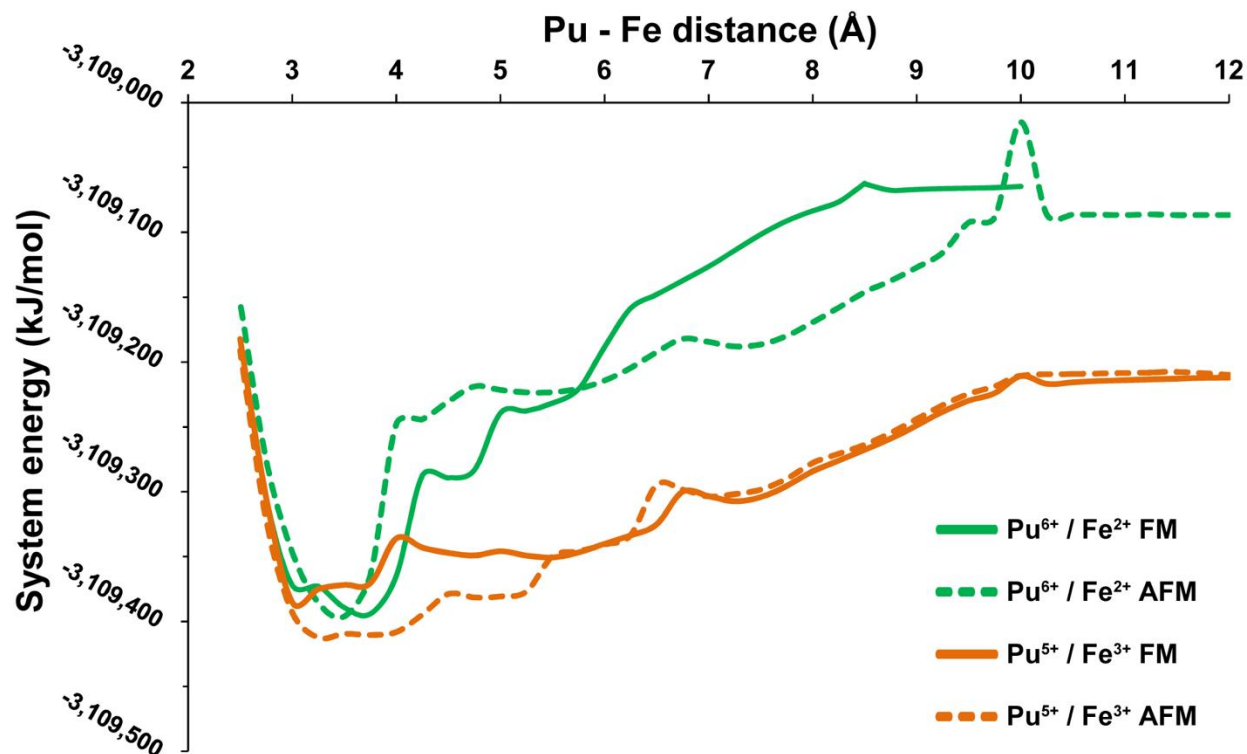


**Figure 3.6** Calculated energy surfaces for some select plutonyl and iron systems in vacuum. Energy surfaces show a variety of features including parabolic wells, sloped steps, and spikes. These changes in the energy surface are related to changes in the geometry (such as H bond formation and tilting of the plutonyl molecule) and also, in the  $\text{Fe}^{2+}$  reactions, transfer of electron density to reduce  $\text{Pu}^{6+}$  to  $\text{Pu}^{5+}$  at  $\sim 4 \text{ \AA}$ .

could be a smoother energy surface with fewer steep steps like we observe in some of our calculations. With these smoother features, the data would be easier to fit directly with a parabolic function to derive the attempt frequency, without having to rely on a methodology originally developed for solid-state diffusion.

Previous Marcus theory work on the reduction of U species by  $\text{Fe}^{2+}$  has yielded a suite of calculated electron transfer rates. These rates are dependent on the geometry of the complex, outer- versus inner-sphere, and also on the specific bonding nature of said complex. For example, rates between bidentate and monodentate inner-sphere complexes are different by several orders of magnitude. In solution, homogeneous electron transfer between  $\text{Fe}^{2+}$  and  $\text{UO}_2(\text{OH})_2^0$ , analogous

to the  $\text{PuO}_2(\text{OH})_2^0$  used in half of our calculations, yields electron transfer rates between  $7.6 \times 10^2$  and  $7.2 \times 10^4 \text{ s}^{-1}$ , depending on the complex geometry.<sup>57</sup> The fastest calculated electron transfer rate is for a bidentate inner-sphere complex. Our calculations, although not a rigorous probing of the electron transfer process (or its rate) as is done using Marcus theory, do agree with the geometry of the structure of this bidentate species, where two  $\text{OH}^-$  serve as the linking ligands. Our calculations suggest that for electron transfer from  $\text{Fe}^{2+}$  to  $\text{Pu}^{6+}$  and  $\text{Pu}^{5+}$  takes place following the formation of analogous structures at nearly the same actinide-Fe distances.

For these electron transfer processes to take place, the inner- or outer-sphere complex geometry must be reached. Our calculations reveal rates of complex formation for the different reactions of  $\text{PuO}_2^{2+}$  and  $\text{PuO}_2^+$  to be rapid. The rates vary based on the hydration model used (explicit first hydration sphere versus models with the explicit water *and* C-PCM) and on the spin configuration. For nearly all of the tested reactions, formation of inner-sphere complexes takes place at Pu-reactant distances in the 3.25-4.25 Å range. The species generally assume bidentate configurations with  $\text{OH}^-$  serving as the bridging ligand between the two species.

The reactions with  $\bullet\text{OH}$  proved somewhat harder to control as the radical had a tendency to react with neighboring water molecules to effectively shift the radical species around the coordination sphere. In some of the distance series attempts, the radical species would end up under-coordinated, with no water molecules on one side. This sort of configuration is visible in Figure 3.3, where  $\bullet\text{OH}$  (labeled R) is on the far side of the cluster. Here  $\text{H}_2\text{O}$  and  $\text{OH}^-$  prefer to position themselves between the  $\text{PuO}_2^{2+}$  and  $\bullet\text{OH}$ . Without fixing the positions of more of the atoms in the system, six- or higher-fold coordination of the radical species is unable to be maintained throughout all of the distance steps. However, if one were to fix more, or all, of the

H<sub>2</sub>O positions around •OH, it essentially defeats the purpose of documenting the energy and geometry change of the coordination environment as it is pushed into the plutonyl.

In the case of Fe<sup>2+</sup> and Fe<sup>3+</sup>, the coordination environments of these species remain more intact during reaction. However, when electron transfer takes place in the Fe<sup>2+</sup> reactions with PuO<sub>2</sub><sup>2+</sup> and PuO<sub>2</sub><sup>+</sup>, the coordination number of Fe drops from 6 to 5 or 4 in some of the series. This unusual coordination environment is thought to be related to the spin state of Fe that is assumed after the electron transfer. Since Gaussian requires that the global spin multiplicity be fixed, the Fe cation is forced to assume an intermediate spin configuration for Fe<sup>3+</sup> (spin of ~3) to compensate for the spin increase on the Pu (going from either 2 to 3 during the transition from Pu<sup>6+</sup> to Pu<sup>5+</sup>; 3 to 4 for Pu<sup>5+</sup> to Pu<sup>4+</sup>). The coordination environment of the Pu also changes during these reactions with a lengthening of the Pu-O<sub>axial</sub> distances from the plutonyl length of approximately 1.85 Å and even further, to ~2.25 Å when Pu<sup>4+</sup> is formed.

### *Expanding this framework to other systems*

It is envisioned that this computational approach and three-step framework can be applied to a wide range of reactions. In the realm of actinides, this will include building up a kinetic dataset that encompasses uranyl and neptunyl and their reactions with other redox-active species, such as HS<sup>-</sup> and H<sub>2</sub>S. Also, other coordinating ligands other than water must be explored to determine the impact of these species on redox reaction rates. One especially important ligand to investigate will be carbonate.<sup>59-60</sup> As calculated here, the transitions between different complex configurations and the breaking and forming of H<sub>2</sub>O and OH<sup>-</sup> bonds with the reactants proceed quickly. Strong and stable complexes with ligands like carbonate, as well as other inorganic and organic species, may prove to be recalcitrant to redox reactions if the formation of an inner-sphere complex with the

electron donor is required to achieve reasonable rates of reaction. In these cases, a mineral may serve as a catalyzing surface that aids in this decomplexation.

In addition to expanding the catalog of rates for these the first two sub-processes, the rate of the last step of the redox reaction, electron transfer, must also be calculated. The Marcus theory calculations required for determining that rate are time-consuming and require different computational codes than those used here.<sup>61</sup> The theoretical basis for these calculations is, however, sound and work in our group on the homogenous and heterogeneous (that is, those mediated by a mineral surface) redox reactions of uranyl has been promising.<sup>11-12</sup> Building upon the methodology employed in those studies and others<sup>10,62</sup>, we can hope to describe the complete kinetic picture using this three-step model for a range of different reactant pairs and include reactions that take place on mineral surfaces.

## Conclusions

Reactions of charge-neutral hydrolysis products of plutonyl,  $\text{PuO}_2(\text{OH})_2^0$  and  $\text{PuO}_2(\text{OH})^0$ , are found to rapidly form outer-sphere complexes with charge-neutral coordination complexes of  $\text{Fe}^{2+}$ ,  $\text{Fe}^{3+}$ , and  $\bullet\text{OH}$ , using a collision theory-based methodology. Rates of collision are high for a wide range of reactant concentrations, even down to the environmentally-relevant sub-nM level. The energy trajectory of these systems over decreasing Pu-reactant distances reveals energy barriers between different outer- and inner-sphere complex configurations. Energy barriers during this approach are related to changes in the geometry of complexes, with major influences being the breaking and forming of new H bonds between the coordinating  $\text{H}_2\text{O}$  and  $\text{OH}^-$ . Decreases in the overall energy of the system are also found in situations where electron transfer from  $\text{Fe}^{2+}$  has occurred. Reduction of Pu is revealed through Bader population analysis and occurs in reactions

of both plutonyl species with  $\text{Fe}^{2+}$ . Following electron transfer, Fe is forced to assume an intermediate spin configuration in some cases due to the constraints of the computational methodology. That this reaction is still exothermic indicates that it would be likely to proceed and is broadly in agreement with the findings of favorable thermodynamics for the reduction of  $\text{UO}_2(\text{OH})_2^0$  by  $\text{Fe}^{2+}$ .<sup>57</sup>

Reactions with observed electron transfer show the reduction of Pu to occur once inner-sphere configurations have been reached, at or below Pu-Fe distances of 4.25 Å. This preference for inner-sphere electron transfer is in line with the understanding of actinide- $\text{Fe}^{2+}$  electron transfer rates as revealed by Marcus theory calculations.<sup>58,62</sup> The energy barriers along the path of inner-sphere complex formation are found to be relatively small in the reactions of  $\text{Fe}^{2+}$ . Calculated activation energies and attempt frequencies for the transitions between the different tested configurations show that  $\text{Fe}^{2+}$  reactions proceed rapidly with the concentration of the inner-sphere complex dominating in solution over short time scales. Reactions with  $\text{Fe}^{3+}$  and  $\bullet\text{OH}$  show higher activation energies for certain transitions and do not all show the same thermodynamically- or kinetically-favorable path to an inner-sphere configuration. The rapid formation of the initial encounter complex, followed by conversion to an inner-sphere configuration suggests that if rates of homogenous electron transfer between  $\text{Fe}^{2+}$  and uranyl are comparable to those with plutonyl, then electron transfer would be the rate-limiting step in the overall redox reaction between high pH hydrolysis species.

With this combination of collision theory, quantum-mechanical calculations, and the speciation computer program, we can describe how these compounds change over time along the path from bulk solution to inner-sphere complex. While this work has only attempted to extract the kinetics of these processes for homogenous reactions between specific coordination

complexes, the computational framework could be extended to encompass complex formation and redox reactions at mineral surfaces. To further develop this kinetic picture for redox reactions in particular, Marcus theory will need to be employed to calculate specific electron transfer rates for the inner- and outer-sphere complexes. With this combination of approaches, we will be able to make better predictions about the behavior of metals in the environment and learn about the small-scale phenomena that govern these reactions.

## **Acknowledgements**

This work was made possible through funding from the U.S. Department of Energy's (DOE) Office of Science, Office of Basic Energy Sciences (BES), Chemical Sciences, Geosciences, & Biosciences (CSGB) Division for the topics of Heavy Element Chemistry and Geoscience (grant number DE-FG02-06ER15783). This research was partially carried out on the Flux cluster managed by Advanced Research Computing at the University of Michigan, Ann Arbor. The authors thank Evan Killeen (U. of Michigan) for fruitful discussions regarding the direction of this research.

## Appendix 3A: Testing of computational parameters

### *Basis set superposition error (BSSE)*

As molecular species are brought closer and closer together, the use of Gaussian-like atom-centered basis functions (that drop off faster than actual electron densities) can lead to what is called basis set superposition error (BSSE). This error can be partially corrected for using in the Gaussian software package by using the so-called counterpoise scheme.<sup>63-64</sup> To address how the inclusion of the BSSE error term would affect the energy of the systems that we explore (which involve short inter-molecular distances) and thus the derived reaction kinetics, some testing has been carried out on a subset of the ferromagnetic systems. Single point counterpoise energy calculations, with the structure divided into two fragments, the Pu and Fe coordination “molecules”, were carried for two full reaction series (see Figure 3.7). The curves of the vacuum-

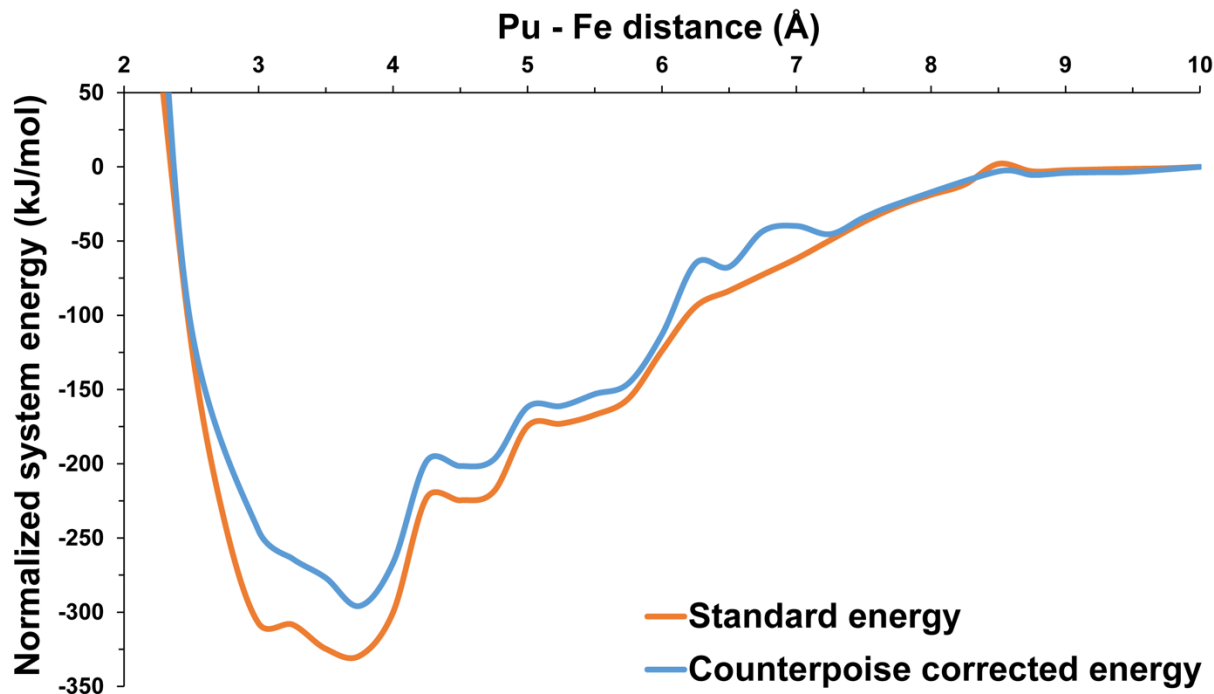


**Figure 3.7** Comparison of the original calculated system energies (orange line) to those calculated with the counterpoise keyword and have the basis set superposition error (BSSE) correction applied (blue line) for the ferromagnetic  $\text{PuO}_2^+/\text{Fe}^{3+}$  reaction in vacuum.

state  $\text{PuO}_2^{2+}/\text{Fe}^{2+}$  and  $\text{PuO}_2^+/\text{Fe}^{3+}$  series show remarkably similar energy well features and positions. The energy barriers between these minima are also remarkably similar, differing by  $<7$  kJ/mol. Differences on this scale do not affect the overall kinetics (for example,  $t_{1/2}$  of the aqueous species, growth in concentration of the inner-sphere complex) of the reaction significantly when these values are plugged in to the program script we developed.

### *Zero-point vibrational energies*

While the inclusion of zero-point vibrational energies would have been prohibitively computational expensive for each data point along each reaction path, frequency calculations were carried out for two full series ( $\text{Pu}^{6+}/\text{Fe}^{2+}$  FM and  $\text{Pu}^{5+}/\text{Fe}^{3+}$  FM, both in vacuum). The series show remarkably similar energy features as shown for one of these examples in Figure 3.8. When including ZPVE, the overall trends and positioning of the energy minima, barriers, and reactive

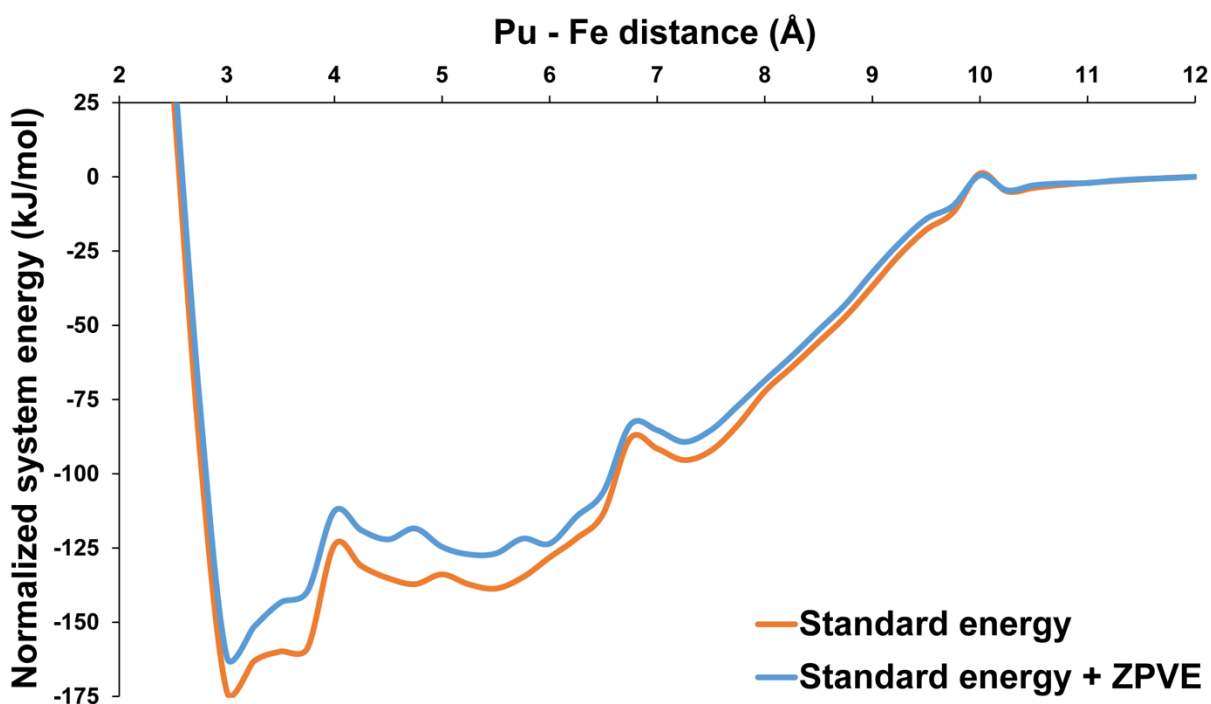


**Figure 3.8** Comparison of the relative energy vs. distance curves for the ferromagnetic  $\text{PuO}_2^+/\text{Fe}^{3+}$  system in vacuum with (blue line) and without (orange line) the inclusion of the zero-point vibrational energy as calculated using the frequency module of Gaussian 09.

radius are essentially the same as the standard calculations whose results are included in the manuscript. Energy barriers change by a maximum of  $\sim 7$  kJ/mol and energy maxima and minima move by no more than  $0.25 \text{ \AA}$ . As such, the derived kinetics and timescales of reaction remain unchanged and the conceptual interpretation of the reaction is unaffected.

### *Choice of basis set*

Especially for the treatment of redox reactions of actinides, the choice of basis set can be crucial, but can also significantly add to the computational expense. While the used LANL2DZ is on the computationally lighter side, a subset of series were recalculated using the more rigorous AUG-cc-pVTZ basis (applied to H, O and Fe) to check if the energy surface differed significantly

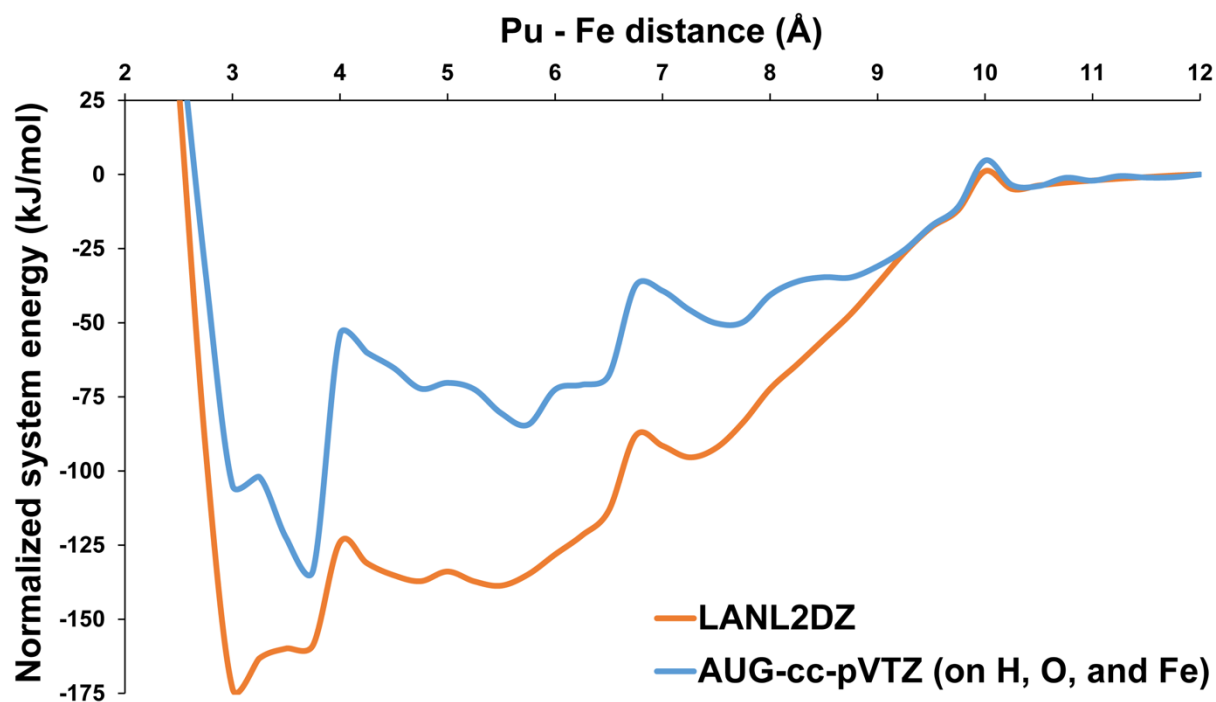


**Figure 3.9** Energy vs. distance curves for the ferromagnetic  $\text{PuO}_2^+/\text{Fe}^{3+}$  system in vacuum using two different basis set combinations. The orange line represents our standard computational settings using the LANL2DZ basis with pseudopotentials on Fe and Pu. The blue line is the same series calculated with the AUG-cc-pVTZ all-electron correlation consistent basis set on H, O, and Fe. There is a significant shift in the trajectory of the curve with this basis set, however, the positions of energy minima corresponding to different complex configurations and the energy of forwards and backward reaction barriers do not result in different conclusions regarding the kinetics of this reaction.

from that calculated with LANL2DZ.<sup>42-44</sup> The shape of the energy distance curve (see Figure 3.9) does change somewhat in its trajectory. However, the positions of the energy minima and barriers along the path are remarkably similar. The positions of the minima differ by a maximum of 0.25 Å. The change in the activation energy barriers is not fixed. For example, the first forward energy barrier increases from 7.3 to 12.7 kJ/mol with the new basis set; whereas its back reaction decreases from 50.6 to 46.9 kJ/mol. The biggest change is observed for the back reaction of the inner-sphere position where the activation energy barrier increases from 49.3 to 79.4 kJ/mol. These activation energies and barrier positions were put into our reaction kinetics script to see how they affected the concentration changes of the different species (aqueous reactants, multiple outer-sphere complexes, and the inner-sphere complex). Despite the changes to the activation energies, the breakdown of concentrations and how they develop over time is essentially the same. In this system, concentration builds in the outer-sphere position at 5.5-5.75 Å.

## References

1. Luo, W.; Gu, B., Dissolution of uranium-bearing minerals and mobilization of uranium by organic ligands in a biologically reduced sediment. *Environmental Science & Technology* **2011**, *45* (7), 2994-2999.
2. Warren, L. A.; Haack, E. A., Biogeochemical controls on metal behaviour in freshwater environments. *Earth-Science Reviews* **2001**, *54* (4), 261-320.
3. Borch, T.; Kretzschmar, R.; Kappler, A.; Van Cappellen, P.; Ginder-Vogel, M.; Voegelin, A.; Campbell, K., Biogeochemical redox processes and their impact on contaminant dynamics. *Environmental Science & Technology* **2010**, *44* (1), 15-23.
4. Liger, E.; Charlet, L.; Van Cappellen, P., Surface catalysis of uranium(VI) reduction by iron(II). *Geochimica et Cosmochimica Acta* **1999**, *63* (19-20), 2939-2955.
5. Scott, T. B.; Tort, O. R.; Allen, G. C., Aqueous uptake of uranium onto pyrite surfaces; reactivity of fresh versus weathered material. *Geochimica et Cosmochimica Acta* **2007**, *71* (21), 5044-5053.
6. Yu, K. C.; Tsai, L. J.; Chen, S. H.; Ho, S. T., Chemical binding of heavy metals in anoxic river sediments. *Water Research* **2001**, *35* (17), 4086-4094.
7. Aqueous Solutions, L. *The Geochemist's Workbench*, 11.0.6; Aqueous Solutions, LLC: Champaign, IL, 2017.
8. Gustafsson, J. P. *Visual MINTEQ 3.1*, 3.1; KTH Royal Institute of Technology: Stockholm, 2013.
9. Manion, J. A.; R. E. Huie; R. D. Levin; D. R. Burgess Jr.; V. L. Orkin, W. T.; W. S. McGivern; J. W. Hudgens; V. D. Knyazev; D. B. Atkinson; E. Chai; A. M. Tereza; C.-Y. Lin; T. C. Allison; W. G. Mallard; F. Westley; J. T. Herron; R. F. Hampson; Frizzell, D. H., NIST Chemical Kinetics Database. In *NIST Standard Reference Database 17, Version 70, Release 168*, National Institute of Standards and Technology: Gaithersburg, Maryland, 2015.
10. Zarzycki, P.; Kerisit, S.; Rosso, K. M., Molecular dynamics study of Fe(II) adsorption, electron exchange, and mobility at goethite (alpha-FeOOH) surfaces. *Journal of Physical Chemistry C* **2015**, *119* (6), 3111-3123.
11. Taylor, S. D.; Becker, U.; Rosso, K. M., Electron transfer pathways facilitating U(VI) reduction by Fe(II) on Al- vs. Fe-oxides. *Journal of Physical Chemistry C* **2017**, *121* (36), 19887-19903.
12. Taylor, S. D.; Marciano, M. C.; Becker, U., A first principles investigation of electron transfer between Fe(II) and U(VI) on insulating Al- vs. semiconducting Fe-oxide surfaces via the proximity effect. *Geochimica et Cosmochimica Acta* **2017**, *197*, 305-322.

13. Huss, G. R.; Meyer, B. S.; Srinivasan, G.; Goswami, J. N.; Sahijpal, S., Stellar sources of the short-lived radionuclides in the early solar system. *Geochimica et Cosmochimica Acta* **2009**, 73 (17), 4922-4945.
14. Bros, R.; Turpin, L.; Gauthierlafaye, F.; Holliger, P.; Stille, P., Occurrence of naturally enriched U-235 - Implications for plutonium behavior in natural environments. *Geochimica et Cosmochimica Acta* **1993**, 57 (6), 1351-1356.
15. Choppin, G. R., Actinide speciation in the environment. *Journal of Radioanalytical and Nuclear Chemistry* **2007**, 273 (3), 695-703.
16. Szabo, Z.; Toraiishi, T.; Vallet, V.; Grenthe, I., Solution coordination chemistry of actinides: Thermodynamics, structure and reaction mechanisms. *Coordination Chemistry Reviews* **2006**, 250 (7-8), 784-815.
17. Silva, R. J.; Nitsche, H., Actinide environmental chemistry. *Radiochimica Acta* **1995**, 70 (1), 377-396.
18. Dodge, C. J.; Francis, A. J.; Gillow, J. B.; Halada, G. P.; Eng, C.; Clayton, C. R., Association of uranium with iron oxides typically formed on corroding steel surfaces. *Environmental Science & Technology* **2002**, 36 (16), 3504-3511.
19. Du, X.; Boonchayaanant, B.; Wu, W.-M.; Fendorf, S.; Bargar, J.; Criddle, C. S., Reduction of uranium(VI) by soluble iron(II) conforms with thermodynamic predictions. *Environmental Science & Technology* **2011**, 45 (11), 4718-4725.
20. Skomurski, F. N.; Ilton, E. S.; Engelhard, M. H.; Arey, B. W.; Rosso, K. M., Heterogeneous reduction of U<sup>6+</sup> by structural Fe<sup>2+</sup> from theory and experiment. *Geochimica et Cosmochimica Acta* **2011**, 75 (22), 7277-7290.
21. Huber, F.; Schild, D.; Vitova, T.; Rothe, J.; Kirsch, R.; Schaefer, T., U(VI) removal kinetics in presence of synthetic magnetite nanoparticles. *Geochimica et Cosmochimica Acta* **2012**, 96, 154-173.
22. Yang, Z.; Kang, M.; Ma, B.; Xie, J.; Chen, F.; Charlet, L.; Liu, C., Inhibition of U(VI) reduction by synthetic and natural pyrite. *Environmental Science & Technology* **2014**, 48 (18), 10716-10724.
23. Hixon, A. E.; Arai, Y.; Powell, B. A., Examination of the effect of alpha radiolysis on plutonium(V) sorption to quartz using multiple plutonium isotopes. *Journal of Colloid and Interface Science* **2013**, 403, 105-112.
24. Amme, M.; Bors, W.; Michel, C.; Stettmaier, K.; Rasmussen, G.; Betti, M., Effects of Fe(II) and hydrogen peroxide interaction upon dissolving UO<sub>2</sub> under geologic repository conditions. *Environmental Science & Technology* **2005**, 39 (1), 221-229.

25. Amme, M.; Pehrman, R.; Deutsch, R.; Roth, O.; Jonsson, M., Combined effects of Fe(II) and oxidizing radiolysis products on UO<sub>2</sub> and PuO<sub>2</sub> dissolution in a system containing solid UO<sub>2</sub> and PuO<sub>2</sub>. *Journal of Nuclear Materials* **2012**, *430* (1-3), 1-5.
26. Begg, J. D.; Zavarin, M.; Kersting, A. B., Plutonium desorption from mineral surfaces at environmental concentrations of hydrogen peroxide. *Environmental Science & Technology* **2014**, *48* (11), 6201-6210.
27. McQuarrie, D. A.; Simon, J. D., *Physical chemistry: A molecular approach*. University Science Books: United States, 1997; p 1360.
28. Shriver, D.; Weller, M.; Overton, T.; Rourke, J.; Armstrong, F., *Inorganic chemistry*. 6 ed.; W.H. Freeman and Company: New York, 2014; p 875.
29. Reich, M.; Ewing, R. C.; Ehlers, T. A.; Becker, U., Low-temperature anisotropic diffusion of helium in zircon: Implications for zircon (U-Th)/He thermochronometry. *Geochimica et Cosmochimica Acta* **2007**, *71* (12), 3119-3130.
30. Taube, H., *Electron transfer reactions of complex ions in solution*. Academic Press: New York, 1970; p 103.
31. Marcus, R. A., Theory of oxidation-reduction reactions involving electron transfer. V. Comparison and properties of electrochemical and chemical rate constants. *Journal of Physical Chemistry* **1963**, *67* (4), 853-857.
32. Marcus, R. A.; Sutin, N., Electron transfers in chemistry and biology. *Biochimica et Biophysica Acta - Reviews in Bioenergetics* **1985**, *811* (3), 265-322.
33. Frisch, M. J.; Trucks, G. W.; Schlegel, H. B.; Scuseria, G. E.; Robb, M. A.; Cheeseman, J. R.; Scalmani, G.; Barone, V.; Petersson, G. A.; Nakatsuji, H.; Li, X.; Caricato, M.; Marenich, A.; Bloino, J.; Janesko, B. G.; Gomperts, R.; Mennucci, B.; Hratchian, H. P.; Ortiz, J. V.; Izmaylov, A. F.; Sonnenber, J. L.; Williams-Young, D.; Ding, F.; Lipparini, F.; Egidi, F.; Goings, J.; Peng, B.; Petrone, A.; Henderson, T.; Ranasinghe, D.; Zakrzewski, V. G.; Gao, J.; Rega, N.; Zheng, G.; Liang, W.; Hada, M.; Ehara, M.; Toyota, K.; Fukuda, R.; Hasegawa, J.; Ishida, M.; Nakajima, T.; Honda, Y.; Kitao, O.; Nakai, H.; Vreven, T.; Throssell, K.; Montgomery, J., J. A.; Peralta, J. E.; Ogliaro, F.; Bearpark, M.; Heyd, J. J.; Brothers, E.; Kudin, K. N.; Staroverov, V. N.; Keith, T.; Kobayashi, R.; Normand, J.; Raghavachari, K.; Rendell, A.; Burant, J. C.; Iyengar, S. S.; Tomasi, J.; Cossi, M.; Millam, J. M.; Klene, M.; Adamo, C.; Cammi, R.; Ochterski, J. W.; Martin, R. L.; Morokuma, K.; Farkas, O.; Foresman, J. B.; Fox, D. J. *Gaussian 09*, Revision A.02; Gaussian, Inc.: Wallingford, CT, 2016.
34. Becke, A. D., Density-functional thermochemistry. III. The role of exact exchange. *Journal of Chemical Physics* **1993**, *98* (7), 5648-5652.
35. Lee, C. T.; Yang, W. T.; Parr, R. G., Development of the Colle-Salvetti correlation-energy formula into a functional of the electron-density. *Phys Rev B* **1988**, *37* (2), 785-789.

36. Perdew, J. P.; Burke, K.; Ernzerhof, M., Generalized gradient approximation made simple. *Phys Rev Lett* **1996**, *77* (18), 3865-3868.
37. Dunning Jr., T. H.; Hay, P. J., Gaussian basis sets for molecular calculations. In *Methods of Electronic Structure Theory*, 1 ed.; Schaefer, H. F., Ed. Springer US: New York, 1977; pp 1-27.
38. Hay, P. J.; Wadt, W. R., *Ab initio* effective core potentials for molecular calculations. Potentials for main group elements Sc to Hg. *Journal of Chemical Physics* **1985**, *82* (1), 270-283.
39. Hay, P. J.; Wadt, W. R., *Ab initio* effective core potentials for molecular calculations. Potentials for K to Au including the outermost core orbitals. *Journal of Chemical Physics* **1985**, *82* (1), 299-310.
40. Feller, D., The role of databases in support of computational chemistry calculations. *J Comput Chem* **1996**, *17* (13), 1571-1586.
41. Schuchardt, K. L.; Didier, B. T.; Elsethagen, T.; Sun, L.; Gurumoorthi, V.; Chase, J.; Li, J.; Windus, T. L., Basis set exchange: A community database for computational sciences. *Journal of Chemical Information and Modeling* **2007**, *47* (3), 1045-1052.
42. Balabanov, N. B.; Peterson, K. A., Systematically convergent basis sets for transition metals. I. All-electron correlation consistent basis sets for the 3d elements Sc-Zn. *Journal of Chemical Physics* **2005**, *123* (6).
43. Kendall, R. A.; Dunning, T. H.; Harrison, R. J., Electron-affinities of the 1st-row atoms revisited - Systematic basis-sets and wave-functions. *Journal of Chemical Physics* **1992**, *96* (9), 6796-6806.
44. Dunning, T. H., Gaussian basis sets for use in correlated molecular calculations. I. The atoms boron through neon and hydrogen. *Journal of Chemical Physics* **1989**, *90*, 1007-1023.
45. Cossi, M.; Rega, N.; Scalmani, G.; Barone, V., Energies, structures, and electronic properties of molecules in solution with the C-PCM solvation model. *J Comput Chem* **2003**, *24* (6), 669-681.
46. Kraus, K. A.; Nelson, F., Chemistry of aqueous uranium(V) solutions. II. Reaction of uranium pentachloride with water. Thermodynamic stability of  $\text{UO}_2^+$ . Potential of U(IV)/(V), U(IV)/(VI) and U(V)/U(VI) couples. *J Am Chem Soc* **1949**, *71* (7), 2517-2522.
47. Kraus, K. A.; Nelson, F.; Johnson, G. L., Chemistry of aqueous uranium(V) solutions. I. Preparation and properties. Analogy between uranium(V), neptunium(V) and plutonium(V). *J Am Chem Soc* **1949**, *71* (7), 2510-2517.
48. Lide, D. R.; Kehiaian, H. V., *CRC handbook of thermophysical and thermochemical data*. CRC Press, Inc.: Boca Raton, 1994; p 518.
49. Dorfman, L. M.; Adams, G. E. *Reactivity of the hydroxyl radical in aqueous solutions*; NSRDS-NBS 46; U.S. Department of Commerce: Washington, DC, 1973; p 72.

50. Shannon, R. D., Revised effective ionic radii and systematic studies of interatomic distances in halides and chalcogenides. *Acta Crystallogr A* **1976**, *32* (5), 751-767.
51. Moelwyn-Hughes, E. A., *The chemical statics and kinetics of solutions*. Academic Press: London, 1971; p 530.
52. Bader, R. F. W.; Anderson, S. G.; Duke, A. J., Quantum topology of molecular charge distributions. 1. *J Am Chem Soc* **1979**, *101* (6), 1389-1395.
53. Bader, R. F. W.; Nguyendang, T. T.; Tal, Y., Quantum topology of molecular charge distributions. II. Molecular structure and its change. *Journal of Chemical Physics* **1979**, *70* (9), 4316-4329.
54. Cancès, E.; Mennucci, B.; Tomasi, J., A new integral equation formalism for the polarizable continuum model: Theoretical background and applications to isotropic and anisotropic dielectrics. *Journal of Chemical Physics* **1997**, *107* (8), 3032-3041.
55. Wolfsberg, A.; Dai, Z. X.; Zhu, L.; Reimus, P.; Xiao, T.; Ware, D., Colloid-facilitated plutonium transport in fractured tuffaceous rock. *Environmental Science & Technology* **2017**, *51* (10), 5582-5590.
56. Zhao, P. H.; Begg, J. D.; Zavarin, M.; Tumey, S. J.; Williams, R.; Dai, Z. R. R.; Kips, R.; Kersting, A. B., Plutonium(IV) and (V) sorption to goethite at sub-femtomolar to micromolar concentrations: Redox transformations and surface precipitation. *Environmental Science & Technology* **2016**, *50* (13), 6948-6956.
57. Collins, R. N.; Rosso, K. M., Mechanisms and rates of U(VI) reduction by Fe(II) in homogeneous aqueous solution and the role of U(V) disproportionation. *Journal of Physical Chemistry A* **2017**, *121* (35), 6603-6613.
58. Taylor, S. D.; Marcano, M. C.; Rosso, K. M.; Becker, U., An experimental and ab initio study on the abiotic reduction of uranyl by ferrous iron. *Geochimica et Cosmochimica Acta* **2015**, *156*, 154-172.
59. Morse, J. W.; Choppin, G. R., Laboratory studies of plutonium in marine systems. *Marine Chemistry* **1986**, *20* (1), 73-89.
60. Riedel, T.; Kubeck, C., Uranium in groundwater - A synopsis based on a large hydrogeochemical data set. *Water Research* **2018**, *129*, 29-38.
61. Valiev, M.; Bylaska, E. J.; Govind, N.; Kowalski, K.; Straatsma, T. P.; Van Dam, H. J. J.; Wang, D.; Nieplocha, J.; Apra, E.; Windus, T. L.; de Jong, W., NWChem: A comprehensive and scalable open-source solution for large scale molecular simulations. *Computer Physics Communications* **2010**, *181* (9), 1477-1489.
62. Privalov, T.; Macak, P.; Schimmelpfennig, B.; Fromager, E.; Grenthe, I.; Wahlgren, U., Electron transfer in uranyl(VI)-uranyl(V) complexes in solution. *J Am Chem Soc* **2004**, *126* (31), 9801-9808.

63. Boys, S. F.; Bernardi, F., Calculation of small molecular interactions by differences of separate total energies - some procedures with reduced errors. *Molecular Physics* **1970**, *19* (4), 553-566.
64. van Duijneveldt, F. B.; van Duijneveldt-van der Rjdt, J. G. C. M.; van Lenthe, J. H., State-of-the-art in counterpoise theory. *Chemical Reviews* **1994**, *94* (7), 1873-1885.

## CHAPTER 4

# Resolving the kinetics of individual aqueous reaction steps of actinyl ( $\text{AnO}_2^+$ and $\text{AnO}_2^{2+}$ ; An = U, Np, and Pu) tricarbonate complexes with ferrous iron and hydrogen sulfide from first principles

In review with *Radiochimica Acta* as of January 2019

Co-authors: Will M. Bender and Udo Becker

### Abstract

The solubility and mobility of actinides (An), like uranium, neptunium, and plutonium, in the environment largely depends on their oxidation states. Actinyls ( $\text{An}^{\text{V,VI}}\text{O}_2^{+/2+}(\text{aq})$ ) form strong complexes with available ligands, like carbonate ( $\text{CO}_3^{2-}$ ), which may inhibit reduction to relatively insoluble  $\text{An}^{\text{IV}}\text{O}_2(\text{s})$ . Here we use quantum-mechanical calculations to explore the kinetics of aqueous homogeneous reaction paths of actinyl tricarbonate complexes ( $[\text{AnO}_2(\text{CO}_3)_3]^{5-/4-}$ ) with two different reductants,  $[\text{Fe}(\text{OH})_2(\text{H}_2\text{O})_4]^0$  and  $[\text{H}_2\text{S}(\text{H}_2\text{O})_6]^0$ . Energetically-favorable outer-sphere complexes (OSC) are found to form rapidly, on the order of milliseconds to seconds over a wide actinyl concentration range (pM to mM). The systems then encounter energy barriers ( $E_a$ ), some of which are prohibitively high ( $>100$  kJ/mol for some neptunyl and plutonyl reactions with  $\text{Fe}^{2+}$  and  $\text{H}_2\text{S}$ ), that define the transition from outer- to inner-sphere complex (ISC; for example, calculated  $E_a$  of ISC formation between  $\text{UO}_2^+$  and  $\text{UO}_2^{2+}$  with  $\text{Fe}^{2+}$  are 35 and 74 kJ/mol,

respectively). In some reactions, multiple OSCs are observed that represent different hydrogen bonding networks between solvent molecules and carbonate. Even when forming ISCs, electron transfer to reduce  $An^{6+}$  and  $An^{5+}$  is not observed (no change in atomic spin values or lengthening of  $An-O_{ax}$  bond distances). Proton transfer from bicarbonate and water to actinyl O was tested as a mechanism for electron transfer from  $Fe^{2+}$  to  $U^{6+}$  and  $Pu^{6+}$ . Not all proton transfer reactions yielded reduction of  $An^{6+}$  to  $An^{5+}$  and only a few pathways were energetically-favorable (*e.g.*,  $H^+$  transfer from  $H_2O$  to drive  $Pu^{6+}$  reduction to  $Pu^{5+}$  with  $\Delta E = -5$  kJ/mol). The results suggest that the tricarbonato complex serves as an effective shield against actinide reduction in the tested reactions and will maintain actinyl solubility at elevated pH conditions. The results highlight reaction steps, such as inner-sphere complex formation and electron transfer, which may be rate-limiting. Thus, this study may serve as the basis for future research on how they can be catalyzed by a mineral surface in a heterogeneous process.

## Introduction

The chemistry of early actinide elements in the environment is a major concern with regards to the long-term storage of nuclear waste. Elements like uranium, neptunium, and plutonium are radioactive and pose a hazard to humans and other biota if released. These three elements assume a range of oxidation states (most commonly between +3 and +6) and can exist in a diverse array of solid and aqueous species.<sup>1</sup> In oxidizing environments, higher-valent forms of these actinides form the actinyl molecule with the formula  $AnO_2^{x+}$ . The molecular charge of +1 and +2 corresponds to the penta- and hexavalent actinide oxidation states, respectively. These species are soluble and mobile under a range of solution conditions and form strong complexes with various inorganic and organic ligands.<sup>2-4</sup> These soluble forms of the actinides pose the greatest

threat in terms of their ability to disperse radioactivity in the environment. The reduction of actinides to the +4 and +3 oxidation states, in most cases, results in the precipitation of insoluble oxide mineral phases (*e.g.*, uraninite,  $\text{UO}_2(\text{s})$ ).<sup>5</sup> Therefore, reactions of actinyls and their aqueous complexes with various reductants, including  $\text{Fe}^{2+}$  and  $\text{H}_2\text{S}$ , are of utmost concern when thinking of ways in which the mobility of these contaminants may be attenuated.

Some of the most stable and abundant actinide complexes in natural waters are the ones formed with carbonate ( $\text{CO}_3^{2-}$ ).<sup>6</sup> These complexes are expected to be the major forms of dissolved U, Np, and Pu in carbonate-bearing waters (*e.g.*, seawater and limestone-hosted groundwater).<sup>6-8</sup> As such, the chemical behavior and reactions of these complexes are of particular interest. The thermodynamics of complex formation and the structure of U, Np, and Pu carbonate complexes has been explored in detail by experimental<sup>9-13</sup> and computational<sup>14-16</sup> approaches alike. From these efforts, it is clear that the actinyl tricarbonate complex,  $[\text{AnO}_2(\text{CO}_3)_3]^{5-/4-}$ , is the dominant form of uranyl, neptunyl, and plutonyl species at higher pH (>8) and moderate ionic strength.<sup>8,13,17</sup> The stability of these complexes is even harnessed in analytical settings when adsorbed or precipitated actinides species need to be desorbed or (re)dissolved for analysis.<sup>18-20</sup> Depending on the solution conditions, a number of other carbonate-bearing complexes are known to form as well, including those with just one or two carbonate ligands<sup>13-14</sup> and tricarbonate complexes with counter-ions (*e.g.*,  $\text{Ca}^{2+}$  in  $[\text{Ca}_2\text{AnO}_2(\text{CO}_3)_3]^0$ ).<sup>21-22</sup> This study focuses on the tricarbonate complex without any counter ions. In this structure, each of the carbonate molecules assumes bidentate configuration and lays flat in an equatorial plane to produce a six-fold ring of An- $\text{O}_{\text{carbonate}}$  coordination. A representative calculated structure, that of  $[\text{UO}_2(\text{CO}_3)_3]^{4-}$  is presented in Figure 4.1.

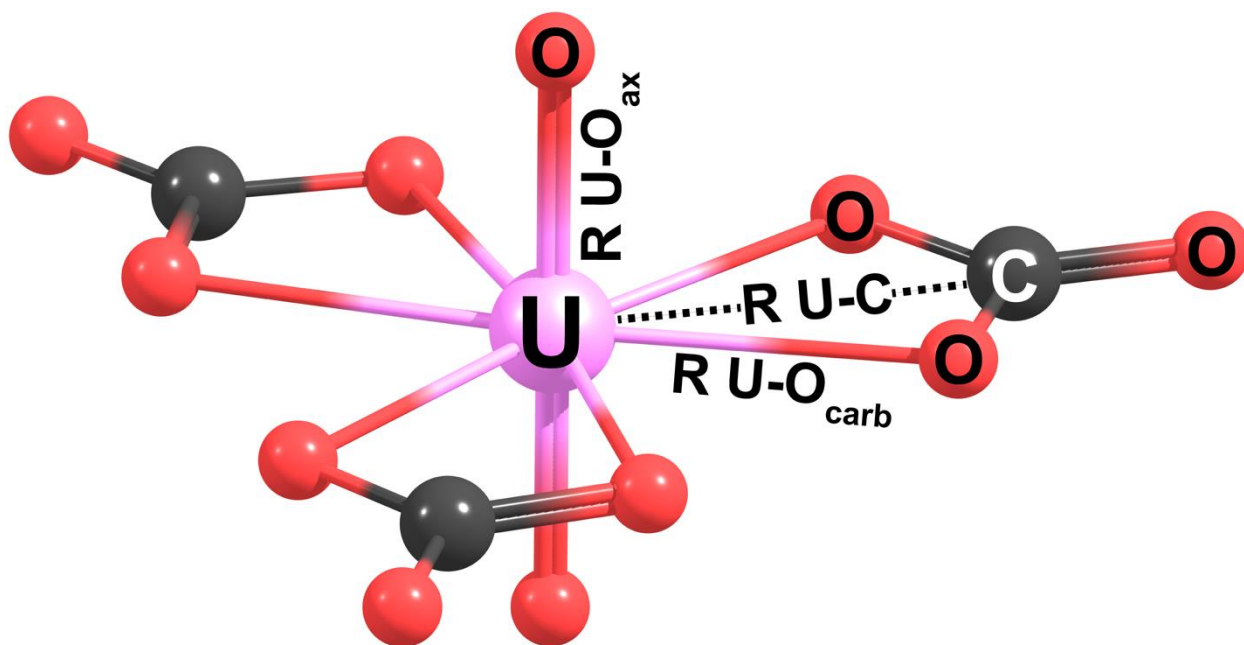
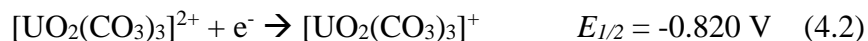


**Figure 4.1** The calculated structure of  $[\text{UO}_2(\text{CO}_3)_3]^{4-}$ . The three carbonate groups are in bidentate coordination of the central  $\text{U}^{6+}$  in the linear uranyl molecule. The  $\text{U}-\text{O}_{\text{ax}}$  bond length (labeled as R), an indicator of oxidation state, is slightly longer than those found in uranyl water or hydroxide complexes. The  $\text{U}-\text{O}_{\text{carbonate}}$  and  $\text{U}-\text{C}$  distances are also an important measure of the actinide valence in this configuration and all these distances increase if  $\text{U}^{6+}$  is reduced to  $\text{U}^{5+}$ . Analogous complexes and structural responses are observed for the complexes of neptunyl and plutonyl.

The aqueous redox chemistry of actinyls is an area of ongoing research. Many reactions are possible in solution (*i.e.* homogeneous reactions) or at mineral surfaces (*i.e.* heterogeneous reactions). Prior experimental and computational research has focused on the reactions of actinides with aqueous  $\text{Fe}^{2+}$  and Fe (oxyhydr)oxide mineral phases as these species constitute some of the most widespread reductants in natural and engineered environments where (corroding) steel may be present.<sup>23-25</sup> A smaller body of research has explored reactions with Fe sulfide minerals<sup>26-29</sup> and  $\text{H}_2\text{S}$ .<sup>30</sup> Reduction of actinides in solution has been shown to be possible, however, complete reduction of  $\text{An}^{6+}$  to  $\text{An}^{4+}$  is not observed in all cases, possibly due to large energy costs associated with alteration of the cation coordination environment between  $\text{An}^{6+/5+}$  and  $\text{An}^{4+}$ .<sup>3,7,31-32</sup> In some experiments, it has been observed that increasing the pH to 7 or above and/or carbonate concentration can dramatically decrease  $\text{U}^{6+}$  reduction to nearly zero in reactions with

anthraquinone-2,6,-disulfonate<sup>33</sup> (an organic reductant), amorphous FeS<sup>20</sup>, and zero-valent iron.<sup>34</sup> In addition, higher pH conditions drive desorption or maintain solubility of negatively-charged actinide complexes above the points of zero charge for many minerals.<sup>22,35-36</sup> This indicates that homogeneous reactions of these complexes are likely most important as controls on actinide mobility at alkaline pH conditions.

Investigation of the redox behavior of actinyl carbonate complexes has broadly found that carbonate complexation inhibits reduction, particularly when compared with redox reactions involving the  $[\text{AnO}_2(\text{H}_2\text{O})_5]^{+2+}$  complex. This effect is made clear by comparing the reduction potentials in Equations 4.1 and 4.2, as measured via cyclic voltammetry<sup>37</sup> versus the Ag/AgCl reference electrode:



Clearly, the redox potential of the carbonate complex is significantly lower than that of the pentaquo complex. In this same study, rate constants ( $k^0$ ) of heterogeneous electron transfer at the mercury drop electrode interface were found to be two orders of magnitude slower for the carbonate complex reaction versus that of the water complex ( $k^0 = 2.6 \times 10^{-5}$  vs.  $2.8 \times 10^{-3}$  cm/s).

This study seeks to characterize the redox behavior and kinetics of complex formation between actinyl tricarbonates of uranyl, neptunyl, and plutonyl with  $\text{Fe}^{2+}$  and  $\text{H}_2\text{S}$  to see how carbonate may protect these species from reduction and maintain actinide mobility and solubility in the environment. The results are compared to a computational study<sup>38</sup> of the reduction of uranyl tr carbonate by  $\text{Fe}^{2+}$  and various experimental findings.<sup>6,22,34-35,39-40</sup> In addition, the computational methodology, previously employed to investigate the kinetics of redox reactions of plutonyl hydrolysis complexes<sup>41</sup>, is evaluated and reaction rates of aqueous complexes with and

without carbonate ligands are compared. The results presented here elucidate which transition steps (outer-sphere complex formation *vs.* inner-sphere complex formation *vs.* electron transfer), are rate-limiting for homogeneous actinyl reduction and indicate which steps may be catalyzed by mineral surfaces. Such heterogeneous reactions of adsorbed species on mineral or colloid surfaces and acidic solution conditions, more readily able to facilitate proton transfer, are likely to be more favorable for actinyl reduction.

## Computational methods

Quantum-mechanical calculations to optimize the atomic and electronic structures of the tested compounds were carried out using the Gaussian 09 (revision A.02) code<sup>42</sup>. The calculations were carried out using the B3LYP hybrid density functional<sup>43-44</sup> coupled with the LANL2DZ<sup>45-47</sup> (for H, O, C, and S) and Stuttgart relativistic small-core<sup>48-49</sup> (for Fe, U, Np, and Pu) basis sets. Corresponding pseudopotentials were used for S, U, Np, and Pu atoms to lessen computational expense. The S, Fe, and actinide pseudopotentials account for the contribution of 10, 10, and 60 inner shell electrons, respectively. The basis set and pseudopotential information was acquired from the EMSL Basis Set Library.<sup>50-51</sup> To simulate an aqueous environment, a combination of explicit and implicit hydration approaches was used. The first coordination shell of Fe<sup>2+</sup> and H<sub>2</sub>S was modeled explicitly with six H<sub>2</sub>O and/or OH<sup>-</sup> in an octahedral arrangement. Hydroxide was used to balance the charge of the Fe<sup>2+</sup> cation and minimize the electrostatic attraction to the negatively-charged actinyl tricarbonato complex and so both reductant species were charge-neutral. The net charge of the models was either -4 or -5 depending on the charge of actinyl carbonate complex. The unpaired spins on actinides (present for all except U<sup>6+</sup>) and Fe<sup>2+</sup> were set in a ferromagnetic configuration with net alpha (upward) spin. The atomic charges and spins in

the system were determined using Mulliken population analysis. Mulliken results were compared with Bader<sup>52-53</sup> and natural<sup>54-55</sup> population analyses and the difference was  $\leq 0.2$  charge or spin units.<sup>41</sup> The use of a more rigorous population analysis approach did not change the interpretation of charge or spin change in the system. A small subset of models in this system were tested and verified to have similar variability between the different population analysis methods. From here on, discussion of atomic charge and spin refer to the results of Mulliken population analyses. All three carbonate groups of the  $[\text{AnO}_2(\text{CO}_3)_3]^{5-/4-}$  complex are in a bidentate configuration and lay in the equatorial plane around the actinyl molecule as has been described by various experimental<sup>11-13,15-17,56-57</sup> and computational studies.<sup>14-16,58</sup> Our calculated structures for these complexes align, in terms of bond distances and angles, with these previously reported data. The C-PCM implicit polarizable conductor model was used to simulate the contribution of higher-order solvation shells to the energy of the system.<sup>59-60</sup>

To evaluate the kinetics of reactions between a given actinyl and reductant complex, a series of geometry optimization calculations, in which the distance between the actinide and reductant (either the Fe or S atom) was held constant for a given configuration along the reaction path (while all other atoms were allowed to relax), were conducted at progressively shorter distances. Starting from a relatively large actinide-reductant distance (9-12 Å), the reductant is stepped towards the actinide in 0.25 Å increments, to a distance of  $\sim 2$  Å. The geometry is optimized at each step and the atoms comprising the reductant and its first coordination shell are taken and shifted to generate the next input orientation. The wavefunction from the previous geometry is supplied as a starting point for the initial electronic configuration. The incoming reductant was set to travel along the x axis of the system on a trajectory to impact the actinyl tricarbonate complex between two carbonate groups that are lying in the x-y plane. The actinyl

molecule is positioned along the z axis, with the An center defining the origin of the coordinate system.

For the purpose of deriving kinetic parameters, the goal of these calculations is to generate an energy versus distance curve (see Figure 4.2 for an idealized schematic). At large reactant distances, the energy of the system is nearly a plateau with a very shallow slope. There is very little interaction between the two complexes at these distances and the slope, however small, is due to long-range electrostatic forces. Testing of this distance regime has revealed that the slope directly correlates to Coulomb interaction energy and is very small when the distance is  $>10 \text{ \AA}$  and the atoms are screened by a solvent (*e.g.*, water in explicit and/or implicit form via C-PCM)<sup>41</sup>. Eventually, there is a point at which this energy slope increases and the energy becomes more

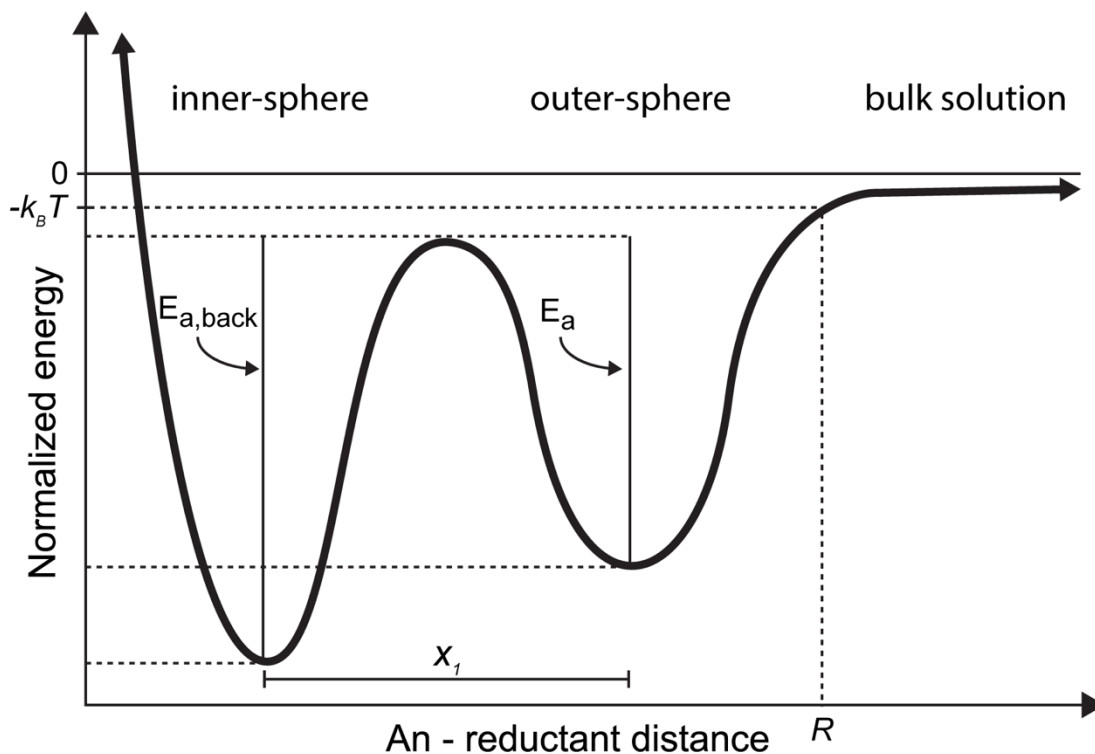


**Figure 4.2** A schematic energy vs. distance relationship showing the decrease in energy associated with bringing a reductant closer to an actinide (An) species in solution. The position of the reactive radius ( $R$ ) is indicated, as are the activation energies ( $E_a$ ) for the forward and backward reactions and the distance between the two energy minima ( $x$ ). These parameters are gathered from the calculated reaction distance series and used to evaluate the rates of transitions between different complex configurations.

negative to a local minimum corresponding to the energy of an outer-sphere complex. This configuration is defined by hydrogen bonding between the intact coordination shells of the two reactants and the lack of direct bonding interaction between Fe or S with carbonate O or the actinyl (these latter features define the inner-sphere complex configurations). The point along this downward trajectory when one  $k_B T$  unit (2.49 kJ/mol vs. the energy of infinite separation between the actinyl and reductant) of energy has been gained is defined as the reactive radius ( $R$ ). With this amount of energy gained, the system is far enough down the path toward the formation of the outer-sphere complex such that escape back to the solution bulk is unlikely.

The reactive radius is used in this study to determine the rate of encounter complex formation from the collisions of free coordination complexes in a bulk solution. The following equation, based on collision theory, is used to determine this initial collision rate ( $r$ ):

$$r = \pi R^2 v N_A [X][Y] \quad (4.3)$$

Where  $R$  is the reactive radius (in dm; dm is used here to correspond to the unit for volume of solution, which is L or dm<sup>3</sup>),  $v$  is the geometric mean of the diffusion velocities of the reactants (in dm/s),  $N_A$  is Avogadro's number, and  $[X]$  and  $[Y]$  represent the concentrations of the reactant species (in M). Diffusion coefficients for the reductants Fe<sup>2+</sup> ( $7.19 \times 10^{-8}$  dm<sup>2</sup>/s) and H<sub>2</sub>S ( $1.48 \times 10^{-7}$  dm<sup>2</sup>/s) are taken from the experimental literature.<sup>61-62</sup> The diffusion coefficient of the actinyl tricarboxylate complex ( $5.52 \times 10^{-8}$  dm<sup>2</sup>/s) is assumed to be constant across the different actinide elements and valence states.<sup>63</sup> This assumption is a fair one given that variability in the diffusion coefficients of different actinyl water and carbonate complexes is minor or not measureable.<sup>37,64-65</sup> If one reactant is considered to be much larger than the other, say the concentration of reductant  $[Y]$  is in great excess to the actinyl carbonate complex,  $[X]$ , then nearly all of Equation 4.3 can be simplified into a pseudo-first order rate constant. Within the calculated

reactive radii range found in this study, and assuming  $[Y] = 1 \mu\text{M}$ , this constant falls within 4502-6018  $\text{s}^{-1}$ .

This collision rate is used to calculate the formation of outer-sphere complexes from bulk solution concentrations. Next, the rate(s) of transition from outer- to inner-sphere complex configurations, or between consecutive outer-sphere complex configurations, are determined. Both the forward and backward transitions between different complexes are considered. In some cases, the system energy *vs.* distance relationships show smooth parabolic energy wells, but others appear less symmetrical and even appear like sloped steps. These aberrations from an idealized energy surface, as shown in Figure 4.2, are due to the complexities of hydrogen bonding networks and the “snap” formation of new bonds for which the energy response is dramatic due to the relatively low number of explicit solvent molecules included in the system.<sup>41</sup> The rate constants ( $k_r$ ) for these transitions are calculated using the Arrhenius equation:

$$k_r = Ae^{\frac{-E_a}{RT}} \quad (4.4)$$

Which depends on a pre-exponential factor, also called the attempt frequency ( $A$ ), the activation energy of the process ( $E_a$ , in kJ/mol), the gas constant ( $R$ ; not to be confused here with the reactive radius), and temperature ( $T$ ; in this case, 298.15 K). The attempt frequency of the transition is itself a function of several factors and is also related to the activation energy, the mass of the incoming reductant complex ( $\text{Fe}(\text{OH})_2(\text{H}_2\text{O})_4$  or  $\text{H}_2\text{S}(\text{H}_2\text{O})_6$ ), moving over the energy barrier ( $m$ , in kg), and the distance between the two energy minima on either side of the activation energy peak ( $x$ , in m):

$$A = \frac{1}{\sqrt{2}} \sqrt{\frac{E_a}{mx^2}} \quad (4.5)$$

Equation 4.5 was originally applied to diffusion of atoms in crystal lattices<sup>66-67</sup>, but comparison of the calculated attempt frequencies with those derived from fitting a parabolic function was found

to be minimal.<sup>41</sup> As such, this simpler approach, for which all the necessary inputs can be extracted readily without any curve fitting, is applied again here.

For every reactive pair, a minimum of three different rates are considered: (1) the rate of encounter complex formation from collision theory using Equation 4.3, (2) the rate of the transition from outer- to inner-sphere complex using Equations 4.4 and 4.5; and (3) the rate of the back reaction where inner-sphere complexes return to the outer-sphere complex configuration. For systems with more than one energy barrier, more forward and backward reactions are added to the model. These different rates are used as inputs to a computer program that evaluates the change in concentration of different complex species starting from concentrations of the free reactants, the actinyl tricarbonate and reductant-water complexes, in the simulated solution. These aqueous reactants are consumed via the collision reaction and are then subject to the outer- and inner-sphere complex transition rates. The concentrations of all the different species (*e.g.*, [H<sub>2</sub>S in bulk solution], [outer-sphere complex], [inner-sphere complex]) are evaluated over small time increments to learn about the overall kinetics of the outer- and inner-sphere complex formation.

For further information regarding this approach for deriving aqueous redox reaction kinetics, the reader is referred to its first implementation in a prior study<sup>41</sup> focused on the reactions of PuO<sub>2</sub><sup>+</sup> and PuO<sub>2</sub><sup>2+</sup> hydrolysis complexes, [PuO<sub>2</sub>OH(H<sub>2</sub>O)<sub>4</sub>]<sup>0</sup> and [PuO<sub>2</sub>(OH)<sub>2</sub>(H<sub>2</sub>O)<sub>3</sub>]<sup>0</sup>, with Fe<sup>2+</sup>, Fe<sup>3+</sup>, and hydroxyl radical, where the methodology is described and evaluated in more detail.

## Results

This section starts with the calculation of the collision frequency of the actinyl tricarbonate complex with a reductant. For this calculation, the reactive radius (*i.e.*, the distance at which reactants interact more strongly than their thermal motion) in solution is a governing variable. This

step, which is followed by outer- and inner-sphere complex formation, is calculated using a combination of statistical mechanics and quantum mechanics.

### *Calculated reactive radii*

The reactive radius ( $R$ ) for all of the different reactant pair combinations was determined by making a linear fit between the two distance steps bracketing the energy gain of one  $k_B T$  unit from the bulk solution energy plateau. The calculated distances are presented in Table 4.1 and fall within 8.2 to 9.5 Å. The distances for reactions with  $[\text{Fe}(\text{OH})_2(\text{H}_2\text{O})_4]^0$  are generally smaller than those for  $[\text{H}_2\text{S}(\text{H}_2\text{O})_6]^0$ . The two exceptions are the reaction of the  $\text{PuO}_2^{2+}$  and  $\text{NpO}_2^{2+}$  tricarbonate complexes with  $\text{Fe}^{2+}$ , which have reactive radii that are 0.2 and 0.3 Å larger than their  $\text{H}_2\text{S}$  counterparts, respectively. The shorter radii observed for most of the  $\text{Fe}^{2+}$  reactions may be explained by the coordination of iron by the two hydroxide ions. It is possible that the interaction between  $\text{OH}^-$  and  $\text{Fe}^{2+}$  masks some of the long-range electrostatic interaction and that there may even be a slight repulsive component between  $\text{OH}^-$  and the  $\text{CO}_3^{2-}$  groups. In addition, the charged Fe cation more tightly binds the members of its first coordination shell relative to  $\text{H}_2\text{S}$ . As a result, the  $\text{H}_2\text{O}$  molecules that were initially placed in octahedral coordination around the  $\text{H}_2\text{S}$  are more likely to drift out of position. The formation of H bond chains connecting several waters stretching into the gap separating the actinyl carbonate and reductant coordination complexes effectively shortens the reactive radius. These water chain structures were found to form for nearly all of the  $\text{H}_2\text{S}$  reactions, but did not form as coherently in the reactions with divalent neptunyl and plutonyl, explaining the relatively short reactive radii compared to the others.

These reactive radii, along with the diffusion coefficients of the reactant species, are used to calculate the rate of encounter complex formation (see Equation 4.3). This aqueous encounter rate increases with increasing concentrations and diffusion velocities. The more molecules or

complexes that are present and the faster they are traveling, the more likely they are to pass within  $R$  Å of each other and form an energetically-favorable outer-sphere complex.

**Table 4.1** Calculated reactive radii ( $R$ , in Å) for different  $[\text{AnO}_2(\text{CO}_3)_3]^{x-6}$ -reductant<sup>a</sup> pairs

Actinyl	Reductant	
	$\text{Fe}^{2+}$	$\text{H}_2\text{S}$
$\text{UO}_2^+$	8.5	9.3
$\text{UO}_2^{2+}$	9.2	9.5
$\text{NpO}_2^+$	8.6	9.5
$\text{NpO}_2^{2+}$	9.0	8.7
$\text{PuO}_2^+$	8.2	9.2
$\text{PuO}_2^{2+}$	8.9	8.7

<sup>a</sup>Unpaired spins on  $\text{Fe}^{2+}$  and actinyl, when present, are in a ferromagnetic arrangement.

### *Rates of outer-sphere complex formation*

Once the reactive radius is reached, energy surfaces for all of the tested reactions paths show an increase in slope, representing the energy gain associated with the start of outer-sphere complex formation. The rate of collision and formation of the outer-sphere complexes was assessed using the computer script described above in the Computational Methods section. Initial collision rates were calculated and then reevaluated over small time increments. These subsequent rates take into account the decrease in concentration of free aqueous reactants over time as outer-sphere (and inner-sphere complexes) are formed. One way to frame the rate at which this process occurs is to consider a half-life ( $t_{1/2}$ ) of the free actinyl tricarbonato complex which has not yet formed an outer-sphere complex via collision with a reactant in solution. The concentration of the free actinyl carbonate complex decreases rapidly and effectively goes to zero if the concentration of the second reactant (in this case, the  $\text{Fe}^{2+}$  and  $\text{H}_2\text{S}$  water  $\pm$  hydroxide complexes) is in

significantly higher concentration. The half-lives for several of the reaction pairs, with different initial reactant concentrations, are presented in Table 4.2. Larger reactive radii, faster diffusion, and higher concentration all decrease  $t_{1/2}$ . Even at environmentally-relevant actinyl concentrations, typically in the nM to pM range, outer-sphere complex formation is calculated to proceed rapidly with significant complex formation occurring over several ms to s. Half of the available free actinyl tricarbonate complexes will form outer-sphere complexes with reductant species within 11.5-15.4 s with starting concentrations of 1 pM and 1 nM, respectively. These half-lives decrease to milliseconds and microseconds if concentrations are increased to the  $\mu\text{M}$  and mM level.

**Table 4.2** Calculated half-lives ( $t_{1/2}$ ) of free actinyl tricarbonate complexes in solutions with the reductants  $\text{Fe}^{2+}$  and  $\text{H}_2\text{S}$  at different reactant concentrations

[actinyl]	[reductant]	$\text{UO}_2^{2+}/\text{Fe}^{2+}$	$\text{UO}_2^+/\text{H}_2\text{S}$	$\text{NpO}_2^+/\text{H}_2\text{S}$	$\text{PuO}_2^+/\text{Fe}^{2+}$
<b>1 <math>\mu\text{M}</math></b>	<b>1 mM</b>	12.2 $\mu\text{s}$	14.4 $\mu\text{s}$	11.5 $\mu\text{s}$	15.4 $\mu\text{s}$
<b>1 nM</b>	<b>1 <math>\mu\text{M}</math></b>	12.2 ms	14.4 ms	11.5 ms	15.4 ms
<b>1 pM</b>	<b>1 nM</b>	12.2 s	14.4 s	11.5 s	15.4 s

Energy minima associated with outer-sphere complex formation are noticeably different for reactions with  $\text{Fe}^{2+}$  and  $\text{H}_2\text{S}$ . In the case of reactions with  $\text{Fe}^{2+}$ , the outer-sphere positions are defined by smooth-sided energy wells with local minima at An-Fe = 6 Å. This distance is almost the same nearly independent of type of actinide or oxidation state. For the reactions with  $\text{H}_2\text{S}$ , the energy surfaces are less uniform across the different actinyls. Energy minima positions for the outer-sphere complexes with  $\text{H}_2\text{S}$  range between An-S distances of 4.3 to 5.5 Å. Of the six tested  $\text{H}_2\text{S}$  reactions, the outer-sphere complex with  $\text{UO}_2^+$  tricarbonate has the largest An-S distance at 5.5 Å. No other outer-sphere complex has an An-reductant separation larger than 5 Å. The energy wells with  $\text{H}_2\text{S}$  are also steeper-sided than those of  $\text{Fe}^{2+}$  and show particularly rapid energy increases as the An-S distance is decreased. After the reactive radius, energy vs. distance curves

of H<sub>2</sub>S show relatively shallow slopes leading up to the edges of these steep-sided outer-sphere energy wells, whereas the Fe<sup>2+</sup> curves show a steeper, but smoother, trajectory down into the local minimum. The energy curves of all of the different tested reaction pairs are presented in Figure 4.3.

The structures of these different outer-sphere configurations reveal that beginnings of the energy wells correspond to the formation of multiple H bonds between the coordinating water molecules around Fe<sup>2+</sup> and H<sub>2</sub>S and the O atoms of actinyl-coordinating carbonate groups. In the

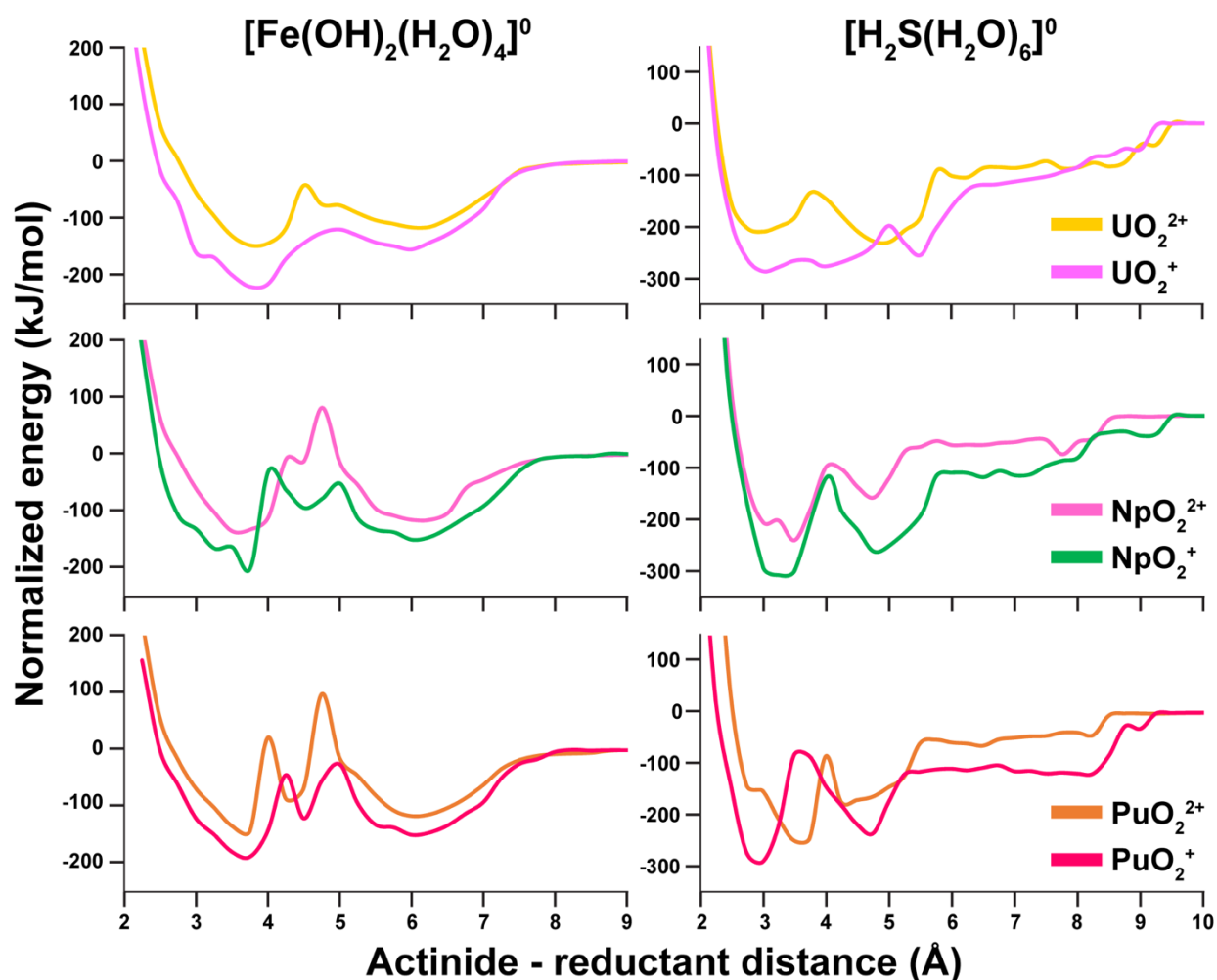


**Figure 4.3** Calculated energy versus distance curves for actinyl tricarbonate,  $[\text{AnO}_2(\text{CO}_3)_3]^{x-6}$ , complexes reacted with  $[\text{Fe}(\text{OH})_2(\text{H}_2\text{O})_4]^0$  and  $[\text{H}_2\text{S}(\text{H}_2\text{O})_6]^0$ . Energies (in kJ/mol) are normalized so that zero represents the energy of the reactants in the bulk solution (An-reductant distances  $>9$  Å). Outer- and inner-sphere energy minima are defined in the regions of 4.25-6 Å and 3-3.75 Å, respectively, and vary between different actinyls and valences.

calculations, H<sub>2</sub>S has a less ordered coordination environment and as such, the formation of these bonds between carbonate and water is more varied. Once a H bonding network is established, the water in these models quickly seeks to arrange itself which results in the steeper-sided energy wells. In the case of Fe<sup>2+</sup>, the water and hydroxide are more ordered around the cation and thus, the changes to these water molecules are more gradual as they balance the energy gains associated with coordinating the cation versus forming a H bond to carbonate.

In the case of H<sub>2</sub>S, the formation of the outer-sphere complex is coincident with the loss of a proton and conversion to HS<sup>-</sup>. This behavior is observed in all H<sub>2</sub>S series that were tested. This proton is passed first to an adjacent water molecule, which in turn gives up one of its own protons to a carbonate group to create bicarbonate (HCO<sub>3</sub><sup>-</sup>). The bicarbonate initially remains in bidentate configuration around the actinyl, but eventually as the An-S distance decreases becomes monodentate. An example of this structure immediately following H<sup>+</sup> transfer, for the reaction with UO<sub>2</sub><sup>2+</sup>, is presented in Figure 4.4. This change is also accompanied by spreading and bending of the two (bi)carbonate groups out of the plane due to electrostatic repulsion between negatively-charged S and O of carbonate. In comparison, incoming [Fe(OH)<sub>2</sub>(H<sub>2</sub>O)<sub>4</sub>]<sup>0</sup> causes only minor changes to carbonate coordination of the actinyls. The An-O<sub>carbonate</sub> and An-C distances lengthen slightly as H bonds form to water, but the change is on the order of 0.1-0.2 Å. The carbonate molecules rotate like a wheel as Fe<sup>2+</sup> is brought closer such that the inner carbonate O atoms are pushed in towards the An center. As such, each An-O<sub>carbonate</sub> distance on the two carbonates closest to the Fe changes by about the same amount, but some increase and some decrease. No proton transfer from water to carbonate is observed in the Fe reaction series. A representative outer-sphere complex configuration is presented for the reaction of [Fe(OH)<sub>2</sub>(H<sub>2</sub>O)<sub>4</sub>]<sup>0</sup> with [PuO<sub>2</sub>(CO<sub>3</sub>)<sub>3</sub>]<sup>5-</sup> in Figure 4.5A. In this configuration, a water molecule has oriented itself flat in the x-y plane to form

H bonds with two carbonate groups; this geometry corresponds to the outer-sphere energy minimum in this reaction.

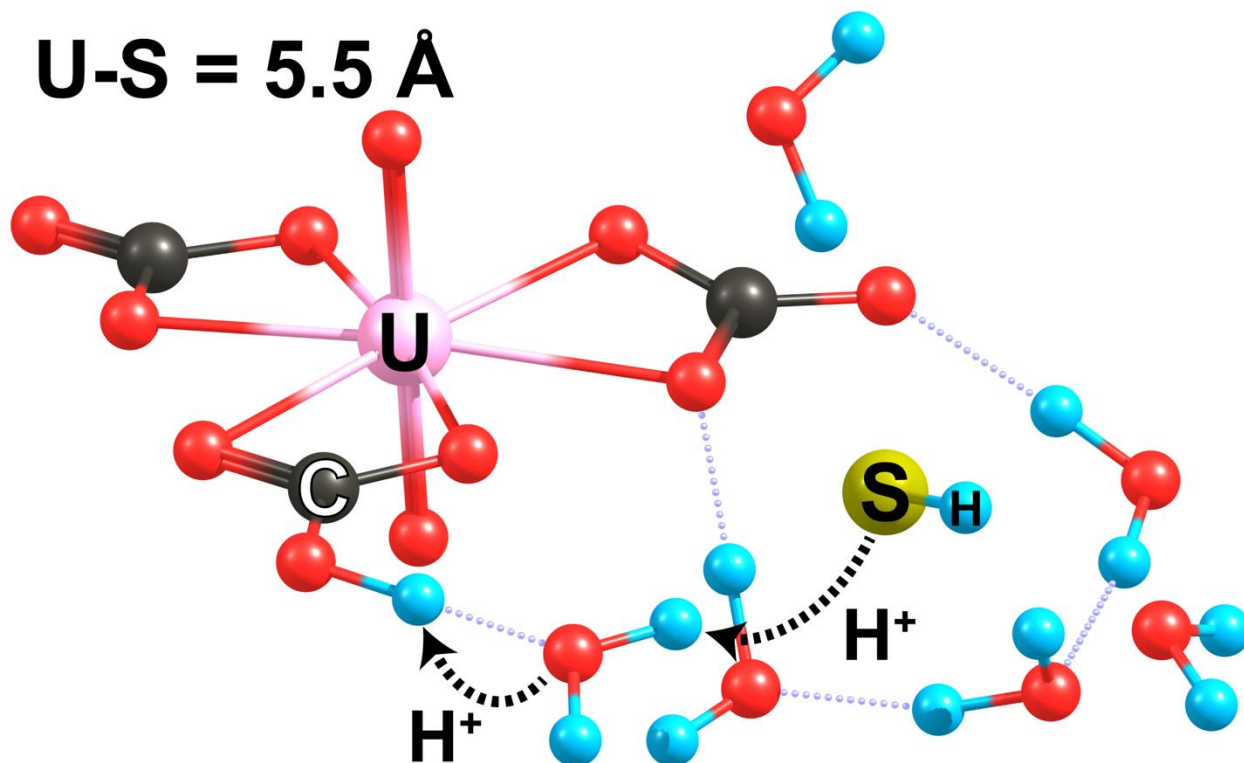


**Figure 4.4** The structure of an outer-sphere complex of H<sub>2</sub>S with [UO<sub>2</sub>(CO<sub>3</sub>)<sub>3</sub>]<sup>4-</sup> at a U-S distance of 5.5 Å. At this distance, H<sub>2</sub>S has passed a proton via a neighboring water molecule to CO<sub>3</sub><sup>2-</sup> to form HCO<sub>3</sub><sup>-</sup> and HS<sup>-</sup>. The bicarbonate molecule remains in bidentate configuration at this distance, but as the HS<sup>-</sup> is brought closer to U, both the bicarbonate and adjacent carbonate will begin to bend out of the equatorial plane and rotate to become monodentate around the central actinyl. This motion will result in an energy barrier between outer- and inner-sphere energy minima. Similar structures are observed for the other actinyl complexes in reactions with H<sub>2</sub>S.

#### *Formation of inner-sphere complexes and associated energy barriers*

In all tested reactions, there is an energy barrier associated with the transition from an outer- to inner-sphere complex. This energy barrier is observed in the An-reductant distance range of 3.5 to 5 Å. In several reactions with Fe<sup>2+</sup>, two energy barriers are present that separate multiple outer-sphere complex configurations from the inner-sphere complex. The barriers for the reactions with Fe<sup>2+</sup> fall in a narrower An-reductant range (4-5 Å) than for H<sub>2</sub>S. The activation energies range

widely between 11-215 kJ/mol across the different reactant pairs. A full accounting of the calculated activation energies for the forward and backward reactions over these barriers, as well as the distance between energy minima for the different reactant pairs, is presented in Table 4.3. The large spread in energies is related to the variety of different structural changes that happen as the reductant is brought closer to the actinyl tricarbonate complex and the behavior of the explicit water molecules. Hydrogen bonds between water and carbonate, and in the case of H<sub>2</sub>S, proton transfer to form HCO<sub>3</sub><sup>-</sup> and HS<sup>-</sup>, define the outer-sphere complex regime. As Fe<sup>2+</sup> and HS<sup>-</sup> move closer to the carbonate groups, these systems undergo different styles of structural reorganization.

For both reductants, water and/or hydroxide molecules that comprise the explicitly-modeled first coordination shells are forced to rearrange themselves. The one or two molecules that are between the incoming reductant and the carbonate ring are most affected by the shrinking An-reductant distance. Several optimized structures are shown in Figure 4.5 as [Fe(OH)<sub>2</sub>(H<sub>2</sub>O)<sub>4</sub>]<sup>0</sup> is brought closer to [PuO<sub>2</sub>(CO<sub>3</sub>)<sub>3</sub>]<sup>5-</sup>. The H bonds of one water molecule to two carbonate groups are shown in the first panel, corresponding to a Pu-Fe distance of 6 Å. The second structure, in panel B, shows the system at a distance of 5 Å at the crest of an energy barrier to form a second outer-sphere configuration. In the third step, the water molecule has no interaction with the carbonate at all and is now H bonded with one of the actinyl O atoms. This position of H<sub>2</sub>O in an H bonding configuration with actinyl O is observed for approximately half of the reaction pairs. There does not seem to be an obvious reason why some systems adopt this configuration in the inner-sphere complex when others do not. In the cases where it does occur, it always corresponds to the minimum energy configuration for the reaction distance series. However, similar energy gains over the outer-sphere complex energy are still achieved in systems where H bonding to actinyl does not occur.

**Table 4.3** Calculated activation barrier parameters for reaction of actinyl tricarbonate complexes with  $[\text{Fe}(\text{OH})_2(\text{H}_2\text{O})_4]^0$  and  $[\text{H}_2\text{S}(\text{H}_2\text{O})_6]^0$  using the C-PCM solvation model

Reductant	Actinyl	Activation energies ( $E_a$ , in kJ/mol) and distances between energy minima ( $x$ , in Å)			
		$E_a$	$E_{a,\text{back}}$	$x$	
Fe <sup>2+</sup>	UO <sub>2</sub> <sup>+</sup>	$E_{a1} = 35$	101	2.25	
	UO <sub>2</sub> <sup>2+</sup>	$E_{a1} = 74$	106	2.25	
	NpO <sub>2</sub> <sup>+</sup>		$E_{a1} = 99$	43	1.5
			$E_{a2} = 65$	171	0.75
			$E_{a3} = 37$	2	0.5
	NpO <sub>2</sub> <sup>2+</sup>	$E_{a1} = 199$	217	2.5	
PuO <sub>2</sub> <sup>+</sup>		$E_{a1} = 125$	96	1.5	
		$E_{a2} = 77$	145	0.75	
PuO <sub>2</sub> <sup>2+</sup>		$E_{a1} = 215$	185	1.75	
		$E_{a2} = 35$	165	0.5	
H <sub>2</sub> S	UO <sub>2</sub> <sup>+</sup>	$E_{a1} = 57$	79	1.5	
		$E_{a2} = 11$	21	1	
	UO <sub>2</sub> <sup>2+</sup>		$E_{a1} = 12$	137	1.25
			$E_{a2} = 96$	75	2
	NpO <sub>2</sub> <sup>+</sup>	$E_{a1} = 142$	188	1.5	
	NpO <sub>2</sub> <sup>2+</sup>	$E_{a1} = 59$	142	1.25	
PuO <sub>2</sub> <sup>+</sup>	$E_{a1} = 152$	208	1.75		
PuO <sub>2</sub> <sup>2+</sup>	$E_{a1} = 89$	164	0.75		

In the case of the reaction shown in Figure 4.5, the energy barrier between panels A and B is quite large (125 kJ/mol). As such, the concentration of the inner-sphere complex remains negligible over time if the tested pathway of structural change is assumed. This reaction, along with others, were tested over time periods of up to 15 s and for reactions with  $E_a$  values larger than ~100 kJ/mol, the transitions are prohibitively slow at standard temperature conditions. This varies somewhat with the distance between the energy minima ( $x$ ), which affects the attempt frequency

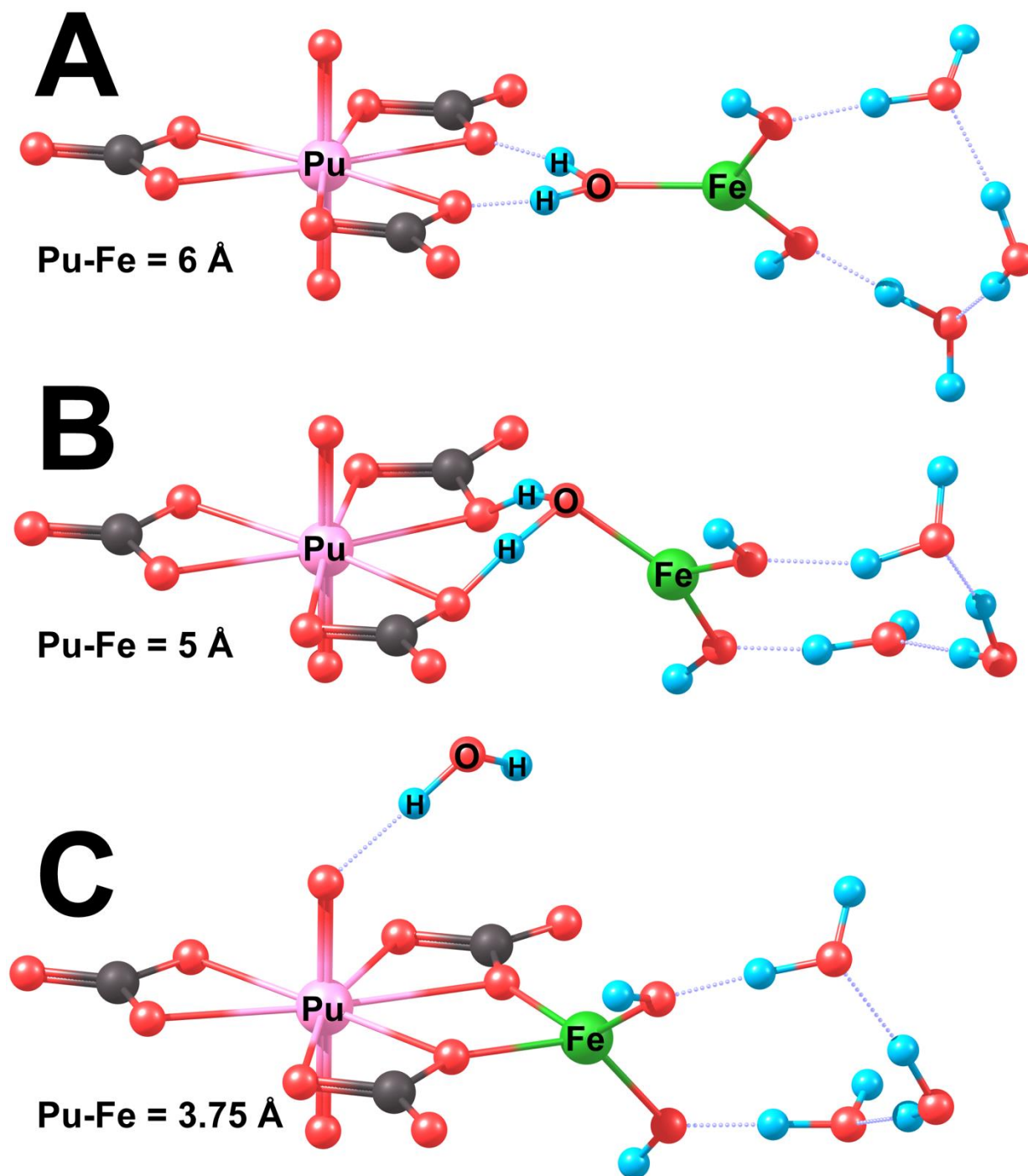


**Figure 4.5** Panels A, B, and C show the approach of an  $[\text{Fe}(\text{OH})_2(\text{H}_2\text{O})_4]^0$  cluster towards  $[\text{PuO}_2(\text{CO}_3)_3]^{5-}$  at Pu-Fe distances of 6, 4, and 3.75 Å, respectively. These distances correspond to an outer-sphere complex (A), and inner-sphere complex (C), and a transition state between them (B). A water molecule forms a hydrogen bond to two carbonate groups in panel C, but in the transition to the inner-sphere complex this molecule is squeezed up out of the x-y plane which holds the carbonate groups, Pu, and Fe. In panel C, this molecule is now hydrogen bonded to one of the plutonyl O atoms. The energy cost associated with breaking the water hydrogen bonds the main source of the  $E_a$  between the outer- and inner-sphere complex.

as shown in Equation 4.5, but this cutoff value encompasses the majority of the data. The change in concentration of the different complex configurations (bulk solution, outer-sphere and inner-sphere) is shown in Figure 4.6 for the reactions of monovalent and divalent uranyl tricarbonate and their reactions with incoming  $\text{Fe}^{2+}$ . The calculated concentration changes show that for  $\text{UO}_2^+$  (Figure 4.6A) the outer-sphere complex is rapidly consumed due to the relatively low energy barrier for inner-sphere complex formation. In the case of  $\text{UO}_2^{2+}$  (Figure 4.6B), the kinetic barriers are such that the outer-sphere complex is more slowly converted into the inner-sphere complex configuration over time.

Large activation energy barriers also exist in reactions with incoming  $\text{H}_2\text{S}$ . In these reactions, the molecules initially move in a similar fashion to the  $\text{Fe}^{2+}$  calculations, but after a

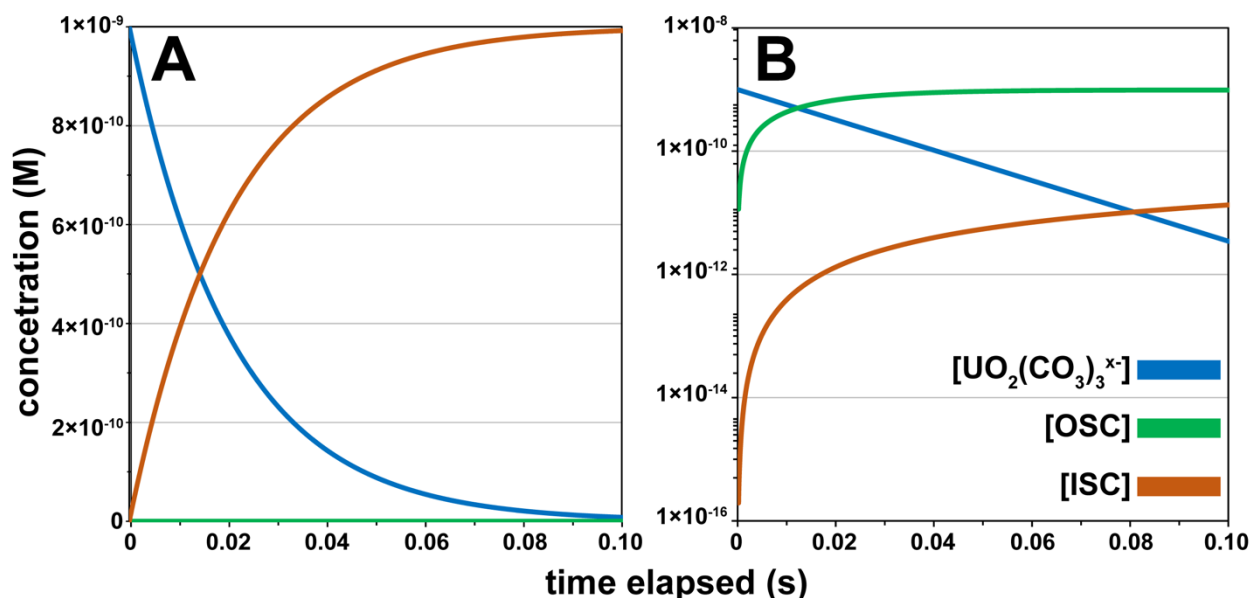


**Figure 4.6** Panels A and B show the change in concentration of bulk aqueous uranyl tricarbonate along with inner- and outer-sphere complexes (OSC and ISC) with  $[\text{Fe}(\text{OH})_2(\text{H}_2\text{O})_4]^0$  over time starting from initial bulk uranyl and iron complex concentrations of 1 nM and 1  $\mu\text{M}$ , respectively. The reaction with  $\text{UO}_2^+$  in panel A has a small energy barrier for the formation of the ISC and, as such, the aqueous complex is rapidly converted to the ISC with no appreciable pool of OSC forming over time. The reaction of  $\text{UO}_2^{2+}$  on the other hand has an activation energy large enough to allow for relatively rapid build up of the OSC followed by a slower increase in the concentration of the ISC. The concentrations in panel B are shown on a log scale to better capture the large concentration range.

proton is transferred from H<sub>2</sub>S to form bicarbonate, the (bi)carbonate groups begin to experience significant electrostatic repulsion. As HS<sup>-</sup> gets closer to the actinyl, water molecules move out of the x-y plane as the Fe-coordinating waters did in Figure 4.5. However, within An-S distances of ~4.75 Å, the (bi)carbonate groups begin to bend and rotate out of this plane to position their O atoms further from HS<sup>-</sup>. There is a significant energy cost associated with this disruption of the actinyl coordination environment. These changes to the geometry, along with breaking and forming of different hydrogen bonds between water and (bi)carbonate, are the source of the energy barriers in these reactions. The carbonate groups around the actinyl molecules can show extreme disruption from their initial equatorial configuration, tilting by up to ~70° out of the x-y plane when HS<sup>-</sup> is brought to its closest distances. In all of these inner-sphere configurations, the two (bi)carbonate groups that have been split by the incoming bisulfide switch to monodentate coordination of the actinyl and the overall coordination of the actinide drops from 6 to 5. Surprisingly, the energies of these inner-sphere complex geometries, where An is directly coordinated by S are energetically favorable compared to the outer-sphere complexes. However, some, like the reactions with NpO<sub>2</sub><sup>+</sup> and PuO<sub>2</sub><sup>+</sup>, are kinetically prohibited given the large activation barriers (see Table 4.3).

In nearly all reactions, the inner-sphere configuration represents the minimum for the system (see Figure 4.3). The one exception is the reaction of UO<sub>2</sub><sup>2+</sup> tricarbonato with H<sub>2</sub>S, which has an outer-sphere complex that is 20 kJ/mol more favorable than the inner-sphere configuration. This is due to bending of (bi)carbonate out of the plane and a relatively unfavorable H bonding network, specifically, with no H bonds formed to the actinyl O as is observed in other H<sub>2</sub>S reactions. The energy gains associated with inner-sphere complex formation come from changes to the physical structure (*i.e.* hydrogen bonding and An coordination) and are not due to significant

changes in the electronic structure of the system (*i.e.* electron transfer from  $\text{Fe}^{2+}$  or  $\text{HS}^-$  to the  $\text{An}^{5+/6+}$ ). In every one of the tested reaction paths, population analysis of the atomic charge and spin reveals that the oxidation states of the actinides, and reductants, are preserved throughout the reactions. The ferromagnetic spin configuration, which orients all of the unpaired electrons in the same direction (upward spin), can allow transfer of minority spin electrons (downward spin) electrons while preserving the overall spin multiplicity of the system. This result is surprising given that it suggests that the reduction of  $\text{An}^{6+}$  to  $\text{An}^{5+}$  by  $\text{Fe}^{2+}$  or  $\text{H}_2\text{S}$  is not guaranteed even if the kinetic barriers to inner-sphere complex formation have been overcome.

### ***Testing of proton-coupled electron transfer as a mechanism for actinyl reduction***

Prior work on plutonyl pentaquo complexes<sup>41</sup> and another computational study of uranyl tricarbonate<sup>38</sup> have found that proton-coupled electron transfer (PCET) may be a critical step in the reduction of actinyl species. Since no spontaneous proton transfer (PT) to actinyl O was observed in the reaction paths described above, some further investigation of post-PT structures, where the proton was moved manually, was carried out to see if this would trigger electron transfer (ET). This subset of calculations used a representative inner-sphere complex geometry of uranyl and plutonyl tricarbonate with  $\text{Fe}^{2+}$  ( $\text{An-Fe} = 3.75 \text{ \AA}$ ) as a starting point. This geometry was selected because it represents the minimum energy distance from our calculations and rates of inner-sphere ET are known to be faster versus the outer-sphere for  $\text{Fe}^{2+}$  reactions with uranyl species.<sup>31,38,68</sup> The system was made charge-neutral by adding four protons to the  $[\text{AnO}_2(\text{CO}_3)_3]^{4-} - [\text{Fe}(\text{OH})_2(\text{H}_2\text{O})_4]^0$  system. These protons were placed on the two hydroxide groups (to form two additional explicit water molecules) and the two carbonate groups closest to Fe to create two  $\text{HCO}_3^-$ . Different post-PT geometries were then tested to see what PT mechanism was most energetically favorable and to explore if these changes to the geometry are accompanied

by reduction of the actinyl. Proton transfer from bicarbonate and water was tested and protonation of a single and both actinyl O was explored. Additionally, ferromagnetic and antiferromagnetic (where Fe is spin up and the An is spin down) spin configurations were tested to see if this had an impact on the energetics of the reaction and behavior of the Gaussian code in assigning spins in the system.

We determine that for uranyl, the PT with or without ET process is very selective with only one of the tested pathways yielding exothermic PCET. This reaction corresponds to a ferromagnetic system where the spin multiplicity of the pre-ET and post-ET models is not the same (multiplicity increase from 5 to 7 for the post-ET state with  $U^{5+}$  and  $Fe^{3+}$ ) and a single proton is transferred from bicarbonate. The reaction energy ( $\Delta E$ ) of this process is -2.5 kJ/mol. Several other PT pathways also resulted in reduction of  $U^{6+}$  to  $U^{5+}$ , but they are all endothermic with  $\Delta E$  values ranging between 20 and 207 kJ/mol. For the uranyl complexes, reaction energies are lower when  $H^+$  is transferred from bicarbonate ( $\Delta E = -2.5-24$  kJ/mol) versus water ( $\Delta E = 56-207$  kJ/mol). The most unfavorable reactions correspond to the transfer of two  $H^+$  each from a different water molecule to protonate both actinyl O atoms. In reactions that do show reduction, the net spin on U changes from 0 to 1.1 as expected for a transition from  $U^{6+}$  with no unpaired electron to  $U^{5+}$  with one; the Fe spin increases from  $\sim 3.7$  ( $\equiv Fe^{2+}$  with 4 upward spins) to  $\sim 4.4$  ( $\equiv Fe^{3+}$  with 5 upward spins). Representative pre- and post-PCET structures with projected spin densities on U and Fe are presented in Figure 4.7. Aside from the one exothermic reaction, the other pathways that record ET have higher reaction energies ( $\Delta E = 20-207$  kJ/mol) compared to PT reactions without ET ( $\Delta E = 8-16$  kJ/mol). An example is the transfer of a single proton from  $HCO_3^-$  with an antiferromagnetic spin configuration (*i.e.* no change in multiplicity of the system pre- and post-ET). This reaction did not cause ET, but had a relatively low reaction energy of 16 kJ/mol. Proton

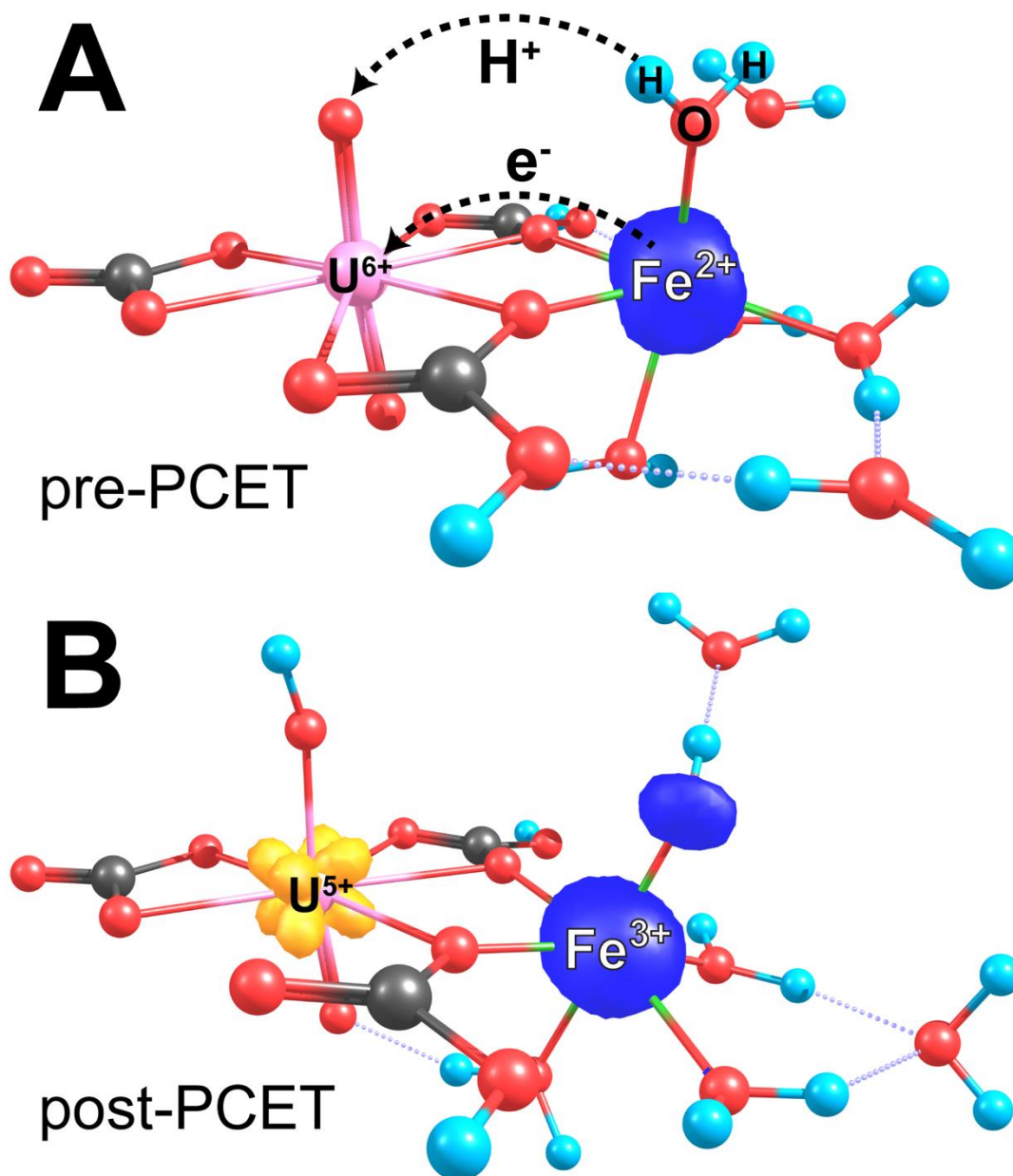


**Figure 4.7** Structures of a charge-neutral  $[\text{FeUO}_2\text{CO}_3(\text{HCO}_3)_2(\text{H}_2\text{O})_6]^0$  inner-sphere complex before (A) and after (B) a proton-coupled electron transfer (PCET) reaction. This particular reaction has a  $\Delta E = 56$  kJ/mol. Alpha (blue) and beta (yellow) spin density are shown overlain on the structure and clearly describe the transition from a  $\text{U}^{6+}/\text{Fe}^{2+}$  to  $\text{U}^{5+}/\text{Fe}^{3+}$  electronic state. The overall spin multiplicity of the system is preserved as  $\text{U}^{5+}$  takes on beta (downward) spin orientation. The  $\text{H}^+$  is transferred from a water molecule to the uranyl O at the top of the structure and causes the  $\text{U}-\text{O}_{\text{ax}}$  bond to lengthen from 1.8 to 2.0 Å. The remaining  $\text{U}-\text{O}$  double bond also lengthens, to 1.87 Å, with reduction to  $\text{U}^{5+}$ .

transfer from a water molecule to create OH<sup>-</sup>, similar to the PCET reaction observed in prior calculations of plutonyl hydrolysis complexes<sup>41</sup>, results in reduction of U<sup>6+</sup> by Fe<sup>2+</sup>, but has an endothermic reaction energy of 57 kJ/mol. In order to test how much of an electric field gradient would be required to “help” in the electron transfer process, a small subset of these UO<sub>2</sub><sup>2+</sup> inner-sphere complex structures were tested with an applied electric field. This field was approximately parallel to the line connecting Fe and U (the x axis of our system) and was set to pull electron density from the Fe<sup>2+</sup> to the actinyl to see if ET was possible without PT. It was found that while eventually the system did reduce U<sup>6+</sup> to U<sup>5+</sup>, the electric field strength required (0.0125 atomic units) is relatively high and reflects the ability of carbonate to effectively shield actinyl molecules from reductants.

For the PuO<sub>2</sub><sup>2+</sup> tricarbonato complex, the same pre- and post-PT configurations were tested. The PCET reactions are more likely to be energetically-favorable and reduction of Pu<sup>6+</sup> to Pu<sup>5+</sup> occurred in nearly all cases where one or two protons are transferred. Reaction energies for the tested PCET reactions range between -5 and 172 kJ/mol (spin on Pu increasing from ~2.5 to ~3.6 indicating reduction to Pu<sup>5+</sup>). The only reaction that does not yield ET is the transfer of one H<sup>+</sup> from HCO<sub>3</sub><sup>-</sup> with a ferromagnetic spin arrangement ( $\Delta E = 120$  kJ/mol). Two of the tested PT mechanisms resulted in negative reaction energies: transfer of one H<sup>+</sup> from a water molecule and transfer of two H<sup>+</sup> from two bicarbonates. Both of these reactions have antiferromagnetic spin configurations where multiplicity is conserved after ET (Fe spin up and Pu spin down) and have comparable reaction energies of -5 kJ/mol. The spread in reaction energies is similar to that of uranyl, but with far more PT reaction pathways resulting in ET ( $\Delta E$  values between -5 and 171 kJ/mol). Broadly, the reaction energies of PT and PCET for plutonyl are lower than those of equivalent uranyl reactions.

## Discussion

The calculations in this study build upon a methodology that was initially applied to the reactions of  $\text{Fe}^{2+}$ ,  $\text{Fe}^{3+}$ , and hydroxyl radical with monovalent and divalent plutonyl hydrolysis complexes without carbonate ligands.<sup>41</sup> The results presented here are the first fully quantum-mechanical treatment of actinyl tricarbonate reactions with  $\text{Fe}^{2+}$  and  $\text{H}_2\text{S}$  using a mixture of discrete water molecules and a dielectric continuum model to treat solvation. The calculations evaluate changes to the complex structures and the associated energy barriers over the selected reaction path. A number of phenomena captured in these calculations are in agreement with prior work on plutonyl.<sup>41</sup> For example, the energy gains and losses associated with changing the H bonding networks of colliding complexes are one of the major factors in the overall energetics of the reaction process. Indeed, in the reactions with  $\text{Fe}^{2+}$ , the energy changes are fully due to the arrangement of the  $\text{H}_2\text{O}$  and  $\text{OH}^-$  in the system and changes to the H bonding networks between them and eventually to the carbonate and/or actinyl O atoms. In the reactions with  $\text{H}_2\text{S}$ , the systems respond somewhat different as the reductant molecule eventually deprotonates to form  $\text{HS}^-$  and  $\text{HCO}_3^-$ . The energy barriers present in these reactions, while of similar magnitudes to the reactions with  $\text{Fe}^{2+}$ , are partly related to the significant disturbance of the (bi)carbonate molecules from their initial orientation caused by the approach of the negatively-charged species,  $\text{HS}^-$ . The rotation of these carbonates and their bending out of the equatorial plane imposes significant energy penalties on the system that are only partially recovered by the formation of new H bonds and the eventual coordination of  $\text{An}^{5+/6+}$  directly by  $\text{HS}^-$  in the inner-sphere complex geometries ( $\text{An-S} = 3\text{-}3.5 \text{ \AA}$ ).

The activation energy barriers calculated for the tricarbonate complexes are larger than those for plutonyl hydrolysis complexes, which had a maximum  $E_a$  value for the forward reaction of 46 kJ/mol when using the C-PCM solvation model.<sup>41</sup> The coordination environments of the

hydrolysis complexes, which consist of  $\text{OH}^-$  and  $\text{H}_2\text{O}$ , are apparently much more easily reorganized during the collision of an incoming reactant to form an inner-sphere complex. Coordination by carbonate, particularly three carbonate molecules which form a complete ring around the actinide center, represent a much more rigid complex geometry that is much harder to disrupt. As such, the calculated activation energies for these complexes are significantly higher (see Table 4.3). From this, it is reasonable to infer that actinyl complexes with a one or two carbonate molecules might have faster kinetics for inner-sphere complex formation with various reductants.

In this study, reduction of actinyls by the two tested reductants is not observed. Population analysis of atomic charge and spin, as well as  $\text{An-O}_{\text{ax}}$  bond lengths, do not indicate electron transfer from  $\text{Fe}^{2+}$  or  $\text{H}_2\text{S}/\text{HS}^-$  to either  $\text{An}^{6+}$  or  $\text{An}^{5+}$ . In our prior study of plutonyl hydrolysis complexes, reduction of  $\text{Pu}^{6+}$  to  $\text{Pu}^{5+}$  by  $\text{Fe}^{2+}$  is coincident with the formation of the inner-sphere complex and PT from coordinating water to one of the actinyl O atoms.<sup>41</sup> In another computational study<sup>38</sup>, the redox reactions of a ternary complex of  $\text{UO}_2^{2+}$  tricarboxylate with two  $\text{Fe}^{2+}$  were explored using a combination of atomistic molecular dynamics and quantum-mechanical calculations. The structure of this complex, with the formula  $[\text{Fe}_2\text{UO}_2(\text{CO}_3)_3(\text{H}_2\text{O})_8]^0$ , is analogous to other actinyl tricarboxylate complexes with two counter ions.<sup>10,21-22</sup> Each  $\text{Fe}^{2+}$  in this structure is coordinated by two carbonate groups and four water molecules. The positioning of the  $\text{Fe}^{2+}$  in this configuration is the most energetically-favorable configuration in Wander, et al.<sup>38</sup> and is the same as the Fe position chosen for the collision trajectory in our models (see Figure 4.5C for an example). A PCET mechanism wherein a proton from water is transferred to create bicarbonate is thermodynamically- and kinetically-favorable for the reduction of  $\text{U}^{6+}$  to  $\text{U}^{5+}$  via a sequential reaction pathway (where ET and PT are considered as separate steps). Further reduction to  $\text{U}^{4+}$  by

the second  $\text{Fe}^{2+}$  required significant structural reorganization and resulted in unfavorable reaction thermodynamics and kinetics.

With unlimited time and computational power, the most rigorous treatment of these systems would be accomplished via a quantum-mechanical molecular dynamics (MD) simulations using a large number of explicit solvent molecules in addition to a dielectric continuum surrounding them. This approach would capture the dynamic process of  $\text{H}^+$  transfer and a large number of solvent molecules would present multiple pathways for shuttling the proton and/or electron through the system. This is, however, very computationally expensive. In this study, we opted for static quantum-mechanical calculations with a modest number of explicit solvent molecules for the first coordination shell and representing the rest of the solvation with the C-PCM model. This approach allows explicit water to move about during geometry optimization (including positions where they may serve as  $\text{H}^+$  donors) and for the solvation energies to be, at least partially, recovered by the dielectric continuum model. Spontaneous transfer of protons is observed in the calculations with  $\text{H}_2\text{S}$  to form bicarbonate. In prior work on plutonyl hydrolysis complexes<sup>41</sup> using the same computational scheme, PCET from  $\text{Fe}^{2+}$  to reduce  $\text{Pu}^{6+}$  is observed with  $\text{H}^+$  donation from  $\text{H}_2\text{O}$  to a plutonyl O. In the current study, spontaneous PCET from  $\text{H}_2\text{S}/\text{HS}^-$  and  $\text{Fe}^{2+}$  is not observed over any of the tested distance series. Instead, manual placement of a proton, from either bicarbonate or water, on an actinyl O is required to induce electron transfer from  $\text{Fe}^{2+}$ . In the tested cases for the uranyl and plutonyl complexes, the systems are selective for specific PCET pathways: the transfer of  $\text{H}^+$  from  $\text{HCO}_3^-$  to actinyl O in the case of uranyl and transfer of  $\text{H}^+$  from  $\text{H}_2\text{O}$  for plutonyl. These pathways represent a minority of the tested configurations; the other mechanisms are endothermic and/or did not yield electron transfer. In comparison, the study by Wander, et al.<sup>38</sup> finds energetically- and kinetically-favorable PCET

from  $\text{Fe}^{2+}$  to reduce  $\text{UO}_2^{2+}$  in a ternary complex with three carbonates and a second  $\text{Fe}^{2+}$ . This second  $\text{Fe}^{2+}$  in their study causes significantly more reducing power and represents a system with more dissolved Fe. Additionally, the treatments of the solvent, water, are different. Our model mixes explicit water and hydroxide with a dielectric model, C-PCM, compared to explicit hydration in vacuum in Wander, et al. <sup>38</sup>. Although more explicit water molecules are used in the study of the ternary  $\text{Fe}^{2+}$  complex, the water may be unphysically constrained to the  $\text{Fe}^{2+}$  and carbonate because of the vacuum approach. This could influence the energy of  $\text{H}^+$  transfer to  $\text{CO}_3^-$  because the molecule is not satisfied by any form of explicit or implicit solvation (*i.e.*, C-PCM). This potential overestimation of the energy gain associated with PT may also affect the calculated kinetics of the PCET process. Our approach seeks to find a middle ground between a fully quantum-mechanical MD approach and a static calculation in vacuum. By using the C-PCM implicit hydration scheme in our models, in addition to a modest number of explicit water molecules, we should be able to capture more realistic system energies versus calculations conducted with explicit hydration alone. The C-PCM model allows coordinating water molecules to move within the system. This behavior results in spontaneous PT from  $\text{H}_2\text{S}$  to carbonate and H bonding of water to actinyl O in a number of the models. However, PCET to the actinyls is not observed without the manual transfer of water or bicarbonate  $\text{H}^+$  to actinyl O.

The calculated energetics of these PT and PCET reactions with the manually-adjusted uranyl and plutonyl inner-sphere complexes with  $\text{Fe}^{2+}$  are consistent with the relative electron affinities of  $\text{U}^{6+}$  and  $\text{Pu}^{6+}$ .<sup>69</sup> Notably, our systems show that protonation of one or two carbonate groups alone does not result in ET as was observed by Wander, et al. <sup>38</sup>; only PT to the actinyl O can cause reduction of  $\text{An}^{6+}$  to  $\text{An}^{5+}$ . This finding is supported by our previous work on the reaction of  $[\text{PuO}_2(\text{OH})_2(\text{H}_2\text{O})_3]^0$  with  $[\text{Fe}(\text{OH})_2(\text{H}_2\text{O})_4]^0$  where PT to actinyl O from coordinating water

resulted in reduction of Pu<sup>6+</sup> to Pu<sup>5+</sup> by Fe<sup>2+</sup>.<sup>41</sup> The computational approach taken here should be capable of capturing a PCET process if one is energetically favorable. Since the vast majority of the tested PT pathways do not appear to be energetically favorable it is understandable that our optimizations did not spontaneously arrive at the post-PT and/or post-ET atomic and electronic configurations.

The formation of inner-sphere complexes of [Fe(OH)<sub>2</sub>(H<sub>2</sub>O)<sub>4</sub>]<sup>0</sup> and [H<sub>2</sub>S(H<sub>2</sub>O)<sub>6</sub>]<sup>0</sup> with AnO<sub>2</sub><sup>+</sup> and AnO<sub>2</sub><sup>2+</sup> tricarbonate complexes is slow for a majority of the tested reactions. Some reactions even show prohibitively-large E<sub>a</sub> values for inner-sphere complex formation. Reactions with energy barriers larger than ~100 kJ/mol have typically very slow kinetics of inner-sphere complex formation and increase concentration of the outer-sphere complex over time, similar to the course of the ISC curve over time in Figure 4.6A. The approach of HS<sup>-</sup> and the reorganization of tightly-bound OH<sup>-</sup> around Fe<sup>2+</sup> as the An-reductant distance is decreased result in energetically-unfavorable geometries corresponding to the transition states between the energy minima of the outer- and inner-sphere complexes. Since the inner-sphere complexes represent the global energy minimum in all cases except for UO<sub>2</sub><sup>2+</sup> reaction with H<sub>2</sub>S, it is possible that the E<sub>a</sub> could be lower for a number of these transitions. Models with more explicit water (ideally a quantum-mechanical MD calculation with more H<sub>2</sub>O and a surrounding dielectric fluid which is computationally intensive) would likely be able to lessen the impact of one or two H bonds breaking during a given distance step. As such, it is important to consider the kinetic parameters presented in Table 4.3 as values that represent one specific reaction path and corresponding structural response. The behavior of the explicit solvent molecules in the models is semi-random and will be different if the trajectory of the incoming reactant is changed. Performing replicate distance series calculations and averaging the results may be a way to work towards a more statistically-relevant and robust

measure of the  $E_a$  for a given reaction, but that would require significant computational effort that is beyond the scope of this study.

Direct evaluation of the calculated parameters in this study with other computational or experimental data is a challenge as no data for these reactions of uranyl, neptunyl, and plutonyl exist at this time. The rates of formation and conversion between different outer- and inner-sphere complexes can be determined analytically, but traditional colorimetric methods require that the different analyte complexes are distinctly colored.<sup>70-71</sup> These methods can be applied to a range of different metal complexes, but are generally more appropriate for highly-conjugated organic ligands that absorb in the visible spectrum. As time-resolved infrared and x-ray spectroscopy methods develop further, it may eventually be possible to characterize the formation of different complex *in situ* based on bond distances, vibrational modes, and oxidation state changes.<sup>72-74</sup> However, if the time scales of these reactions are very fast it may be beyond the resolution of these approaches and necessitate computational treatment.

The results of this study support the understanding that actinyl tricarbonate complexes are more resistant to reduction than water or hydrolysis complexes.<sup>37</sup> This is in agreement with a wide array of experimental studies that have investigated the ability of actinyl molecules to participate in sorption and heterogeneous redox reactions on mineral surfaces. The formation of actinyl tricarbonate complexes is dependent on a sufficiently high  $\text{CO}_3^{2-}$  concentrations and  $\text{pH} > 8$ . At this pH, many minerals are very close to or above their points of zero charge.<sup>75-76</sup> While sorption of positively-charged actinyls and their complexes in carbonate-free solutions is strong at elevated pH, the opposite effect is observed when negatively-charged carbonate complexes are present. Increasing pH and carbonate concentrations diminish the formation of various ternary actinyl-carbonate inner-sphere complexes on a wide range of mineral surfaces including Fe<sup>35,39-40,77</sup> and

Mn<sup>78</sup> (oxyhydr)oxides, and silicate minerals (including clays).<sup>79-80</sup> Decreased propensity for inner-sphere complex formation also lowers the likelihood of heterogeneous ET reactions that can reduce actinides to their less-soluble An<sup>4+</sup> state on minerals containing electron donors like Fe<sup>2+</sup>.<sup>81-82</sup> Based on the calculations of homogeneous reactions in this study, it appears that carbonate complexation also serves to protect these species even if reductants like Fe<sup>2+</sup> and H<sub>2</sub>S are present as dissolved components in solution. With minimal sorption to mineral surfaces and slow kinetics of inner-sphere complex formation and PCET, most AnO<sub>2</sub><sup>+</sup> and AnO<sub>2</sub><sup>2+</sup> tricarbonato complexes likely remain highly-mobile species at elevated pH conditions.

## Conclusions

This work indicates that homogeneous electron transfer (ET) from Fe<sup>2+</sup> and H<sub>2</sub>S to AnO<sub>2</sub><sup>2+</sup> and AnO<sub>2</sub><sup>+</sup> tricarbonato complexes is unlikely to proceed without the transfer of a proton (or two) to the actinyl O atoms. While carbonate is known to impede the reduction of uranyl in heterogeneous reactions at electrode surfaces, it was expected that there would be some evidence for ET if the reductant is brought into close enough proximity to the actinyl. Neptunyl and plutonyl, which preferentially form monovalent actinyl species in most aqueous settings<sup>83-84</sup>, are stabilized as An<sup>6+</sup> in the presence of these two reductants. The reduction of An<sup>5+</sup> to An<sup>4+</sup> involves significant reorganization of the local coordination environment (increase in CN from 5 to 7 or 8) and it has been calculated that this process is energetically-unfavorable and will not proceed with Fe<sup>2+</sup> as the electron donor.<sup>31-32,38</sup> Our calculations support and provide further evidence for the understanding that carbonate can stabilize higher-valent actinides and prevent reduction to the more insoluble An<sup>4+</sup> state, particularly under higher pH conditions where sorption to mineral surfaces is less prevalent.

The calculated rates of collision (encounter complex formation) and transition from outer- to inner-sphere complex reveal that the formation of outer-sphere complexes is energetically-favorable and the rate is largely dependent on the diffusion velocities of both reactants and the concentration of the less abundant species. Even at very low actinyl concentrations (nM and pM) the reaction to form the outer-sphere complex between an actinyl tricarbonates and  $[\text{H}_2\text{S}(\text{H}_2\text{O})_6]^0$  or  $[\text{Fe}(\text{OH})_2(\text{H}_2\text{O})_4]^0$  is expected to proceed rapidly with nearly all of the actinyl species consumed over a time period on the order of seconds. After that, the conversion to the inner-sphere complex, which should increase the likelihood of ET, is highly-sensitive to changes in the H bonding environment of the first solvation shell. Differences in the H bonding networks between  $\text{H}_2\text{O}$ ,  $\text{OH}^-$ , and (bi)carbonate yield a wide range of  $E_a$  values for different reactant pairs. The variability in the calculated energy barriers appears to be somewhat random and dependent on the trajectory of just a few water molecules in the system.

The results of this study highlight the need for further investigation and testing of the appropriate computational approaches for calculating reactions in which proton-coupled electron transfer (PCET) may be a key pathway for reduction. In some cases, a geometry optimization calculation may capture PCET without specific user inputs nudging the geometry towards this reaction pathway.<sup>41</sup> In other cases, like the calculations presented here, manual placement of  $\text{H}^+$  on the actinyl O atoms is required for reduction of  $\text{An}^{6+}$  to  $\text{An}^{5+}$  to occur. No reduction is observed spontaneously in any of the reactions of uranyl, neptunyl, or plutonyl tricarbonate complexes when hydration is modeled with explicit water and C-PCM. Exploration of different post-PT structures indicate that this process can yield thermodynamically-favorable one electron reduction of  $\text{An}^{6+}$  to  $\text{An}^{5+}$ ; however, not all pathways are energetically favorable or accompanied by ET. Simulating an

electric field to pull electron density towards the actinyl molecule from the reductant yielded ET without PT, but the field strength required is relatively high.

In future work, it may be beneficial to consider how the computational methodology may be altered to permit more solvent molecules to be included explicitly in the model. These sort of calculations may be an excellent candidate for the use of a hybrid quantum mechanics/molecular mechanics (QM/MM) approach that allows a certain subset of the atoms or molecules to be treated at the more robust quantum-mechanical level, while the rest of the system, perhaps including several higher order shells of explicit solvent molecules, is treated with a reactive atomistic reactive force field approach that allows for donating and accepting protons.<sup>85</sup> In this way, the redox process between a given reactant pair could be explored in detail while including a large number of explicit solvent molecules that provide a buffer for the energy changes associated with reorganization of a H bonding network. Having a large number of solvent molecules available around, for example, the actinyl tricarbonato complex may also aid the system's ability to capture PCET pathways that are not observed in our calculations, as proton donors would be nearby and the improbable "hopping" of a proton from a bicarbonato or an Fe<sup>2+</sup>-coordinating water molecule would not be required.

Overall, much of the chemical behavior of actinyl (tri)carbonato complexes remains to be explored in both experimental and computational settings. Adsorption of these complexes to a range of different mineral surfaces under different solution conditions has been studied.<sup>35,73,78,80,86-88</sup> Broadly, it can be said that at high pH, the negatively-charged bi- and tricarbonato complexes of actinyls are less likely to sorb to a wide range of mineral phases with negatively-charged surfaces (*i.e.* above their points of zero charge). Heterogeneous reactions of these complexes dominate at lower pH where they adsorb, strongly in some cases, to mineral

surfaces which may contain possible electron donors like  $\text{Mn}^{2+}$  and  $\text{Fe}^{2+}$ .<sup>36,81,89-90</sup> The homogeneous reactions of the actinyl carbonate complexes appear to require the PCET mechanism in order for reduction to occur.<sup>31,38</sup> This process is likely more challenging at higher pH conditions where systems are relatively proton-poor.

The calculated reaction kinetics presented here suggest that inner-sphere complex formation between actinyls and  $\text{Fe}^{2+}$  and  $\text{H}_2\text{S}$ , and PCET, is kinetically and, in some cases, thermodynamically inhibited by carbonate complexation. In a number of reactions, the transition from outer- to inner-sphere complex appears to be the rate-limiting step for the homogeneous reduction of these actinide species. With this in mind, these reactions may be good candidates for receiving assistance from a mediating mineral surface. In the future, a modified version of the computational approach used in this study could be used to investigate the role of a mineral surface in lowering energy barriers associated with decomplexation, decarbonation, and/or dehydration during the formation of inner-sphere complexes. While eventually it may be feasible to perform quantum-mechanical molecular-dynamics calculations on large systems with many solvent molecules, for now applying the sequential reactant distance series approach of this work to heterogeneous reactions could be a relatively straightforward means of learning more about these processes on a fundamental level. Combining these calculations with Marcus Theory, as has been applied to homogeneous<sup>31,38,68</sup> and heterogeneous<sup>91-93</sup> reactions of actinide complexes, would allow for a complete description of the kinetics of these processes. These approaches warrant further testing and application to actinide complexes and other contaminants of interest and can serve to support experimental findings and their interpretation.

## **Acknowledgements**

This research was supported by funding from the U.S. Department of Energy's (DOE) Office of Science, Office of Basic Energy Sciences (BES), Chemical Sciences, Geosciences, & Biosciences (CSGB) Division for the topics of Heavy Element Chemistry and Geoscience (grant number DE-FG02-06ER15783). The calculations for this study were carried out in part on the Flux high-performance computing cluster managed by University of Michigan Advanced Research Computing Technology Services (ARC-TS).

## References

1. Maher, K.; Bargar, J. R.; Brown, G. E., Environmental speciation of actinides. *Inorganic Chemistry* **2013**, *52* (7), 3510-3532.
2. Geckeis, H.; Lutzenkirchen, J.; Polly, R.; Rabung, T.; Schmidt, M., Mineral-water interface reactions of actinides. *Chemical Reviews* **2013**, *113* (2), 1016-1062.
3. Szabo, Z.; Toraiishi, T.; Vallet, V.; Grenthe, I., Solution coordination chemistry of actinides: Thermodynamics, structure and reaction mechanisms. *Coordination Chemistry Reviews* **2006**, *250* (7-8), 784-815.
4. Newsome, L.; Morris, K.; Lloyd, J. R., The biogeochemistry and bioremediation of uranium and other priority radionuclides. *Chem Geol* **2014**, *363*, 164-184.
5. Neck, V.; Kim, J. I., Solubility and hydrolysis of tetravalent actinides. *Radiochimica Acta* **2001**, *89* (1), 1-16.
6. Clark, D. L.; Hobart, D. E.; Neu, M. P., Actinide carbonate complexes and their importance in actinide environmental chemistry. *Chemical Reviews* **1995**, *95* (1), 25-48.
7. Choppin, G. R., Actinide speciation in the environment. *Journal of Radioanalytical and Nuclear Chemistry* **2007**, *273* (3), 695-703.
8. Djogic, R.; Sipos, L.; Branica, M., Characterization of uranium(VI) in seawater. *Limnology and Oceanography* **1986**, *31* (5), 1122-1131.
9. Docrat, T. I.; Mosselmans, J. F. W.; Charnock, J. M.; Whiteley, M. W.; Collison, D.; Livens, F. R.; Jones, C.; Edmiston, M. J., X-ray absorption spectroscopy of tricarbonatodioxouranate(V),  $\text{UO}_2(\text{CO}_3)_3^{5-}$ , in aqueous solution. *Inorganic Chemistry* **1999**, *38* (8), 1879-1882.
10. Dong, W. M.; Brooks, S. C., Determination of the formation constants of ternary complexes of uranyl and carbonate with alkaline earth metals ( $\text{Mg}^{2+}$ ,  $\text{Ca}^{2+}$ ,  $\text{Sr}^{2+}$ , and  $\text{Ba}^{2+}$ ) using anion exchange method. *Environmental Science & Technology* **2006**, *40* (15), 4689-4695.
11. Geipel, G.; Amayri, S.; Bernhard, G., Mixed complexes of alkaline earth uranyl carbonates: A laser-induced time-resolved fluorescence spectroscopic study. *Spectrochimica Acta Part A - Molecular and Biomolecular Spectroscopy* **2008**, *71* (1), 53-58.
12. Geipel, G.; Bernhard, G.; Brendler, V.; Nitsche, H., Complex formation between  $\text{UO}_2^{2+}$  and  $\text{CO}_3^{2-}$ : Studied by laser-induced photoacoustic spectroscopy (LIPAS). *Radiochimica Acta* **1998**, *82*, 59-62.
13. Kato, Y.; Kimura, T.; Yoshida, Z.; Nitani, N., Carbonate complexation of neptunyl(VI) ion. *Radiochimica Acta* **1998**, *82*, 63-68.

14. Gagliardi, L.; Roos, B. O., Coordination of the neptunyl ion with carbonate ions and water: A theoretical study. *Inorganic Chemistry* **2002**, *41* (5), 1315-1319.
15. Ikeda-Ohno, A.; Tsushima, S.; Takao, K.; Rossberg, A.; Funke, H.; Scheinost, A. C.; Bernhard, G.; Yaita, T.; Hennig, C., Neptunium carbonate complexes in aqueous solution: An electrochemical, spectroscopic, and quantum chemical study. *Inorganic Chemistry* **2009**, *48* (24), 11779-11787.
16. de Jong, W. A.; Apra, E.; Windus, T. L.; Nichols, J. A.; Harrison, R. J.; Gutowski, K. E.; Dixon, D. A., Complexation of the carbonate, nitrate, and acetate anions with the uranyl dication: Density functional studies with relativistic effective core potentials. *Journal of Physical Chemistry A* **2005**, *109* (50), 11568-11577.
17. Grenthe, I.; Ferri, D.; Salvatore, F.; Riccio, G., Studies on metal carbonate equilibria. Part 10. A solubility study of the complex formation in uranium(VI)-water-carbon dioxide (g) system at 25 °C. *Journal of the Chemical Society - Dalton Transactions* **1984**, (11), 2439-2443.
18. De Pablo, J.; Casas, I.; Gimenez, J.; Molera, M.; Rovira, M.; Duro, L.; Bruno, J., The oxidative dissolution mechanism of uranium dioxide. I. The effect of temperature in hydrogen carbonate medium. *Geochimica et Cosmochimica Acta* **1999**, *63* (19-20), 3097-3103.
19. Zhou, P.; Gu, B. H., Extraction of oxidized and reduced forms of uranium from contaminated soils: Effects of carbonate concentration and pH. *Environmental Science & Technology* **2005**, *39* (12), 4435-4440.
20. Hua, B.; Deng, B. L., Reductive immobilization of uranium(VI) by amorphous iron sulfide. *Environmental Science & Technology* **2008**, *42* (23), 8703-8708.
21. Bernhard, G.; Geipel, G.; Reich, T.; Brendler, V.; Amayri, S.; Nitsche, H., Uranyl(VI) carbonate complex formation: Validation of the  $\text{Ca}_2\text{UO}_2(\text{CO}_3)_3(\text{aq.})$  species. *Radiochimica Acta* **2001**, *89* (8), 511-518.
22. Stewart, B. D.; Mayes, M. A.; Fendorf, S., Impact of uranyl-calcium-carbonate complexes on uranium(VI) adsorption to synthetic and natural Sediments. *Environmental Science & Technology* **2010**, *44* (3), 928-934.
23. Duro, L.; Missana, T.; Ripoll, S.; Grive, M.; Bruno, J., Modelling of Pu sorption onto the surface of goethite and magnetite as steel corrosion products. In *Scientific Basis for Nuclear Waste Management XXVII*, Oversby, V. M.; Werme, L. O., Eds. 2004; Vol. 807, pp 659-664.
24. Pearce, C. I.; Rosso, K. M.; Patrick, R. A. D.; Felmy, A. R., Impact of iron redox chemistry on nuclear waste disposal. In *Redox-Reactive Minerals: Properties, Reactions and Applications in Clean Technologies*, Ahmed, I. A. M.; Hudson-Edwards, K. A., Eds. 2017; Vol. 17, pp 229-272.
25. Dodge, C. J.; Francis, A. J.; Gillow, J. B.; Halada, G. P.; Eng, C.; Clayton, C. R., Association of uranium with iron oxides typically formed on corroding steel surfaces. *Environmental Science & Technology* **2002**, *36* (16), 3504-3511.

26. Wersin, P.; Hochella, M. F.; Persson, P.; Redden, G.; Leckie, J. O.; Harris, D. W., Interaction between aqueous uranium(VI) and sulfide minerals - spectroscopic evidence for sorption and reduction. *Geochimica et Cosmochimica Acta* **1994**, *58* (13), 2829-2843.
27. Renock, D.; Mueller, M.; Yuan, K.; Ewing, R. C.; Becker, U., The energetics and kinetics of uranyl reduction on pyrite, hematite, and magnetite surfaces: A powder microelectrode study. *Geochimica et Cosmochimica Acta* **2013**, *118*, 56-71.
28. Moyes, L. N.; Jones, M. J.; Reed, W. A.; Livens, F. R.; Charnock, J. M.; Mosselmans, J. F. W.; Hennig, C.; Vaughan, D. J.; Patrick, R. A. D., An X-ray absorption spectroscopy study of neptunium(V) reactions with mackinawite (FeS). *Environmental Science & Technology* **2002**, *36* (2), 179-183.
29. Scott, T. B.; Tort, O. R.; Allen, G. C., Aqueous uptake of uranium onto pyrite surfaces; reactivity of fresh versus weathered material. *Geochimica et Cosmochimica Acta* **2007**, *71* (21), 5044-5053.
30. Hua, B.; Xu, H. F.; Terry, J.; Deng, B. L., Kinetics of uranium(VI) reduction by hydrogen sulfide in anoxic aqueous systems. *Environmental Science & Technology* **2006**, *40* (15), 4666-4671.
31. Collins, R. N.; Rosso, K. M., Mechanisms and rates of U(VI) reduction by Fe(II) in homogeneous aqueous solution and the role of U(V) disproportionation. *Journal of Physical Chemistry A* **2017**, *121* (35), 6603-6613.
32. Odoh, S. O.; Schreckenbach, G., Theoretical study of the structural properties of plutonium(IV) and (VI) complexes. *Journal of Physical Chemistry A* **2011**, *115* (48), 14110-14119.
33. Wang, Z.; Wagon, K. B.; Ainsworth, C. C.; Liu, C.; Rosso, K. M.; Fredrickson, J. K., A spectroscopic study of the effect of ligand complexation on the reduction of uranium(VI) by anthraquinone-2,6-disulfonate (AH<sub>2</sub>DS). *Radiochimica Acta* **2008**, *96* (9-11), 599-605.
34. Yan, S.; Hua, B.; Bao, Z. Y.; Yang, J.; Liu, C. X.; Deng, B. L., Uranium(VI) removal by nanoscale zerovalent iron in anoxic batch systems. *Environmental Science & Technology* **2010**, *44* (20), 7783-7789.
35. Duff, M. C.; Amrhein, C., Uranium(VI) adsorption on goethite and soil in carbonate solutions. *Soil Science Society of America Journal* **1996**, *60* (5), 1393-1400.
36. Barnett, M. O.; Jardine, P. M.; Brooks, S. C.; Selim, H. M., Adsorption and transport of uranium(VI) in subsurface media. *Soil Science Society of America Journal* **2000**, *64* (3), 908-917.
37. Morris, D. E., Redox energetics and kinetics of uranyl coordination complexes in aqueous solution. *Inorganic Chemistry* **2002**, *41* (13), 3542-3547.

38. Wander, M. C. F.; Kerisit, S.; Rosso, K. M.; Schoonen, M. A. A., Kinetics of triscarbonato uranyl reduction by aqueous ferrous iron: A theoretical study. *Journal of Physical Chemistry A* **2006**, *110* (31), 9691-9701.
39. Kohler, M.; Honeyman, B. D.; Leckie, J. O., Neptunium(V) sorption on hematite ( $\alpha$ -Fe<sub>2</sub>O<sub>3</sub>) in aqueous suspension: The effect of CO<sub>2</sub>. *Radiochim Acta* **1999**, *85* (1-2), 33-48.
40. Wazne, M.; Korfiatis, G. P.; Meng, X. G., Carbonate effects on hexavalent uranium adsorption by iron oxyhydroxide. *Environmental Science & Technology* **2003**, *37* (16), 3619-3624.
41. Bender, W. M.; Becker, U., Determining the kinetics of discrete aqueous redox reaction sub-steps using computational methods: Application to reactions of plutonyl (PuO<sub>2</sub><sup>+2+</sup>) with Fe<sup>2+</sup>, Fe<sup>3+</sup>, and hydroxyl radical ( $\bullet$ OH). *Am J Sci* **2018**, *318*, 893-920.
42. Frisch, M. J.; Trucks, G. W.; Schlegel, H. B.; Scuseria, G. E.; Robb, M. A.; Cheeseman, J. R.; Scalmani, G.; Barone, V.; Petersson, G. A.; Nakatsuji, H.; Li, X.; Caricato, M.; Marenich, A.; Bloino, J.; Janesko, B. G.; Gomperts, R.; Mennucci, B.; Hratchian, H. P.; Ortiz, J. V.; Izmaylov, A. F.; Sonnenber, J. L.; Williams-Young, D.; Ding, F.; Lipparini, F.; Egidi, F.; Goings, J.; Peng, B.; Petrone, A.; Henderson, T.; Ranasinghe, D.; Zakrzewski, V. G.; Gao, J.; Rega, N.; Zheng, G.; Liang, W.; Hada, M.; Ehara, M.; Toyota, K.; Fukuda, R.; Hasegawa, J.; Ishida, M.; Nakajima, T.; Honda, Y.; Kitao, O.; Nakai, H.; Vreven, T.; Throssell, K.; Montgomery, J., J. A.; Peralta, J. E.; Ogliaro, F.; Bearpark, M.; Heyd, J. J.; Brothers, E.; Kudin, K. N.; Staroverov, V. N.; Keith, T.; Kobayashi, R.; Normand, J.; Raghavachari, K.; Rendell, A.; Burant, J. C.; Iyengar, S. S.; Tomasi, J.; Cossi, M.; Millam, J. M.; Klene, M.; Adamo, C.; Cammi, R.; Ochterski, J. W.; Martin, R. L.; Morokuma, K.; Farkas, O.; Foresman, J. B.; Fox, D. J. *Gaussian 09*, Revision A.02; Gaussian, Inc.: Wallingford, CT, 2016.
43. Becke, A. D., Density-functional thermochemistry. III. The role of exact exchange. *Journal of Chemical Physics* **1993**, *98* (7), 5648-5652.
44. Lee, C. T.; Yang, W. T.; Parr, R. G., Development of the Colle-Salvetti correlation-energy formula into a functional of the electron-density. *Phys Rev B* **1988**, *37* (2), 785-789.
45. Wadt, W. R.; Hay, P. J., Ab initio effective core potentials for molecular calculations - potentials for main group elements Na to Bi. *Journal of Chemical Physics* **1985**, *82*, 284-298.
46. Dunning Jr., T. H.; Hay, P. J., Gaussian basis sets for molecular calculations. In *Methods of Electronic Structure Theory*, 1 ed.; Schaefer, H. F., Ed. Springer US: New York, 1977; pp 1-27.
47. Dunning, T. H., Gaussian basis sets for use in correlated molecular calculations. I. The atoms boron through neon and hydrogen. *Journal of Chemical Physics* **1989**, *90*, 1007-1023.
48. Dolg, M.; Wedig, U.; Stoll, H.; Preuss, H., Energy-adjusted *ab initio* pseudopotentials for the first row transition elements. *Journal of Chemical Physics* **1987**, *86* (2), 866-872.
49. Kuchle, W.; Dolg, M.; Stoll, H.; Preuss, H., Energy-adjusted pseudopotentials for the actinides. Parameter sets and test calculations for thorium and thorium monoxide. *Journal of Chemical Physics* **1994**, *100* (10), 7535-7542.

50. Feller, D., The role of databases in support of computational chemistry calculations. *J Comput Chem* **1996**, *17* (13), 1571-1586.
51. Schuchardt, K. L.; Didier, B. T.; Elsethagen, T.; Sun, L.; Gurumoorthi, V.; Chase, J.; Li, J.; Windus, T. L., Basis set exchange: A community database for computational sciences. *Journal of Chemical Information and Modeling* **2007**, *47* (3), 1045-1052.
52. Bader, R. F. W.; Anderson, S. G.; Duke, A. J., Quantum topology of molecular charge distributions. 1. *J Am Chem Soc* **1979**, *101* (6), 1389-1395.
53. Bader, R. F. W.; Nguyendang, T. T.; Tal, Y., Quantum topology of molecular charge distributions. II. Molecular structure and its change. *Journal of Chemical Physics* **1979**, *70* (9), 4316-4329.
54. Reed, A. E.; Weinstock, R. B.; Weinhold, F., Natural population analysis. *Journal of Chemical Physics* **1985**, *83* (2), 735-746.
55. Reed, A. E.; Weinhold, F., Natural localized molecular orbitals. *Journal of Chemical Physics* **1985**, *83* (4), 1736-1740.
56. Ikeda, A.; Hennig, C.; Tsushima, S.; Takao, K.; Ikeda, Y.; Scheinost, A. C.; Bernhard, G., Comparative study of uranyl(VI) and -(V) carbonate complexes in an aqueous solution. *Inorganic Chemistry* **2007**, *46* (10), 4212-4219.
57. Kato, Y.; Meinrath, G.; Kimura, T.; Yoshida, Z., A study of U(VI) hydrolysis and carbonate complexation by time-resolved laser-induced fluorescence spectroscopy (TRLFS). *Radiochimica Acta* **1994**, *64* (2), 107-111.
58. Kerisit, S.; Liu, C. X., Molecular simulation of the diffusion of uranyl carbonate species in aqueous solution. *Geochimica et Cosmochimica Acta* **2010**, *74* (17), 4937-4952.
59. Cossi, M.; Rega, N.; Scalmani, G.; Barone, V., Energies, structures, and electronic properties of molecules in solution with the C-PCM solvation model. *J Comput Chem* **2003**, *24* (6), 669-681.
60. Barone, V.; Cossi, M., Quantum calculation of molecular energies and energy gradients in solution by a conductor solvent model. *Journal of Physical Chemistry A* **1998**, *102*, 1995-2001.
61. Haimour, N.; Sandall, O. C., Molecular diffusivity of hydrogen sulfide in water. *Journal of Chemical and Engineering Data* **1984**, *29* (1), 20-22.
62. Lide, D. R.; Kehiaian, H. V., *CRC handbook of thermophysical and thermochemical data*. CRC Press, Inc.: Boca Raton, 1994; p 518.
63. Kerisit, S.; Liu, C. X., Diffusion and adsorption of uranyl carbonate species in nanosized mineral fractures. *Environmental Science & Technology* **2012**, *46* (3), 1632-1640.

64. Kraus, K. A.; Nelson, F., Chemistry of aqueous uranium(V) solutions. II. Reaction of uranium pentachloride with water. Thermodynamic stability of  $\text{UO}_2^+$ . Potential of U(IV)/(V), U(IV)/(VI) and U(V)/U(VI) couples. *J Am Chem Soc* **1949**, *71* (7), 2517-2522.
65. Kraus, K. A.; Nelson, F.; Johnson, G. L., Chemistry of aqueous uranium(V) solutions. I. Preparation and properties. Analogy between uranium(V), neptunium(V) and plutonium(V). *J Am Chem Soc* **1949**, *71* (7), 2510-2517.
66. Glicksman, M. E., *Diffusion in solids: Field theory, solid-state principles, and applications*. John Wiley & Sons: New York, 1999; p 498.
67. Reich, M.; Ewing, R. C.; Ehlers, T. A.; Becker, U., Low-temperature anisotropic diffusion of helium in zircon: Implications for zircon (U-Th)/He thermochronometry. *Geochimica et Cosmochimica Acta* **2007**, *71* (12), 3119-3130.
68. Privalov, T.; Schimmelpfennig, B.; Wahlgren, U.; Grenthe, I., Reduction of uranyl(VI) by iron(II) in solutions: An ab initio study. *Journal of Physical Chemistry A* **2003**, *107* (4), 587-592.
69. Steele, H. M.; Guillaumont, D.; Moisy, P., Density functional theory calculations of the redox potentials of actinide(VI)/actinide(V) couple in water. *Journal of Physical Chemistry A* **2013**, *117* (21), 4500-4505.
70. Taube, H., *Electron transfer reactions of complex ions in solution*. Academic Press: New York, 1970; p 103.
71. Marcus, R. A.; Sutin, N., Electron transfers in chemistry and biology. *Biochimica et Biophysica Acta - Reviews in Bioenergetics* **1985**, *811* (3), 265-322.
72. Guckel, K.; Rossberg, A.; Muller, K.; Brendler, V.; Bernhard, G.; Foerstendorf, H., Spectroscopic identification of binary and ternary surface complexes of Np(V) on gibbsite. *Environmental Science & Technology* **2013**, *47* (24), 14418-14425.
73. Muller, K.; Groschel, A.; Rossberg, A.; Bok, F.; Franzen, C.; Brendler, V.; Foerstendorf, H., In situ spectroscopic identification of neptunium(V) inner-sphere complexes on the hematite-water interface. *Environmental Science & Technology* **2015**, *49* (4), 2560-2567.
74. Zhu, M. Q.; Legg, B.; Zhang, H. Z.; Gilbert, B.; Ren, Y.; Banfield, J. F.; Waychunas, G. A., Early stage formation of iron oxyhydroxides during neutralization of simulated acid mine drainage solutions. *Environmental Science & Technology* **2012**, *46* (15), 8140-8147.
75. Parks, G. A.; de Bruyn, P. L., The zero point charge of oxides. *The Journal of Physical Chemistry* **1962**, *66* (6), 967-973.
76. Pechenyuk, S. I., The use of the pH at the point of zero charge for characterizing the properties of oxide hydroxides. *Russian Chemical Bulletin* **1999**, *48* (6), 1017-1023.

77. Tinnacher, R. M.; Zavarin, M.; Powell, B. A.; Kersting, A. B., Kinetics of neptunium(V) sorption and desorption on goethite: An experimental and modeling study. *Geochimica et Cosmochimica Acta* **2011**, 75 (21), 6584-6599.
78. Duff, M. C.; Hunter, D. B.; Triay, I. R.; Bertsch, P. M.; Reed, D. T.; Sutton, S. R.; Shea-Mccarthy, G.; Kitten, J.; Eng, P.; Chipera, S. J.; Vaniman, D. T., Mineral associations and average oxidation states of sorbed Pu on tuff. *Environmental Science & Technology* **1999**, 33 (13), 2163-2169.
79. Bertetti, F. P.; Pabalan, R. T.; Almendarez, M. G., Studies of neptunium<sup>V</sup> sorption on quartz, clinoptilolite, montmorillonite, and  $\alpha$ -alumina. In *Adsorption of metals by geomedial*, Jenne, E. A., Ed. Academic Press: San Diego, 1998; pp 132-149.
80. Catalano, J. G.; Brown, G. E., Uranyl adsorption onto montmorillonite: Evaluation of binding sites and carbonate complexation. *Geochimica et Cosmochimica Acta* **2005**, 69 (12), 2995-3005.
81. Begg, J. D.; Edelman, C.; Zavarin, M.; Kersting, A. B., Sorption kinetics of plutonium (V)/(VI) to three montmorillonite clays. *Appl Geochem* **2018**, 96, 131-137.
82. Zhao, P. H.; Begg, J. D.; Zavarin, M.; Tumey, S. J.; Williams, R.; Dai, Z. R. R.; Kips, R.; Kersting, A. B., Plutonium(IV) and (V) sorption to goethite at sub-femtomolar to micromolar concentrations: Redox transformations and surface precipitation. *Environmental Science & Technology* **2016**, 50 (13), 6948-6956.
83. Vallet, V.; Macak, P.; Wahlgren, U.; Grenthe, I., Actinide chemistry in solution, quantum chemical methods and models. *Theoretical Chemistry Accounts* **2006**, 115 (2-3), 145-160.
84. Silva, R. J.; Nitsche, H., Actinide environmental chemistry. *Radiochimica Acta* **1995**, 70 (1), 377-396.
85. Tirler, A. O.; Hofer, T. S., Structure and dynamics of the uranyl tricarbonate complex in aqueous solution: Insights from quantum mechanical charge field molecular dynamics. *Journal of Physical Chemistry B* **2014**, 118 (45), 12938-12951.
86. Bargar, J. R.; Reitmeyer, R.; Davis, J. A., Spectroscopic confirmation of uranium(VI)-carbonato adsorption complexes on hematite. *Environmental Science & Technology* **1999**, 33 (14), 2481-2484.
87. Ho, C. H.; Miller, N. H., Adsorption of uranyl species from bicarbonate solution onto hematite particles. *Journal of Colloid and Interface Science* **1986**, 110 (1), 165-171.
88. Bargar, J. R.; Reitmeyer, R.; Lenhart, J. J.; Davis, J. A., Characterization of U(VI)-carbonato ternary complexes on hematite: EXAFS and electrophoretic mobility measurements. *Geochimica et Cosmochimica Acta* **2000**, 64 (16), 2737-2749.

89. Qafoku, N. P.; Zachara, J. M.; Liu, C. X.; Gassman, P. L.; Qafoku, O. S.; Smith, S. C., Kinetic desorption and sorption of U(VI) during reactive transport in a contaminated Hanford sediment. *Environmental Science & Technology* **2005**, *39* (9), 3157-3165.
90. Singer, D. M.; Chatman, S. M.; Ilton, E. S.; Rosso, K. M.; Banfield, J. F.; Waychunas, G. A., U(VI) sorption and reduction kinetics on the magnetite (111) surface. *Environmental Science & Technology* **2012**, *46* (7), 3821-3830.
91. Taylor, S. D.; Becker, U.; Rosso, K. M., Electron transfer pathways facilitating U(VI) reduction by Fe(II) on Al- vs. Fe-oxides. *Journal of Physical Chemistry C* **2017**, *121* (36), 19887-19903.
92. Taylor, S. D.; Marcano, M. C.; Rosso, K. M.; Becker, U., An experimental and ab initio study on the abiotic reduction of uranyl by ferrous iron. *Geochimica et Cosmochimica Acta* **2015**, *156*, 154-172.
93. Taylor, S. D.; Marcano, M. C.; Becker, U., A first principles investigation of electron transfer between Fe(II) and U(VI) on insulating Al- vs. semiconducting Fe-oxide surfaces via the proximity effect. *Geochimica et Cosmochimica Acta* **2017**, *197*, 305-322.

## CHAPTER 5

### Conclusions

The chapters of this dissertation present the results of three studies that use quantum-mechanical methods to characterize chemical reactions of actinides (An) in geochemical environments. Each chapter develops a new<sup>1</sup>, or extends an existing<sup>2</sup>, computational framework that allows for a given chemical process to be broken down into different sub-reactions and explored in ways that cannot easily, or at all, be accomplished with current experimental and analytical approaches.<sup>3-4</sup> The calculations also allow us to learn something about the atomic- and molecular-scale processes that define the thermodynamics and kinetics of these reactions. These approaches are applied to a suite of reactions that pertain to the speciation and mobility of actinides in the environment and can ultimately inform future avenues of research and decision-making about actinide waste management and remediation.

Chapter 2 explored the incorporation of U and Pu into magnetite ( $\text{Fe}_3\text{O}_4$ ), a steel corrosion product and widespread accessory mineral phase, using a computational methodology that permits the mixing of cluster and periodic models. Incorporation of actinides into mineral phases represents an effective immobilization pathway for these species in repository near-field environments<sup>5-7</sup>, other contaminated settings<sup>8-9</sup>, or for use in permeable reactive barriers.<sup>10-11</sup> The selected computational approach allows An source and replaced Fe sinks to be considered either as solid or aqueous species. This is a powerful methodology that has been applied to a range of

different contaminant-mineral interactions.<sup>12-14</sup> Computational treatment has the advantage of probing the equilibrium thermodynamics of the reactions, which is generally not achieved in laboratory co-precipitation experiments where such co-precipitation is forced to proceed at high levels of supersaturation.<sup>2</sup> Calculated incorporation reaction energies indicate that U and Pu prefer incorporation into the octahedral cation site. Analysis of the charge and spin distribution within the An-incorporated phases indicates that U and Pu assume an oxidation state between +4 and +5. This finding confirms the results of recent analytical studies on synthesized U-bearing magnetite which have found evidence for the structural-incorporation of U<sup>5+</sup>.<sup>6,15</sup> The calculated atomic structures of the U-incorporated phases agree with available data gathered from experimental products.<sup>6-7,15-16</sup> Our study reports the first structural parameters for Pu-incorporated magnetite and these results can now be used to identify structurally-incorporated Pu in laboratory co-precipitates or samples collected from contaminated environments.

Calculated incorporation energies are sensitive to the speciation of the An source and replaced Fe sink phases. In general, incorporation is most favorable when the An source species is already in the penta- or tetravalent state. Plutonium also has access to a simple substitution pathway in which Pu<sup>3+</sup> replaces Fe<sup>3+</sup> directly without the need for a charge-balancing vacancy. The energetics of this process are comparable to the incorporation of Pu<sup>4+</sup> and Pu<sup>5+</sup> and suggest this pathway may be relevant in reducing environments where aqueous Pu<sup>3+</sup> may be present in low concentrations. Possible sources of error in the incorporation energies are linked to the biases imposed on the reaction equations based on the choice of unpaired spin configuration, solid oxide polymorph, and/or the treatment and accuracy of modeled hydration energies. Future work may consider the incorporation of these contaminants into larger mineral host unit cells, adding steps to model adsorption of aqueous species and incorporation into the surface layer of a growing

mineral, and applying more rigorous, albeit computationally-expensive, methods of modeling hydration (*e.g.*, using more explicit solvent molecules). As it stands, the approach can easily continue to be applied to a wide range of contaminants and minerals to learn something about the structures and relative incorporation thermodynamics.

In Chapter 3, we move on to consider the reactions of actinides in aqueous solution without a mineral phase. This chapter<sup>1</sup> introduces a new computational methodology for calculating the thermodynamics and kinetics of individual sub-processes that constitute a homogeneous redox reaction. The approach draws upon statistical mechanics to calculate the collision frequency of aqueous reactants and then utilizes quantum-mechanical calculations to determine the structures and energies along a reaction path (*i.e.*, sequential geometry optimization calculations at reactant distances of  $\sim 12$  Å down to  $\sim 2$  Å in increments of 0.25 Å). This procedure allows us to extract rates for collision, encounter (outer-sphere) complex formation, and inner-sphere complex formation, as well as the back reactions. The computational scheme is applied to the reactions of plutonyl hydrolysis complexes,  $[\text{PuO}_2(\text{OH})(\text{H}_2\text{O})_5]^0$  and  $[\text{PuO}_2(\text{OH})_2(\text{H}_2\text{O})_4]^0$ , with a suite of reductants and oxidants:  $\text{Fe}^{2+}$ ,  $\text{Fe}^{3+}$ , and hydroxyl radical ( $\bullet\text{OH}$ ). Different chemical and computational parameters, such as ferromagnetic versus antiferromagnetic spin configurations and the use of a dielectric continuum solvation model, are tested to assess their effect on the calculated reaction kinetics. The rates of energetically-favorable outer-sphere complex formation are calculated to be rapid in solutions even at low, environmentally-relevant reactant concentrations (nM and pM). Energy gain associated with outer-sphere complex formation is related to the formation of H bonding networks between the explicitly-modeled coordinating solvent molecules,  $\text{H}_2\text{O}$  and  $\text{OH}^-$ , around the two reactants. Activation energies associated with the transition from outer- to inner-sphere complex are related to the reorganization of these H bonding networks.

Formation of an inner-sphere complex between  $\text{PuO}_2^{2+}$  and  $\text{Fe}^{2+}$  is coincident with proton-coupled electron transfer (PCET; involving the protonation of plutonyl O by  $\text{H}^+$  sourced from water) to reduce  $\text{Pu}^{6+}$  to  $\text{Pu}^{5+}$ . Energetically- and kinetically-favorable inner-sphere complexes are found to form between both plutonyl species with  $\text{Fe}^{3+}$  and  $\bullet\text{OH}$ , but they do not coincide with any redox reactions (*e.g.*, oxidation of  $\text{Pu}^{5+}$  to  $\text{Pu}^{6+}$ ). The results are compared to relevant computational studies of complex formation and homogeneous electron transfer<sup>17-20</sup> and calculated kinetic parameters are compared with available literature data.<sup>21</sup> Future work could easily extend this approach to model complex formation and redox reactions of reactants in solution.

To understand the effect of stronger ligands on complex formation kinetics and redox reactions, the method developed in Chapter 3 was applied to the actinyl carbonate system and reactions with two reductants,  $\text{Fe}^{2+}$  and  $\text{H}_2\text{S}$ . Uranyl, neptunyl, and plutonyl all form stable complexes with carbonate molecules. For this study, the isostructural U, Pu, and Np tricarbonato complex,  $[\text{AnO}_2(\text{CO}_3)_3]^{5-/4-}$ , which is stable at alkaline pH conditions and is assumed to be the most common carbonate complex under carbonate-rich conditions<sup>22</sup> that are relevant to certain groundwater and marine environments, was selected for further investigation. It was hypothesized that the ring of coordinating carbonate molecules around the actinyl center would result in slower kinetics for inner-sphere complex formation versus the less rigid water and hydroxide complexes explored in Chapter 3. The calculations reveal that rapid outer-sphere complex formation occurs between all actinyl tricarbonato complexes with  $\text{Fe}^{2+}$  and  $\text{H}_2\text{S}$ . As An-reductant distances are decreased to move towards an inner-sphere configuration, large energy barriers are measured for many of the reactant pairs. These energy barriers are caused by the disruption of the coordinating carbonate groups and H bonding networks between solvent molecules. The kinetics of inner-sphere complex formation are prohibitively slow for several of the tested reactions. Unlike the reactions

of plutonyl hydrolysis complexes, we do not observe spontaneous electron transfer from either  $\text{Fe}^{2+}$  or  $\text{H}_2\text{S}$  to reduce  $\text{An}^{6+}$  or  $\text{An}^{5+}$ . Manual transfer of protons onto actinyl O atoms was tested for a set of uranyl and plutonyl inner-sphere structures. Thermodynamically-favorable PCET pathways were found for both  $\text{UO}_2^{2+}$  and  $\text{PuO}_2^{2+}$  tricarbonates reacted with  $\text{Fe}^{2+}$  indicating that this reaction mechanism appears to be necessary for redox to occur. Plutonyl tr carbonate reduction was calculated to be more thermodynamically-favorable which is in line with our understanding of the relative electron affinities for the  $\text{An}^{6+}$  species.<sup>23</sup> These results indicate that reduction of actinyls is inhibited by complexation with carbonate, with the tr carbonate complex likely being the most effective shield against electron transfer. We find that PCET is required for reduction to occur and in the elevated pH environments where these carbonate complexes dominate, this process may be less likely to proceed due to the relatively proton-poor conditions. Overall, these complexes will maintain the solubility and thus, mobility, of these contaminants in solution and protect them from reaction with available reductants.

The method presented and applied to actinyl reactions in Chapters 3 and 4 also allows us to learn something about which sub-processes in a multi-step reaction are rate-limiting. Comparing the results of the plutonyl hydrolysis complex reactions with the calculated kinetics of the tr carbonate species, we find that inner-sphere complex formation rates are significantly lower for the carbonate complexes. From this result, we can infer that this step is one that may be catalyzed by a mineral surface. Complex formation on mineral surfaces may be stronger than the homogenous outer- and inner-sphere complexes and lead to more favorable energetics for the decarbonation of actinyl groups. Overall, a comparison of the results for the plutonyl reactions in Chapters 3 and 4 illustrates the effect of the relatively strong ligand, carbonate, on the thermodynamics of inner-sphere complex formation. Our research group is now working on

studies of actinyl incorporation into carbonate minerals and calculating the reaction energies of individual sub-steps in this process, including adsorption of aqueous actinyls to mineral (*e.g.*, calcite) surfaces, incorporation of into the first atomic layer, and incorporation into the bulk structure. In a carbonate-bearing system, homogeneous reactions, adsorption of actinyls to mineral surfaces, and precipitation of An-incorporated carbonate minerals are competing processes. By comparing the results presented in this dissertation with the ongoing study of An-carbonate solid phases, we can discern which process is most likely to control the speciation of actinyls under different solution conditions.

Moving forward, the computational methods used in the studies of structural incorporation and reactions of aqueous complexes could be applied to a wide range of mineral and contaminant interactions. With further refinement, these models may be able to better capture the role of hydration, which appears to be a major control on reaction thermodynamics and kinetics. Modifying these methodologies to include more explicit solvent molecules is perhaps the most straightforward path, but comes at increased computational cost. Mixing reactive force field and quantum-mechanical approaches, possibly in a molecular dynamics calculation, may be another avenue and has shown promise particularly for reactions where the transfer of H<sup>+</sup> could be important.<sup>24</sup> Additionally, the method presented and implemented in Chapters 3 and 4 could relatively easily be extended to reactions at mineral surfaces. In both homogeneous and heterogeneous applications, different hydration schemes and degrees of computational rigor (*e.g.*, density functionals and basis sets) can be selected to suit the goals of the study.

It is envisioned that the thermodynamic and kinetic parameters calculated in all three of the main chapters of this dissertation may serve as data points in a growing catalog of information about actinide geochemistry. With a large enough catalog, it may eventually be possible to develop

a kinetic Monte Carlo approach<sup>25-26</sup> for evaluating, in a probabilistic manner, the equilibrium interactions between a comprehensive suite of processes that define a chemical system. The methods and results presented here encompass only some of the reactions that would be needed to fully describe a natural system, however, the bulk incorporation and homogenous redox reaction processes are certainly important components. Further research, potentially utilizing modified versions of the approaches taken in this dissertation, will be required to describe the thermodynamics and kinetics of adsorption to mineral surfaces, the formation of inner-sphere complexes on those minerals, the rates of homo- and heterogeneous electron transfer, and incorporation into the surface layers of minerals. In addition, the types of reactions calculated in Chapter 2 (bulk solid incorporation) and Chapters 3 and 4 (aqueous diffusion, outer- and inner-sphere complex formation, homogeneous redox) will need to be extended to other mineral phases, complex-forming ligands, reductants, and oxidants. Ideally, with effort on all of these fronts, it will eventually be possible to describe and predict the speciation, reactivity, and mobility of contaminants in realistic chemical environments with accuracy.

## References

1. Bender, W. M.; Becker, U., Determining the kinetics of discrete aqueous redox reaction sub-steps using computational methods: Application to reactions of plutonyl ( $\text{PuO}_2^{+/2+}$ ) with  $\text{Fe}^{2+}$ ,  $\text{Fe}^{3+}$ , and hydroxyl radical ( $\bullet\text{OH}$ ). *Am J Sci* **2018**, *318*, 893-920.
2. Shuller-Nickles, L. C.; Bender, W. M.; Walker, S. M.; Becker, U., Quantum-mechanical methods for quantifying incorporation of contaminants in proximal minerals. *Minerals* **2014**, *4* (3), 690-715.
3. Cygan, R. T., Molecular modeling in mineralogy and geochemistry. *Molecular Modeling Theory: Applications in the Geosciences* **2001**, *42*, 1-35.
4. Kubicki, J. D., *Molecular modeling of geochemical reactions*. Wiley: West Sussex, UK, 2016; p 422.
5. Duff, M. C.; Coughlin, J. U.; Hunter, D. B., Uranium co-precipitation with iron oxide minerals. *Geochimica et Cosmochimica Acta* **2002**, *66* (20), 3533-3547.
6. Marshall, T. A.; Morris, K.; Law, G. T. W.; Mosselmans, J. F. W.; Bots, P.; Roberts, H.; Shaw, S., Uranium fate during crystallization of magnetite from ferrihydrite in conditions relevant to the disposal of radioactive waste. *Mineralogical Magazine* **2015**, *79* (6), 1265-1274.
7. Nico, P. S.; Stewart, B. D.; Fendorf, S., Incorporation of oxidized uranium into Fe (hydr)oxides during Fe(II) catalyzed remineralization. *Environmental Science & Technology* **2009**, *43* (19), 7391-7396.
8. Abdelouas, A., Uranium mill tailings: Geochemistry, mineralogy, and environmental impact. *Elements* **2006**, *2* (6), 335-341.
9. Burns, P. C.; Sigmon, G. E. In *Uranium - Cradle to grave*, Uranium - Cradle to Grave, Winnipeg, Burns, P. C.; Sigmon, G. E., Eds. Mineralogical Society of Canada: Winnipeg, 2013; pp 7-14.
10. Kober, R.; Welter, E.; Ebert, M.; Dahmke, A., Removal of arsenic from groundwater by zerovalent iron and the role of sulfide. *Environmental Science & Technology* **2005**, *39* (20), 8038-8044.
11. Vermeul, V. R.; Szecsody, J. E.; Fritz, B. G.; Williams, M. D.; Moore, R. C.; Fruchter, J. S., An injectable apatite permeable reactive barrier for in situ Sr-90 immobilization. *Ground Water Monitoring and Remediation* **2014**, *34* (2), 29-42.
12. Shuller, L. C.; Ewing, R. C.; Becker, U., Quantum-mechanical evaluation of Np-incorporation into studtite. *Am Mineral* **2010**, *95* (8-9), 1151-1160.
13. Shuller, L. C.; Ewing, R. C.; Becker, U., Np-incorporation into uranyl phases: a quantum-mechanical evaluation. *Journal of Nuclear Materials* **2013**, *434* (1-3), 440-450.

14. Walker, S. M.; Becker, U., Uranyl (VI) and neptunyl (V) incorporation in carbonate and sulfate minerals: Insight from first-principles. *Geochimica et Cosmochimica Acta* **2015**, *161*, 19-35.
15. Roberts, H. E.; Morris, K.; Law, G. T. W.; Mosselmans, J. F. W.; Bots, P.; Kvashnina, K.; Shaw, S., Uranium(V) incorporation mechanisms and stability in Fe(II)/Fe(III) (oxyhydr)oxides. *Environmental Science & Technology Letters* **2017**, *4* (10), 421-426.
16. Pidchenko, I.; Kvashnina, K. O.; Yokosawa, T.; Finck, N.; Bahl, S.; Schild, D.; Polly, R.; Bohnert, E.; Rossberg, A.; Gottlicher, J.; Dardenne, K.; Rothe, J.; Schafer, T.; Geckeis, H.; Vitova, T., Uranium redox transformations after U(VI) coprecipitation with magnetite nanoparticles. *Environmental Science & Technology* **2017**, *51* (4), 2217-2225.
17. Collins, R. N.; Rosso, K. M., Mechanisms and rates of U(VI) reduction by Fe(II) in homogeneous aqueous solution and the role of U(V) disproportionation. *Journal of Physical Chemistry A* **2017**, *121* (35), 6603-6613.
18. Taylor, S. D.; Marcano, M. C.; Rosso, K. M.; Becker, U., An experimental and ab initio study on the abiotic reduction of uranyl by ferrous iron. *Geochimica et Cosmochimica Acta* **2015**, *156*, 154-172.
19. Privalov, T.; Macak, P.; Schimmelpfennig, B.; Fromager, E.; Grenthe, I.; Wahlgren, U., Electron transfer in uranyl(VI)-uranyl(V) complexes in solution. *J Am Chem Soc* **2004**, *126* (31), 9801-9808.
20. Privalov, T.; Schimmelpfennig, B.; Wahlgren, U.; Grenthe, I., Reduction of uranyl(VI) by iron(II) in solutions: An ab initio study. *Journal of Physical Chemistry A* **2003**, *107* (4), 587-592.
21. Moelwyn-Hughes, E. A., *The chemical statics and kinetics of solutions*. Academic Press: London, 1971; p 530.
22. Clark, D. L.; Hobart, D. E.; Neu, M. P., Actinide carbonate complexes and their importance in actinide environmental chemistry. *Chemical Reviews* **1995**, *95* (1), 25-48.
23. Steele, H. M.; Guillaumont, D.; Moisy, P., Density functional theory calculations of the redox potentials of actinide(VI)/actinide(V) couple in water. *Journal of Physical Chemistry A* **2013**, *117* (21), 4500-4505.
24. Tirlir, A. O.; Hofer, T. S., Structure and dynamics of the uranyl tricarbonate complex in aqueous solution: Insights from quantum mechanical charge field molecular dynamics. *Journal of Physical Chemistry B* **2014**, *118* (45), 12938-12951.
25. Voter, A. F., Introduction to the kinetic Monte Carlo method. *Radiation Effects in Solids* **2007**, *235*, 1-23.
26. Battaile, C. C., The kinetic Monte Carlo method: Foundation, implementation, and application. *Computer Methods in Applied Mechanics and Engineering* **2008**, *197* (41-42), 3386-3398.

